UNIVERSITY OF CALIFORNIA, SAN DIEGO

Harnessing Biology for Bioinspired Structural Materials with Intrinsic and Extrinsic Freeze Casting

A dissertation submitted in partial satisfaction of the requirements for the degree Doctor of Philosophy

in

Materials Science and Engineering

by

Steven Eric Naleway

Committee in charge:

Professor Joanna McKittrick, Co-Chair
Professor Marc A. Meyers, Co-Chair
Professor Olivia A. Graeve
Professor John A. Hildebrand
Professor Michael T. Tolley

2016

The Dissertation of Steven Eric Naleway is approved, and it is acceptable in quality and form for publication on microfilm and electronically:

_____

_____

_____

_____
Co-Chair

_____
Co-Chair

University of California, San Diego

2016

TABLE OF CONTENTS

LIST OF FIGURES

LIST OF TABLES

ACKNOWLEDGEMENTS

I would like to gratefully acknowledge my co-advisors, Joanna McKittrick and Marc Meyers for their intellectual guidance and financial support of my research. I would also like to thank my committee members, Olivia Graeve, John Hildebrand and Michael Tolley for their commitment, suggestions and support. I am grateful to all of my colleagues and collaborators as well as to my mentees, most prominently Yajur N. Maker, Christopher Yu, Rachel Hsiong, and Michael Ix whose hard work has made my research possible. Finally, I would like to thank my family and my wife, Kate for their love and support.

Some of the text and figures presented in this dissertation have been published in peer reviewed journals. In these cases, explicit, written permission for the reproduction of this material in this dissertation has been attained. Specific citations are noted here:

Chapter 1.2 and 1.3, in part, are a reprint of the material as it appears in "Structure and mechanical properties of selected protective systems in marine organisms" Materials Science and Engineering C, vol. 59, pp 1143-1167, 2016. The dissertation author was the primary investigator and author on this paper. This work was also co-authored by Jennifer R. A. Taylor, Michael M. Porter, Marc A. Meyers and Joanna McKittrick.

Chapter 2, in part, is a reprint of the material as it appears in "Structural design elements in biological materials: Application to bioinspiration" Advanced Materials, vol. 27, pp 5455-5476, 2015. The dissertation author was the primary investigator and author on this paper. This paper was co-authored by Michael M. Porter, Joanna McKittrick and Marc A. Meyers.

Chapter 3, in part, is a reprint of the material as it appears in "Bioinspired composites from freeze casting using clathrate hydrates" Materials & Design, vol. 71, pp

62-67, 2015. The dissertation author was the primary investigator and author on this paper. This paper was co-authored by Christopher F. Yu, Michael M. Porter, Arijit Sengupta, Peter M. Iovine, Marc A. Meyers and Joanna McKittrick.

Chapter 4, in part, is a reprint of the material as it appears in "Bioinspired intrinsic control of freeze cast composites: Harnessing hydrophobic hydration and clathrate hydrates" Acta Materialia, vol. 114, pp 67-79, 2016. The dissertation author was the primary investigator and author on this paper. This paper was co-authored by Christopher F. Yu, Rachel L. Hsiong, Arijit Sengupta, Peter M. Hildebrand, Marc A. Meyers and Joanna McKittrick.

Chapter 7, in part, is a reprint of the material as it appears in "Reproducibility of ZrO_2-based freeze casting for biomaterials" Materials Science and Engineering C, vol. 61, pp 105-112, 2016. The dissertation author was the primary investigator and author on this paper. This paper was co-authored by Kate C. Fickas, Yajur N. Maker, Marc A. Meyers and Joanna McKittrick.

This work is supported financially by a Multi-University Research Initiative through the Air Force Office of Scientific Research of the United States (AFOSR-FA9550-15-1-0009).

VITA

2011	Bachelor of Science, Oregon State University
2011-2013	Graduate Teaching Assistant, Department of Mechanical Engineering, Oregon State University
2013	Master of Science, Oregon State University
2013-2016	Graduate Research Assistant, Materials Science and Engineering Program, University of California, San Diego
2016	Doctor of Philosophy, University of California, San Diego

PUBLICATIONS

"A highly fatigue-resistant Zr-based bulk metallic glass" Metallurgical and Materials Transactions A, vol. 44A, pp 5688-5693, 2013.

"Advancing the understanding of bulk metallic glasses as structural materials through exploration of mechanical properties" M. S. Thesis, Oregon State University, 2013.

"Size-dependent fracture toughness of bulk metallic glasses" Acta Materialia, vol. 70, pp 198-207, 2014.

"β relaxation and low-temperature aging in a Au-based bulk metallic glass: From elastic properties to atomic-scale structure" Physical Review B, vol. 89, pp 174204, 2014.

"Mechanical properties of suture materials in general and cutaneous surgery" Journal of Biomedical Materials Research B, vol. 103B, pp 735-742, 2015.

"Bioinspired composites from freeze casting using clathrate hydrates" Materials & Design, vol. 71, pp 62-67, 2015.

"Cyclic mechanical loading promotes bacterial penetration along composite restoration marginal gaps" Dental Materials, vol. 31, pp 702-701, 2015.

"The armored carapace of the boxfish" Acta Biomaterialia, vol. 23, pp 1-10, 2015.

"Structural design elements in biological materials: Application to bioinspiration" Advanced Materials, vol. 27, pp 5455-5476, 2015.

"Structure and mechanical properties of selected protective systems in marine organisms" Materials Science and Engineering C, vol. 59, pp 1143-1167, 2016.

"Reproducibility of ZrO_2-based freeze casting for biomaterials" Materials Science and Engineering C, vol. 61, pp 105-112, 2016.

"A protocol for bioinspired design: A ground based sampler based on sea urchin jaws" Journal of Visualized Experiments, pp e53554, 2016.

"Structural analysis of the tongue and hyoid apparatus in a woodpecker" Acta Biomaterialia, vol. 37, pp 1-13, 2016.

"Bioinspired intrinsic control of freeze cast composites: Harnessing hydrophobic hydration and clathrate hydrates" Acta Materialia, vol. 114, pp 67-79, 2016.

ABSTRACT OF THE DISSERTATION

Harnessing Biology for Bioinspired Structural Materials with Intrinsic and Extrinsic Freeze Casting

by

Steven Eric Naleway

Doctor of Philosophy in Materials Science and Engineering

University of California, San Diego, 2016

Professor Joanna McKittrick, Co-Chair

Professor Marc A. Meyers, Co-Chair

Bioinspiration (also known as bioinspired design) utilizes engineering and science to take lessons from nature and employ them to advanced materials and techniques to create designs that can bring benefit to society. One such bioinspired process is that of freeze casting. This process mimics the templating fabrication method used by many biological composites where a template of a biopolymer will form and direct the deposition of

biomineral. Similarly, freeze casting uses a template of growing ice crystals to form and direct the formation of a porous ceramic scaffold. The true advantage of the freeze casting process is the ability to alter the final material's microstructure with relatively simple alterations to the processing conditions and parameters. Here these alterations and methods of controlling the final material structure are suggested to be grouped as either intrinsic control methods, those working within the freeze casting process that affect the chemistry and/or freezing dynamics, or extrinsic control methods, those working on the freeze casting process though outside forces. This dissertation describes examples of each intrinsic and extrinsic control of the freeze casting process. Intrinsic control was demonstrated through the use of chemical additives (ethanol, isopropanol, *n*-propanol and *n*-butanol) that induced enlarged structures through the formation of clathrate hydrates and hydrophobic hydration. These structures were shown to be the cause of enlarged porosity in the final scaffolds. Bioinspired, two-phase polymer-ceramic composites created from these scaffolds were shown to have increased strength over both the infiltrating polymeric phase and the uninfiltrated scaffolds due to a resistance to the primary ceramic failure mode of buckling. Extrinsic control was demonstrated through the use of sacrificial 3D printed templates that created bone-like materials with porosity at multiple length scales. These materials were shown to be biocompatible and cell viable for use as biomedical implants. Finally, while control of these structures is impressive, it was shown through statistical analyses that there is significant variability in the final microstructures and mechanical properties of materials created through freeze casting. Therefore, while the technique holds great promise, additional research is required to mass produce similar materials for biomedical and commercial applications.

1. Introduction

Providing sophisticated and ingenious solutions to the myriad of challenges that plague the human race is a task that has fallen upon science for millennia. While this is a burden that most scientists willingly accept, the process of providing these solutions is an arduous one. The scientific steps of synthesis, processing and analysis are a challenge, however, it is often the nucleation of novel ideas and designs that stands in the way of progress. Famous examples of miraculous and spontaneous genius (think of Sir Isaac Newton and his apple tree) notwithstanding, true inspiration is difficult. However, there are methods of circumventing this obstacle by drawing upon pre-approved solutions. Perhaps the most successful of these is the act of bioinspiration (also known as bioinspired design), which learns from nature to develop novel scientific and engineering designs.

Appreciation for the power of bioinspiration can be better understood by considering how one looks at nature. Most would think of a lush forest or white, sandy beaches. However, bioinspiration suggests a different way of thinking of nature. Natural structures and organisms have been created through hundreds of millions of years' worth of evolution, which can be considered design experience driven by natural selection. These structures are self-assembled from the bottom-up, which is difficult even with our most advanced current fabrication techniques. This is done with materials that are renewable, biodegradable and multi-functional and assembled using life-friendly processes and processing conditions (pressures at ~1 atm and temperatures at ~300 K). In spite of these requirement, natural structures offer a wide range of impressive structural and mechanical properties that are tailored to specific loading conditions and balance a variety of needs from weight reduction to wear resistance to fracture toughness. Therefore, a very different

way of thinking about nature is to consider it green, high performance engineering. Observing nature through this guise allows for the inspiration of many scientific designs that learn from or mimic nature and its constructs; this is the essence of bioinspiration.

Performing bioinspiration can seem nebulous to those unfamiliar in connecting biology and nature to engineering and science. It is, by necessity, multidisciplinary and collaborative. However, to ease this process, Frank, Naleway et al. [1] recently developed a system, known as the bioinspiration cycle, that provides a framework for the development of new bioinspired science and engineering.

1.1 The Bioinspiration Cycle

Through the bioinspiration cycle, bioinspiration and bioinspired design can be considered to be a four part cycle that, ideally, both learns from and gives back to nature. These four components are defined as:

(1) *Biology*: Developing an understanding of what materials and processes organisms employ from a biological perspective. This process requires the input of biologists, evolutionary biologists and ecologists as it strives to bring the organisms perspective (so to speak) into relief. It answers the "why", "what", "who" and "where" questions such as: Why was this structure or behavior evolved (e.g. to attract a mate, to capture prey, to defend against predation)? What are the environmental conditions that this organism faces? Who are the predators and/or prey of this organism? Where is this organism's habitat? This step can also provide excellent guidance for the birthing of new designs as a clear understanding of biology can identify exemplary organisms and behaviors that may be of interest in developing new bioinspired designs.

(2) *Materials Science*: Using the tools and techniques available in the fields of engineering, chemistry and physics to dissect (physically and/or theoretically) organisms and understand how they thrive in their natural environments. While step (1) provides biology and ecology's input, materials science (also known as biological materials science) provides input from the rest of the STEM fields. Here structures and behaviors can be analyzed independently of their natural environment to determine their structural, mechanical, chemical, optical or electromagnetic properties. Materials science strives to answer the "how" questions such as: How does this structure provide high toughness with brittle constituents? How can this organism survive under such harsh conditions (e.g. the

humongous pressures at the bottom of the ocean, the sub-freezing temperatures at the polar ice caps)? How is this organism capable of making the best of its limited resources? While connected here to the bioinspiration cycle, a multitude of biological materials science research is done with the sole focus of better understanding the natural world for environmental, ecological, engineering and commercial applications.

(3) *Bioinspiration*: Employing the lessons learned from nature to modern materials and techniques to form advanced designs that can bring benefit to society. With the answers supplied by biology and materials science, bioinspiration picks and chooses important structures, designs and concepts and employs them to novel designs. Here, engineering is the key to the implementation of the laws of nature and creation of new products.

(4) *Bioexploration and Ecology*: Developing a deeper understanding of biology and biological materials from the process of bioinspiration. This is a relatively new aspect of the bioinspiration cycle, first proposed by Porter et al. [2]. In addition, the concept of ecology can also be located here. While most bioinspiration is a linear path, learning from nature to create a final design, this fourth step completes the cycle and provides a benefit back to biology, ecology and nature. This can take place either through a deeper understand of natural structures (bioexploration) or a better appreciation of the benefit that nature can provide to humanity and an associated drive to protect it (ecology).

To better explain this process, the four components of this bioinspiration cycle are diagramed in Figure 1 through the guise of a bioinspired sediment sampler inspired by the sea urchin’s jaws. To provide a tangible example of the bioinspiration cycle, this work by Frank and Naleway et al. [1] will be described in greater detail.

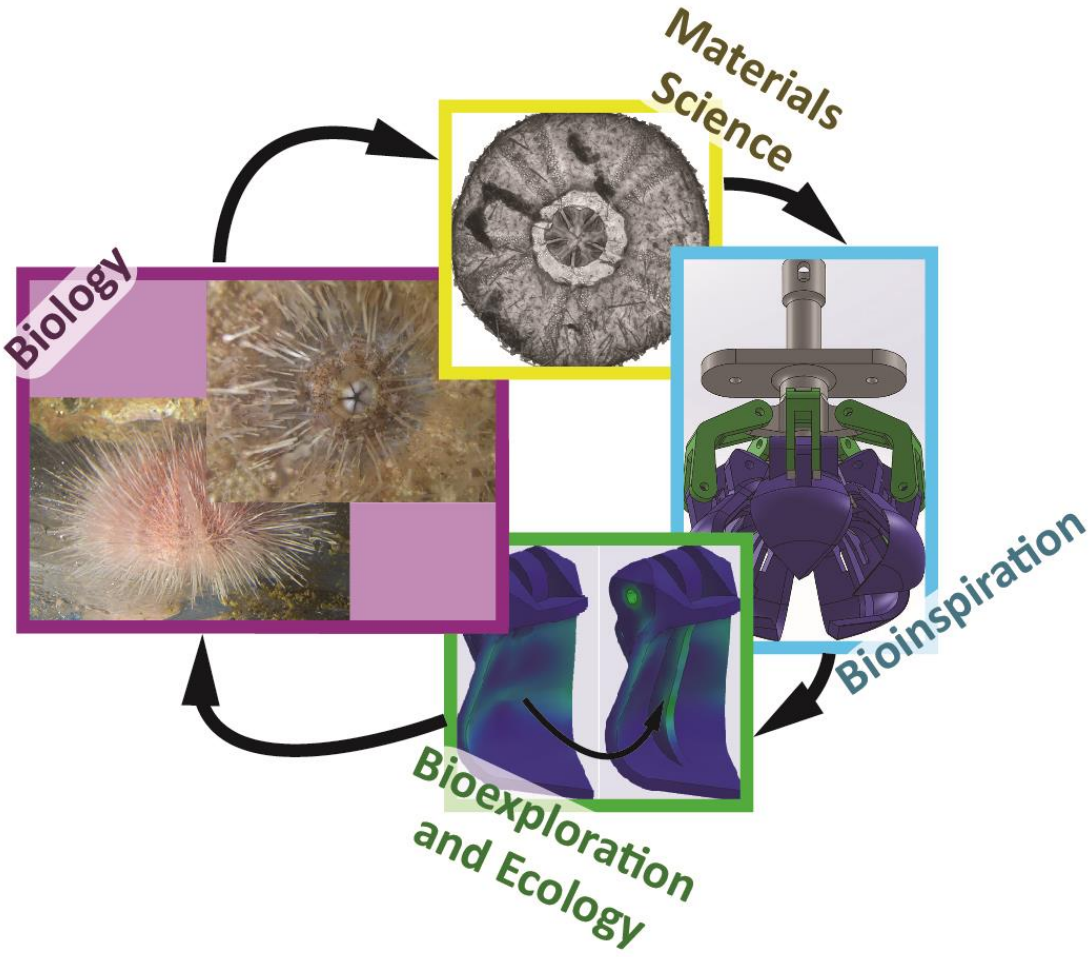

Figure 1. The bioinspiration cycle highlighting the important steps of biology, materials science, bioinspiration and bioexploration. This particular example focuses upon a bioinspired sediment sampler from the jaws of the sea urchin. Inspired by [1].

Through *Biology*, collaborations were formed with the Scripps Institution of Oceanography (La Jolla, CA, USA) and experts on the pink sea urchin (*Strongylocentrotus fragilis*). This allowed for better understanding of the sea urchin, a marine invertebrate that is generally covered with sharp defensive spines, whose habitat is the rocky beds of the ocean floor and tidal zone. These organisms feed by scraping vegetation and algae off of hard rocks and corals. It is this feeding that provides the inspiration in this bioinspired design, as it is driven by the jaws (named the "Aristotle's lantern" after the famous

philosopher), which display beautiful five-fold symmetry. Finally, through these collaborations, fresh specimens were provided.

Materials Science went about the process of investigating these jaws. Samples were dissected and imaged in their entirety through nano-computed tomography (nano-CT, Figure 2). Imaging through nano-CT allowed for clear visualization of the tooth structure and design.

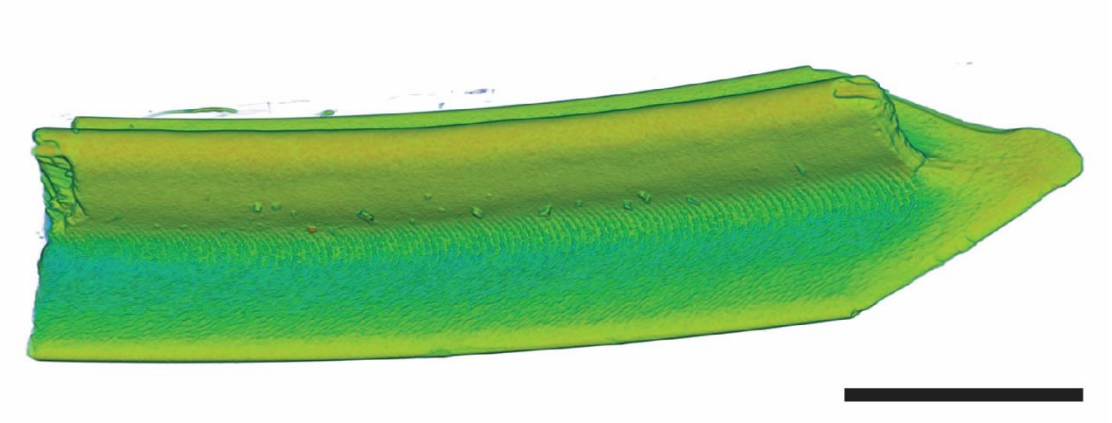

Figure 2. Nano-CT image of an individual sea urchin tooth with the reinforcing keel protruding upwards. Scale bar: 500 μm.

Bioinspiration utilized the knowledge provided through biology collaborations and the imagery provided by materials science to design and construct a sediment sampler. Within this step it is important to understand that the design was not copied exactly, but important features were selected and mimicked through computer aided design (CAD) modeling. These features included the five-fold symmetry, the reinforcing keel and the overlapping nature of the teeth. To augment these features, the teeth were given a more rounded design to increase the amount of material that could be collected and the entire design was affixed to a slider-crank system to provide actuation. It is important to understand that decisions of which features to incorporate (or omit) from the design were

dictated by engineering knowledge as well as an iterative process of fabrication, testing and redesign. The design was fabricated out of ABS plastic using 3D printing to form a final product, which was affixed to a remote-controlled rover, nicknamed the "Mars Urchin" for its potential use as a sediment sample collection vehicle on the Martian surface (Figure 3).

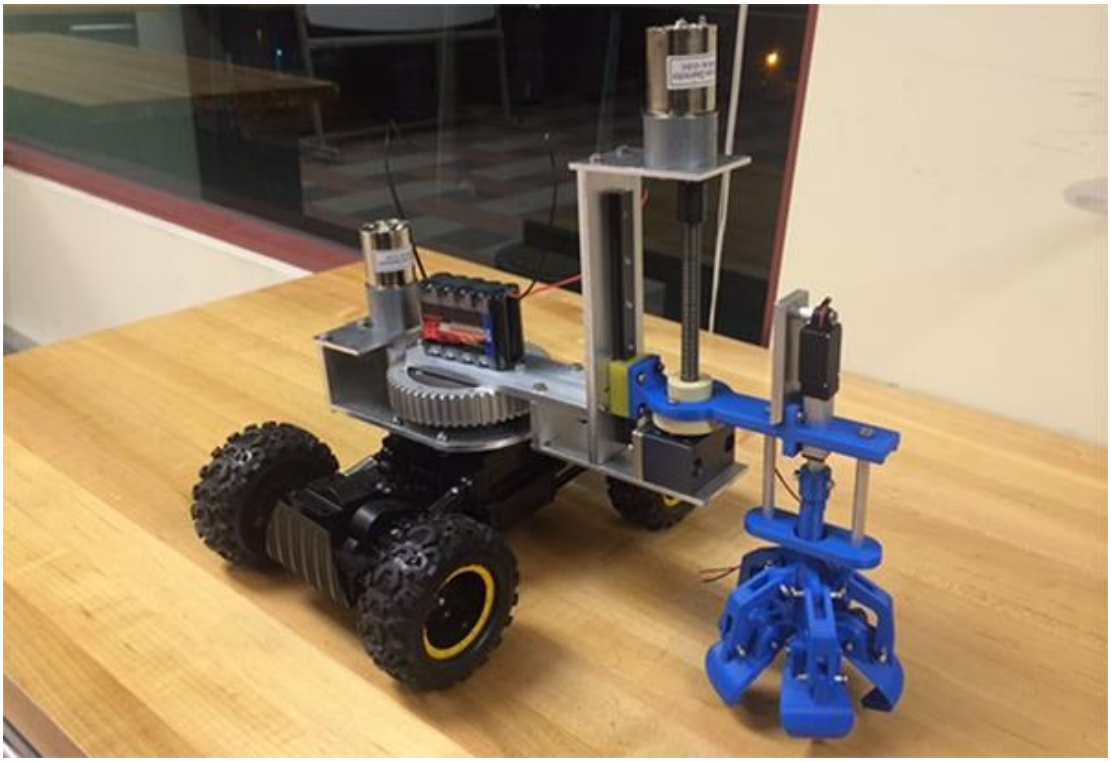

Figure 3. Bioinspired sampler design based upon the sea urchin's jaws attached to a remote control rover. The entire device was nick-named the "Mars Urchin".

Bioexploration was able to provide new insight into the biological structure of the sea urchin. When designing the teeth of the final sampler, an initial design did not include the reinforcing keel. However, experimental and computational analysis of the structure determined that the inclusion of a keel structure to the tooth design could reduce the maximum stress by ~15% when teeth with and without the keel were stressed by the same load [1]. This novel information not only provided greater insight into the bioinspired

design, but also provided a greater understanding of the modern sea urchin, which has evolved the keel design, thus providing it with an advantage over its keel-less ancestors [3].

The bioinspiration cycle and the presented example provides an important understanding of the overarching motivations that drive the research described in this dissertation. The projects and conclusions within this dissertation are focused upon the specific field of bioinspiration. However, to provide a better understanding of this work, certain specific aspects of biological materials science must be presented.

1.2 Biological Materials Science Background

The study of biological materials within materials science provides the nexus where the fields of physics, engineering, chemistry and biology converge to understand and harness the vast body of knowledge that can be learned from the natural world. The findings of this research provide for better biological understanding of the complex and unique organisms and structures in nature. In addition, this knowledge provides inspiration for the peripheral fields of bioinspired materials, where synthetic structures are inspired by nature, and biomaterials, where materials and structures are designed for optimum compatibility with biological systems.

Biological materials are created from a relatively small number of constituents that can be divided into two general categories, biominerals and biopolymers. Common biominerals include calcium carbonate (e.g. calcite and aragonite), calcium phosphate (e.g. hydroxyapatite) and silica [4-7]. Common biopolymers include collagen, keratin, chitin, cellulose and elastin [4-7]. Of note, there are many other examples of biopolymers and biominerals found in biological materials, with those listed here generally the most

common. The biological materials formed from these constituents can be further identified in two groups [5]:

(1) Non-mineralized (or "soft") biological materials that consist of only biopolymers and generally have highly directed properties that depend on their function.

(2) Mineralized (or "hard") biological materials that are hierarchically structured composites of both biopolymers and biominerals.

While still bound by the same physical laws, biological materials are starkly different from synthetic ones. To succinctly describe the unique qualities of biological materials, seven interrelated features have been identified (inspired by Arzt [8] and expanded by Meyers et al. and Chen et al. [4, 5, 7, 9]). These characteristics are: self-assembly (with materials assembled from the bottom-up), multi-functionality (materials often serve more than one purpose within an organism), hierarchical design (materials are organized along multiple length scales and have properties that translate from one level to the next), hydration effects (most materials have properties that vary with the level of hydration, one often observed example is a tradeoff of higher strength to higher toughness with increasing hydration), mild synthesis conditions (materials are formed at or near ambient temperature and pressure), evolutionary design and environmental constraints (materials have been molded by the availability of scarce resources over millions of years), and self-healing capability (materials are often able to regrow, reform and heal when damaged). While these apply throughout biology, a set of characteristic features specific to marine organisms has also been proposed by Naleway et al. [10] that are not shared by their terrestrial counterparts. These marine specific conditions include: complete hydration, variation in hydrostatic pressure (0.1–100MPa), temperature (−2–38 °C) and salinity (34–

36 ppt), as well as near constant motion from currents and swells. These conditions vary throughout the ocean, being more consistent in the pelagic and deep benthic zones while experiencing more variability in the nearshore and shallows (e.g. intertidal zones, shallow bays and lagoons, salt marshes and mangrove forests). Of note, many marine organisms are capable of migrating between these zones, forcing them to be dynamic through many environments. Whether terrestrial or marine, these environmental constraints have shaped all structural biological materials.

The combination of these qualities provides for high levels of complexity and performance within marine biological materials. As an example, the toughness of biological materials and their constituents is plotted as a function of the elastic modulus in Figure 4. The high toughness of biopolymers together with the high strength of biominerals is combined into many composite biological materials (e.g. bone and mollusk shell) [11]. When compared to engineered synthetic materials, metals and ceramics are capable of providing mechanical properties up to an order of magnitude higher than biological materials. However, biominerals and biopolymers are mechanically comparable with many synthetic engineering composites and engineering polymers, respectively [7].

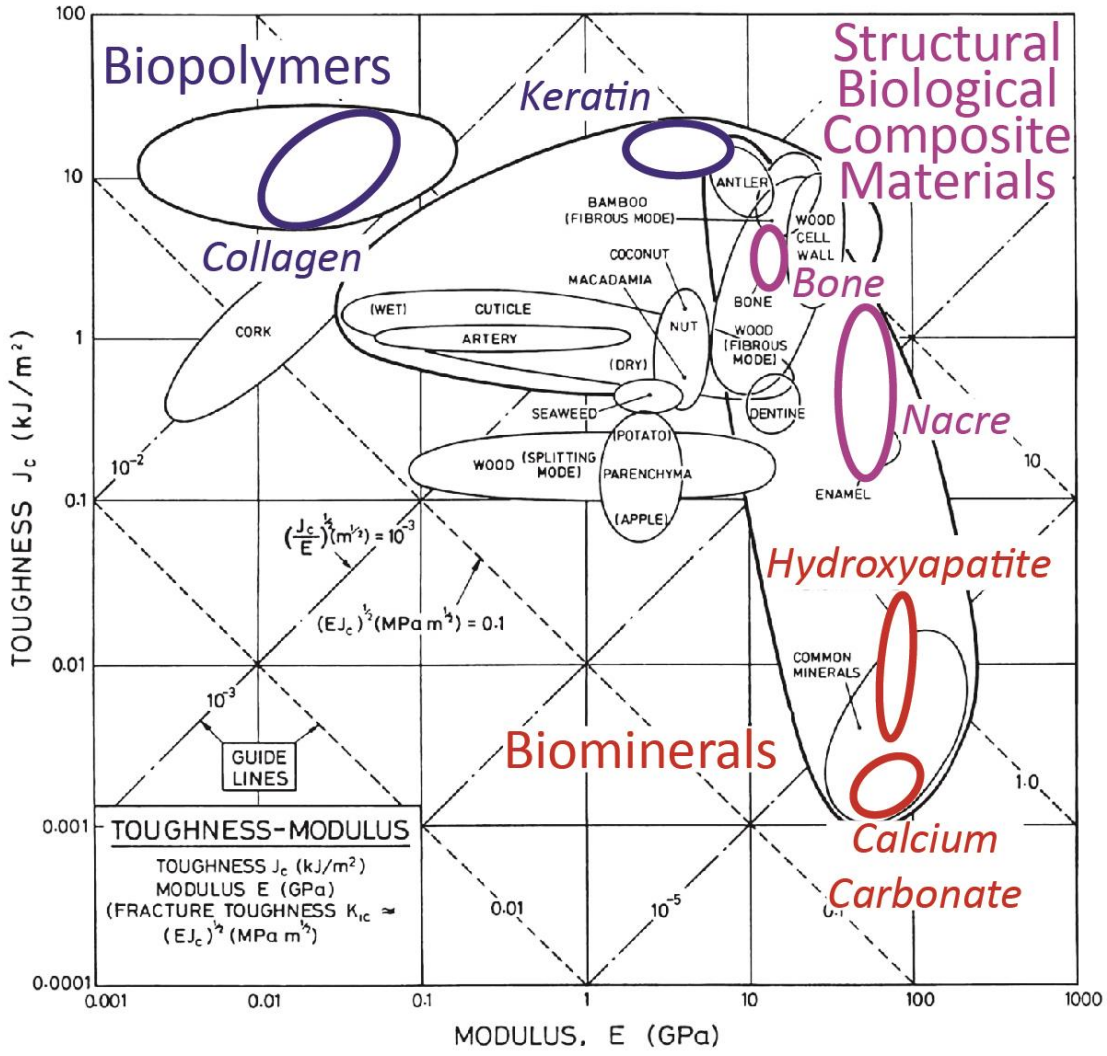

Figure 4. Toughness as a function of elastic modulus for biological materials. Adapted with permission from [10].

These impressive mechanical properties can, in large part, be attributed to the complex hierarchical structuring of these biological materials. This hierarchy, which plays out at length scales from the nano to the macro, allows for a host of structural advantages. These can manifest themselves in a number of common designs, a system of which was proposed by Naleway et al. [12] as "structural design elements" that will be discussed later in this dissertation.

1.3 Bioinspiration from Templating

As described in the bioinspiration cycle, when looking to produce materials and structures that are bioinspired by biological materials it is important to fully understand the concepts behind nature's designs. To this end, natural fabrication techniques can provide great insight into effective bioinspired methodologies. To explore this further, the natural synthesis of two of the most widely researched biological materials, the nacre of abalone shells and cortical bone of mammals, will be discussed and analyzed for their common strategies.

Abalones and many other mollusks protect themselves through shells made of a hard, external calcite layer and a tough internal nacreous layer made of aragonite, chitin and proteins (Figure 5a) [13-16]. These shells forfeit all flexibility in favor of high strength, which is reflected in the relative proportions of rigid biomineral to ductile biopolymer found in the shells of red abalone (19:1) [17], where biomineral severely outweighs biopolymer. In spite of this, many of these shells manage to provide optimized toughness, much higher than pure calcium carbonate [11, 13, 14]. This is realized through the brick-and-mortar structure of nacre (Figure 5b) [13-15]. To grow this tough microstructure, mollusks employ complex assembly techniques. In the example case of abalone, growth is mediated by an organic interlayer comprised of chitin, an organic silk and acidic proteins in such a manner that successive layers of calcium carbonate (aragonite) tablets are deposited [16, 18-21]. Naturally, the growth of aragonite crystals is highly anisotropic, with the C direction in the orthorhombic cell (normal to the largest surface) having a much greater velocity than either of the orthogonal A or B directions. This would lead to the formation of needle-like structures without mediation. To regulate the growth, the

epithelial layer of the organism generates a porous chitin-based membrane and deposits it on the growth surface. The sequence shown in Figure 5c (progressing from top to bottom) shows the deposition of one such layer and the manner by which it alters the growth. The C-growth direction is slowed down, while growth in directions A and B proceeds normally as the Ca^{+2} and CO_3^{-2} ions traverse the membrane. The resulting shape of the crystal is changed from a needle to a hexagonal prism. Lateral growth continues until the tablets (tiles) abut each other. In this manner, terraced cones are created. Figure 5d shows a scanning electron microscopy (SEM) image of the growth surface. This results in growth of a lamellar, brick-and-mortar structure with $CaCO_3$ tablets held together by an organic mortar and mineral bridges [16, 18].

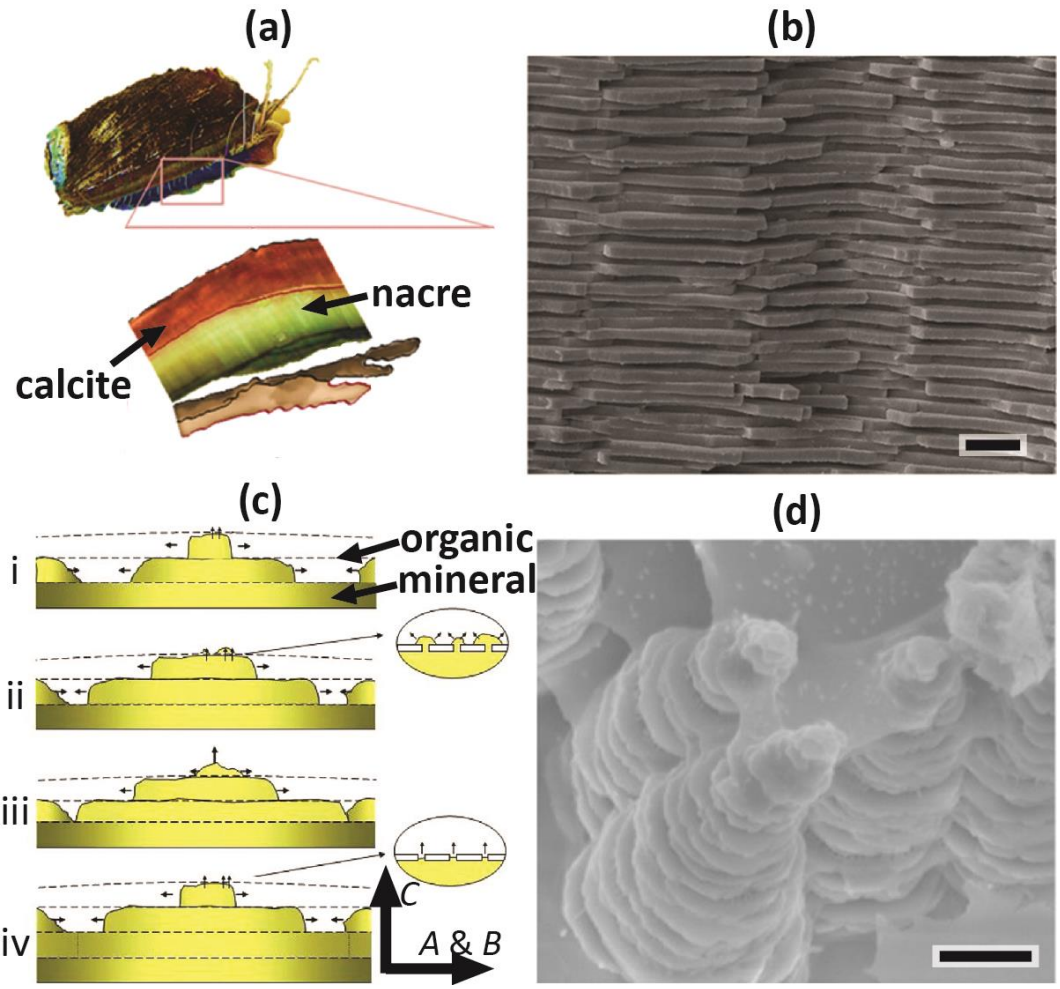

Figure 5. Structure and growth of marine mollusk nacre. **(a)** Cross-section of the abalone shell displaying the calcitic and aragonitic (nacre) layers; **(b)** the brick-and-mortar structure of nacre displaying calcium carbonate plates with mortar-like chitin layers in between; **(c)** Diagram of the process of nacre growth (progressing from top to bottom) where calcium carbonate mineral shelves assemble through an organic membrane. Growth occurs laterally (A and B directions) while it is retarded longitudinally (C direction) by deposition of a porous organic layer (dashed lines); **(d)** SEM image of nacre displaying the growth peaks. Scale bars: 2 μm. Adapted with permission from [10].

While the exact relationship between the biomineral and biopolymer phases of mammalian bone is still of some debate, the general fabrication process is well understood to consist of biogenic hydroxyapatite (a non-stoichiometric form of hydroxyapatite, $Ca_{10}(PO_4)_6(OH)_2$, where 4-6% of the phosphate groups are substituted by carbonate groups [22]), that forms around a collagen scaffold, which directs its growth [23]. As a result, the

reactivity of the templating constituent has a significant effect on the adherence and structuring of hydroxyapatite in bone [24].

When observing these two biological materials, nature enacts a common fabrication approach of guiding the formation of biominerals with a templating structure of biopolymer. This proven natural fabrication method of templating can be mimicked by the bioinspired fabrication technique of freeze casting. Where in nature collagen provides a template for biogenic hydroxyapatite in bone [23] and fish scales [10], in freeze casting the growth of ice itself provides the template for a ceramic material. By employing this similar technique, the hierarchical structures within biological materials can be easily mimicked and explored.

1.4 Freeze Casting

Freeze casting has been an attractive area of research in recent years as it offers the potential to fabricate controlled porous microstructures through a simple and inexpensive technique [25-29]. The process itself is carried out in four steps (visualized in Figure 6): (1) a slurry of solid loading (e.g. ceramic particles) and liquid freezing agent is prepared along with polymeric binders and dispersants, (2) the slurry is frozen in a directional and controlled manner with the solid loading forming lamellar walls (when H_2O is used as a freezing agent) [25-29], (3) the frozen scaffold is lyophilized (freeze dried) to remove the freezing agent, casing aligned pores to result from the sublimated ice crystals, (4) the scaffold is then sintered to densify the structure and enhance its strength. The final scaffold contains pores that are the negative of the initial ice crystals formed by the frozen freezing agent. Once fabricated, a fifth, post-processing step can be implemented. One common form of post-processing is the creation of two-phase interpenetrating scaffold composites

through the infiltration of a second phase. Porous freeze cast scaffolds can be infiltrated with polymers or metal melts [29-32]. There are a number of reported polymer infiltration methods including: particle centrifugation [33], *in situ* polymerization [25, 34] and polymer solvent evaporation [35]. Amongst these, the most commonly applied method is *in situ* polymerization where a liquid monomer and catalyst are infiltrated into a scaffold under vacuum and then allowed to polymerize [25, 27, 34].

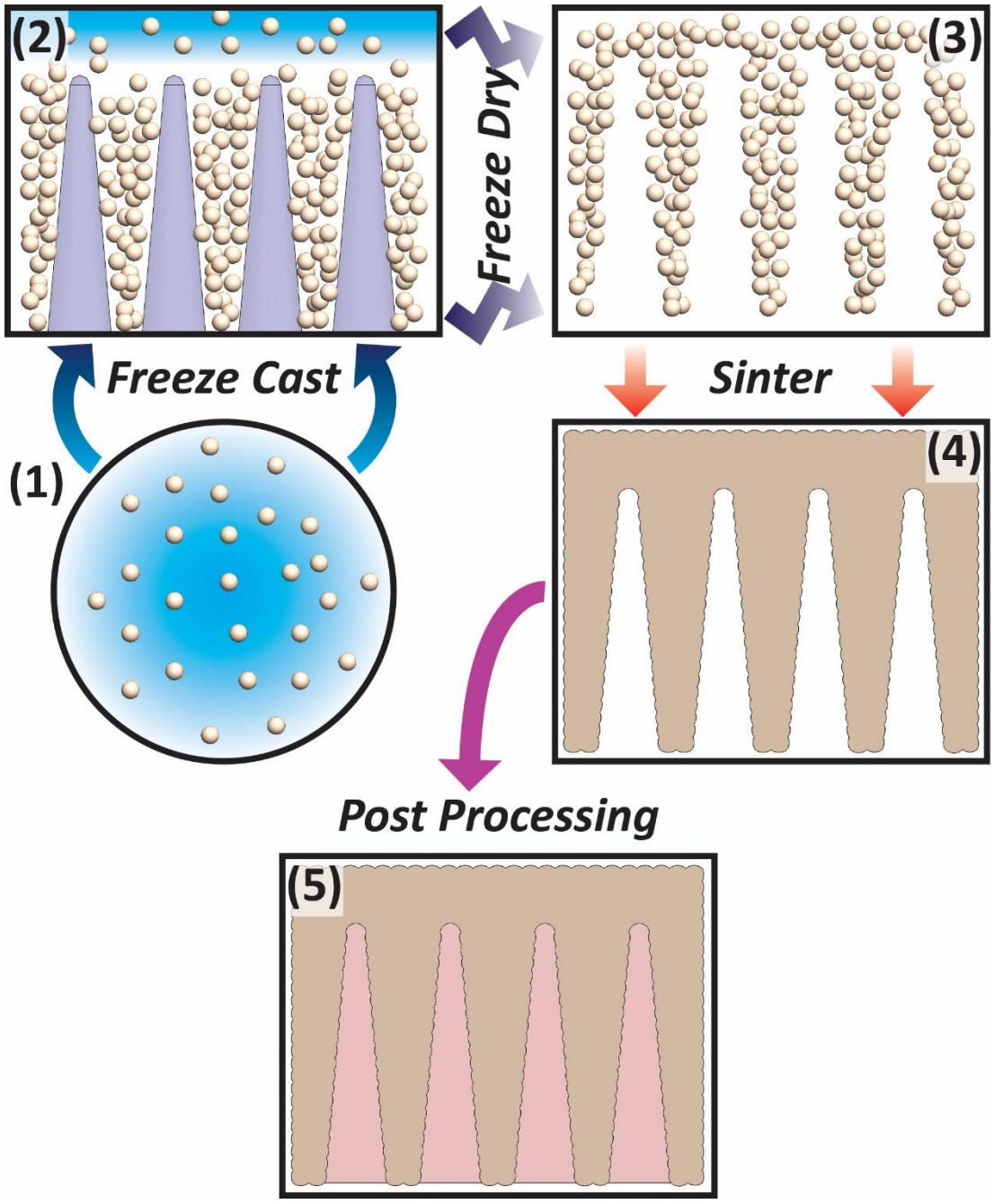

Figure 6. The four steps of the freeze casting process. (1) A slurry of ceramic particles and a liquid freezing agent are mixed and (2) freeze cast, causing alignment of the particles by the directional growth of ice crystals. (3) Once frozen the structure is freeze dried to remove the frozen freezing agent and (4) sintered to form a final porous scaffold. (5) After sintering, an additional, post-processing step can be implemented. One example of this is the infiltration of a second, polymeric phase to create a two-phase composite.

The key to the freeze casting process lies within the freezing itself (step (2) above). In this critical step, the growth of ice crystals at the interface between the solid and liquid phases (i.e. the freezing front) must displace and align the solid loading particles a process that is governed by basic thermodynamics and physics. First, the profile of the freezing front must be such that segregation of particles is possible. Therefore, dendritic growth must occur at the freezing front. The growth of dendrites is governed by the process of constitutional supercooling. Constitutional supercooling occurs in a freezing liquid at the liquid-solid interface when the applied thermal gradient, G^{L}, is less than the liquid's equilibrium thermodynamic temperature [36, 37]:

$$G^{\mathrm{L}} < \frac{v}{D}\left(T^{\mathrm{liq}} - T^{\mathrm{sol}}\right) \qquad 1)$$

where v is the freezing front velocity, D is the liquid's mass diffusivity and T^{liq} and T^{sol} are the equilibrium liquidus and solidus temperatures, respectively. When it occurs, constitutional supercooling, ΔT, is inversely related to the lamellar spacing of the dendritic ice growth, λ [36, 38]:

$$\Delta T \propto \frac{A}{\lambda} \qquad 2)$$

where A is a material constant. A system with no ΔT will result in a planar freezing front, which would make freeze casting fundamentally impossible as the solid particles would simply freeze in place instead of being displaced and aligned. However, as ΔT increases the resultant decrease in λ produces smaller dendrites, which in turn will result in thinner and more numerous lamellar walls within a resultant freeze cast structure.

In systems with some degree of ΔT, where dendritic ice growth is occurring at the freezing front, solid loading particles that contact the freezing front will either be rejected,

thus becoming part of the lamellar walls in the final freeze cast scaffold, or engulfed and form into the mineralized bridging that is often found in the pores of final freeze cast scaffolds. The engulfing or rejection of a particle is related to the thermodynamic free energy of the system [39, 40]. Considering the scenario where the freezing front is approaching a single solid particle, for that particle to be engulfed the free energy of the system, $\Delta\gamma_0$, must be negative [39]:

$$\Delta\gamma_0 = \gamma_{ps} - (\gamma_{pl} + \gamma_{sl}) < 0 \quad (3)$$

where $\Delta\gamma_0$ is dependent on the interfacial energies of the particle and solid ice phase, γ_{ps}, the particle and the unfrozen liquid phase, γ_{pl}, and the solid and liquid phases, γ_{sl}. As shown in Equation 3, for a particle to be engulfed, the free energy of the interface created between the particle and the solid ice, γ_{ps}, must be larger than the sum of the energies that are lost to the system (γ_{pl} + γ_{sl}), thus moving to a lower energy state [39]. In addition, the particle in the liquid phase will experience both repulsive, F_R, and attractive, F_A, forces to the freezing front due to van der Waals interactions at the liquid-solid interface and viscous drag respectively [39]:

$$F_R = 2\pi r \Delta\gamma_0 \left(\frac{a_0}{d}\right)^n \quad (4)$$

$$F_A = \frac{6\pi\eta v r^2}{d} \quad (5)$$

where r is the radius of the solid particle, a_0 is the mean distance between molecules in the liquid phase, d is the thickness of the liquid layer between the solid-liquid interface and the particle, n is an empirical factor that is a correction to the repulsive forces acting on the particle and generally ranging from 1 to 4 [39, 41] and η is the dynamic viscosity of the

liquid. Equating F_R and F_A and solving for v results in an expression for the critical freezing front velocity, v_{cr}, at which a particle will be engulfed:

$$v_{cr} = \frac{\Delta\gamma_0 d}{3\eta r}\left(\frac{a_0}{d}\right)^n \quad (6)$$

Therefore, for $v < v_{cr}$, particles will be engulfed by the solid phase, creating mineral bridges within the resultant porosity and for $v > v_{cr}$, particles will be rejected and become part of the lamellar walls of the final freeze cast scaffold.

The resultant scaffolds of freeze casting have been fabricated into bioinspired designs similar in structure and properties to bone [39, 42-44] and the nacre of abalone [25, 45]. These biological layered structures are also found in successful organisms from deep sea sponges to beetles to humans where they are capable of providing significantly improved mechanical properties due to their hierarchical structuring [12]. These composites are known for their excellent mechanical properties, which often exceed what would be expected from a simple mixture of their constituents [25].

As there is no accepted standard of processing conditions (e.g. solid loading concentration, polymeric binder and dispersant use/variety) for the freeze casting process, any discussion of the effect of isolated variables must be referenced to some baseline. As a result, a "basic" freeze cast scaffold is described here (imaged in Figure 7). This basic scaffold is one that was frozen using a simple ceramic solid loading (in this case at 15 vol.%) and a pure distilled H_2O freezing agent. These processing conditions produce a scaffold whose microstructure features aligned lamellar porosity with a cross-sectional area of ~500 μm^2. These scaffold processing parameters were chosen as they are, to the

knowledge of the author, close to what the majority of the freeze casting community would consider the simplest and most basic.

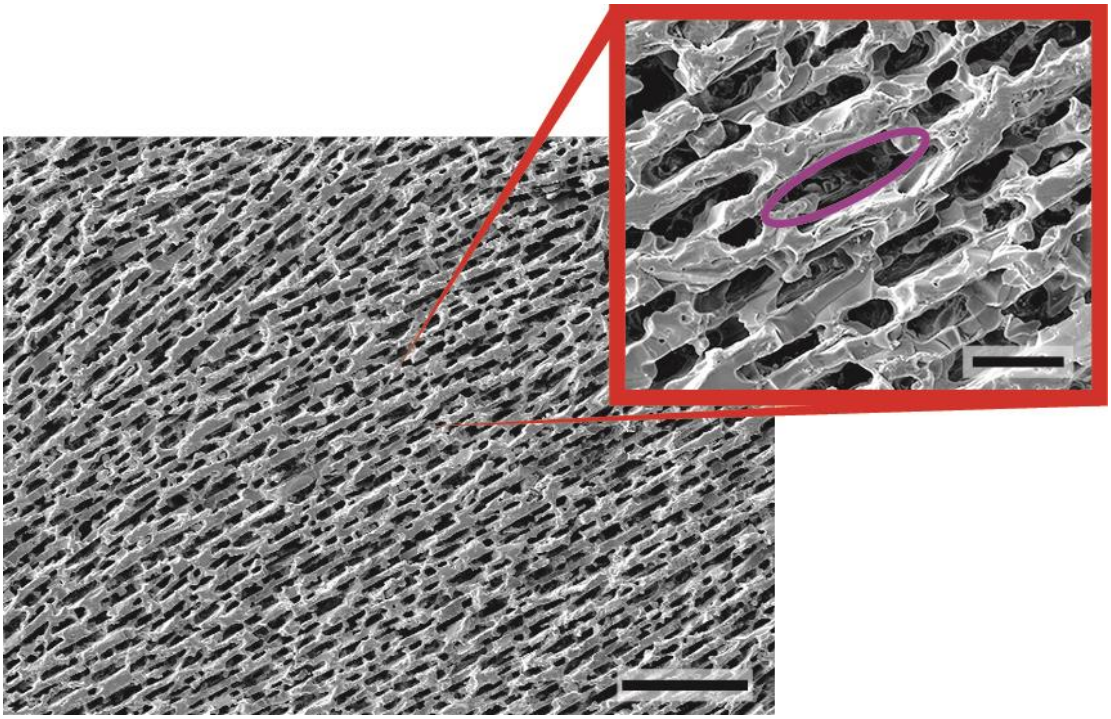

Figure 7. An example, basic freeze cast scaffold. Inset displays the roughly elliptical porosity. Scale bars: 100 μm, inset: 20 μm.

1.5 Intrinsic and Extrinsic Freeze Casting

When considering control of the freeze casting process, an analogy can be drawn to the processes involved with the resistance to crack propagation in fracture mechanics where toughness is imparted through intrinsic mechanisms (those that occur ahead of a growing crack, occur on smaller length scales and are generally inherent to the material itself) or extrinsic mechanisms (those that occur in the wake of a growing crack, act on larger length scales and are often controlled by structural features) [42, 46]. While both of these can provide the same toughening benefit, they do so in very different ways. Control

of freeze casting can be considered in much the same way and divided into two broad categories:

- *Intrinsic control*; control that *acts within* the freezing process through modification of the constituents.
- *Extrinsic control*; control that *acts upon* the freezing process through the application of exterior forces or templates.

As diagramed in Figure 8, within each category there are a number of currently reported techniques each of which provide different final scaffold structures.

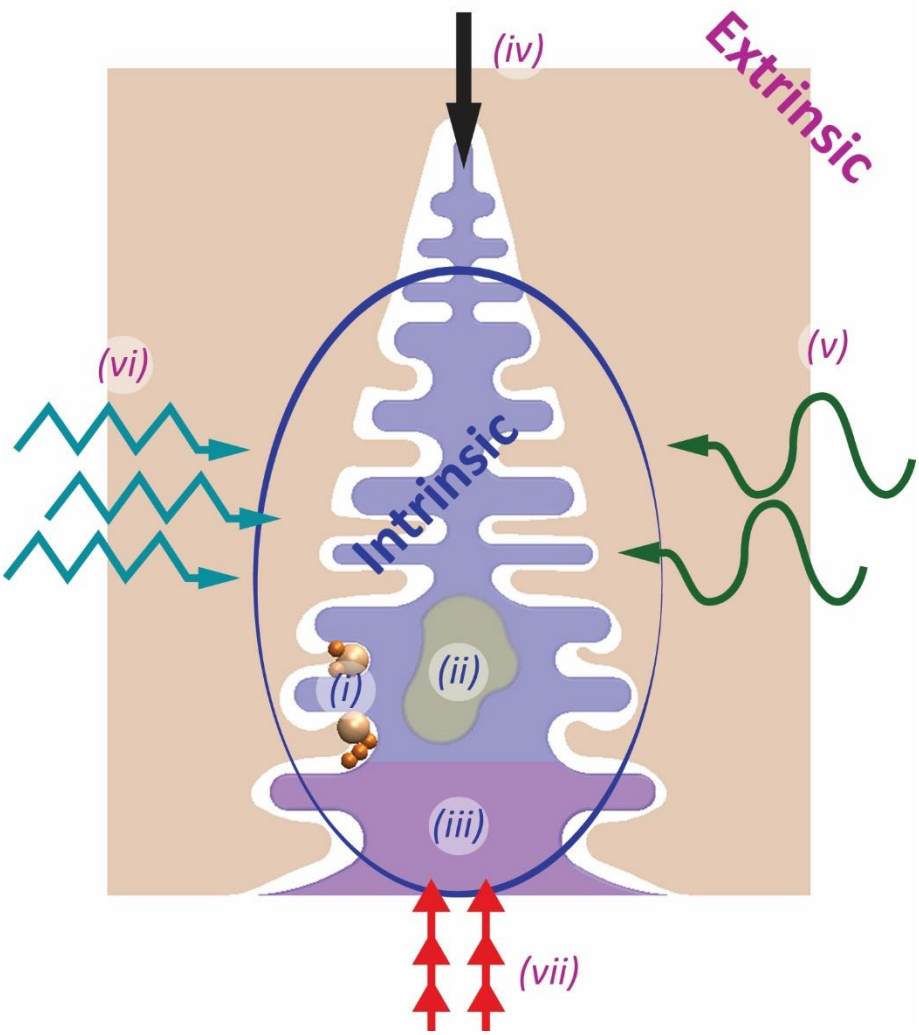

Figure 8. Diagram of intrinsic and extrinsic methods of control over the freeze casting process. Intrinsic methods: *(i)* Variations of particle size; *(ii)* Additives to the slurry; *(iii)* The use of different freezing agents. Extrinsic methods: *(iv)* The use of external templates; *(v)* The use of magnetic fields; *(vi)* The use of electrical fields; *(vii)* Variations to the freezing rate.

Intrinsic freeze casting mechanisms include the use of varying freezing agents (Figure 9a) [47], additives to the slurry (Figure 9b) [36] including ice structuring proteins (Figure 9c) [48] and altering the particle size of the solid loading (Figure 9d) [49]. As there could be confusion between intrinsic control through the use of a different freezing agent and an additive, it is suggested by the author that the use of greater than 30 vol. of a non-

H_2O liquid freezing agent will be considered a different freezing agent, while less than 30 vol.% of a liquid mixed with H_2O will be considered an additive. These intrinsic control methods tend to result in changes at the length scale of the individual pores by altering the pore size, shape and/or structure.

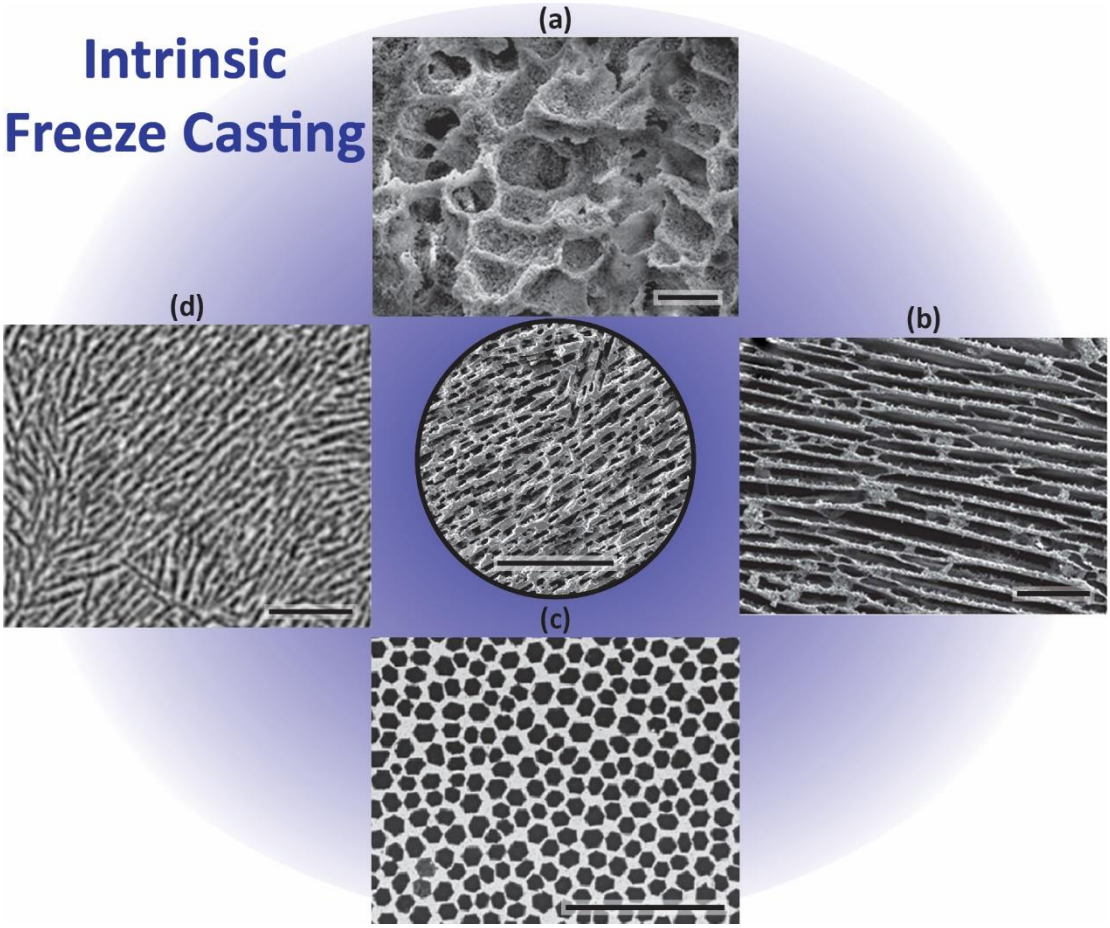

Figure 9. Examples of intrinsic freeze casting. **(a)** Cellular porosity through the use of camphene as a freezing agent; **(b)** Enlarged porosity through the use of isopropanol as a slurry additive; **(c)** Faceted porosity through the use of Zr-acetate ice structuring proteins; **(d)** Dense structure due to large solid loading particle size. For reference, the central image is of a basic scaffold. Scale bars: **(a)** 20 μm, **(b)** 200 μm, **(c)** 150 μm, **(d)** 150 μm, center: 100 μm. Images adapted with permission from: **(a)** [47], **(b)** [36], **(c)** [48], 19 **(d)** [49].

Extrinsic freeze casting mechanisms include applications of mechanical templates (Figure 10a) external magnetic (Figure 10b) [50] and electrical (Figure 10c) [51] fields,

directional control of the freezing (Figure 10d) [52] and control of the freezing rate (Figure 10e) [28]. While not ubiquitous, these extrinsic control methods tend to result in alterations to the microstructure that take place over longer length scales and often affect the entire cross-section.

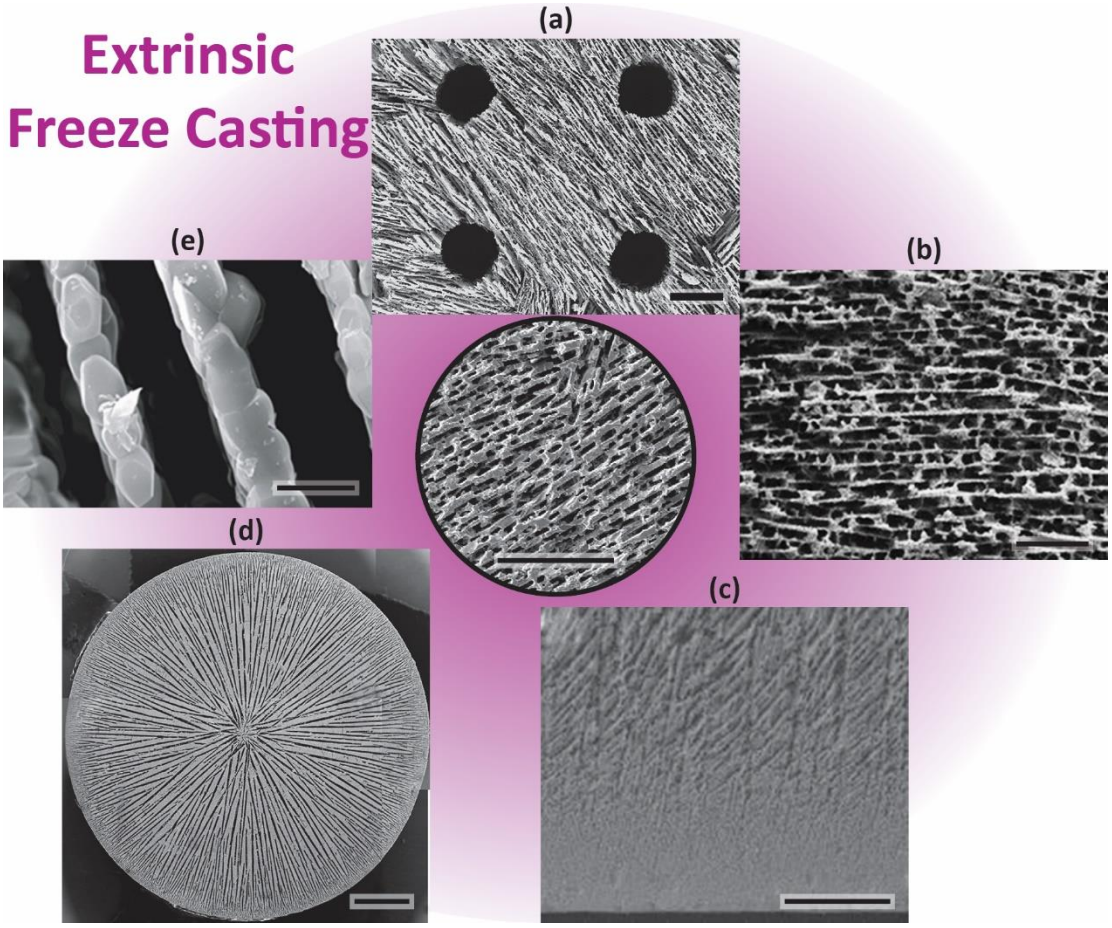

Figure 10. Examples of extrinsic freeze casting. **(a)** Macro-micro porosity caused by secondary templating with 3D printed templates; **(b)** Aligned porosity through the application of magnetic fields; **(c)** Dense/porous bilayered porosity through the application of electric fields; **(d)** Centrosymmetric porosity through radial cooling; **(e)** Thin lamellar walls induced by a high cooling rate. For reference, the central image is of a basic scaffold. Scale bars: **(a)** 500 μm, **(b)** 100 μm, **(c)** 200 μm, **(d)** 2 mm, **(e)** 4 μm, center: 100 μm. Images adapted with permission from: **(b)** [50], **(c)** [51], **(d)** [52], **(e)** [28].

In this dissertation, one example each of intrinsic and extrinsic control of freeze casting will be explored. Intrinsic control through the use of monofunctional alcohol additives will be discussed in Chapters 3, 4 and 5. Extrinsic control through the use of 3D printed mechanical templates will be discussed in Chapter 6. Finally, in Chapter 7, the variability of the basic freeze casting process itself will be discussed so as to promote novel research into advanced control of the freeze casting process through both intrinsic and extrinsic means. The true strength of the freeze casting process lies in its ability to realize drastic microstructural changes through relatively simple alterations to the experimental design. Therefore, it is the hope of the author that the concept of intrinsic and extrinsic freeze casting control along with the research described within this dissertation will inspire new research into the development, functionalization and commercialization of the bioinspired freeze casting fabrication technique.

1.6 Freeze Casting Procedure

This dissertation describes a number of studies that all focus upon the process of freeze casting. Therefore, all of the experiments herein share some common methodologies for the preparation, fabrication, testing and analysis of the produced materials. As to avoid repetition throughout the following chapters, the basic materials and methodologies used within two or more of the chapters will be described here. Materials and methodologies unique to each separate chapter will be noted within the respective "Materials and Methods" sections. In addition, specific concentrations and constituents of the slurries additives and testing conditions will be noted in each chapter.

1.6.1 Slurry Preparation

Aqueous slurries for freeze casting were prepared utilizing four main constituents: solid ceramic loading particles, liquid freezing agent, polymeric binders and an anionic dispersant. Ceramic loading particles were included at a concentration of 10 - 20 vol.% of either ZrO_2 (200 - 500 nm diameter) (Sigma Aldrich, St. Louis, MO, USA) or hydroxyapatite (HA) (2000 - 2600 nm diameter) (Trans-Tech, Adamstown, MD, USA). The liquid freezing agent base was always distilled H_2O, though in many cases additional additives were included. The polymeric binders were included at 2 wt.% of the ceramic solid loading and consisted of combinations of polyethylene glycol (PEG) with a molecular weight of 10,000 g/mole (Alfa Aesar, Ward Hill, MA, USA) and polyvinyl alcohol (PVA) with a molecular weight of 100,000 g/mole (Alfa Aesar, Ward Hill, MA, USA). To include these polymeric binders they were first dissolved into distilled H_2O at concentrations of 20 g/L for PVA and 50 g/L for PEG. In all cases, the anionic dispersant was Darvan 811 (R. T. Vanderbilt Company, Inc., Norwalk, CT, USA) and was included in the slurry at 1 wt.% of the ceramic solid loading. All slurries were prepared at a total concentration of 15 - 16 mL so as to create one freeze cast scaffold. All of the slurry constituents were mixed in an arbitrary order. Once combined, alumina grinding media was added to the mixture and the slurries were ball milled for 24 h prior to freeze casting.

1.6.2 Freeze Casting

Once ball milled, aqueous slurries were transferred to a vacuum flask and degassed under low vacuum for 5-10 min so as to remove any excess air bubbles that could disrupt or weaken the final scaffold microstructure. Approximately 10 mL of degassed slurry was poured into a mold mounted on a custom build freeze casting setup. This setup, previously

described by Porter et al. [50] and imaged in Figure 11, consists of four components: a liquid nitrogen bath, a copper cold finger, a heater and the mold itself. The copper cold finger is responsible for ensuring the essential, directional freezing that is the hallmark of the freeze casting process. The cold finger sits with its lower half submerged in the liquid nitrogen bath and its upper surface supporting the mold and therefore contacting the liquid slurry. The mold, a hollow cylinder with and inner diameter of 21 mm, outer diameter of 27 mm and length of 50 mm, is made of polyvinyl chloride so as to limit any thermal effects outside of the directional freezing induced by the liquid nitrogen cooled copper cold finger. To provide control over the cooling rate, a ring heater is fixed to the center of the copper cold finger and controlled so as to produce a constant cooling rate of 10 K/min during the freeze casting process.

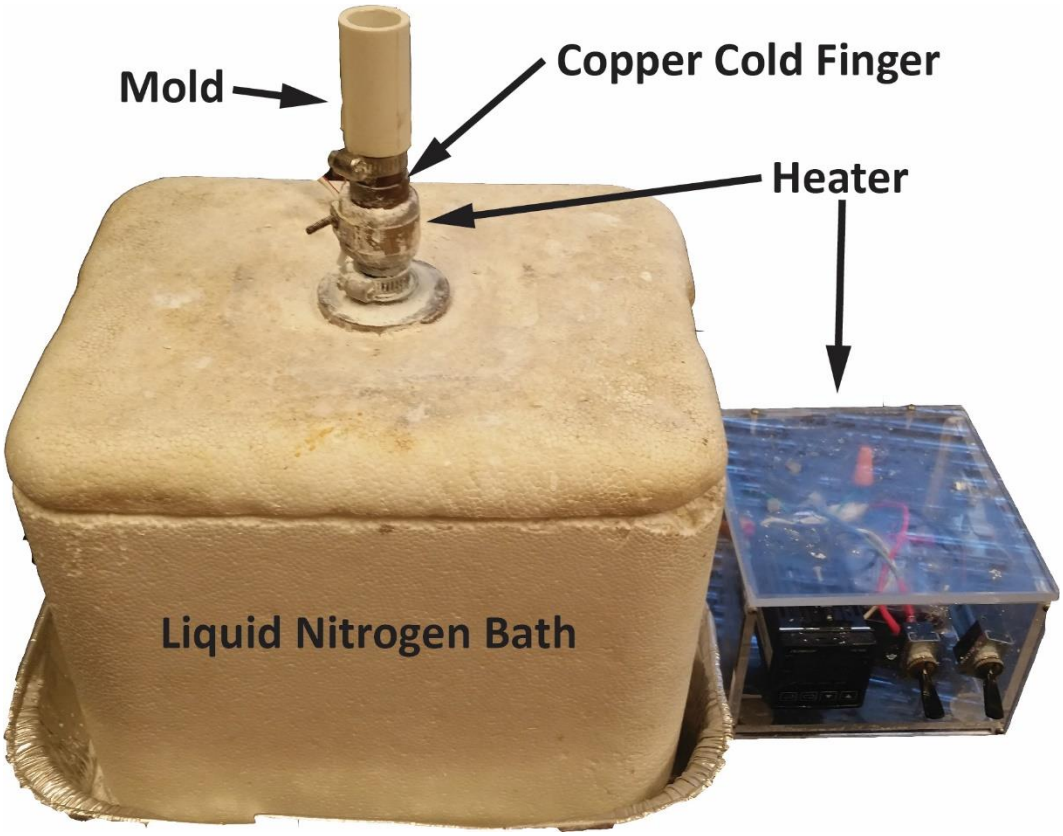

Figure 11. Custom built freeze casting setup consisting of four major components: a liquid nitrogen bath, a copper cold finger, a heater (and associated PID controller) and a PVC mold.

After freezing, samples were lyophilized using a bench-top freeze drier (Labconco, Kansas City, MO, USA) at 223 K and 350 Pa for 48 - 72 h so as to remove all of the frozen freezing agent without allowing for degradation of the structure, which would occur upon melting of the freezing agent. The resultant green scaffolds, held together by the polymeric binders, were sintered in an open air furnace (Keith, Pico Rivera, CA, USA) for 3 h at 1623 K with heating and cooling rates of 2 K/min. This sintering procedure was similar to previously reported procedures for ZrO_2 and HA [50] and through experimentation provided stable but highly porous ceramic scaffolds.

1.6.3 Polymer Infiltration

In the majority of the experiments described in this dissertation, the porous ceramic scaffolds were infiltrated with a second, polymeric phase so as to create a strengthened composite. This was done by *in situ* polymerization using Epoxicure or Epoxicure 2 (Buehler, Lake Bluff, IL, USA) two part polymer epoxies. The porous ceramic scaffolds were immersed in a mixture of liquid epoxy monomer and catalyst under low vacuum (~0.02 Pa) for 20 - 30 min to force the liquid to fully infiltrate the porosity. The infiltrated scaffolds were then removed from the vacuum and allowed to polymerize for 24 h. At the same time, samples of pure epoxy were created as a baseline for mechanical properties. Based upon microstructural evaluation of a large number of these scaffolds through scanning electron microscopy (SEM), it is assumed that the final scaffold composites created by this methodology are fully infiltrated and free of air pockets.

1.6.4 Microstructural Characterization

The microstructure of the scaffolds was observed using SEM at 10 kV and a spot size of 3.0 nm using a Philips XL30 field emission environmental scanning electron microscope (FEI Company, Hillsboro, OR, USA). For SEM preparation thin disks of each scaffold were removed and polished so as to provide a flat surface and accurately reveal the microstructure. Given the insulating nature of the constituents of these scaffolds, all samples were sputter-coated with iridium using an Emitech K575X sputter coater (Quorum Technologies Ltd., West Sussex, UK). Microstructural measurements of the pore sizes observed in each scaffold were performed post hoc using ImageJ software (National Institutes of Health, Bethesda, MD, USA). For each scaffold $N = 40$ individual pores were measured to calculate a mean pore size/shape and standard deviation. These measurements

were taken by adjusting the threshold of the micrographs (using a constant threshold for all measurements within each study) so as to fit an ellipse to the pores. The major axis, *a*, and minor axis, *b*, of these fitted ellipses was then measured, as shown in Figure 12. From these values, the pore area, A_p, and pore aspect ratio, X_p, for each pore were calculated using Equation 7 and Equation 8, respectively.

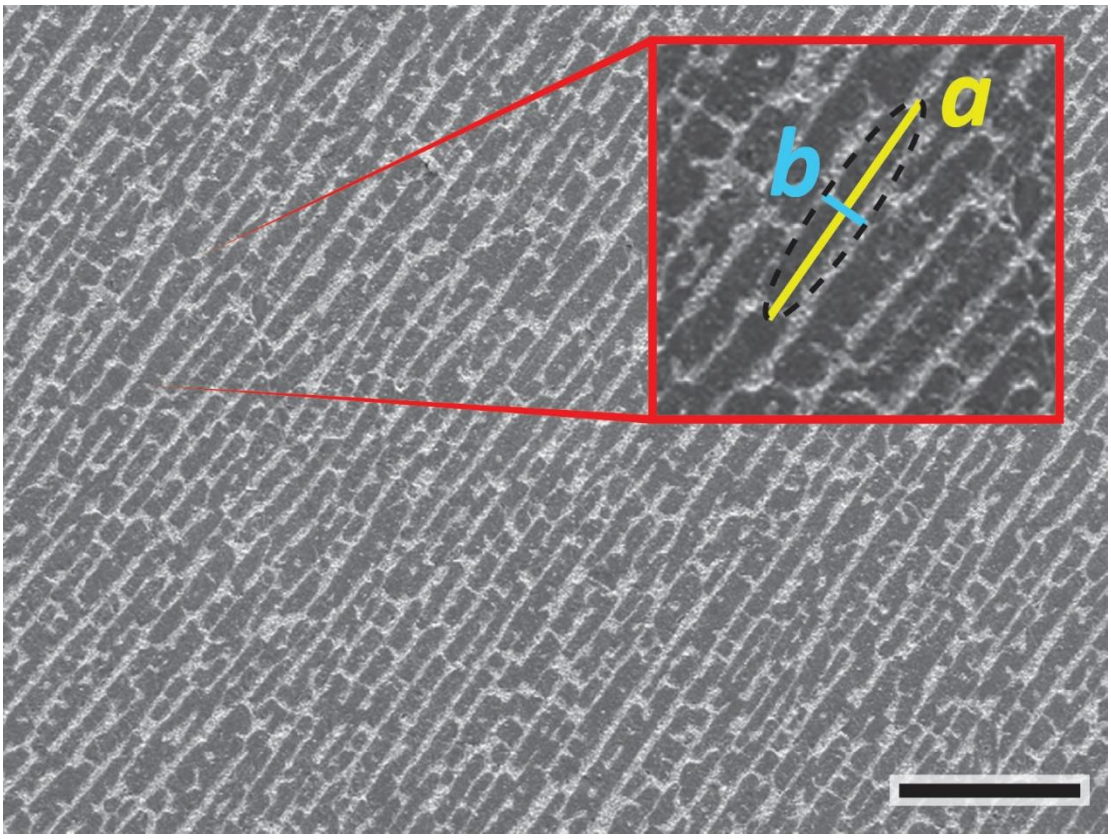

Figure 12. Example micrograph of a two-phase freeze cast bioinspired composite scaffold. Sintered ceramic is light gray and epoxy polymer is dark gray. Inset highlights an individual pore to show the major axis, *a*, and minor axis, *b*. Scale bar: 100 μm. Adapted with permission from [53].

$$A_p = \frac{ab\pi}{4} \quad (7)$$

$$X_p = \frac{a}{b} \quad (8)$$

1.6.5 Mechanical and Structural Characterization

To determine the mechanical properties of the freeze cast scaffolds, each was sectioned into cubic samples of roughly 5 x 5 x 5 mm^3. Each of the three axial dimensions were measured five times to calculate the sample volume, initial height and cross-sectional area and the samples were weighed. Compression testing was performed using a 3367 Intron materials testing machine (Instron, Norwood, MA, USA) with a 30 kN static load cell. All tests were performed at that constant crosshead velocity of 0.005 mm/s. In all cases, five to seven samples were tested from each scaffold so as to determine the mean and standard deviation. The ultimate compressive strength, *UCS*, and elastic modulus, *E*, were calculated from the peak stress and linear elastic slope of the stress-strain curve, respectively.

In some cases where infiltrated composite scaffolds were examined, the ceramic volume percent, V_c, of these cubic samples was calculated from a rule of mixtures for a two-phase composite:

$$V_c = \frac{\rho_{cs} - \rho_p}{\rho_c - \rho_p} \qquad 9)$$

where ρ_{cs}, ρ_p and ρ_c are the densities of the final composite scaffold, infiltrated polymer epoxy and ceramic respectively. Archimedes' principle was used to calculate ρ_{cs} and ρ_p from the experimentally measured dimensions listed above. For ρ_c the density of the pure ceramic was used (for ZrO_2, ρ_c = 5.89 g/cm^3). In all cases, V_c of five to seven samples was calculated so as to determine the mean and standard deviation.

1.6.6 Differential Scanning Calorimetry

When analyzing the phases present in the structure of the frozen slurry, differential scanning calorimetry (DSC) was employed. DSC has been previously used to investigate the phase transformations occurring during the freezing of binary, non-hydrogen bonded liquids and H_2O [54-58]. DSC was performed using a Q20 Differential Scanning Calorimeter (TA Instruments, New Castle, DE, USA) and cycled from room temperature to 213 K with heating and cooling rates of 10 K/min so as to imitate the freeze casting process. To ensure that this lower temperature limit was accurate to the freeze casting process, experiments were conducted by placing a thermocouple within the slurry during the freezing step of a freeze casting procedure. The thermocouple was situated roughly at the height were samples are extracted from the final scaffolds (~20 mm from the top surface). The temperature was shown to only reach a minimum of ~ 210 K by the end of the freezing process.

DSC results were quantitatively analyzed by applying a linear integration method to determine the area under the exo- and endo-thermic peaks and dividing by the mass of each sample to determine the enthalpy of each transition.

Chapter 1.2 and 1.3, in part, are a reprint of the material as it appears in "Structure and mechanical properties of selected protective systems in marine organisms" Materials Science and Engineering C, vol. 59, pp 1143-1167, 2016. The dissertation author was the primary investigator and author on this paper. This work was also co-authored by Jennifer R. A. Taylor, Michael M. Porter, Marc A. Meyers and Joanna McKittrick.

2. Biological Structural Design Elements

In spite of an estimated 7 million animal species living on earth [59], there is remarkable repetition in the structures observed among the diversity of biological materials. This is due to the fact that many different organisms have developed similar solutions to natural challenges (e.g. ambient environmental conditions, predation). As a result, the vast body of research on biological materials often presents similar solutions, since the number of materials available in nature is fairly limited and therefore resourceful combinations of them have to be developed to address specific environmental constraints. Naleway et al. [12] have identified these common designs and named them "structural design elements." This new system of eight structural design elements are most common amongst a wide variety of animal taxa. These structural elements have each evolved to improve the mechanical properties, namely strength, stiffness, flexibility, fracture toughness, wear resistance, and energy absorption of different biological materials for specific multi-functions (e.g. body support, joint movement, impact protection, mobility, weight reduction). These structural design elements are visually displayed in Figure 13:

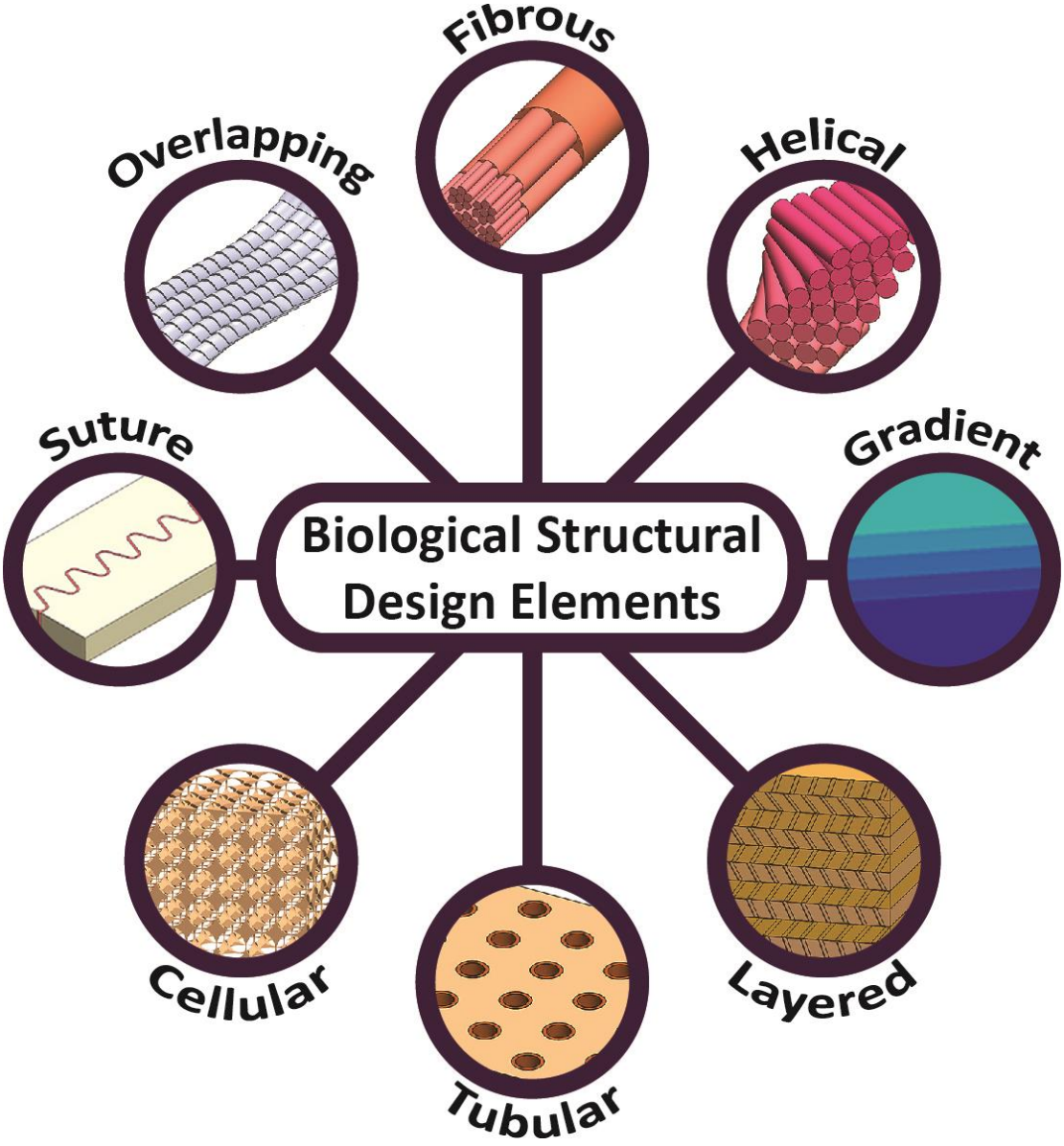

Figure 13. Diagram of the eight most common biological structural design elements. Adapted with permission from [12].

- *Fibrous structures*: offering high tensile strength when aligned in a single direction, with limited to nil compressive strength.
- *Helical structures*: common to fibrous or composite materials, offering toughness in multiple directions and in-plane isotropy.

- *Gradient structures*: materials and interfaces that accommodate property mismatch (e.g. elastic modulus) through a gradual transition in order to avoid interfacial mismatch stress buildup, resulting in an increased toughness.
- *Layered structures*: complex composites that increase the toughness of (most commonly) brittle materials through the introduction of interfaces.
- *Tubular structures*: organized porosity that allows for energy absorption and crack deflection.
- *Cellular structures*: lightweight porous or foam architectures that provide directed stress distribution and energy absorption. These are often surrounded by dense layers to form sandwich structures.
- *Suture structures*: interfaces comprising wavy and interdigitating patterns that control strength and flexibility.
- *Overlapping structures*: featuring multiple plates or scutes that overlap to form flexible and often armored surfaces.

As with all biological materials, these structural design elements are composed of biopolymers (e.g. collagen, chitin, keratin) and biominerals (e.g. calcium carbonate, calcium phosphates, silica) that are hierarchically assembled from the nano- to mesoscales [4, 7, 10]. However, the extraordinary mechanical properties observed in these natural materials are often a product of the intricate structural organization at different spatial scales (nano, micro, meso, and macro) where these structural design elements are observed (Table 1). As a result, in many cases organisms with different base materials will employ the same structure for the same purpose (e.g. tubules found in human dentin composed of

hydroxyapatite/collagen and also in ram horns composed of keratin can both absorb energy [60]).

Table 1. Length scales of each structural design element along with representative examples. In each case, dimensions are given that represent the characteristic length scale (i.e. fibrous: fiber diameter, helical: layer/reinforcement thickness, gradient: gradient thickness, layered: layer thickness, tubular: tubule diameter, cellular: cell diameter, suture: sutured wavelength, overlapping: plate length). These dimensions are meant to provide an understanding of the length scales at which these structures occur, as dimensions will vary with species. Adapted with permission from [12].

Fibrous nano- to micro-scale		
Hagfish Slime Intermediate Filaments: 10 nm [61]	Collagen Fibril: 100 - 500 nm [62]	Spider Silk: <10 μm [63]
Helical nano- to micro-scale (twisted-ply) or macro-scale (reinforcement)		
Beetle Exoskeleton: 50 - 200 nm [64]	Stomatopod Club: ~75 μm [65]	Sea Sponge Ridge: ~1 mm [66]
Gradient micro- to macro-scale		
Tooth Dental/Enamel Junction: ~20 μm [67]	Crab Claw: 10 - 20 μm [68]	Squid Beak: ~50 mm [69]
Layered micro-scale		
Sea Sponge Spicule: 0.2 - 1.5 μm [66]	Abalone Nacre: ~0.4 μm [14]	Fish Scale: ~25 - 50 μm [70]
Tubular micro-scale		
Tooth Dentin: ~1 μm [71]	Fish Scale: ~6.5 μm [72]	Horn Tubule: ~40 - 100 μm [73]
Cellular nano- to micro-scale (sandwich) or macro-scale (bulk)		
Porcupine Quill: ~100 nm [74]	Elk Antler: ~300 μm [75]	Coral: 10 - 40 μm [76]
Suture micro-scale		
Boxfish Scute: ~65 μm [77]	Turtle Shell: 230 - 400 μm [78]	Deer Skull: 640 - 2500 μm [79]
Overlapping macro-scale		
Seahorse Plate: 1 - 10 mm [80]	Striped Bass Scale: 8 - 10 mm [81]	Chiton Plate: ~5 mm [82]

Examples of the structure–function relationships of the common structural design elements in biological materials can be found in a number of different organisms from varying biological classes (shown herein), illustrating the wide range of environments where these design elements are observed. In addition, bioinspired materials that incorporate these common structures are becoming more prevalent as modern manufacturing allows for more control at the important spatial scales where these design elements are most often present. This paper organizes these eight elements by their relative size and complexity (e.g. from smaller, less-complex fibrous structures to larger, more-complex overlapping structures) and provides constitutive equations that describe their basic mechanical and/ or structural advantages.

2.1 Fibrous Structures

Biological materials that require high tensile strength or stiffness in a single direction are organized as fibrous structures, designed with numerous aligned fibers (and fibrils or filaments at smaller spatial scales) that often exhibit hierarchy across multiple length scales (Figure 14a). They are commonly found within non-mineralized, soft biological materials, such as muscle, tendon, and silks. However, there are a number of notable exceptions such as the chitin fibers in arthropod exoskeletons and collagen fibers in bones where these fibers are mineralized. These structures occur within the nano- to microstructures of biological materials. Specific examples given here are spider silk (Figure 14b) [63, 83], hagfish slime (Figure 14c) [61, 84, 85], silkworm silk (Figure 14d) [4] and rat tendon (Figure 14e) [62, 86].

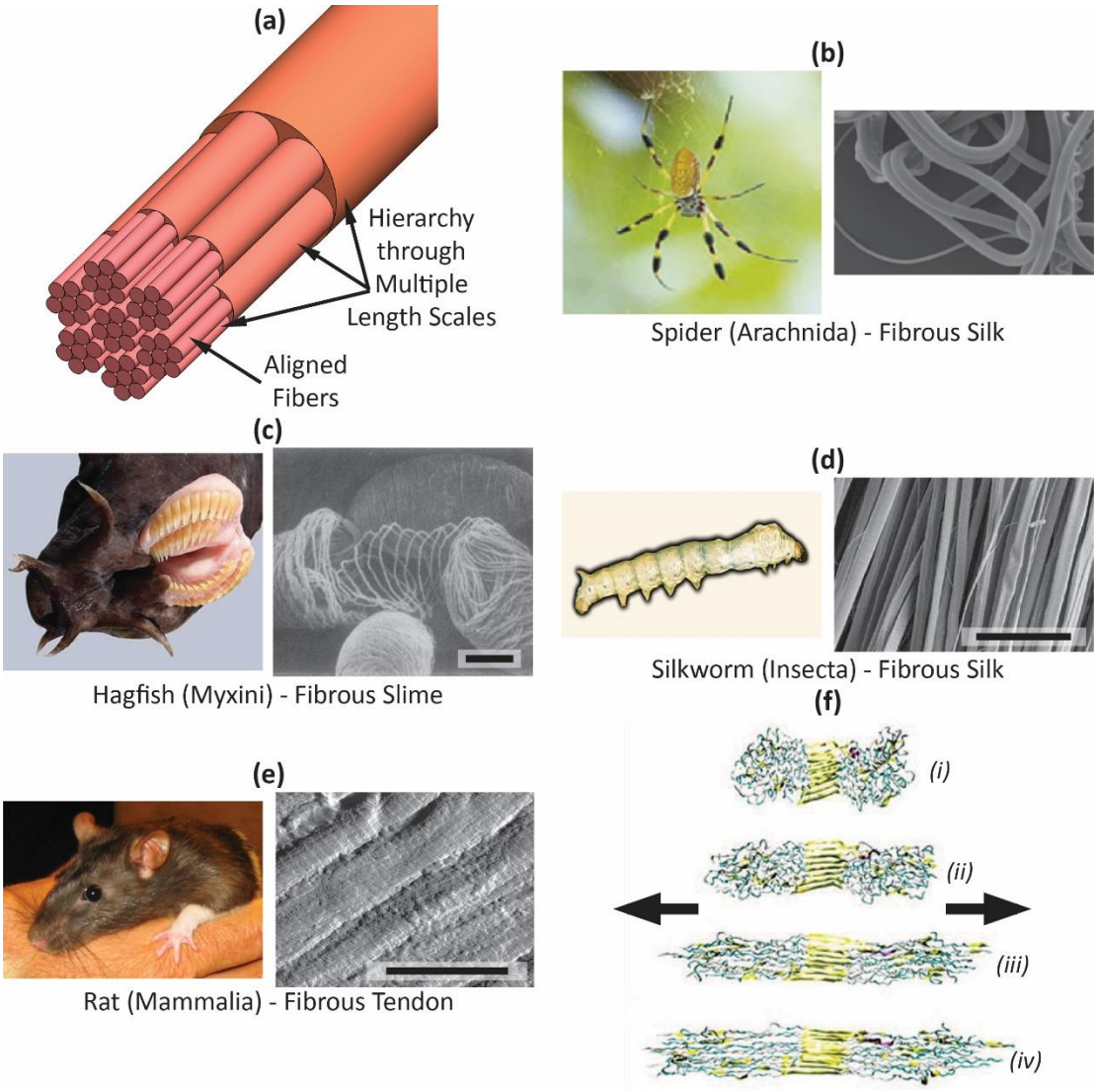

Figure 14. Biological fibrous structures from nature representing a variety of biological classes. **(a)** Diagram of fibrous structures with a hierarchy of aligned fibers at multiple length scales; **(b)** Spider (Arachnida) with fibrous silk; **(c)** Hagfish (Myxini) with fibrous slime; **(d)** Silkworm (Insecta) with fibrous silk; **(e)** Rat (Mammalia) with fibrous tendons; **(f)** Diagram of fibrous structures pulled in tension demonstrating how the fibers align then strain in unison. Scale bars: **(c)** 20 μm, **(d)** 100 μm, **(e)** 100 μm. Adapted with permission from [12].

Mechanically, fibrous structures present a dichotomy of strength, high in tension and low to effectively nil in compression. This results in dramatic tension–compression asymmetric behavior. Thus, they are typically applied in a tensile mode and are only described as such here. These materials tend to exhibit a characteristic *J*-shaped stress–

stain curve resulting in two regimes of elastic-plastic behavior. In the first of these regimes the aligned fibers unfurl, slide past each other, and straighten without significant resistance, following the power law (Figure 14f (i) to (ii)) [5].

$$\frac{d\sigma}{d\varepsilon} \propto \varepsilon^{\mathrm{n}} (n > 1) \quad 10)$$

where σ is the stress, ε is the strain, and n varies with the material, with $n = 1$ associating with the mechanical behavior of aligned collagen [87]. A number of models have been presented to characterize the unfurling and straightening of the fibers during this initial regime. These include modeling the waviness as a sine function [88], a helical structure [89], or as circular segments. Additionally, the initial mechanical behavior, as the fibers first begin to slide past one another, has been modeled as a dashpot–spring series combination to account for viscoelasticity. In the second regime, the fibers become taut and experience increased strain, resulting in a higher and effectively linear stiffness following Hooke's law (Figure 14f (iv)) [5]:

$$\frac{d\sigma}{d\varepsilon} = E \quad 11)$$

where E is the elastic modulus. To form a single constitutive equation, Equation 10 and Equation 11 can be integrated and combined to form Equation 12, describing the comprehensive stress–strain behavior of fibrous structures in tension [5]:

$$\sigma = k_1 \varepsilon^{\mathrm{n}+1} + H(\varepsilon_{\mathrm{c}}) E(\varepsilon - \varepsilon_{\mathrm{c}}) \quad 12)$$

where k_1 is a material parameter and H is the Heaviside function, which activates when the second regime is reached ($\varepsilon = \varepsilon_{\mathrm{c}}$, where ε_{c} is the characteristic strain at which the fibers have become fully extended). This simplified equation by Meyers et al. [5] can be replaced

by more complex constitutive equations originally derived for polymers by Ogden [90] and Arruda and Boyce [91], and specifically applied to biological tissue by Fung [92].

As a result of the physical unfurling of fibers associated with the first regime of elastic–plastic behavior, the initial ordering of a fibrous structure (e.g. wave/kink of the individual fibers, interweave of fibers, length of fibers, sliding between fibrils) determines a broad range of mechanical responses that are often tailored to specific needs. This *J*-curve elastic–plastic behavior is critical for many biological materials. Specifically, the nature of these materials, where the rate of change of the slope increases with strain, initially allows for a large amount of deformation with minimal energy consumption followed by a large energy consumption before fracture. In tendons and muscles, this allows for energy savings on small tasks while maintaining high stiffness needed for heavy lifting. In the silk of spider webs, at low stress the web is flexible, allowing the spider to detect the small vibrations of trapped prey. However, the same web is much stiffer at high stress to avoid fractures that could allow prey to escape.

2.2 Helical Structures

Helical structures generally provide increased strength and toughness in multiple directions by employing numerous fibers, fibrils, or reinforcements at varying angles (Figure 15a). These structures are often employed in non-mineralized or relatively low-mineralized structural materials, which can be referred to as twisted-ply structures. Though often formed from the same constituents as fibrous structures, helically organized fibrous structures can result in in-plane isotropy and enhance the toughness of the resulting material. When formed as reinforcements in the macrostructure, helically reinforcing structures are most often employed on exterior surfaces to improve the torsional rigidity.

Twisted-ply structures occur in the nano- to microstructures while helically reinforcing structures generally occur in the macrostructure of biological materials and organisms. Specific examples include crustacean exoskeletons (e.g. stomatopod dactyl club, Figure 15b) [65], mammalian bone collagen (e.g. rat, Figure 15c) [93], highly mineralized sea sponge exoskeletons (Figure 15d) [66, 94], insect exoskeletons (e.g. grasshopper, Figure 15e) [64, 95] and fish scales [81, 96, 97]. In an idealized arrangement described by Bouligand [95], each layer of fibers is rotated from the previous stacked layer by a constant angle and the arrangement completes a full 180° rotation. However, many variations of this structure have been observed in biological materials with rotations at varying angles or even in opposing directions, where these arrangements can provide significant resistance to mechanical stress (e.g. the increased puncture resistance in orthogonally aligned fish scales) [96, 98, 99].

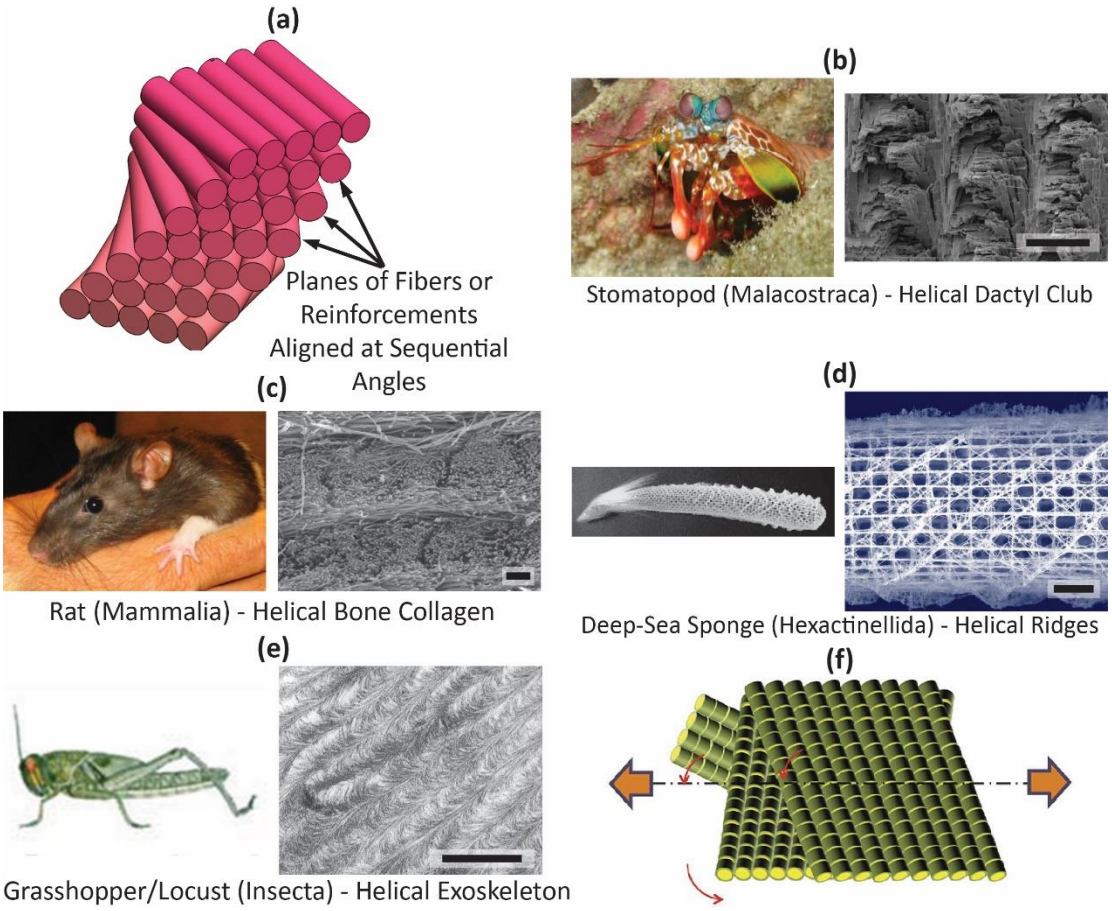

Figure 15. Biological helical structures from nature representing a variety of biological classes. **(a)** Diagram of a helical structure showing planes of fibers or reinforcements aligned at sequential angles; **(b)** Stomatopod (Malacostraca) with helical structures in its dactyl club; **(c)** Rat (Mammalia) with helical collagen in its bones; **(d)** Deep-sea sponge (Hexactinellida) with helical reinforcing ridges in its skeleton; **(e)** Grasshopper/locust (Insecta) with helical structures in its exoskeleton; **(f)** Diagram displaying how helical structures can rotate and align to better absorb tensile forces. Scale bars: **(b)** 75 μm, **(c)** 1 μm, **(d)** 5 mm, **(e)** 1 μm. Adapted with permission from [12].

Mechanically, less-mineralized helical structures provide three principal structural attributes: (1) they provide increased isotropy in multiple directions along the fiber plane by stacking layers of fibers or fibrils at varying angles (Figure 16a), (2) they provide increased toughness as the misaligned fiber planes can distract crack advance, forcing it to propagate in multiple planes (Figure 16b), and (3) the aforementioned isotropy provides a significant increase in the compressive strength and stiffness over fibrous structures,

despite consisting of the same constituents. Perhaps most impressive is that many twisted-ply structures are capable of realigning their fibrous structure to accommodate external forces applied in-plane (as shown schematically in Figure 15f) [96, 97].

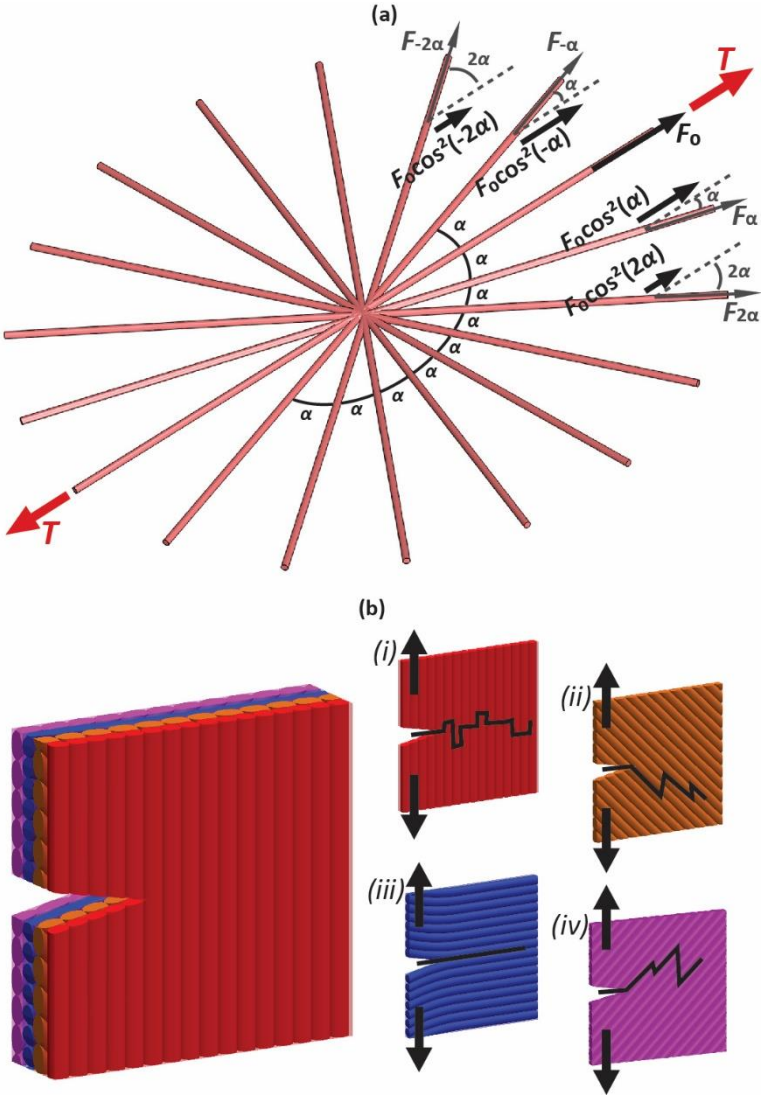

Figure 16. Examples of the mechanical advantages of helical structures. **(a)** Fibers oriented in different directions allow for a load, *T*, applied in any direction to be resisted, thus creating in-plane isotropy. **(b)** When a sharp crack grows within a helical structure, each offset plane results in a different preferred crack path (i) – (iv) thus increasing the fracture toughness. Adapted with permission from [12].

As there is a current lack of constitutive equations describing the mechanics of helical structures, Naleway et al. [12] provided their own interpretation. Such an in-plane

isotropy is accomplished by the layering of highly anisotropic fibers along different orientations. Figure 16a displays a proposed arrangement where fibers are subjected to an external load or tension, *T*. Note that, in this example all of the fibers make discrete and equal angles, α, to each other and rotate a full 180° thus creating a Bouligand structure. However, the same could be applied for a structure consisting of varying angles (e.g. α_1, α_2, α_3). In this model, it is assumed that the fiber(s) perfectly aligned with the direction of tension are fully loaded. In other fibers, it is assume that the tensile load decreases with the cosine of the angle:

$$T = F_0 + F_\alpha \cos(\alpha) + F_{2\alpha} \cos(2\alpha) + \cdots + F_{-\alpha} \cos(-\alpha) + F_{-2\alpha} \cos(-2\alpha) + \cdots \quad 13)$$

where F_0 is the force experienced by fibers oriented parallel to the loading direction and $F_{i\alpha}$ is the load resisted by each individual fiber. In the case of tensile loading, those fibers are only capable of resisting load in the direction of tension. Therefore, Equation 13 can be modified in order to account only for the force resisted in the loading direction:

$$T = F_0 + F_0 \cos^2(\alpha) + F_0 \cos^2(2\alpha) + \cdots + F_0 \cos^2(-\alpha) + F_0 \cos^2(-2\alpha) + \cdots \quad 14)$$

which can also be simplified to a summation:

$$T = F_0 \sum_{i=1}^{n} [1 + 2\cos^2(i\alpha)] \quad 15)$$

This relationship holds for any loading orientation within the fiber plane, thus creating an effective in-plane isotropy. This force can be converted to stress by dividing it by the combined projected area, normal to the direction of loading, of all the fibers.

The relatively high toughness of helical structures is the result of an increase in resistance to crack propagation due to the differing orientations of the fiber layers. Figure 16b displays an example four-layer helical structure where the angle between the layers is

roughly 45°. Each layer reacts differently to a propagating crack tip (Figure 16b (i) to (iv)). Layers parallel (Figure 16b (iii)) to the crack growth front undergo separation, while those at an angle (Figure 16b (ii) and (iv)) deflect the crack and layers perpendicular (Figure 16b (i)) provide significant resistance as the fibers will need to fracture before the crack can propagate. Thus fracture, separation, and deflection, along with the previously mentioned rotation of fibers, all contribute to the delocalization of the stresses at the crack tip. Dastjerdi and Barthelat [81] have experimentally demonstrated this effect in teleost fish scales, and shown that these mechanisms allow the scales to be amongst the toughest biological materials known. In addition, through studies on the stomatopod dactyl club, the periodicity of these helical structures has recently been shown to be capable of filtering shear waves induced during dynamic loading, thus increasing the impact resistance of the biological material [100]. The scattering effect on waves by multiple layers is an important energy-dissipation mechanism.

Another type of helical structure often observed in nature is that generally found in connection with continuous helices. These are usually found along the outer plane of cylindrical-like organisms (e.g. narwhal tusks [101] and glass sponges (Figure 15d) [94]) as well as many woody plants [102], acting as a reinforcing structure to resist the bending and torsion caused by environmental stresses (e.g. ocean currents). Such external helical-reinforcements grow in response to induced torsion and provide a significant amount of torsional rigidity along their cylindrical axes [103]. As seen in Figure 15d [94], these reinforcing ridges typically grow ~45° to the cylindrical axis that, under an applied torque, is oriented parallel to the directions of maximum compressive and tensile stresses that build-up in these materials. Similar to fiber-reinforced composite panels with angled fiber

orientations, it can be shown that helix-reinforcements aligned at $\Phi = 45°$ with respect to the cylindrical axis provide a maximum normalized shear modulus (G_{XY}/G_{12}) in these types of structures [103]:

$$G_{XY}/G_{12} = \frac{1}{m^4 + n^4 + 2m^2n^2\left[2\frac{G_{12}}{E_1}\left(1 + 2\nu_{12} + 2\frac{G_{12}}{E_2} - 1\right)\right]} \quad 16)$$

where

$$m = \cos\left(\frac{\pi}{2} - \Phi\right) \quad 17)$$

$$n = \sin\left(\frac{\pi}{2} - \Phi\right) \quad 18)$$

where G_{XY} is the effective shear modulus of the material in the *XY*-plane (*X* is the circumferential axis and *Y* is parallel to the cylindrical axis), G_{12} and ν_{12} are the shear modulus and Poisson's ratio in the 12-plane respectively (1 and 2 are axes parallel and perpendicular to the helix reinforcement), and E_1 and E_2 are the elastic moduli of the material parallel and perpendicular to the helical-reinforcement, respectively. Similar to these reinforcing helical structures, spirals are also found in the overall morphology of a wide variety of biological materials (e.g. antelope horns and seashells) [104, 105]. While spiral structures are ubiquitous in nature, the majority exists on a much larger size scale than the primary structural design elements discussed here. Therefore, further discussion on spiral structures has been omitted here, which are detailed in original work by Thompson [104] and modeled by Harary and Tal [105].

2.3 Gradient Structures

Gradient structures are composites that combine materials of varying mechanical properties or composition, resulting in a property or structure gradient through their cross-

section or thickness, as opposed to an abrupt change (Figure 17a). These structural elements accommodate a property mismatch (e.g. elastic modulus, strength) between materials and provide toughness, resist wear, or arrest crack growth. They are commonly found in dermal armors and teeth where rigid surfaces are combined with ductile bases. These gradient structures vary in size, from the microstructural dental/enamel junction (DEJ) in human teeth, which has been measured at ~20 μm (<1% of the total tooth thickness) [67], to the macrostructural squid beak where the gradient extends across the entire length [69]. Specific examples include gradients between the hard exterior and tough interior of fish scales (e.g. Senegal bichir, Figure 17b) [106] and crab claws (Figure 17c) [68] and the DEJ in many teeth Figure 17d,e [70, 107].

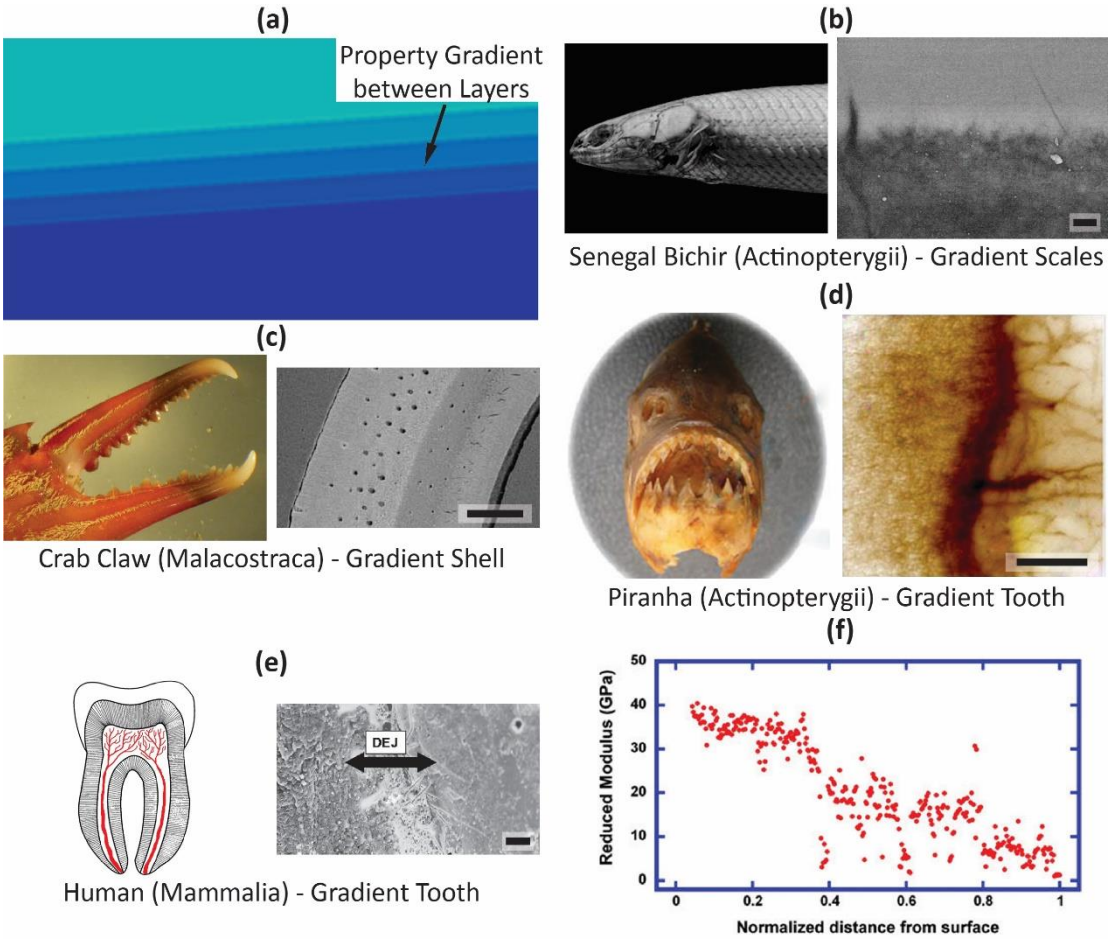

Figure 17. Biological gradient structures from nature representing a variety of biological classes. **(a)** Diagram of gradient structures displaying a gradient in properties between layers; **(b)** Senegal Bichir (Actinopterygii) with gradient scales; **(c)** Crab (Malacostraca) with a gradient structure in its claws; **(d)** Piranha (Actinopterygii) with a gradient dental-enamel junction (DEJ) in its teeth; **(e)** Human tooth (Mammalia) with a gradient DEJ; **(f)** Modulus data from a fish scale displaying the gradual shift in properties between layers through the scale thickness. Scale bars: **(b)** 1 μm, **(c)** 30 μm, **(d)** 15 μm, **(e)** 10 μm. Adapted with permission from [12].

Mechanically, gradient structures provide stress relief at the interfaces between dissimilar materials, which are characterized through a smooth transition in properties as is shown for the modulus through the thickness of a fish scale (Figure 17f) [70]. Suresh [108-110], Giannakopoulos [111, 112], Kim [113, 114], and co-authors have reported extensively on the mechanical and structural properties of gradient structures in many

different loading configurations. Gradients can be described for a given mechanical property, Q, (e.g. elastic modulus, yield strength, toughness) as a function of position through the interface, z, adapted from [111]:

$$Q = f(z) \text{ where: } f(z) = \begin{matrix} \text{Linear: } Q_0(1-z) \\ \text{Power: } Q_0\left(1-z^{\mathrm{k}}\right) \\ \text{Exponential: } Q_0 e^{-\alpha \mathrm{z}} \end{matrix} \quad (19)$$

where Q_0 is the initial value of the property (e.g. the value at the beginning or end of the gradient interface), k is a non-dimensional exponent that varies from $0 \leq k < 1$ and α is a material constant with dimensions of length^{-1}. Equation 19 is presented so that, in each case, the value of Q begins at Q_0 then decreases throughout the gradient (for $\alpha >> 1$). While there are other possible profiles, the three listed here are those suggested and examined by Suresh and Giannakopoulos [108, 111]. A gradient structure that follows a power-law relationship will become a linear gradient structure when $k = 1$ and a homogenous structure (non-gradient) when $k = 0$. For gradient structures that vary exponentially, $\alpha > 0$ results in a decrease through the bulk while $\alpha < 0$ inversely results in an increase through the bulk.

An abrupt or non-graded interface (similar to layered structures that will be discussed later) can impart additional toughness to a structure through interfacial crack deflection. However, gradient structures can serve to avoid interfacial stresses that exist between materials with significantly different mechanical (or thermal, optical, electromagnetic) properties. A prime example of this is the DEJ within mammalian teeth (Figure 17e). This well-bonded interface creates a gradient barrier between the stiff enamel and tough dentin phases. Importantly, this interface has been reported to arrest cracks propagating from the enamel to the dentin due to the elastic modulus mismatch [67, 115].

An additional example, the squid beak, is a graded structure in which the hardness gradually decreases 100 times from the surface to the interior [69, 116].

2.4 Layered Structures

Layered structures are composite materials that consist of multiple layers or interfaces and are often employed to improve the toughness of otherwise brittle materials (Figure 18a). A foil to gradient structures, the interfaces in layered structures feature abrupt and often large changes in mechanical properties. Layered structures occur in the microstructure of biological materials. Specific examples include the concentric layers of deep-sea sponges (Figure 18b) [66, 117], the brick-and-mortar structure of the abalone shell (Figure 18c) [14, 118, 119], the layers of many fish scales (e.g. the arapaima, Figure 18d) [70, 97] and insect exoskeletons (e.g. beetles, Figure 18e) [64, 120].

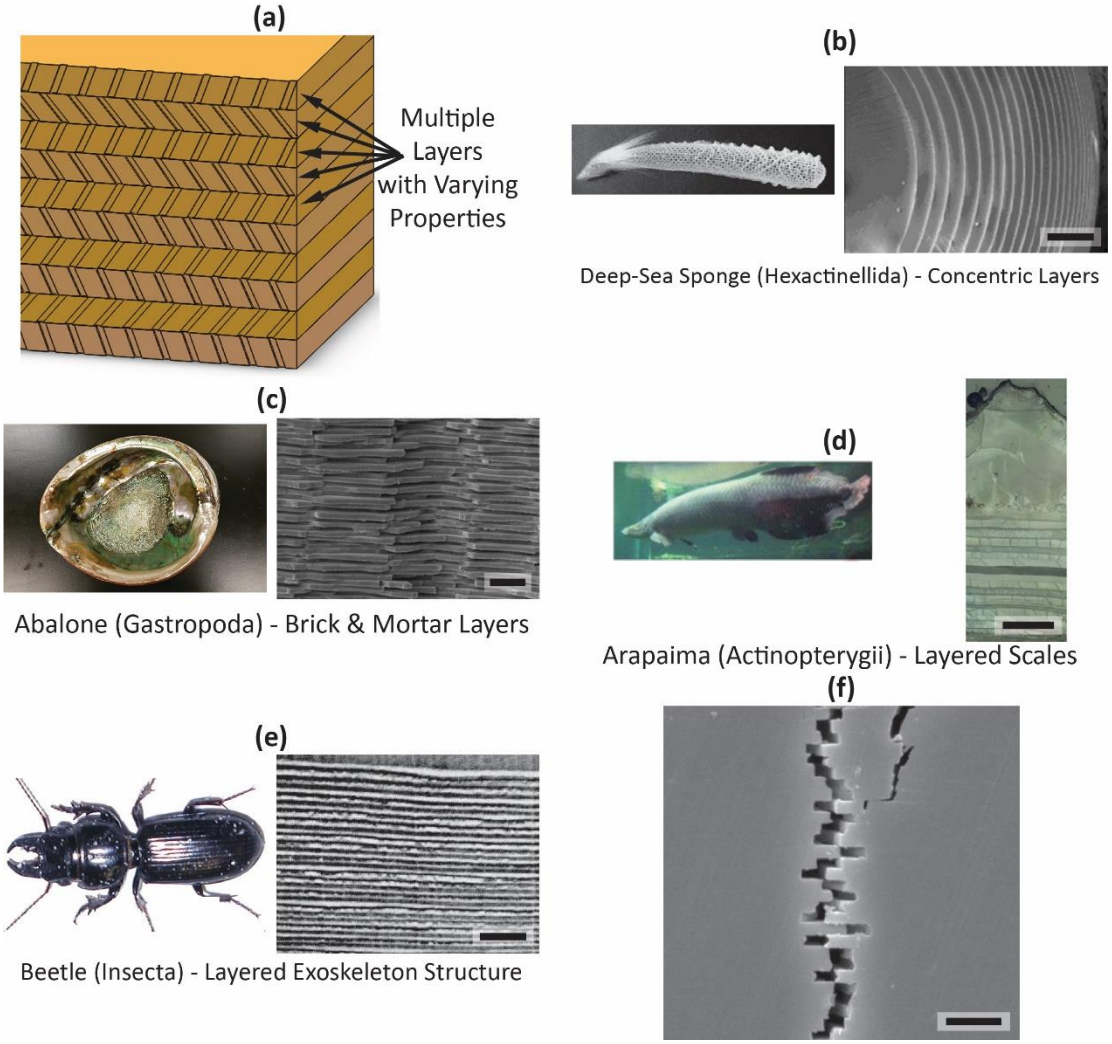

Figure 18. Biological layered structures from nature representing a variety of biological classes. **(a)** Diagram of layered structures displaying multiple layers with varying properties or interfaces to induce anisotropy within the bulk material; **(b)** Deep-sea sponge spicules (Hexactinellida) with concentric layers; **(c)** Abalone shell (Gastropoda) with brick-and-mortar layers; **(d)** Arapaima (Actinopterygii) with a layered structure through the cross-section of its scales; **(e)** Beetle (Insecta) with a layered structure in its exoskeleton; **(f)** Fracture image of a layered structure displaying how the layers deflect the crack and create a high energy, tortuous crack path. Scale bars: **(b)** 5 μm, **(c)** 2 μm, **(d)** 200 μm, **(e)** 1 μm, **(f)** 2 μm. Adapted with permission from [12].

Mechanically, layered structures primarily increase the fracture toughness of a biological material through the introduction of numerous interfaces, which often contain a second more-ductile phase. Toughness is defined as the amount of energy a material can

absorb prior to catastrophic failure. The fracture toughness is a measure of the energy required to induce catastrophic failure; however, it accurately assumes that inorganic and organic materials alike contain flaws and cracks that reduce their strength from the theoretical value (~E/10 to E/30). With this assumption, the maximum stress before failure, σ_{max}, of any real material is governed by the Griffith equation [121]:

$$\sigma_{\max} = \sqrt{\frac{2\gamma E}{\pi a}} = \frac{Y K_{\mathrm{Ic}}}{\sqrt{\pi a}} \qquad 20)$$

where γ is the material's energy that can be considered the sum of the surface energy, γ_s, and an energy related to plastic/permanent deformation, γ_p, ($\gamma = \gamma_s + \gamma_p$), a is the length of a crack or void in the material, Y is a geometric parameter, and K_{Ic} is the Mode I (opening) critical fracture toughness. This equation shows that the fracture strength and crack length are related by the material's parameter, K_{Ic}.

Unlike most helical structures that are generally found in more ductile materials, layered structures are most commonly composed of brittle constituents (e.g. calcium carbonate, hydroxyapatite, silica, and other biominerals), although they both impart toughness. Ritchie and co-workers [46, 122-125] have reported extensively on the mechanisms that increase toughness in otherwise brittle materials. These mechanisms can be classified according to both their relative location with respect to a growing crack tip and their inherent length scale as either intrinsic (ahead of the crack tip, <1 μm) or extrinsic (behind the crack tip, >1 μm) [126]. In layered biological structures, most toughening mechanisms are extrinsic, including crack deflection and twisting, uncracked ligament and fibril bridging, and microcracking. Each of these mechanisms serves to either increase the energy required to propagate a crack or shield stress from the crack tip. Among these, the

energy required to cause catastrophic failure in most layered brittle biological materials is predominantly increased by two extrinsic mechanisms. First, by deflecting or twisting a crack, the applied stress is taken out of the preferred Mode I (opening) orientation, resulting in a more-tortuous crack path. Second, any deflection of the crack will result in an inherently longer crack path over a straight crack (as seen in Figure 18f), thus increasing the work required to propagate a crack, W_s [121]:

$$W_s = 2aB\gamma \tag{21}$$

where B is the out-of-plane thickness of the solid material. Though simplified, this provides an indication of the increase in toughness caused by the longer crack paths induced by predominately brittle layered structures. In addition to the increase in the cracked surface area, the introduction of relatively weaker interfaces can improve the toughness. As a crack approaches a weak interface, the stresses ahead of the crack tip can be sufficiently large to cause the interface to fracture. This creates, directly ahead of the crack tip, a second offset (or ideally perpendicular) crack that, when merged, will significantly increase the crack-tip radius of curvature, ρ. This, known as the Cook–Gordon toughening mechanism, decreases the stress at the crack tip, σ_{tip}, as it is inversely related to ρ through the Inglis equation [7]:

$$\sigma_{tip} = \sigma_a \left(1 + 2\sqrt{\frac{a}{\rho}} \right) \tag{22}$$

where σ_a is the applied stress. It is this Cook–Gordon mechanism that is most effectively able to harness the numerous interfaces of layered structures to increase the facture toughness. However, the frictional sliding at the interfaces between lamellae created by crack deflection also contributes to the toughening in a manner similar to the toughening

of fiber-reinforced composites. As a result, the toughness of many layered structures is much higher than a simple mixture of their constituents. The fracture toughness of abalone and conch, both of which have elements of a layered brick-and-mortar architecture (Figure 18c), is up to seven times higher than their main constituent, calcium carbonate, which makes up ~ 95% of their mass [118, 127].

2.5 Tubular Structures

Tubular structures consist of arrays of long aligned pores (tubules) within a bulk material (Figure 19a). These structural elements are commonly found in impact- and pierce resistant materials, such as hooves, teeth, and the scales of fish. Tubules are microstructural elements in biological materials. Specific examples of materials that feature tubules include keratin-based horse hooves (Figure 19b) [128] and ram horns (Figure 19c) [73, 129], chiton-based crab exoskeletons (Figure 19d) [130], collagen/hydroxyapatite-based human teeth (Figure 19e) [60], compact bone, and some fish scales [72]. Functionally, tubules provide nutrients (as is the case of dentin, osteons in bone and crustacean exoskeletons) and provide ductile attachment (in crustaceans). Mechanically, these structures improve fracture toughness and energy absorption by arresting crack growth through removing the stress singularity at the crack tip (Figure 19f) and/or by collapsing the tubules when compressed. They can also serve as scattering centers that decrease the amplitude of longitudinal stress pulses generated by impact. This is important in hooves and horns, which are subjected to high velocity loading (up to 10 m s^{-1}). This loading generates elastic waves of significant amplitude. The scattering of these waves can result in a decrease of their overall amplitude, thereby minimizing damage to the underlying live tissues.

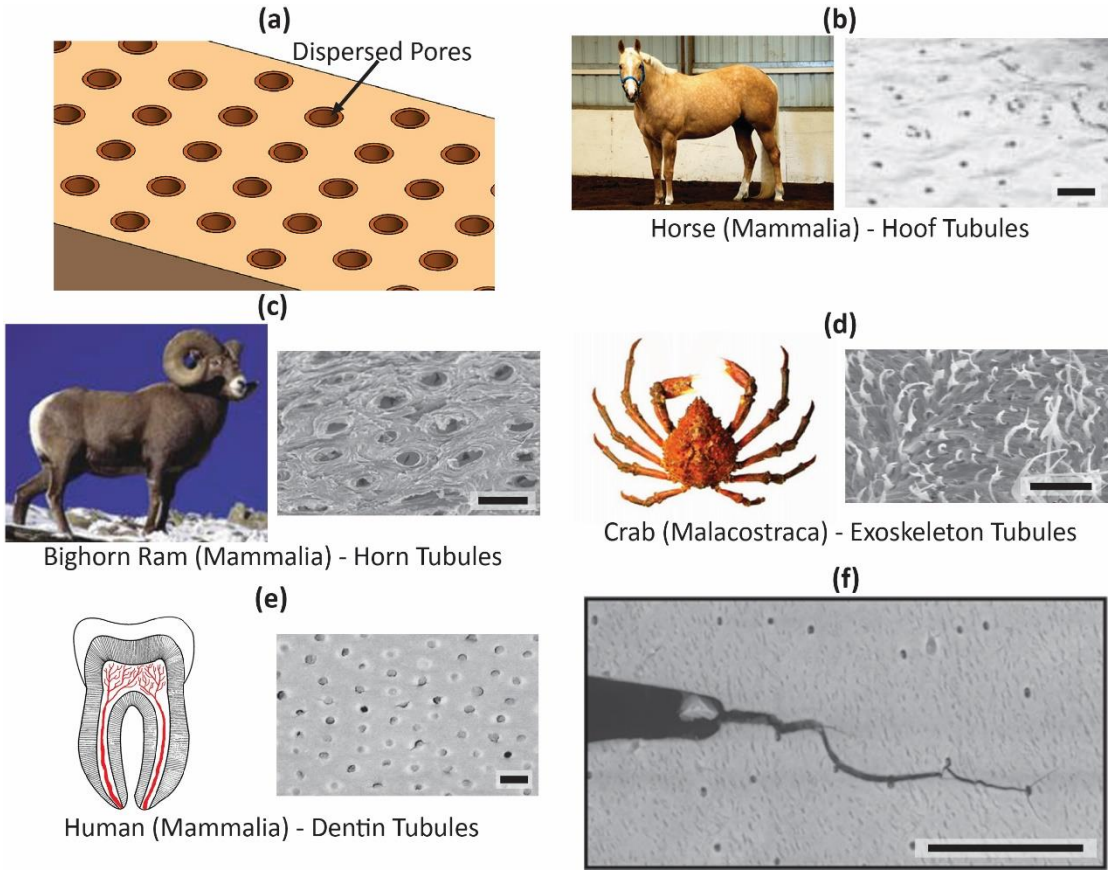

Figure 19. Biological tubular structures from nature representing a variety of biological classes. **(a)** Diagram of dispersed tubules (pores) within a solid matrix; **(b)** Horse (Mammalia) with hoof tubules; **(c)** Bighorn ram (Mammalia) with horn tubules; **(d)** Crab (Malacostraca) with exoskeleton tubules; **(e)** Human tooth (Mammalia) with dentin tubules; **(f)** SEM image of a material with tubules demonstrating how the tubules themselves can deflect a growing crack. Scale bars: **(b)** 200 μm, **(c)** 200 μm, **(d)** 5 μm, **(e)** 5 μm, **(f)** 100 μm. Adapted with permission from [12].

Tubular structures that absorb energy through compression can be subdivided into those where the tubules are aligned perpendicular to the direction of loading (e.g. ram horn, Figure 19c) [73, 129] and those where the tubules are aligned parallel to the direction of loading (e.g. horse hooves, Figure 19b) [128].

Tubular structures, which decrease the stiffness of structures but absorb energy during compression, can, mechanically, be modeled as hollow cylinders. Observing these structures in comparison to solid cylinders allows for the specific influence of the tubules

to be assessed. Compression of an array of hollow cylinders (tubules) perpendicular to the long axis of the tubules results in a decrease in Young's modulus proportional to the volume fraction of the pores:

$$\frac{E}{E_0} = \left(1 - V_p^2\right) \quad (23)$$

where E and E_0 are the elastic moduli of the porous and dense material respectively and V_p is the volume fraction of the pores. Thus, the ratio of the displacement of a solid cylinder to a hollow cylinder is proportional to $(1 - V_p^2)$, demonstrating that a much higher deformation can be achieved by incorporating aligned porosity than without it. Additionally, the relative elastic modulus (E/E_0) in the direction parallel to the tubules is also reduced (by a factor of $(1 - V_p)$), yielding a more-compliant structure than a solid material. Both of these effects result in the ability of the material to deform around the tubules, thereby increasing the energy absorbed over that of a material without tubules, for a constant applied force.

An example of a tubular structure that can absorb energy through compression is that in a sheep horn (Figure 19c). Sheep horns must be structurally robust as they undergo impact forces during seasonal fighting. Since they are a lifetime appendage, it is important that they do not fracture. Horns are composed of α-keratin and have a lamellar structure, which is stacked in the radial direction of the horn (parallel to growth direction), perpendicular to the direction of loading [73]. The lamellae are ~4 μm thick and have long tubules (~40 – 100 μm in diameter) dispersed between the lamellae, and extending along the length of the horn, resulting in a porosity of ~7%. In spite of this small overall tubule density, the lamellar structure coupled with the tubules yields a material that can withstand

large compressive stresses without fracture. Under compression in the radial (impact) direction, the tubules collapse allowing for 60% strain to be sustained without fracture [73].

Similarly, the tubules of horse hooves (Figure 19b) are designed to absorb energy through compression. However, as opposed to horn, the tubular porosity is aligned parallel to the impact direction. The hoof wall has a complex structure consisting of tubular lamellae ranging from 6 – 15 μm in thickness. Hollow tubules (~50 μm in diameter) are embedded in an intertubular matrix [128]. The tubular lamellae have a higher elastic modulus than the intertubular matrix, suggesting that the tubule structure, although porous, increases the elastic modulus of the hoof. In addition, Kasapi and Gosline [128, 131] concluded that the tubules serve to increase crack deflection, thereby increasing the fracture toughness. Mechanically, with the tubule orientation parallel to the direction of compressive loading, the compressive strength, σ_c, can be determined:

$$\sigma_c = \frac{E_m\left(1 - V_p^{1/3}\right)\varepsilon_{mf}}{\nu_m} \qquad 24)$$

where E_m is the elastic modulus of the matrix, ε_{mf} is the intertubular matrix strain at failure and ν_m is the Poisson's ratio of the matrix. From this, it can be seen that, because the tubules are reinforced, the compressive strength depends mainly on the strain to failure and elastic properties of the surrounding matrix.

The tubules in dentin (~1 μm diameter) are well known to improve toughness and radiate from the pulp to the enamel surface, where there is a density of 3×10^4 mm^{-2} and, in addition to their mechanical advantage, allow for cellular activity and nutrient transport. The tubules are filled with a fluid and have a higher density of minerals surrounding them than the intertubular matrix. Therefore, dentin has often been modeled as a continuous

fiber-reinforced matrix, with the highly mineralized tubules serving as the reinforcing fibers and the less-mineralized intertubular matrix as the surrounding phase [71]. Under normal compressive loading, the reinforced tubules are parallel to the load direction, similar to the hoof. The fracture toughness of dentin was found to be over 50% larger in the direction parallel to the tubules compared to the perpendicular direction, which was attributed to extensive crack bridging [132].

In the freshwater Alligator gar fish scales, the tubules (6.5 μm diameter) with a density of ~300 mm^{-2} are oriented perpendicular to the surface of the scale [72]. The toughness and compressive strength is highest for loading parallel to the tubule direction compared to the two orthogonal directions, which is the optimal arrangement for resisting piercing attacks from biting predators. Similar to dentin, crack bridging was reported as the main factor in crack-growth resistance.

Tubules are present in the body of crustaceans, such as lobsters and crabs, and penetrate through the thickness of the exoskeleton (exo- and endocuticle). These tubules (~1 μm diameter) have a high density of 1.5×10^5 mm^{-2} and transport ions that are critical for forming a new exoskeleton when the animal molts [130]. The tubules enhance the toughness for loading in the direction normal to the exoskeleton surface, by holding together the layered Bouligand structured exo- and endocuticles through ductile interfaces.

An important subset of tubular structures is cylindrical-cross-ply or Haversian structures. These structures are characterized by cylindrical cross-plies, layered around a tubule, and thus provide additional fracture toughness by acting as uncracked ligaments that shield stresses [123, 133]. These Haversian structures are commonly found in mammalian bone [123, 133, 134].

2.6 Cellular Structures

Cellular structures include open and closed cell foams, scaffolds, and other highly porous materials (e.g. honeycombs) (Figure 20a), resulting in high-strength low-weight structures, capable of resisting buckling and bending and/or increasing toughness. Given their weight savings, cellular structures are commonly observed in birds and other flying organisms. However, many terrestrial and marine organisms also contain some form of cellular structures to reduce weight in otherwise dense materials (e.g. bone, shell). Cellular structures can exist as nano- to microstructural elements within a biological composite material or as the macrostructure of a bulk biological material. Specific examples include porcupine quills (Figure 20b) [74], toucan beaks (Figure 20c) [9, 135], turtle shells (Figure 20d) [136], antlers (Figure 20e) [4, 75], bird bones (Figure 20f) [7], horseshoe crab shells (Figure 20g) [4], and mammalian trabecular bone [60, 75].

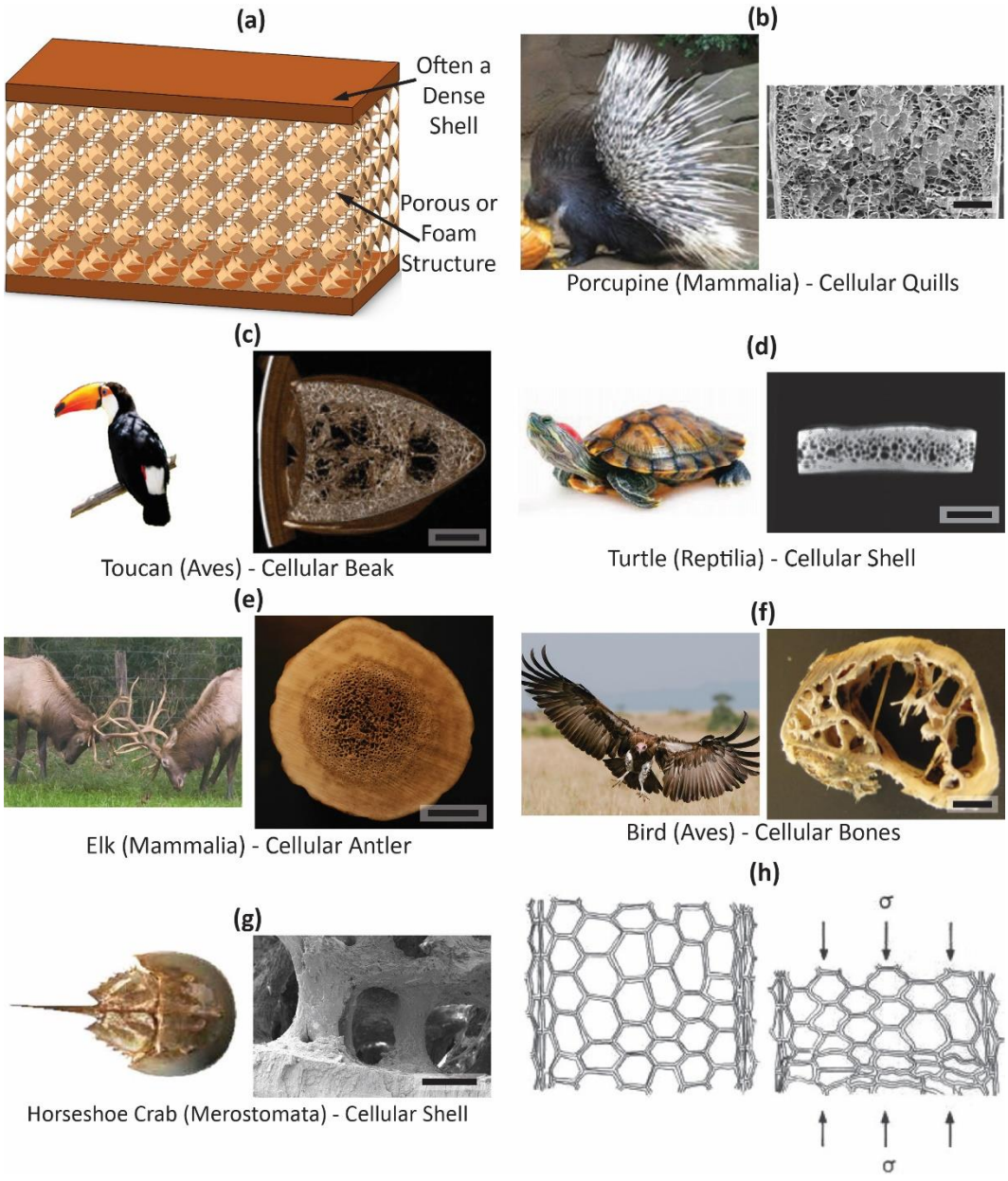

Figure 20. Biological cellular structures from nature representing a variety of biological classes. **(a)** Diagram of a cellular structure displaying a porous or foam structure that is often surrounded by a dense shell; **(b)** Old world porcupine (Mammalia) with foam-filled, cellular quills; **(c)** Toucan (Aves) with a foam-filled, cellular beak; **(d)** Turtle (Reptilia) with a cellular shell; **(e)** Elk (Mammalia) with cellular antlers; **(f)** Birds (Aves) with cellular bones, showing struts extending through the interior and ridges that add thickness locally; **(g)** Horseshoe Crab (Merostomata) with a cellular shell; **(h)** Diagram of a cellular foam structure under compression showing how the structure buckles and compresses in order to increase deformation and toughness. Scale bars: **(b)** 500 μm, **(c)** 1 cm, **(d)** 2 mm, **(e)** 10 mm, **(f)** 2 mm, **(g)** 500 μm. Adapted with permission from [12].

Mechanically, cellular structures provide some strength while minimizing weight. There are two general classes of cellular solids: open cell, where there are interconnected pathways that traverse the individual pores of the foam or scaffold, and closed cell, where the individual pores are completely isolated. In general, a relative density, ρ^*/ρ_s, (where ρ^* is the measured density of the cellular scaffold and ρ_s is the density of a fully dense solid of the same material) differentiates open cell ($\rho^*/\rho_s < 0.3$) from closed cell ($\rho^*/\rho_s > 0.3$) [7]. Gibson and Ashby [137-139] showed that the relative stiffness of a cellular structure, E^*/E_s, (where E^* is the measured stiffness of the cellular scaffold and E_s is the stiffness of a fully dense solid of the same material) can be determined for open cell (Equation 25) structures and closed cell (Equation 26) structures as functions of the material properties:

$$\frac{E^*}{E_s} \approx \left(\frac{\rho^*}{\rho_s}\right)^n \qquad 25)$$

where n is a power exponent ranging from 1 to 3 that relates to the stiffness of the material (in biological materials; n approaches 3 for heavily mineralized materials and 1 for unmineralized materials) [7], and:

$$\frac{E^*}{E_s} = \Phi^2\left(\frac{\rho^*}{\rho_s}\right)^n + (1-\Phi)\frac{\rho^*}{\rho_s} + \frac{P_0(1-2\nu^*)}{E_s\left(1-\frac{\rho^*}{\rho_s}\right)} \qquad 26)$$

where Φ is the fraction of edges within the closed cell of the cellular solid, ν^* is the measured Poisson's ratio and P_0 is the gas pressure within the closed pores. Unlike open-cell structures, closed-cell cellular structures result in numerous enclosed chambers that act as pressure vessels. As a result, the gas pressure and Poisson's ratio must be taken into account. Mechanically, both open- and closed-cell cellular structures result in a unique stress–strain behavior with an initial linear region (due to cell-wall bending), an uneven,

jagged plateau region (due to cell-wall buckling and fracture) and finally a sharp increase in modulus (due to cellular densification) [137, 138]. These expressions demonstrate that the elastic modulus is very sensitive to the amount of porosity. While the majority of biological cellular structures have low relative densities (~10 – 20%) [139], some such as corals can range between 30 and 50% [76], and sandwich structures such as turtle shell (~50%) [136] are much denser.

Cellular structures are most commonly surrounded by dense walls, forming sandwich structures. Sandwich structures themselves can be considered composites of two phases: the dense shell and the cellular core. There is often a synergism between the cellular interior and the dense walls. As a result, the mechanical properties of sandwich structures are superior to those predicted from a simple rule-of-mixtures. Gibson and Ashby [137] determined a constitutive equation for the bending compliance of panel-shaped sandwich structures:

$$\frac{\delta}{P} = \frac{2}{B_1 E_f b \left(\frac{t}{L}\right)\left(\frac{c}{L}\right)^2} + \frac{1}{B_2 b \left(\frac{c}{L}\right) G_c^*} \qquad 27)$$

where δ is the deflection of the structure, P is the applied load, B_1 and B_2 are constants based upon the loading geometry (see Gibson [139] for more details), b is the width of the structure, t and c are the thickness of the dense shell and porous core respectively, L is the span, E_f is the Young's modulus of the dense shell, and G_c* is the shear modulus of the core (cellular) material. The first and second terms represent the compliance of the dense shell sections and porous core respectively. These panel-shaped structures can be found in a number of biological materials, such as turtle (Figure 20d) [136] and horseshoe crab

shells (Figure 20g) [4]. The internal porous material of the sandwich structure serves to lighten the structure and to absorb energy from bending and crushing attacks (Figure 20h).

Cylindrical sandwich structures are very common in nature, consisting of a dense cylinder filled with a porous or foam core. These structures can be found in porcupine quills (Figure 20b) [74, 140], mammalian bones and antlers (e.g. elk, Figure 20e) [75], bird bones and feathers (Figure 20f) [7], the toucan beak [135, 141], and plant stems [5]. Cylindrical sandwich structures provide resistance to local bulking in order to avoid premature failure. Filling of a hollow structure with a foam, at a constant weight, significantly increases the bending moment at which buckling is initiated because the walls of the shell are supported. It has been experimentally shown that the critical buckling strength of cylindrical sandwich porcupine quills is increased by up to three times over hollow porcupine quills, holding the weight per unit length constant [140]. This has also been shown for the toucan beak [135] and peacock feathers [142]. Karam and Gibson [143] developed a constitutive equation for the local compressive buckling stress in the longitudinal direction, σ_{cr} , of such structures:

$$\sigma_{cr} = \frac{Et}{a}\left[\frac{1}{12(1-\nu^2)}\frac{a/t}{\left(\lambda_{cr}/t\right)^2} + \frac{\left(\lambda_{cr}/t\right)^2}{\left(a/t\right)} + \frac{2}{(3-\nu_c)(1+\nu_c)}\frac{E_c}{E}\frac{\lambda_{cr}a}{t^2}\right] \quad 28)$$

where E, t, a and ν are the stiffness, thickness, radius, and Poisson's ratio respectively of the dense shell, E_c and ν_c are the stiffness and Poisson's ratio, respectively, of the foam core and $2\lambda_{cr}$ is the wavelength of the instability divided by π, which can be calculated from:

$$\frac{\lambda_{\mathrm{cr}}}{t} \approx 0.69\left(\frac{E}{E_{\mathrm{c}}}\right)^{1/3} \quad (29)$$

The buckling strength is a complex function of the geometry and material properties. Specifically, the critical buckling strength increases as *t*/*a* increases; however, in competition, the weight also increases with this ratio. Karam and Gibson [143, 144] have reported on the ratios where strength is maximized and weight is minimized for a variety of materials.

Not all cellular structures take on such a simplified structure. One of the most notable and more complex examples of cellular biological structural materials are avian wing bones. Birds have lightweight skeletons, which, coupled with a high lift-to-weight ratio, makes flight possible. Their pulmonary system is complex; many have pneumatic bones (particularly the proximal bones: humerus and femur) that are directly connected to the respiratory system, thereby increasing buoyancy [145-147]. Bird bones are characterized by a much thinner sheath of cortical bone, compared to terrestrial animals [148]. Bones of flying birds need to be strong and stiff enough to withstand forces during takeoff and landing, which necessitates some reinforcement in the bone interior. Wing bones have to resist both bending and torsion forces, as they are rarely loaded in pure tension or compression. Such structures can be modeled as hollow cylinders. The bending stress acting on a thin-walled hollow cylinder can be approximated as [149]:

$$\sigma = \frac{MR}{I} \approx \frac{M}{\pi R^2 t} \quad (30)$$

where *M* is the bending moment, *R* is the external radius, *I* is the second moment of inertia and *t* is the wall thickness. Similarly, the shear stress (in torsion) of thin-walled hollow cylinders can be determined [149]:

$$\tau = \frac{TR}{J} \approx \frac{T}{2\pi R^2 t} \quad (31)$$

where *T* is the torque and *J* is the polar moment of inertia. Both expressions indicate that increasing the wall thickness decreases both torsional and bending stresses, at the expense of an increase in weight. These external forces have necessitated the development of reinforcing structures (struts and ridges) inside the bones (Figure 20f in a turkey-vulture humerus) [146, 150], instead of uniformly thickening the wall. Struts appear as reinforcing structures that extend through the center of the bone at places "in need", working against extensive bending forces and preventing ovalization and buckling of bone walls. Ridges occur on the walls and add material locally, thereby increasing both *I* and *J* [150].

2.7 Suture Structures

Suture structures are wavy or interdigitating interfaces that are found within a variety of plates, scutes, and bones, and generally consist of two phases: rigid suture teeth and a compliant interface layer (Figure 21a). They often appear in regions where there is a need to control the intrinsic strength and flexibility of a material interface. Sutures occur as microstructural interfacial elements in biological materials. Specific examples where sutures appear include the carapace of the red-eared slider (Figure 21b) [78] and leatherback turtles [151], mammalian skulls (e.g. white-tailed deer, Figure 21c) [152, 153], the pelvis of threespine sticklebacks (Figure 21d) [154], boxfish scute junctions (Figure 21e) [77], the exoskeletal surfaces (called frustules) of diatoms (Figure 21f) [155], armadillo osteoderms (Figure 21g) [156], and ammonite shells [157].

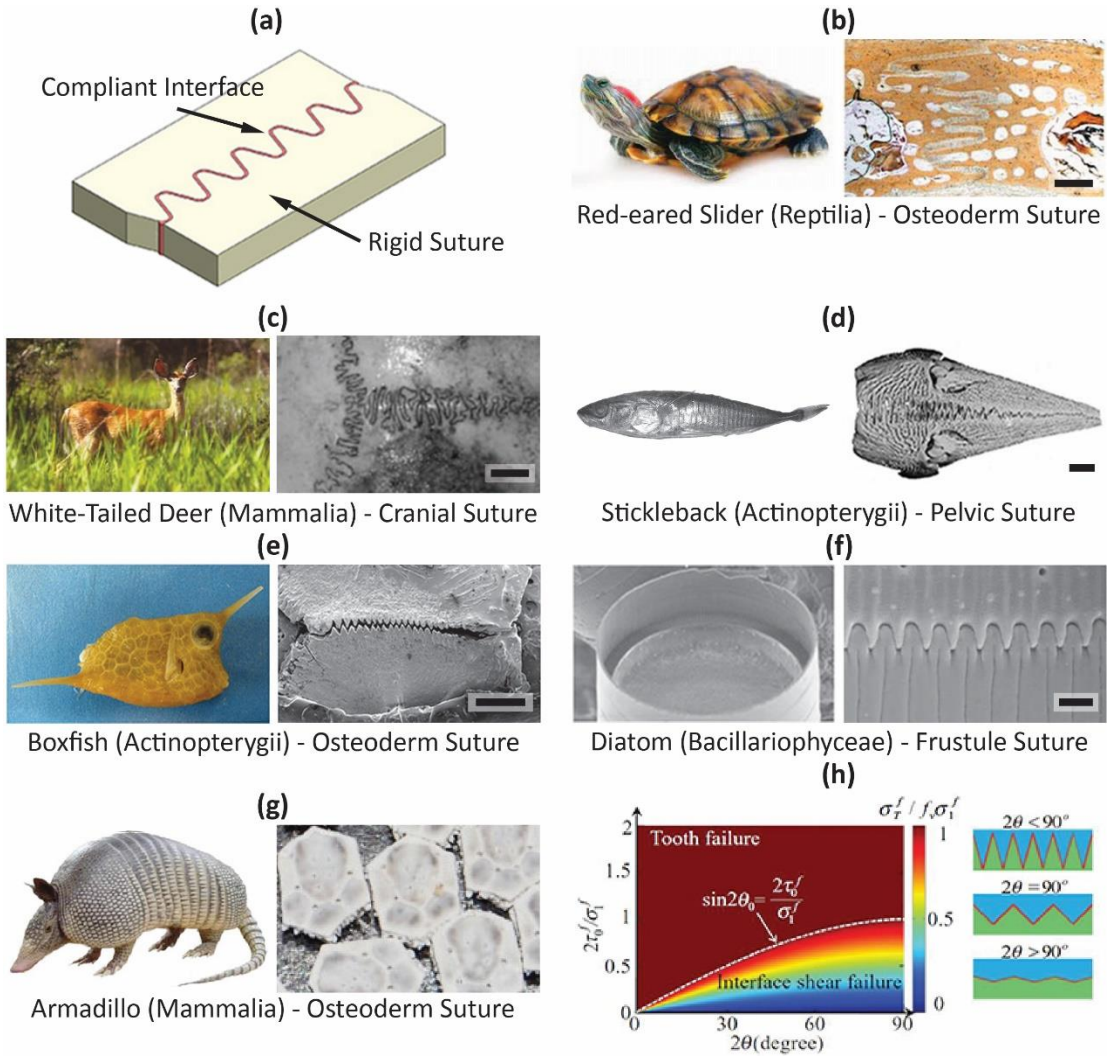

Figure 21. Biological suture structures from nature representing a variety of biological classes. **(a)** Diagram of sutured interfaces displaying the rigid sutures and a compliant interface; **(b)** Red-eared slider (Reptilia) with osteoderm sutures; **(c)** White-tailed Deer (Mammalia) with cranial sutures; **(d)** Stickleback (Actinopterygii) with a pelvic suture; **(e)** Boxfish (Actinopterygii) with scute sutures; **(f)** Diatom (Bacillariophyceae) with exoskeletal (frustule) sutures; **(g)** Armadillo (Mammalia) with osteoderm sutures; **(h)** Mechanical model of the failure mode of triangular suture interfaces based upon the angle of the suture displaying that the maximum strength will occur when the failure modes of tooth and interface shear failure are balanced. Scale bars: **(b)** 1 mm, **(c)** 1 cm, **(d)** 1 mm, **(e)** 500 μm, **(f)** 1 μm. Adapted with permission from [12].

Mechanically, suture structures provide strength at the interfaces of rigid biological components while still controlling the flexibility. Li, Ortiz and Boyce [79, 157-159] have developed a number of constitutive equations for the effective strength of a sutured

interface of arbitrary geometry, the most generalized of which, a single repeating triangular suture, is reported here. For this generalized case, it is assumed that two failure modes are possible: tooth failure where the suture teeth themselves fracture, and interface shear failure where a crack propagates through the interface itself around the suture teeth. For an idealized loading situation (loading in tension with the loading axis perpendicular to the sutured interface where the stress is uniform through both the rigid sutures and compliant interface), a critical suture tooth angle, $2\theta_0$, can be determined, where the suture teeth and interface would simultaneously fail, thus creating a strength-optimized structure [158]:

$$2\theta_0 = \sin^{-1}\frac{2\tau_0^f}{\sigma_1^f}\,, \theta_0 \leq \frac{\pi}{4} \tag{32}$$

where τ_0^f is the critical shear stress that would cause shear failure of the interface and σ_1^f is the critical tensile stress that would cause failure of the suture teeth. Note that this equation is reorganized and plotted in Figure 21h to display the strength optimized boundary between the two failure modes noted above. For any arbitrary suture tooth angle, θ, $\theta \leq \theta_0$ will result in a tooth failure while $\theta > \theta_0$ will result in an interface shear failure.

The effective stiffness of a sutured interface, $\bar{E}$, can be calculated as a function of material and geometric parameters [158]:

$$\frac{\bar{E}}{E_1} = \frac{f_v^2}{(1-f_v)\left(\frac{E_1}{G_0}\sin^2\theta\cos^2\theta + \frac{E_1}{E_0}\sin^4\theta\right) + f_v} \tag{33}$$

where E_1 and E_0 are the Young's moduli of the suture teeth and interface phases respectively, G_0 is the shear modulus of the interface phase, and f_v is a non-dimensional suture phase volume fraction [158]:

$$f_v = \frac{(\lambda - 2g)}{\lambda} \quad (34)$$

where λ is the wavelength of the suture teeth and g is the thickness of the interface layer. These equations, though for an idealized state, allow for basic understanding of the optimized geometry of suture structures. As an example, Li et al. [158] presented a case for a bone-like suture structure (f_v = 0.8) where the suture teeth are assumed to be bone (E_1 = 10 GPa, σ_1^f = 100 MPa) and the interface is collagen (E_0 = 100 MPa, τ_0^f = 20 MPa). With these conditions, the strength-optimized suture tooth angle is $2\theta_0$ = 23.6°. Of note, the experimentally measured sutures of bone-like biological structures in red-eared slider turtles (2θ = 9.4–22°, Figure 21b) [78], white-tailed deer (2θ = 9–25°, Figure 21c) [79], leatherback sea turtle (2θ = 30°) [151], and three spine stickleback fish (2θ = 6–20°, Figure 21d) [154] are all similar to this predicted optimized angle.

Beyond the simplified suture structures described above, recent work by Lin et al. [159] has shown that increasing the level of hierarchy of a sutured interface can significantly improve the mechanical properties. A suture structure with a high level of hierarchy (e.g. deer cranial sutures, Figure 21c) will generally have higher stiffness and toughness than a simple suture (e.g. diatom frustule sutures (Figure 21f), or boxfish scute sutures (Figure 21e)). In addition, the design and level of hierarchy can effectively tailor the tensile strength.

2.8 Overlapping Structures

Overlapping structures are composed of a number of individual plates or scales that can slide or shift past each other, forming a flexible protective surface (Figure 22a). These are most commonly employed as armor. Overlapping structures occur as macrostructural

elements. Specific examples include seahorse tails (Figure 22b) [80], shark skin (Figure 22c) [160], the millipede exoskeleton (Figure 22d) [161], the chiton exoskeleton (Figure 22e) [82], fish scales (e.g. alligator gar (Figure 22f) and arapaima) [72, 162, 163], and pangolin plates (Figure 22g) [7].

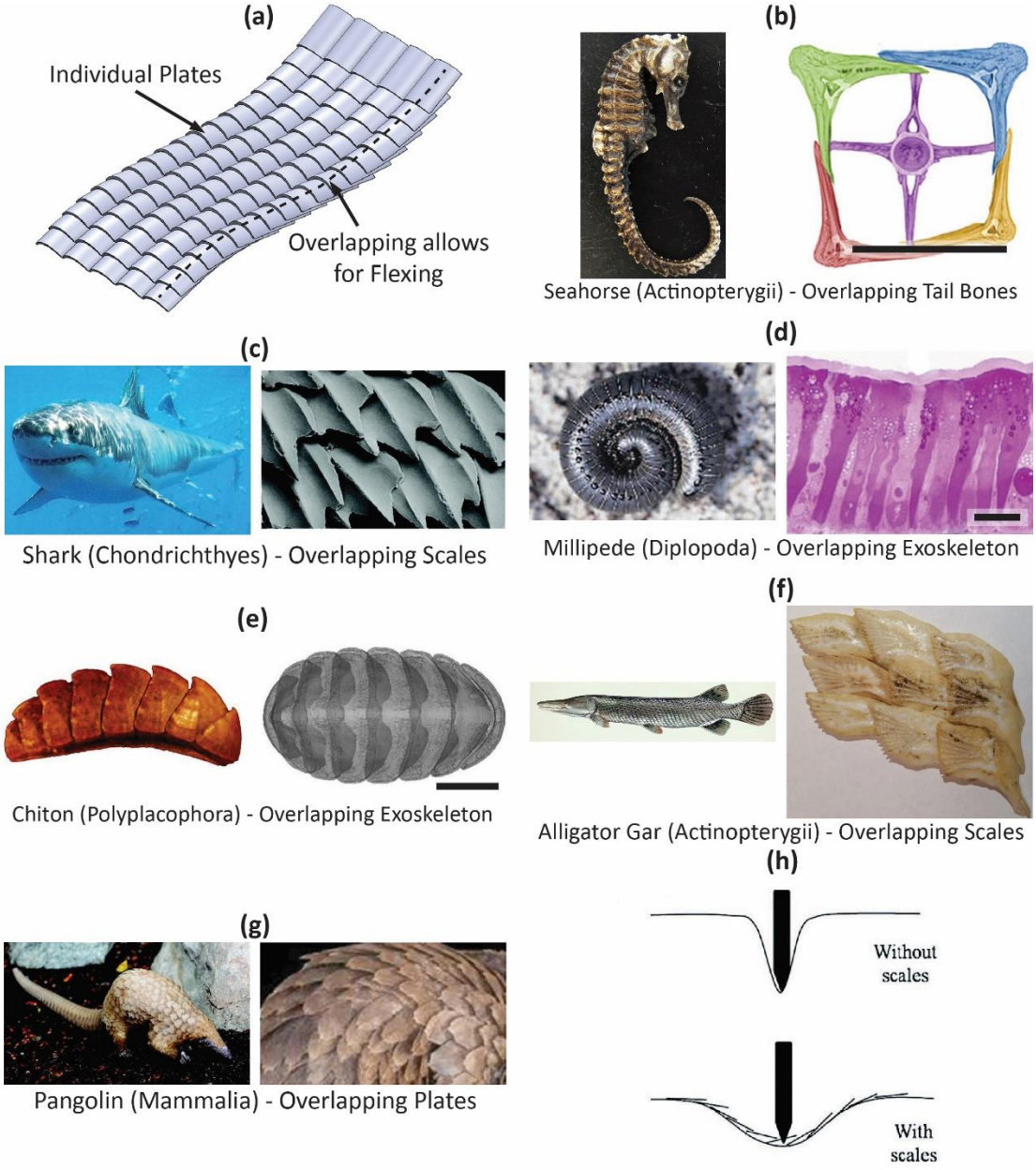

Figure 22. Biological overlapping structures from nature representing a variety of biological classes. **(a)** Diagram of overlapping structures that are made of individual plates and allow for flexing while ensuring full coverage; **(b)** Seahorse (Actinopterygii) with overlapping bony tail plates; **(c)** Shark (Chondrichthyes) with overlapping scales; **(d)** Millipede (Diplopoda) with an overlapping exoskeleton; **(e)** Chiton (Polyplacophora) with an overlapping exoskeleton; **(f)** Alligator gar (Actinopterygii) with overlapping scales; **(g)** Pangolin (Mammalia) with overlapping plates; **(h)** Diagram demonstrating how the use of overlapping scales defends against penetration. Scale bars: **(b)** 5 mm, **(d)** 15 μm, **(e)** 50 mm. Adapted with permission from [12].

Mechanically, overlapping structures are capable of ensuring constant coverage while allowing flexibility. Vernerey and Barthelat [164-166] have developed an analytical model to describe how the individual scales or plates of an overlapping structure contribute to the total curvature. These equations were specifically designed with a focus on the scales of fish; however, they provide valuable insight into most overlapping structures. The normalized curvature of the entire overlapping structure is expressed as $\bar{\kappa} = l/R$, where l is the projected length of a scale (given that all scales, in an undeformed state are raised from the dermal surface by a small angle) and R is the radius of curvature of the entire articulated body. The normalized curvature, $\bar{\kappa}$, is composed of two separate terms [164]:

$$\bar{\kappa} = \bar{\kappa}_{\mathrm{r}} + \bar{\kappa}_{\mathrm{b}} \tag{35}$$

where $\bar{\kappa}_{\mathrm{r}}$ is the normalized curvature due to rotation of the scales at the proximal end and $\bar{\kappa}_{\mathrm{b}}$ is the normalized curvature due to bending of the individual scales. Combined, these two terms account for the ability of the articulated scales to conform to R with the assumption that the bending of the scales is relatively small ($\bar{\kappa}_{\mathrm{b}} < 0.1$). This assumption is valid for most biological scales and plates, which are often rigid due to mineral reinforcements, causing the contribution of scale rotation to dominate. With this in mind, the angle, θ, at which each scale must rotate to accommodate a given $\bar{\kappa}_{\mathrm{r}}$ can be determined [164]:

$$\theta = -\frac{\beta}{2} + \sin^{-1}\left[\bar{\kappa}_{\mathrm{r}} \cos\left(\frac{\beta}{2}\right)\right] \tag{36}$$

where β is the angle between the distal ends of two adjacent scales when the body is in a curved state. This angle can also be expressed for any given body curvature as $\beta = s/R$ where s is the scale spacing between the proximal ends of two adjacent scales. Any

remaining curvature is attributed to $\bar{\kappa}_{\mathrm{b}}$, which given the previously discussed assumption, should be small.

Given that the rotation at the proximal end of embedded scales and plates, θ, is the primary mode of flexing, the variables in Equation 36 provide insight into the important qualities of an overlapping structure that ensure both flexibility and full protection. The dominant independent variables are the scale length (effectively l, found within $\bar{\kappa}_{\mathrm{r}}$), the spacing between scales (s, found within β) and the total body length (that influences R, found within $\bar{\kappa}_{\mathrm{r}}$). Most organisms employ scales that balance these variables/qualities, providing high overall flexibility (R) to facilitate natural motion while minimizing the local rotation of scales (θ) to resist puncture (Figure 22h). This is accomplished by reducing the ratio of scale size to body length (minimizing s and $\bar{\kappa}$). Overlapping structures based on these characteristics are common in many fish such as sharks (Figure 22c) [160], arapaima [97, 163], Senegal bichir [106], striped bass [99, 167] and alligator gar (Figure 22f) [72], and the majority of teleosts, as well as pangolin (a mammal; Figure 22g) [7]. However, a number of fish (e.g. syngnathids; Figure 22b) have also evolved modified overlapping structures (e.g. peg-and-socket connections) designed for specific functions, such as grasping [80, 168]. Although the geometries and resulting mechanics of the different overlapping structures can vary significantly among species, these plated structures provide all organisms some level of combined strength and flexibility.

2.9 Bioinspired Designs from Structural Design Elements

These structural design elements also provide guidance on a variety of bioinspired designs. Indeed, synthetic materials that mimic one or more of the eight structural design elements have been developed in recent years using many different materials processing

routes. With the advent of modern biotechnology and nanoscale manufacturing, hierarchical materials (or composites) composed of ceramics and/or polymers are now becoming viable alternatives to the other dominant class of structural materials: metals. Such ceramic- and polymer-based materials are lightweight and exhibit impressive mechanical properties in spite of their relatively low densities; in many cases, this is the direct result of including the aforementioned structural design elements. Figure 23 provides a few representative examples of different bioinspired materials that utilize these structural design elements for enhanced mechanical performance. This cornucopia of materials (Figure 23) highlights a range of techniques used to fabricate architectures at the micro-, meso- and macroscales, including: recombinant technologies, biomineralization, layer-by-layer deposition, self-assembly, bio-templating, magnetic manipulation, freeze casting, vacuum-casting, extrusion and roll compaction, laser engraving, and 3D-printing (additive manufacturing).

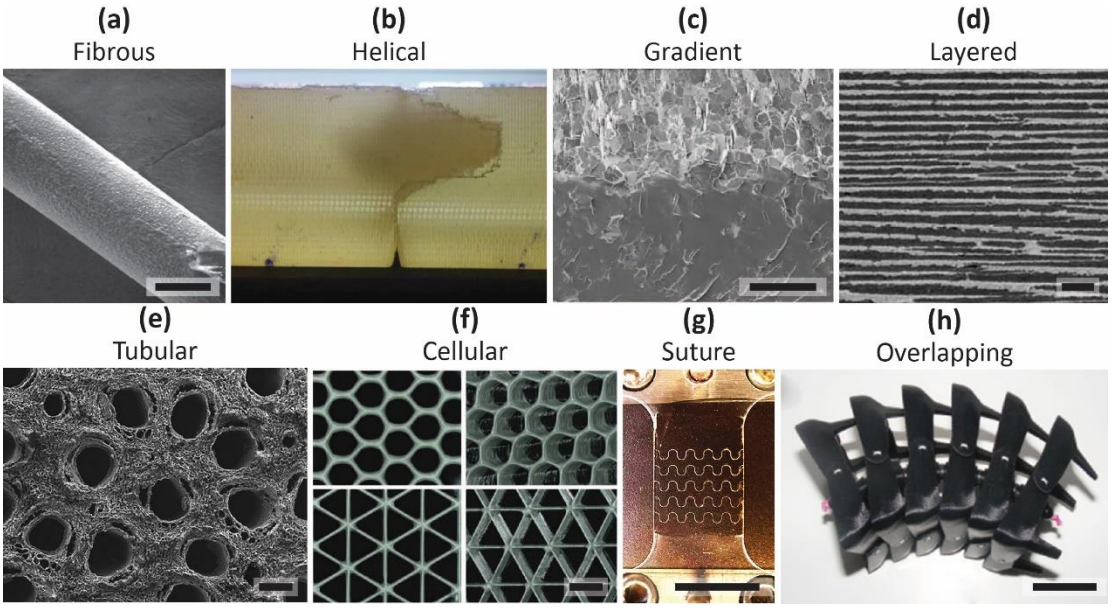

Figure 23. Examples of bioinspired designs for each of the eight structural design elements. **(a)** Fibrous recombinant spider silk from mammalian cells; **(b)** helical fiber reinforced composites that are capable of deflecting crack growth; **(c)** gradient structures formed by applying magnetic fields to a particle-reinforced matrix composite; **(d)** layered composites formed from freeze casting; **(e)** tubules formed from bio-templating; **(f)** 3D-printed cellular structures; **(g)** sutures employed to toughen glass; **(h)** overlapping structures for potential robotics. Scale bars: **(a)** 5 μm, **(c)** 40 μm, **(d)** 100 μm, **(e)** 250 μm, **(f)** 2 mm, **(g)** 8 mm, **(h)** 25 mm. Adapted with permission from [12].

Bioengineered synthetic fibrous structures (Figure 23a) have been developed from recombinant spider silks (proteins), via genetic manipulation of mammalian cells [169], and metabolically engineered bacterial cells [170]. The resulting proteins can be spun into fibers that exhibit tensile properties comparable to native dragline silks with high strengths up to 1.1 GPa [171]. In addition, the use of self-assembly techniques has proven to be an effective method of creating nanoscale bioinspired fibers [172]. Similar fiber-based designs have been employed to mimic helical structures. As an example, carbon-fiber-epoxy composites arranged into helicoidal architectures (Figure 23b), akin to naturally occurring Bouligand structures, were recently shown to exhibit enhanced impact resistance, as compared to unidirectional and quasi-isotropic controls (industry standards)

[173]. The damage mechanisms observed in these fiber composites resembled those observed in the stomatopod dactyl club [65, 174], where crack propagation follows the path of least resistance, forcing damage to spread in-plane rather than through the thickness of the helicoidal composites. The use of magnetic fields to manipulate or align the internal microstructures of materials is another simple method to create bioinspired designs, as demonstrated on polymer–matrix composites (Figure 23c) where embedded particles with varying morphologies (e.g. platelets or rods) are aligned with a magnetic field to create gradient structures with localized properties and three-dimensional reinforcement [175].

Other common synthetic processing techniques used in bioinspiration are those that employ natural phenomena (e.g. ice) as a template. These techniques are gaining popularity due to their ease of use and relatively low environmental impact. Freeze-casting (or ice-templating) is one such process that harnesses the unique crystallographic properties of ice to grow columnar channels within an aqueous slurry of particles (typically ceramic powders). The resulting material is a scaffold with interconnected pores that replicate the structural organization of the ice [25, 27]. Upon removal of the ice, the scaffolds may be subjected to a variety of post-processing methods (e.g. polymer infiltration and/or sintering) to fabricate materials with layered microstructures (Figure 23d). This technique has been remarkably successful for making layered composites that closely mimic the brick-and-mortar architecture of abalone nacre, leading to some of the toughest ceramic-based materials known to date [25, 176] and will be discussed in much greater detail throughout this dissertation. The use of layer-by-layer deposition through sequential absorption of oppositely charged materials into a substrate [177], the extrusion and roll compaction of alternating layers of materials [177], and the self-assembly of polymer-

coated nanolayers [178] are also effective techniques for the creation of bioinspired layered structures. The use of other natural materials (e.g. wood) to act as a sacrificial template, which may be loosely referred to as bio-templating, has been investigated for the design and fabrication of similar structures composed of different material constituents (e.g. hydroxyapatite minerals). This technique has been used to replicate already-existing natural structures, such as the tubular structures present in native rattan and pine woods, into chemically engineered materials composed of hydroxyapatite (the primary mineral constituent of bone) for the development of porous bone implants (Figure 23e) [179].

In contrast to these templating methods, the use of modern technology has given rise to a number of accurate and directed fabrication techniques that allow for the creation of materials in a predefined user-controlled fashion. This allows for the fabrication of designer materials with intricate internal (and external) structures and properties [180]. The technique of 3D-printing has been prolifically employed for the creation of bioinspired cellular structures (Figure 23f) [180]. Similarly, the accuracy of laser etching has been employed to explore the effects of controlled geometry in structures [181]. Brittle glass was toughened by engraving tiny defects into suture patterns that guide cracks through jigsaw-like interfaces (Figure 23g). This allowed for predefined control of crack propagation, leading to a bioinspired glass that is up to 200 times tougher than a non-engraved glass [181]. Finally, this high control of structure forming has allowed for the fabrication of more-complex mimetic structures such as the overlapping skeleton of a seahorse tail for potential robotics applications (Figure 23h) [168].

Chapter 2, in part, is a reprint of the material as it appears in “Structural design elements in biological materials: Application to bioinspiration” Advanced Materials, vol.

27, pp 5455-5476, 2015. The dissertation author was the primary investigator and author on this paper. This paper was co-authored by Michael M. Porter, Joanna McKittrick and Marc A. Meyers.

3. Bioinspired Composites from Freeze Casting with Clathrate Hydrates

The recent work of Porter et al. [36] demonstrated the effect of isopropanol (IPA) as an additive to freeze casting with TiO_2 as the solid loading. The resultant scaffolds showed a large increase in pore area up to an observed maximum at 5 vol.% IPA. This increase in pore area was linked to a decrease in the scaffold mechanical properties. Mechanically, this was shown to be the result of buckling of the lamellar walls. The pore area increase was suggested to be the result of the formation of clathrate hydrates in the freezing process due to their known presence in frozen IPA-H_2O binary mixtures [54]. While this proposed mechanism is supported by previous literature on IPA-H_2O binary mixtures under steady state conditions, there is no current evidence of clathrate hydrates forming at the high cooling rates observed during the freeze casting process.

In this chapter the author build upon our previous experience on IPA-H_2O freeze casting [36]. The author proposes the use of IPA-H_2O freeze casting as a simple method to create bioinspired structural composite materials. Additionally, evidence is presented to prove that clathrate hydrates are indeed forming in the freeze casting process and aiding in the creation of enlarged pores. To isolate the effect of the IPA-H_2O freezing agent, freeze cast scaffolds were based in zirconia (ZrO_2), which has applications as porous solid oxide fuel cells, thermal barrier layers and for biological implants [182].

3.1 IPA Clathrate Hydrates

Clathrate hydrates are defined as non-stoichiometric structures where a hydrogen bonded molecule enclosure lattice (H_2O) surrounds a guest molecule (e.g. IPA) with limited or no chemical bonding to the lattice [183]. While most clathrate hydrates are thermodynamically unstable at room temperature and ambient pressure, there are a number

of H_2O based solutions that produce clathrates at low temperatures or high pressures. Commonly reported clathrate hydrates include propane-H_2O, which has been heavily studied for its effect on the oil and gas industry [184] and methane-H_2O, which is commonly found at the bottom of the ocean [185]. In addition, binary systems of IPA-H_2O have been reported to form clathrate hydrates at low temperatures and ambient pressures [54-56, 58, 186].

In general, clathrate hydrates are capable of forming into a number of different structures depending on the guest molecule size, chemistry and environmental conditions (e.g. pressure and temperature). However, most known clathrate hydrates form either into a structure I (h_1) or structure II (h_2). These structures are differentiated by their stacking and guest molecule cavity size with h_1 stacking on enclosure vertices and h_2 stacking on enclosure faces [184]. In the binary IPA-H_2O system, stable clathrate hydrates form at an IPA concentration of 46 vol.% as an h_1 structure at 243 K, which converts to h_2 at 223 K. The phase diagram displaying this mixture is shown in Figure 24a. Aladko *et al.* [54] reported on the h_1 and h_2 clathrate hydrates of the IPA-H_2O system and determined that, in both cases the hydrophilic hydroxyl group of the guest IPA molecule replaces one of the H_2O molecules in the enclosure lattice. This results in a cubic h_1 unit cell with a_0 = 1.26 nm and a tetragonal h_2 unit cell with a_0 = 0.64 nm and c_0 = 1.12 nm. Both clathrate unit cells are significantly larger than pure (hexagonal) ice where a_0 = ~0.45 nm and c_0 = ~0.73 nm. [187]. Diagrams representative of the unit cells found in the IPA-H_2O binary phase diagram are shown in Figure 24b.

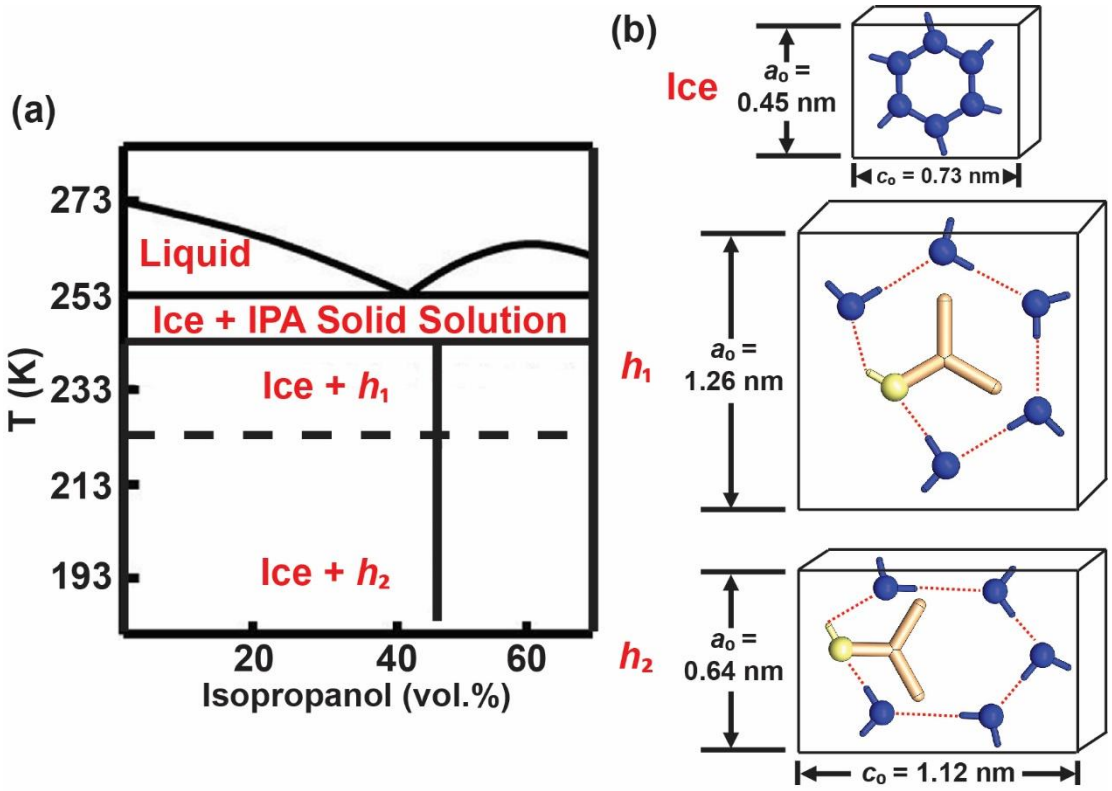

Figure 24. Phase diagram showing relevant features and unit cells for the IPA-H_2O system at steady state. **(a)** Stable clathrate hydrates form at 46 vol.% IPA with an h_1 forming at 243 K then converting to an h_2 at 223 K; **(b)** Diagrams representative of the known unit cells for features of the IPA-H_2O phase diagram: hexagonal ice (a_0 = ~0.45 nm, c_0 = ~0.73), h_1 clathrate hydrate (cubic, a_0 = 1.26 nm) and h_2 clathrate hydrate (tetragonal, a_0 = 0.64 nm, c_0 = 1.12 nm). H_2O molecules are shown in dark blue, IPA molecules are shown in brown (the aliphatic group) and yellow (the hydroxyl group). Phase diagram and clathrate hydrate unit cell data adapted from Aladko et al. [54], hexagonal ice unit cell data adapted from Rottger et al. [187]. Adapted with permission from [188].

3.2 Materials and Methods

Utilizing the methods described in chapter 1.6, freeze cast scaffold composites were prepared, tested and analyzed. Aqueous slurries were prepared to investigate the effects of the monofunctional alcohol, IPA on the freeze casting process. Slurries were prepared with 10 vol.% ZrO_2 powders, 2 wt.% PEG as a polymeric binder and 1 wt.% Darvan 811 as an anionic dispersant. Eleven slurries were prepared by changing the volume fractions of IPA

additive with concentrations of 0, 1, 3, 4, 5, 6, 7, 8, 10, 15 and 20 vol.% IPA. Slurries were freeze cast, freeze dried, sintered and infiltrated with a two part polymer epoxy (Epoxicure) to create two-phase scaffold composites.

The microstructure was investigated with SEM to determine the values of a, b, A_p and X_p of the porosity as a function of IPA additive concentration. Compression testing of $N = 5$ samples from each scaffold composite was conducted to determine values of UCS and E as a function of IPA additive concentration. Finally, binary mixtures of IPA and H_2O at 0, 1, 3, 5, 6, 7, 10 and 15 vol.% IPA were tested by DSC to determine the phases present during the freeze casting process.

3.3 Results and Discussion

3.3.1 Structural Characterization

ZrO_2 scaffolds fabricated with 0 to 15 vol.% IPA and infiltrated with epoxy are shown in Figure 25 showing a significant increase in the pore area up to 5-7 vol.% IPA, then a decrease. Pore area and aspect ratio are shown in Figure 26a and minor axis and lamellar wall thickness in Figure 26b as a function of IPA concentration. The pore area undergoes a clear increase from 0 to 5 vol.% IPA (Figure 25a-c) as well as a decline from 7-15 vol.% IPA (Figure 25d-f). Of significance, the pore area between 5 and 7 vol.% IPA remains constant while the aspect ratio decreases. From measurements of the pore size and shape, this is due to widening of the pores at 7 vol.% (increase in b seen from 5 to 7 vol.% IPA, as shown in Figure 26b). Additionally, the lamellar wall thickness increases up to ~8 vol.% IPA before declining (Figure 26b).

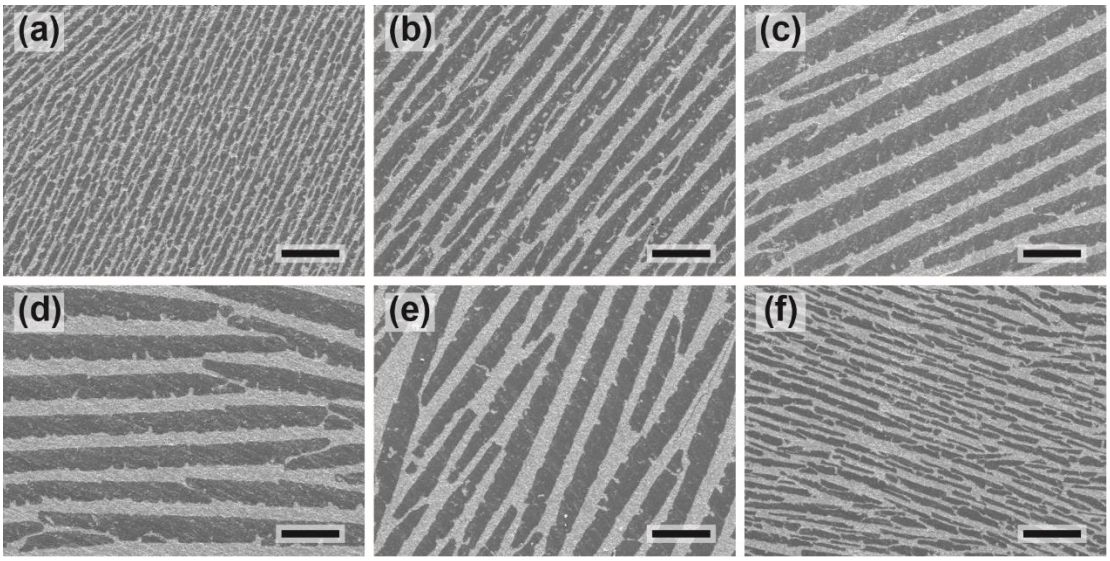

Figure 25. Scanning electron microscopy images of epoxy infiltrated ZrO_2 scaffolds. IPA concentration: **(a)** 0 vol.%; **(b)** 1 vol.%; **(c)** 5 vol.%; **(d)** 7 vol.%; **(e)** 10 vol.%; **(f)** 15 vol.%. Ceramic is shown in light grey, polymer in dark grey. Scale bars: 100 μm. Adapted with permission from [188].

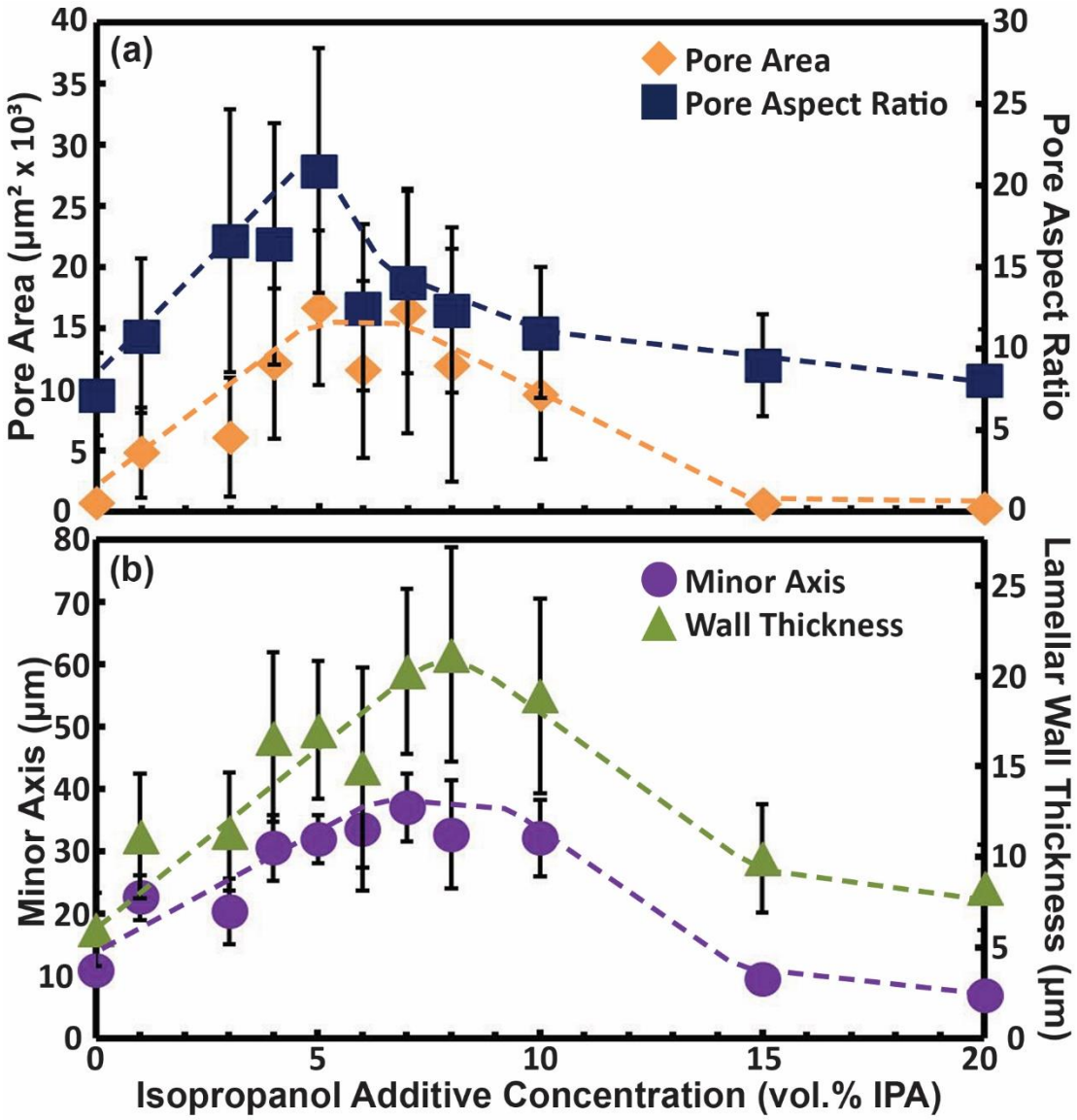

Figure 26. Pore area, aspect ratio, minor axis and lamellar wall thickness as a function of IPA additive concentration. **(a)** Pore area shows a maximum at 5 to 7 vol.% IPA while pore aspect ratio shows a maximum at 5 vol.% IPA and a sharp decline at 6 to 7 vol.% IPA; **(b)** Both minor axis and lamellar wall thickness reach a maximum at ~7 - 10 vol.% IPA. Data points are the mean of N = 40 measurements with error bars representing ± one standard deviation. Adapted with permission from [188].

The trend in pore area in IPA-H_2O freeze cast scaffolds with an increase to a maximum value at ~5 vol.% followed by a decline to a base level (the level observed with no additive) matches the previous report for TiO_2 scaffolds with the same solid loading

[36]. This consistent result provides evidence that this effect is influenced by the characteristics of the ice formed and is not simply an effect of the solid loading.

This effect was further explored through DSC, as shown in Figure 27a. Heating curves are displayed overlaid to highlight the observed trends with increasing IPA concentration. As is reported in literature [54-58], the phases present are determined through the decomposition observed upon heating of a solid, which correspond to first order phase transformations. The baseline is distilled H_2O (0 vol.% IPA) that displays a large, single endothermic peak corresponding to melting of ice at 273 K (Figure 27b). With the addition of 1 vol.% IPA, this sharp transition expands and shifts to lower temperatures, thus decreasing the onset of melting below 273 K. Additionally, a secondary endothermic peak beginning at ~243 - 247 K becomes visible at 3 vol.% IPA and increases in magnitude with greater IPA concentration, though it always occurs at ~243 K. The endotherm is attributed to decomposition of h_1 to a solid solution of ice and IPA, as seen in Figure 27b [54, 58].

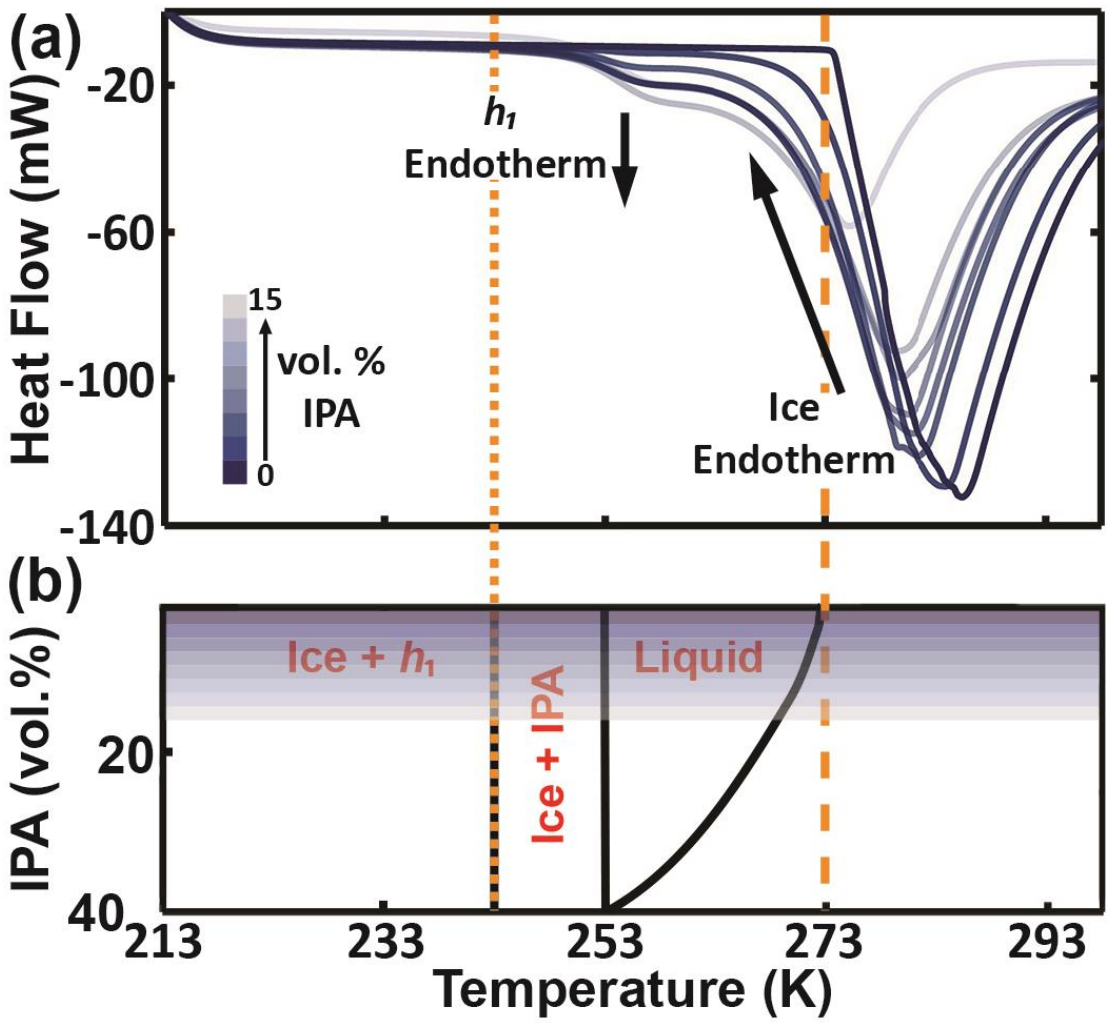

Figure 27. Differential scanning calorimetry results taken during heating for varying concentrations of IPA in H_2O. **(a)** Data is overlaid to show the general trends with increasing IPA concentration. Note the decrease in magnitude and shift to lower temperatures of the ice (ice + IPA solid solution) endotherm as well as the emergence of an h_1 clathrate hydrate endotherm beginning at ~243 - 247 K as IPA concentration increases; **(b)** for reference, the IPA-H_2O equilibrium phase diagram is shown to highlight the transitions occurring at 273 K (melting of ice) and 243 K (decomposition of h_1 clathrate hydrate into ice + IPA solid solution). Adapted with permission from [188].

The change in enthalpy of each of the two observed endotherms (the h_1 clathrate hydrate and the ice + IPA solid solution) is displayed as a function of IPA concentration in Figure 28. As expected, as the IPA concentration increases, the enthalpy change of the h_1 endotherm increases and the ice endotherm decreases. This correlates with phase diagram

analysis using the lever rule that shows as the amount of IPA increases, the amount of h_1 also increases. However, the h_1 endotherm has a larger rate of change with IPA concentration, up to 5 vol.% IPA, where the maximum in pore area is observed. The rate then decreases above 5 vol.% IPA. The presence of the two different slopes indicates that there is a difference in the nature of the clathrate hydrate formation above and below 5 vol.% IPA. This reduction in the enthalpy of the h_1 clathrate hydrate per unit of IPA (the slope) is correlated to the observed maximum in pore area at 5 vol.% IPA. It is hypothesized that this is due to non-equilibrium behavior of the IPA in solution below 5 vol.% IPA where the IPA molecules are fully dispersed. This gives way to equilibrium behavior (as predicted by the phase diagram) at higher concentrations where IPA molecules in suspension begin to agglomerate.

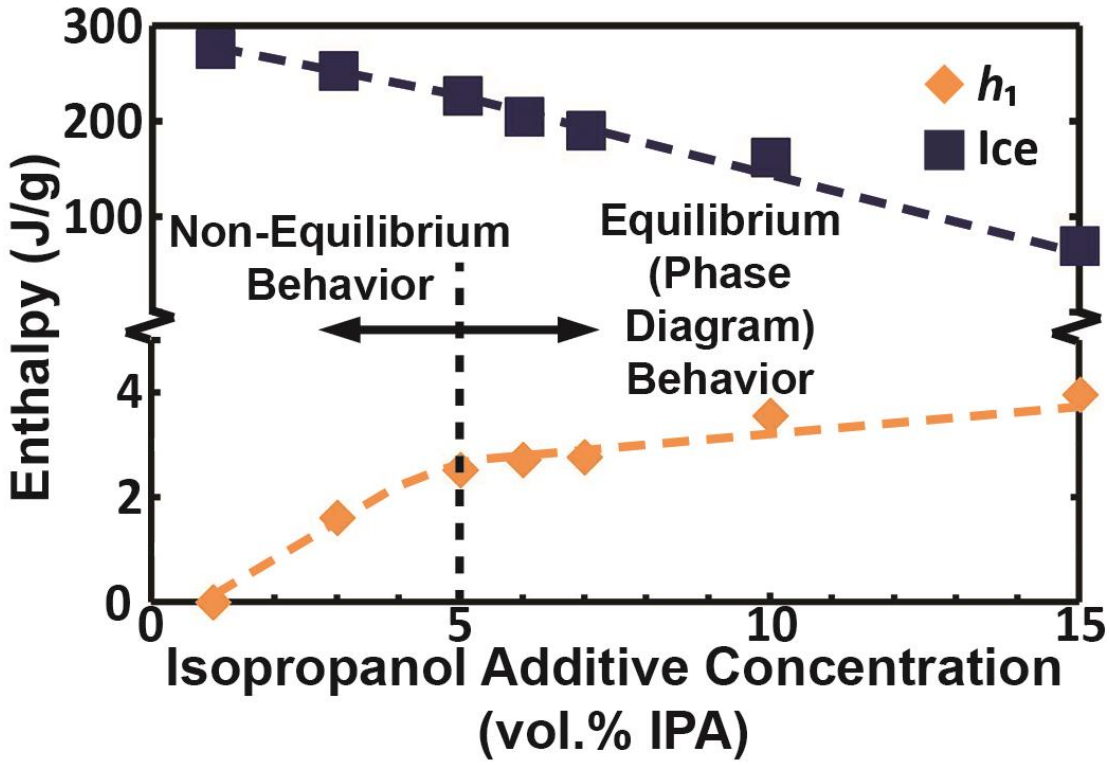

Figure 28. Enthalpy of the transitions observed from the differential scanning calorimetry results as a function of IPA concentration. As vol.% IPA increases, the enthalpy of the h_1 clathrate hydrate endotherm increases with a high initial slope up to 5 vol.% then a lower slope. Inversely, the enthalpy of the ice + IPA solid solution endotherm (ice) decreases with increasing IPA concentration. It is proposed that the change in slope occurs due to non-equilibrium behavior of the IPA in solution at concentrations below 5 vol.% that gives way to equilibrium behavior (as expected from the phase diagram) at high concentrations. Adapted with permission from [188].

These results confirm the formation of h_1, rather than h_2 clathrate hydrates during the current freeze casting process. The proposed process for the increase in pore area due to the observed formation of h_1 clathrate hydrates is diagramed in Figure 29.

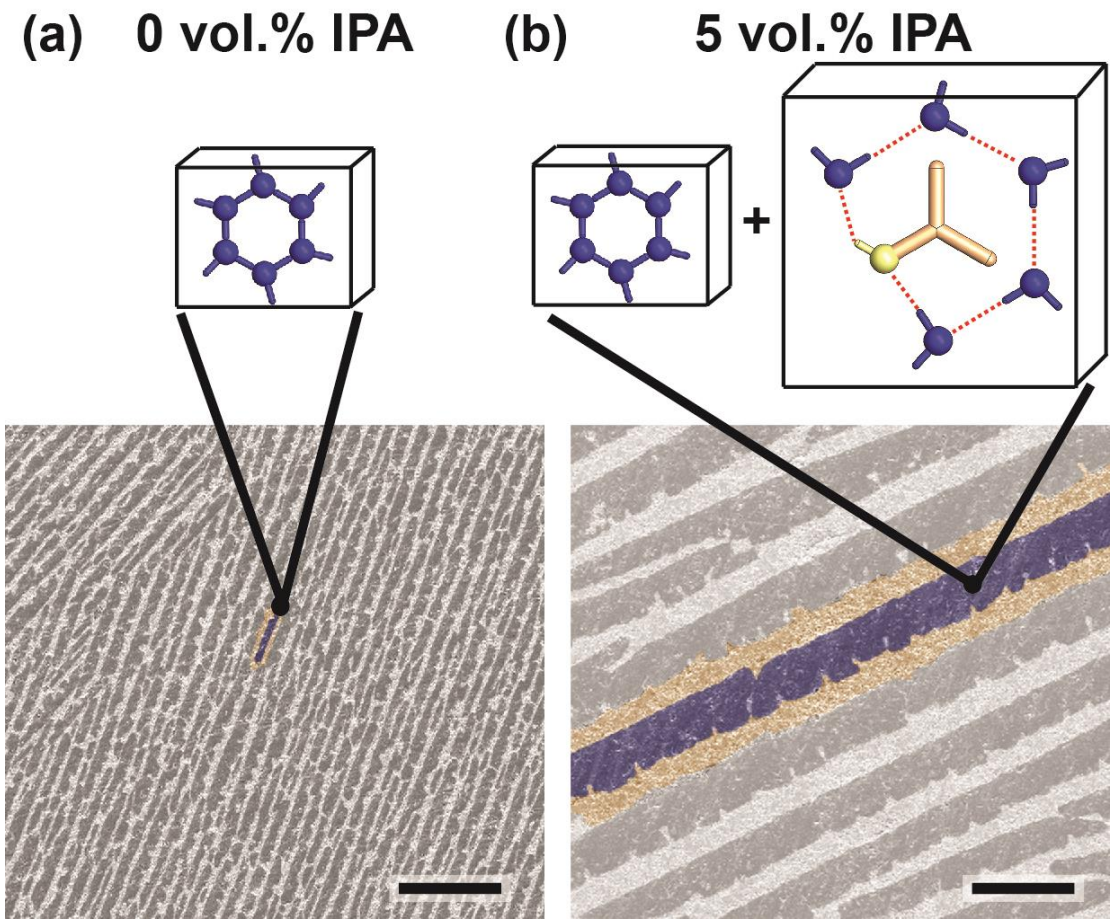

Figure 29. Diagram of the proposed mechanism for the observed increase in pore size due to the formation of h_1 IPA-H_2O clathrate hydrates during the freezing process. **(a)** At 0 vol.% IPA, only hexagonal ice forms, resulting in smaller pore size; **(b)** At 5 vol.% IPA, the formation of both hexagonal ice and the enlarged h_1 clathrate hydrate result in significantly enlarged pores. Scale bars: 100 μm. Adapted with permission from [188].

This drastic increase in pore area provides significant potential for the creation of bioinspired composites by easing infiltration of a second phase. Additionally, the observed decrease in the pore aspect ratio at the maximum pore area between 5 and 7 vol.% may provide insight into the potential for some control of the pore aspect ratio while maintaining high area pores.

3.3.2 Mechanical Characterization

The ultimate compressive strength, *UCS*, and compressive modulus, *E*, of infiltrated ZrO_2-epoxy two phase composites are shown in Figure 30 as a function of IPA additive. In both cases the mechanical properties experience an increase up to ~5 vol.% IPA then remain relatively constant up to 20 vol.%. The addition of IPA increases the mechanical properties above those of the epoxy, a phenomena that is commonly observed in complex biological two-phase composite materials [25]. Previous work demonstrated that the failure mode of scaffolds in the longitudinal (ice growth) direction is buckling of the lamellar walls [36]. For comparison, these previous results, performed on non-infiltrated TiO_2 freeze cast scaffolds of the same solid loading (10 vol.%) and IPA as an additive are shown in Figure 30. The contrasting observed increase in the mechanical properties of the infiltrated scaffolds seen in Figure 30 suggests that, in addition to adding mechanical toughness, the polymer phase supports the lamellar walls and inhibits buckling. The leveling out of the mechanical properties above 5 vol.% IPA can be attributed to several competing factors: although the porosity decreases, which should increase the strength and modulus, the lamellar wall thickness also decreases, which should decrease the strength and modulus.

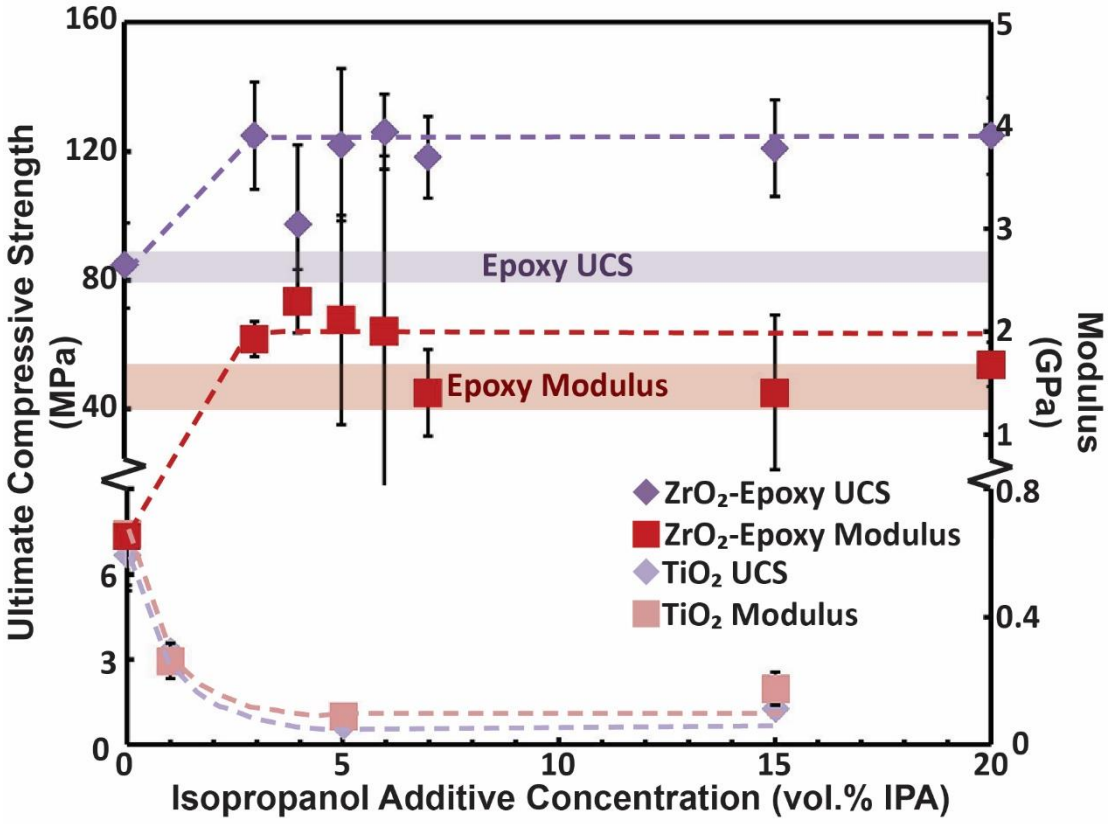

Figure 30. Ultimate compressive strength (*UCS*) and compressive modulus of freeze cast ZrO_2-epoxy composites as a function of IPA additive concentration. In both cases the mechanical properties experience a rise with the IPA additive then remain relatively constant up to 20 vol.% IPA. Compressive modulus and *UCS* for the pure epoxy are shown (band = mean ± standard deviation of $N = 5$ measurements) for reference. Data is compared to previous reports on non-infiltrated freeze cast TiO_2 scaffolds with the same solid loading and IPA as an additive [14] that show a decrease in *UCS* and modulus with increasing IPA additive concentration. Data points are the mean of $N = 5$ measurements with error bars representing ± one standard deviation. Adapted with permission from [188].

Although the mechanical properties of the ZrO_2-epoxy composites are not exceptionally high (Figure 30) the relative increase in strength and stiffness above those of the initial constituents suggests that infiltration with different materials (e.g. metal melts) could result in more high performance composites for a variety of structural applications. As a result, the infiltration of IPA-H_2O freeze cast scaffolds with a variety of constituents warrants further investigation. More importantly, these results suggest that the use of IPA

in the freeze casting process is a simple and beneficial method for the creation of bioinspired composites with enlarged porous microstructures.

3.4. Conclusions

The current experimental study of epoxy-infiltrated, freeze cast ZrO_2 bioinspired composites using isopropanol (IPA)-H_2O as a freezing agent enables the following conclusions.

- The IPA-H_2O system showed an increase in pore area up to a maximum at ~5 - 7 vol.% IPA then a decrease. This result was previously shown for similar freeze casting experiments with TiO_2 as the solid loading and therefore suggests that the effect is strongly influenced by the freezing agent and is not solely an effect of the solid loading. Additionally, little change was observed in the pore area of the scaffolds between 5 to 7 vol.% IPA, however the aspect ratio showed a large decrease due to widening of the pores.
- Differential scanning calorimetry experiments that mimic the freeze casting process showed that h_1 clathrate hydrates are present during freezing of IPA-H_2O binary mixtures. These h_1 clathrate hydrates are shown to be the cause of the enlarged pores observed in the resultant freeze cast scaffolds.
- Analysis of the change in enthalpy of the h_1 clathrate hydrate to an ice + IPA solid solution show that the maximum in pore area is physically caused by the reduction in slope (enthalpy of the h_1 clathrate hydrate per unit of IPA). It is currently hypothesized that this is due to un-saturated behavior of the IPA in solution below 5 vol.% IPA, which gives way to saturated behavior (as predicted by the phase diagram) at higher concentrations.

- Mechanical properties (ultimate compressive strength and compressive modulus) of two-phase, bioinspired ZrO_2-epoxy composites showed an increase with the addition of the IPA additive up to 5 vol.%, which then remained relatively constant up to 20 vol.%. Similar to many biological two-phase composites, these mechanical properties were higher than what would be expected from a simple mixture of the two constituents. This suggests that the infiltration of freeze cast scaffolds will inhibit the reported failure mode of lamellar wall buckling and increase the mechanical properties.

Chapter 3, in part, is a reprint of the material as it appears in "Bioinspired composites from freeze casting using clathrate hydrates" Materials & Design, vol. 71, pp 62-67, 2015. The dissertation author was the primary investigator and author on this paper. This paper was co-authored by Christopher F. Yu, Michael M. Porter, Arijit Sengupta, Peter M. Iovine, Marc A. Meyers and Joanna McKittrick.

4. Bioinspired Intrinsic Control of Freeze Cast Composites: Harnessing Hydrophobic Hydration and Clathrate Hydrates

The work into intrinsic control of freeze casting with the monofunctional alcohol isopropanol (IPA) as an additive to the slurry, reported in chapter 3, has shown the presence of clathrate hydrates in the freezing process lead to enlarged final porosity [36, 188]. Clathrate hydrates are defined as non-stoichiometric structures where a hydrogen bonded molecule enclosure lattice (made of H_2O molecules) surrounds a guest molecule (e.g. monofunctional alcohols) with limited or no chemical bonding to the lattice [183]. These structures can be defined by the hydration number, n_h, which is defined as the number of H_2O molecules per guest molecule. Values of n_h vary depending on the guest molecule with most alcohols producing values of ~1 - 6. The enlarged unit cells of clathrate hydrates occurring during the freezing process have been shown to contribute to the observed increase in pore area in the final freeze cast scaffold [188]. However, there is still a significant unanswered question in this explanation as the pore area shows a parabolic relationship with the concentration of IPA additive. This is illustrated in Figure 31, comparing results generated for this study (using the same parameters described below) along with previous studies for ZrO_2 [188] and TiO_2 [36] scaffolds. To account for the discrepancies in processing parameters, the results in Figure 31 are normalized to the pore area reported for a scaffold with no additive (0 vol.% IPA = A_{p0}). In spite of this, all three trials demonstrated a maximum in pore area, described here as "peak A_p", at the same concentration of 5 - 7 vol.% IPA.

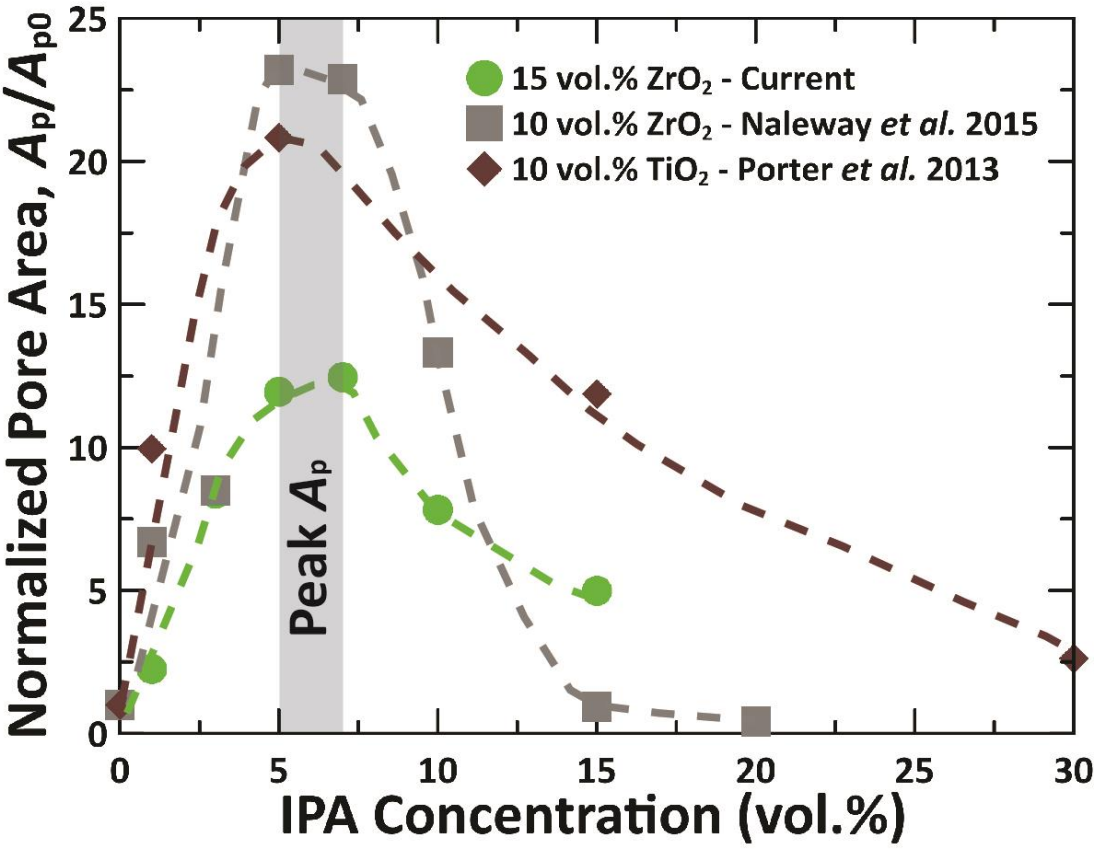

Figure 31. Pore area, A_p, data for previously reported and current results using isopropanol as a freeze casting additive. Results are normalized to the pore area with no additive, A_{p0} (0 vol.% IPA). Solid loading is different in each case: current results use 15 vol.% ZrO_2, Naleway et al. [188] used 10 vol.% ZrO_2 and Porter et al. [36] used 10 vol.% TiO_2. In each case a parabolic relationship between pore area and IPA concentration is shown with a peak A_p at 5 - 7 vol.% IPA. Data taken from [36, 188]. Adapted with permission from [189].

In this chapter the author presents a homologous series of linear monofunctional alcohols as intrinsic templating additives: ethanol (EtOH, C_2H_5OH), *n*-propanol (*n*-PrOH, C_3H_7OH) and *n*-butanol (*n*-BuOH, C_4H_9OH). EtOH [55, 56] and *n*-PrOH [57] have been reported to form clathrate hydrates in dilute binary mixtures at low temperatures. While there are no current reports on the presence of clathrate hydrates in *n*-BuOH, the branched butanol, *tert*-butyl alcohol has been reported to form clathrate hydrates in dilute concentrations [56]. In addition, the author presents data and analysis on the mechanics of

bioinspired composites created with these scaffolds and is able to provide new insight into the structural support provided by the infiltration of freeze cast materials as well as layered structures in nature.

4.1 Materials and Methods

Utilizing the methods described in chapter 1.6, freeze cast scaffold composites were prepared, tested and analyzed. Aqueous slurries were prepared to investigate the effects of a series of linear monofunctional alcohols; EtOH (Koptec, King of Prussia, PA, USA), *n*-PrOH (Fisher Scientific, Fair Lawn, NJ, USA) and *n*-BuOH (J. T. Baker, Center Valley, PA, USA) on the freeze casting process. Slurries were prepared with 15 vol.% ZrO_2 powders, 1 wt.% PEG and 1 wt.% PVA as a polymeric binders and 1 wt.% Darvan 811 as an anionic dispersant. Slurries were prepared by varying two parameters: the volume fraction (0, 1, 3, 5, 7, 10 and 15 vol.%) and the additive (EtOH, *n*-PrOH and *n*-BuOH) for a total of 21. Slurries were freeze cast, freeze dried, sintered and infiltrated with a two part polymer epoxy (Epoxicure 2) to create two-phase scaffold composites. In addition, one set of scaffold composites was created using the exact procedure described above with 0, 1, 3, 5, 7, 10 and 15 vol.% IPA to create a comparison between current and previous results (as seen in Figure 31).

The microstructure of all composite scaffolds was investigated with SEM to determine the values of a, b, A_p and X_p of the porosity as a function of alcohol additive concentration. Volumetric and mechanical analysis of $N = 5$ samples from each scaffold composite were conducted to determine values of V_c, *UCS* and *E*. Given the variability between results of mechanical testing between the different scaffold composites created

with each alcohol additive (i.e. 0 vol.% EtOH ≠ 0 vol.% *n*-PrOH ≠ 0 vol.% *n*-BuOH), all mechanical data was normalized:

$$Q_{\mathrm{N}} = \frac{Q_{\mathrm{i}}}{Q_0} \quad (37)$$

where Q is either E or UCS, Q_{N} and Q_{i} are the normalized and measured values for any given additive concentration and Q_0 is the mean value of the initial scaffold with no additive (0 vol.%) from each set of scaffold composites. Finally, binary mixtures of IPA and H_2O at 0, 1, 3, 5, 6, 7, 10 and 15 vol.% IPA were tested by DSC to determine the phases present during the freeze casting process.

4.1.1 Sound Velocity and Hydration Measurements

Measurements of the liquid density and sound velocity were taken to determine the influence of room temperature effects on the freeze casting process. Two complete sets of liquid freezing agents were created each with concentrations of 0, 1, 3, 5, 7, 10 and 15 vol.% EtOH, *n*-PrOH and *n*-BuOH (21 total samples per set). One set included only binary mixtures of alcohols and H_2O, to reproduce previous results [190-192] and ensure accuracy of the setup; the other included 1 wt.% PEG, 1 wt.% PVA, 1 wt.% Darvan 811 and 15 vol.% ZrO_2 particles so as to mimic the slurry constituents within this study. In addition, as there are no current reports on sound velocity measurements of slurries such as the ones in this study, slurries were also tested to determine the effect of the solid loading particles on the measurements. Two sets of slurries were prepared, one with no additive and one with 7 vol.% *n*-PrOH (which was shown through preliminary testing to have the largest effect on the sound velocity). In each case these were prepared as stated (i.e. including

polymers and dispersant) above but with varying solid loading concentrations of 0, 5, 10 and 15 vol.% ZrO_2 particles.

In all cases, the density was calculated by weighing samples of a constant volume (1 mL). Sound velocity measurements were taken using a USD 10 Ultrasonic Detector (Krautkramer Branson, Lewistown, PA, USA) with a system delay of 1.092 μs and input intensities of 10-25 dB and 55-100 dB for samples without and with solid loading respectively. Five measurements were taken on each sample to calculate the average and standard deviation.

4.2 Results and Discussion

Microstructural and mechanical properties of the scaffold composites are given for EtOH (Table 2), *n*-PrOH (Table 3) and *n*-BuOH (Table 4) as a function of the additive concentration. The largest effect of each additive, as measured by the highest magnitude of A_p, is identified as the "peak A_p" and is given in bold in Table 2, Table 3 and Table 4. This notation is employed throughout the discussion and analysis in this manuscript. The peak A_p value for *n*-PrOH in ZrO_2 based freeze cast scaffolds occurs at 5 - 7 vol.%, the same value observed for experiments performed on IPA (Figure 31) [36, 188]. However, the peak A_p values for EtOH and *n*-BuOH in ZrO_2 based freeze cast scaffolds occur at 10 and 3 vol.% respectively. This is displayed graphically in Figure 32a where it can also be seen that the peak A_p in *n*-PrOH produces the highest magnitude of the three additives. Similarly, X_p (Figure 32b) presents the same maxima, though the maxima observed for *n*-BuOH is relatively smaller than their associated peak A_p. Micrographs of each additive are displayed in Figure 33. In each case, the baseline microstructure with no additive (0 vol.%) and microstructures with 1 and 15 vol.% are displayed along with the microstructure of the

scaffold at the peak A_p. As expected, the baseline microstructures appear very similar given that they have the exact same slurry properties. Additionally, at 15 vol.% each additive displays a collapsed microstructure with pore measurements similar to those at 0 vol.% (as shown in Table 2, Table 3 and Table 4).

Table 2. Structural and mechanical properties for bioinspired composite scaffolds fabricated with ethanol (EtOH) as an additive. Pore major axis = *a*, pore minor axis = *b*, pore area = A_p, pore aspect ratio = X_p, wall thickness = T_w, composite ceramic volume fraction = V_c, ultimate compressive strength = *UCS*, compressive modulus = *E*. Values at the peak A_p (10 vol.%) are in bold. Adapted with permission from [189].

EtOH (vol.%)	*a* (μm)	*b* (μm)	A_p (μm^2)	X_p	T_w (μm)	V_c	*UCS* (MPa)	*E* (GPa)
0	59.6 ± 26.4	15.4 ± 3.7	752 ± 474	3.9 ± 1.6	6.3 ± 2.0	0.27 ± 0.01	138 ± 17	3.8 ± 0.7
1	127.6 ± 46.6	21.2 ± 6.0	2263 ± 1418	6.1 ± 1.7	11.0 ± 4.0	0.27 ± 0.01	160 ± 14	4.4 ± 1.0
3	130.1 ± 53.6	23.5 ± 5.4	2518 ± 1536	5.6 ± 1.9	10.7 ± 3.3	0.27 ± 0.01	155 ± 29	4.3 ± 1.7
5	163.0 ± 66.8	26.2 ± 5.9	3510 ± 1867	6.3 ± 2.2	13.3 ± 4.0	0.28 ± 0.01	131 ± 14	3.6 ± 0.8
7	174.6 ± 73.7	24.1 ± 5.2	3406 ± 1788	7.3 ± 2.9	13.9 ± 4.2	0.29 ± 0.02	125 ± 6	2.7 ± 0.7
10	**258.6 ± 87.2**	**27.9 ± 6.1**	**5964 ± 3006**	**9.2 ± 2.3**	**17.6 ± 4.3**	**0.31 ± 0.03**	**147 ± 10**	**4.5 ± 0.6**
15	72.0 ± 20.2	11.8 ± 2.1	673 ± 249	6.3 ± 1.9	12.9 ± 4.1	0.33 ± 0.01	136 ± 5	3.2 ± 0.6

All data is presented as the mean ± standard deviation.

Table 3. Structural and mechanical properties for bioinspired composite scaffolds fabricated with *n*-propanol (*n*-PrOH) as an additive. Pore major axis = *a*, pore minor axis = *b*, pore area = A_p, pore aspect ratio = X_p, wall thickness = T_w, composite ceramic volume fraction = V_c, ultimate compressive strength = *UCS*, compressive modulus = *E*. Values at the peak A_p (5 - 7 vol.%) are in bold. Adapted with permission from [189].

n-PrOH (vol.%)	*a* (μm)	*b* (μm)	A_p (μm^2)	X_p	T_w (μm)	V_c	*UCS* (MPa)	*E* (GPa)
0	50.9 ± 18.2	13.0 ± 2.6	532 ± 252	4.0 ± 1.3	8.2 ± 2.1	0.26 ± 0.02	90 ± 35	1.4 ± 0.5
1	115.7 ± 46.2	21.2 ± 4.4	2027 ± 1150	5.4 ± 1.6	10.0 ± 2.2	0.26 ± 0.05	90 ± 39	1.9 ± 1.1
3	191.0 ± 92.2	28.8 ± 4.7	4534 ± 2820	6.5 ± 2.4	12.9 ± 4.7	0.30 ± 0.01	132 ± 18	3.3 ± 0.7
5	**365.0 ± 162.8**	**35.3 ± 5.0**	**10540 ± 5662**	**10.1 ± 3.7**	**20.2 ± 4.7**	**0.29 ± 0.01**	**131 ± 17**	**3.3 ± 1.0**
7	**354.4 ± 190.6**	**34.3 ± 6.9**	**10287 ± 7218**	**9.9 ± 3.9**	**19.8 ± 5.4**	**0.30 ± 0.02**	**107 ± 17**	**1.9 ± 0.6**
10	226.4 ± 85.5	26.5 ± 6.2	4969 ± 2900	8.6 ± 2.5	13.8 ± 4.6	0.30 ± 0.03	119 ± 9	2.5 ± 0.9
15	147.1 ± 49.7	20.8 ± 3.8	2436 ± 1004	7.2 ± 2.5	11.7 ± 4.5	0.30 ± 0.01	124 ± 9	3.0 ± 0.6

All data is presented as the mean ± standard deviation.

Table 4. Structural and mechanical properties for bioinspired composite scaffolds fabricated with *n*-butanol (*n*-BuOH) as an additive. Pore major axis = *a*, pore minor axis = *b*, pore area = A_p, pore aspect ratio = X_p, wall thickness = T_w, composite ceramic volume fraction = V_c, ultimate compressive strength = *UCS*, compressive modulus = *E*. Values at the peak A_p (3 vol.%) are in bold. Adapted with permission from [189].

n-BuOH (vol.%)	*a* (μm)	*b* (μm)	A_p (μm^2)	X_p	T_w (μm)	V_c	*UCS* (MPa)	*E* (GPa)
0	49.3 ± 20.6	13.8 ± 3.5	560 ± 315	3.6 ± 1.4	6.8 ± 2.0	0.28 ± 0.01	122 ± 9	2.0 ± 0.6
1	84.7 ± 30.1	18.0 ± 3.4	1211 ± 529	4.8 ± 1.8	10.6 ± 3.3	0.28 ± 0.01	148 ± 37	3.2 ± 0.9
3	**232.4 ± 119.6**	**41.3 ± 7.2**	**7998 ± 5295**	**5.5 ± 2.1**	**20.2 ± 5.1**	**0.27 ± 0.01**	**162 ± 7**	**4.0 ± 0.4**
5	80.3 ± 22.3	20.6 ± 3.9	1325 ± 538	4.0 ± 1.2	8.6 ± 3.0	0.27 ± 0.02	103 ± 30	2.8 ± 0.9
7	82.4 ± 28.4	20.1 ± 4.1	1354 ± 652	4.1 ± 1.1	8.9 ± 3.5	0.28 ± 0.01	115 ± 5	2.1 ± 0.6
10	77.3 ± 23.5	17.7 ± 3.0	1099 ± 426	4.4 ± 1.2	10.7 ± 4.5	0.29 ± 0.02	116 ± 12	2.4 ± 0.7
15	137.4 ± 60.8	22.3 ± 6.8	2645 ± 2161	6.2 ± 2.0	14.1 ± 5.2	0.28 ± 0.01	123 ± 12	2.1 ± 0.7

All data is presented as the mean ± standard deviation.

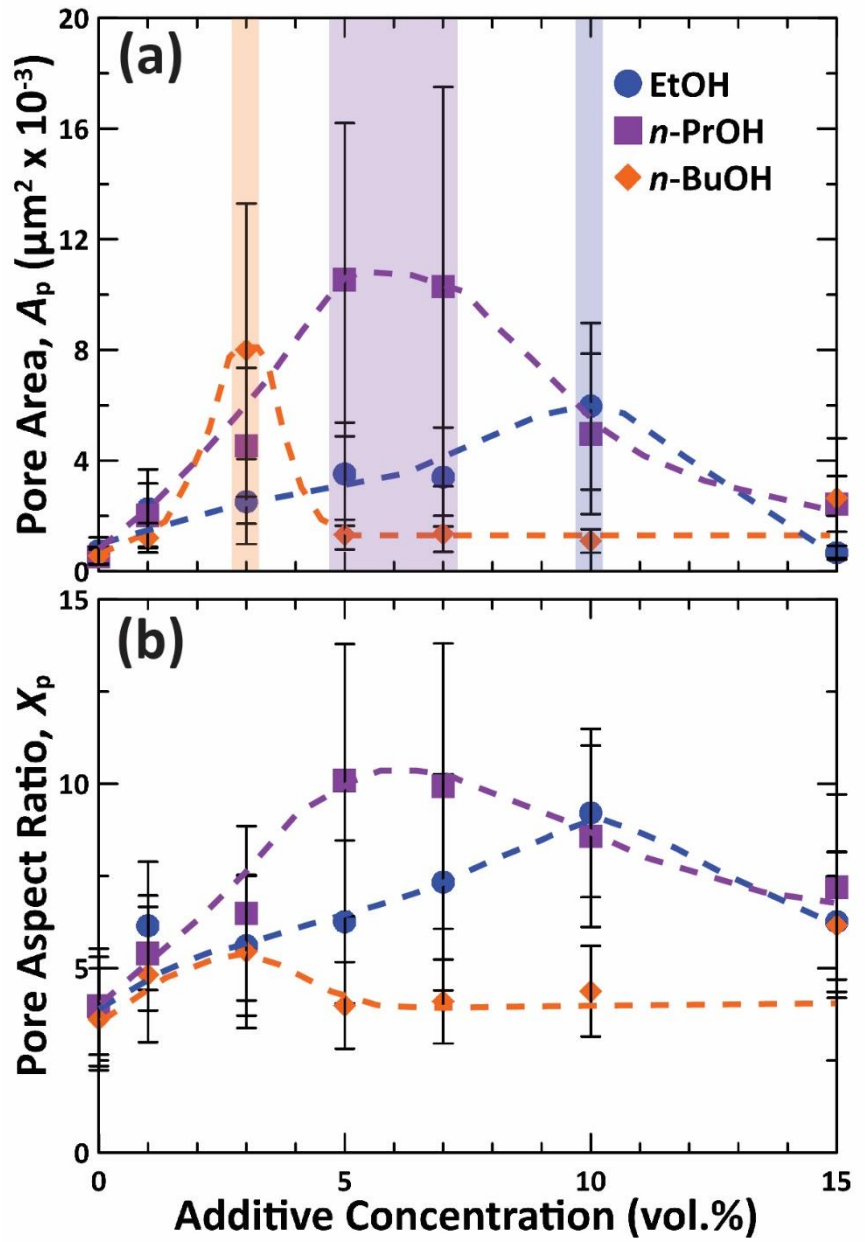

Figure 32. Pore area and pore minor axis as a function of additive concentration for EtOH, *n*-PrOH and *n*-BuOH. **(a)** Pore area shows peak A_p values at 10, 5-7 and 3 vol.% for EtOH, *n*-PrOH and *n*-BuOH respectively (highlighted), with the maximum concentration being inversely proportional to the size of the additive molecule; **(b)** Pore aspect ratio shows the same relationship to additive concentration, though the magnitude of scaffolds with *n*-BuOH is relatively less. Data is presented as the mean ± one standard deviation of 40 measurements. Adapted with permission from [189].

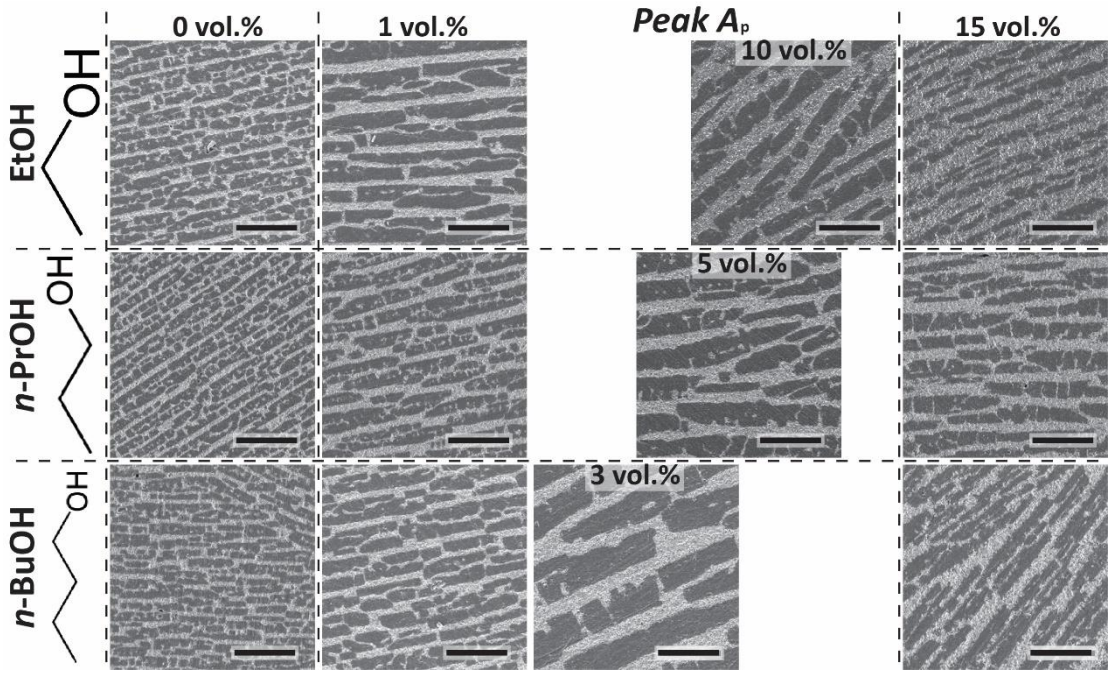

Figure 33. Scanning electron microscopy images of infiltrated ZrO_2 scaffolds. Scaffolds with EtOH, *n*-PrOH and *n*-BuOH are shown. In all cases, micrographs are shown for 0, 1 and 15 vol.% additive along with the additive concentration at the peak A_p. Ceramic is shown in light grey, polymer in dark grey. Scale bars: 100 μm. Adapted with permission from [189].

4.2.1 The Effect of Clathrate Hydrates

Results of DSC experiments upon varying concentrations of binary mixtures of the current monofunctional alcohols with H_2O are shown in Figure 34 along with the associated phase diagrams, where available. EtOH (Figure 34a) displays only a single endotherm at ~273 K that broadens and shifts to slightly lower temperatures with increasing concentration. From the phase diagram, this single endotherm is associated with the decomposition of a solid solution ice phase to a single phase liquid. There are no observed clathrate hydrates forming in these results. *n*-PrOH (Figure 34b) displays two additional endotherms. The first is found at ~263 K and is associated with the decomposition of a solid phase, *X*, to a liquid solution. The nature of *X* is a matter of some

debate: Chapoy *et al.* [193] reported this to be a clathrate hydrate with n_h = 17 while Manakov *et al.* [57] have disputed this claim suggesting that it is only a solid solution ice phase. Given the similar DSC curve structure to previous work on the chemically identical IPA, which was shown to result in clathrate hydrate formation [188], we suggest that clathrate hydrates are present in this system as well. *n*-BuOH (Figure 34c) displays a sharp endotherm at ~273 K. The steep nature of this endotherm at concentrations above 3 vol.% is suggested to be associated with the solubility limit of *n*-BuOH in pure H_2O at ~3 vol.%. Additionally, due to the limited solubility, to our knowledge, no phase diagrams are available for the binary *n*-BuOH-H_2O system. Regardless, the lack of a second endotherm at temperatures lower than 273 K (that is associated with the decomposition of pure ice) negates the possibility of additional clathrate hydrate phases. These results suggest that while there are clathrate hydrates forming during the freeze casting process with *n*-PrOH, there are no strong signs of clathrates forming during the freeze casting process with either EtOH or *n*-BuOH. Therefore a different mechanism must be primarily responsible for the scaffold microstructures presented here.

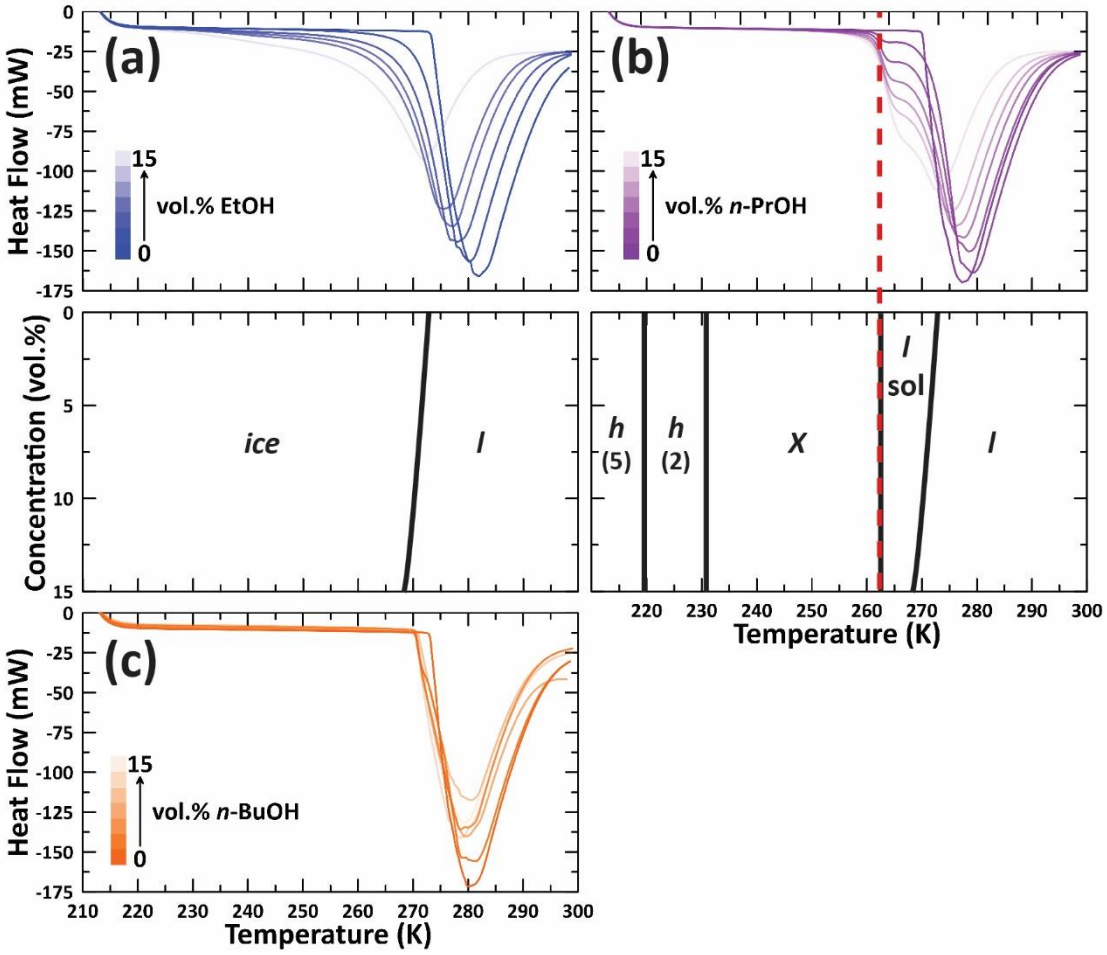

Figure 34. Differential scanning calorimetry data for varying concentrations of binary mixtures of EtOH, *n*-PrOH and *n*-BuOH with H_2O along with associated phase diagrams. **(a)** EtOH displays only a single endotherm at ~273 K, which from the phase diagram is associated with the decomposition of solid solution ice to a single phase liquid (l); **(b)** *n*-PrOH displays one additional endotherm at ~263 K associated with the decomposition of a solid phase, *X*, (either a hydrate with n_h = 17 or solid solution ice); **(c)** *n*-BuOH with only a single steep endotherm at ~273 K. Due to the low miscibility of *n*-BuOH in H_2O (~3 vol.%), to our knowledge there are no available phase diagrams. Phase diagram data taken from **(a)** [194], **(b)** [57]. Adapted with permission from [189].

4.2.2 Hydrophobic Hydration

The phenomenon observed in mixtures of hydrophobic liquids (e.g. monofunctional alcohols) with H_2O, called hydrophobic hydration, may hold the key to these results. Similar to clathrate hydrates, hydrophobic hydration occurs in dilute aqueous solutions where a hydrophobic molecule will bond to and/or order and pattern the

molecules around itself [195-197]. These structures are referred to as hydrates and, similar to clathrate hydrates, can be defined by n_h. Unlike clathrate hydrates, which occur in the solid state and at low temperatures or high pressures, hydrophobic hydration occurs in the liquid state at or around room temperature. While not always associated, the formation of room temperature hydrates has been reported to lead to clathrate hydrate formation upon solidification [198], as diagramed in Figure 35 for the example of *n*-PrOH. Glinski and Burakowski [190, 192, 197, 199-202] reported in depth on the formation of these structures in binary aqueous solutions of monofunctional alcohols and H_2O. These studies include the monofunctional alcohols examined here that have been reported to form hydrates at room temperature with n_h values of 2.2 (EtOH), 3.1 (*n*-PrOH) and 4.0 (*n*-BuOH) [197, 199]. The Laplace equation (Equation 38) was used to determine the adiabatic compressibility coefficient, κ_s, as a function of the liquid sound velocity, c, and density, ρ [190, 192, 197]:

$$\kappa_s = \frac{1}{c^2 \rho} \qquad 38)$$

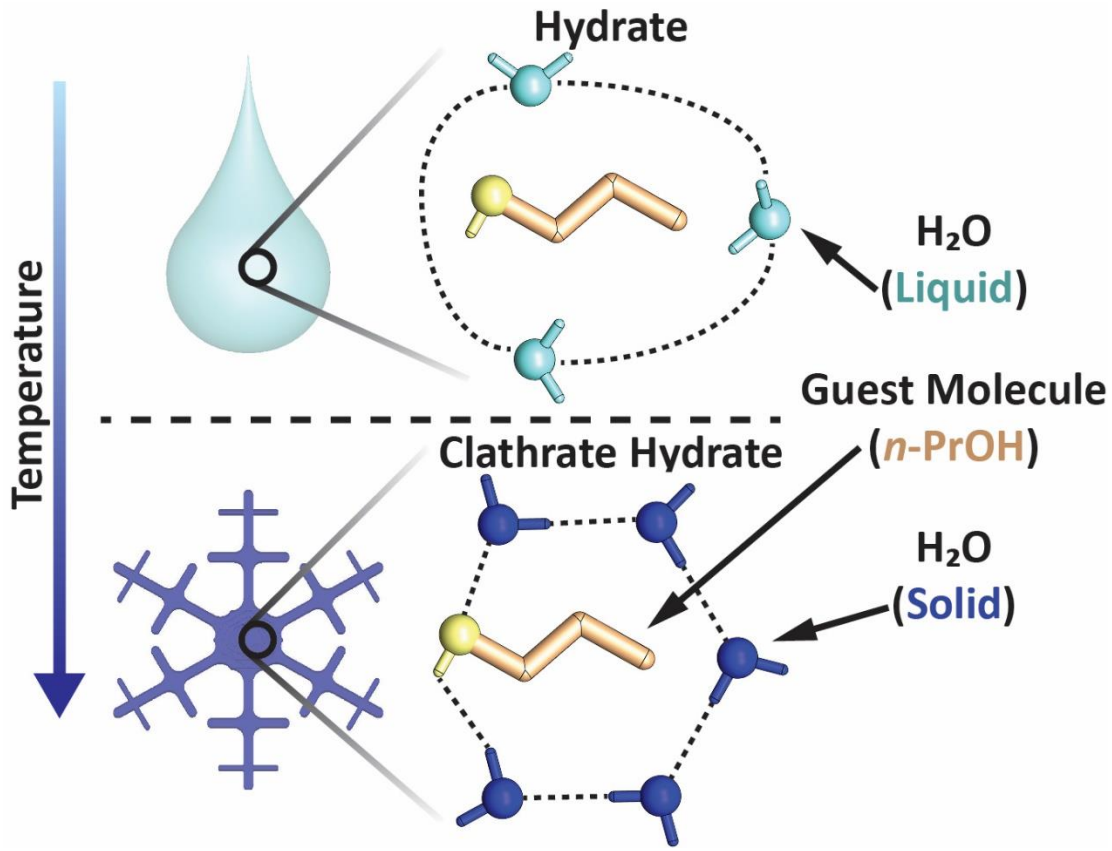

Figure 35. Diagrams of hydrates (from hydrophobic hydration) and clathrate hydrates for an example *n*-PrOH molecule. Hydrates (*n*-PrOH, $n_h = 3$) form at higher temperatures (e.g. room temperature) while clathrate hydrates (*n*-PrOH, $n_h = 5$) form at low temperatures or high pressures. Both processes cause the solute molecule to template the surrounding H_2O molecules. Adapted with permission from [189].

The measurement of κ_s as a function of the solvent concentration is well known to produce a negative parabolic relationship [191, 192]. Previously reported examples of this data for dilute solutions of methanol (MeOH, CH_3OH), EtOH and *n*-PrOH are displayed in Figure 36a. Similar data for *n*-BuOH are only available up to the solubility limit in pure H_2O of ~3 vol.%. As a result, MeOH is presented to display the relative trends within a homologous series of monofunctional alcohols. As the size of the solute increases (from MeOH to *n*-PrOH), the additive concentration where the minimum of κ_s occurs decreases. This decrease in compressibility can be linked to the process of hydrophobic hydration.

The hydrates are relatively more incompressible than pure H_2O, thus lowering the compressibility of the entire solution [197]. As the minimum is approached, each additive molecule is fully dispersed and capable of forming an individual hydrate (Figure 36b). Past the minimum, the liquid becomes saturated resulting in free pockets of the additive solute (Figure 36c) that increase the compressibility of the solution. As a result, this minimum can be considered to be the saturation point of hydrates within the fluid.

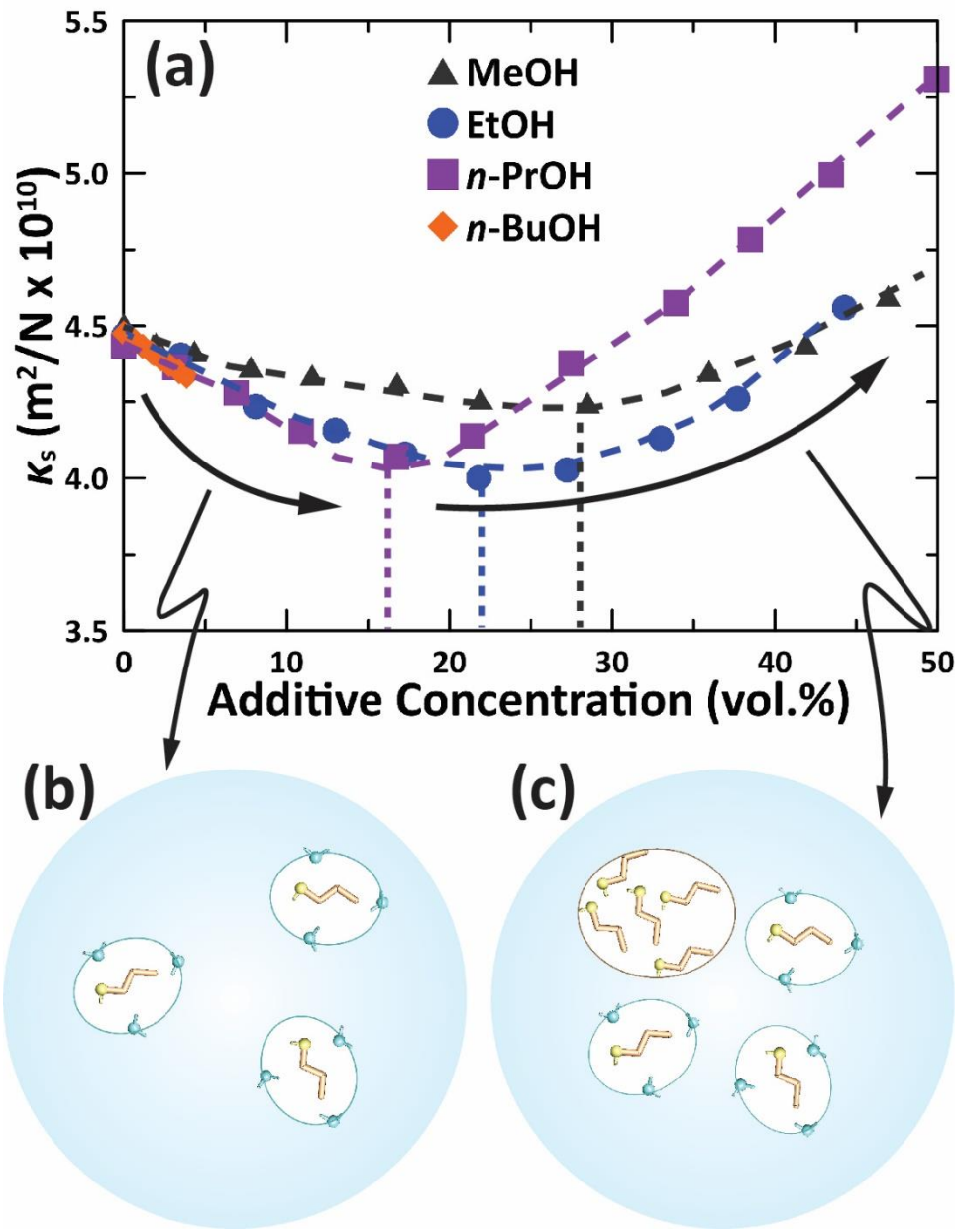

Figure 36. The effect of hydrophobic hydration on the adiabatic compressibility coefficient, κ_S as a function of additives of monofunctional alcohols (solute). **(a)** Historical data for MeOH, EtOH, *n*-PrOH and *n*-BuOH displays a parabolic trend with increasing additive. The minimum value of κ_S decreases as the size of the additive molecule increases; **(b)** As κ_S decreases towards the minimum, additive molecules are completely dispersed and each forms a hydrate; **(c)** Past the minimum, the liquid is saturated with hydrates and free solute becomes present. Data for *n*-BuOH is only available up to the solubility limit of ~3 vol.%. Data for MeOH, EtOH and *n*-PrOH taken from [192], data for *n*-BuOH graciously provided by A. Burakowski. Adapted with permission from [189].

When considering the current series of experiments, it is important to note that many non-electrolytes can be ordered into homologous series with similar structures but increasing numbers of carbon atoms in their alkyl chains. Within monofunctional alcohols, MeOH, EtOH, *n*-PrOH, *n*-BuOH and *n*-pentanol ($C_5H_{11}OH$) all are linear and increase in length with the addition of methylene groups (CH_2). Within this homologous series, n_h has been shown to linearly increase when compared to the number of carbon atoms in the non-electrolyte solute [197].

In addition to studies on pure binary mixtures of liquids, suspensions and slurries consisting of a liquid phase and dispersed solid particles have been studied [203, 204]. To account for the addition of a solid phase, a modified form of Equation 38 can be employed (adapted from [203, 204]):

$$\kappa_s = \frac{1}{1-\Phi}\left(\frac{1}{c^2\rho} - \Phi\kappa_c\right) \quad 39)$$

where κ_s of the isolated liquid phase can be calculated as a function c and ρ measured for the entire mixture as well as the volume fraction of particles in the slurry, Φ, and the adiabatic compressibility of these particles, κ_c.

Previous measurements of the adiabatic compressibility and hydrophobic hydration have only been performed upon binary mixtures (either liquid-liquid or liquid-solid). However, the slurries of freeze casting are much more complex, containing six constituents (H_2O, alcohol additives, PEG, PVA, dispersant and ceramic solid loading) for the cases examined in this study. While there are undoubtedly many interactions occurring within these mixtures, a simplified analysis of the results can be employed by assuming that the slurries are two-phase mixtures of liquid (i.e. H_2O, alcohol, PEG, PVA and dispersant) and

solid (ZrO_2 particles). With this in mind, the sound velocity through the highly incompressible ZrO_2 particles (calculated to be = 5976 m/s [205]) results in a value of κ_c = 5.5 * 10^{-12} m^2/N (as calculated by Equation 38). This is two orders of magnitude smaller than values experimentally calculated for pure H_2O, $\kappa_s \approx 4.4 * 10^{-10}$ m/N^2.

Equation 39 accurately assumes that any compressibility experienced by the slurry would effectively result from only the liquid phase, which is also where any effects of hydrophobic hydration would be felt. However, it would be inappropriate to assume that the solid loading has no effect upon the compressibility data. Previous results have shown that, at low concentrations, the sound velocity decreases with increasing solid loading [203, 204]. This would lead to an increase in the compressibility and could result in a significant effect or even inversion of the compressibility measurements taken on full slurries as opposed to the binary mixtures shown in Figure 36a. This is supported by Horváth-Szabó and Høiland [204], who demonstrated that, in colloidal suspensions, the density and subsequent compressibility of the solid loading is altered by the association of liquid medium to the solid particles. In effect, the density of a solid loading particle, when wetted in a liquid medium, becomes a function of both the original solid body and the liquid attached to it (e,g. penetrating into pores or bound to the surface), thus dispersing the particles and often lowering the effective density. To investigate this, data were collected on two representative solutions (H_2O, PEG, PVA, dispersant and alcohol additive) with varied solid loading and plotted in Figure 37a along with raw data values of *c* in Figure 37b and ρ in Figure 37c. To best visualize the effect, the two slurries chosen were a base sample (with no alcohol additive) and the slurry that showed the largest effect on the final microstructure (7 vol.% *n*-PrOH additive). It can be seen that with the addition of *n*-PrOH

to the slurry, κ_s displays a drastic increase at 15 vol.% solid loading (the concentration present in this study's slurries). Additionally, it can be seen that, when compared to the base sample, with low solid loading concentrations (≤ 5 vol.%) the addition of alcohol results in a decrease in κ_s, corroborating the previous reports on binary mixtures. However, at higher solid loading concentrations (≥ 10 vol.%) this relationship is inverted, with the addition of alcohol resulting in an increase in κ_s.

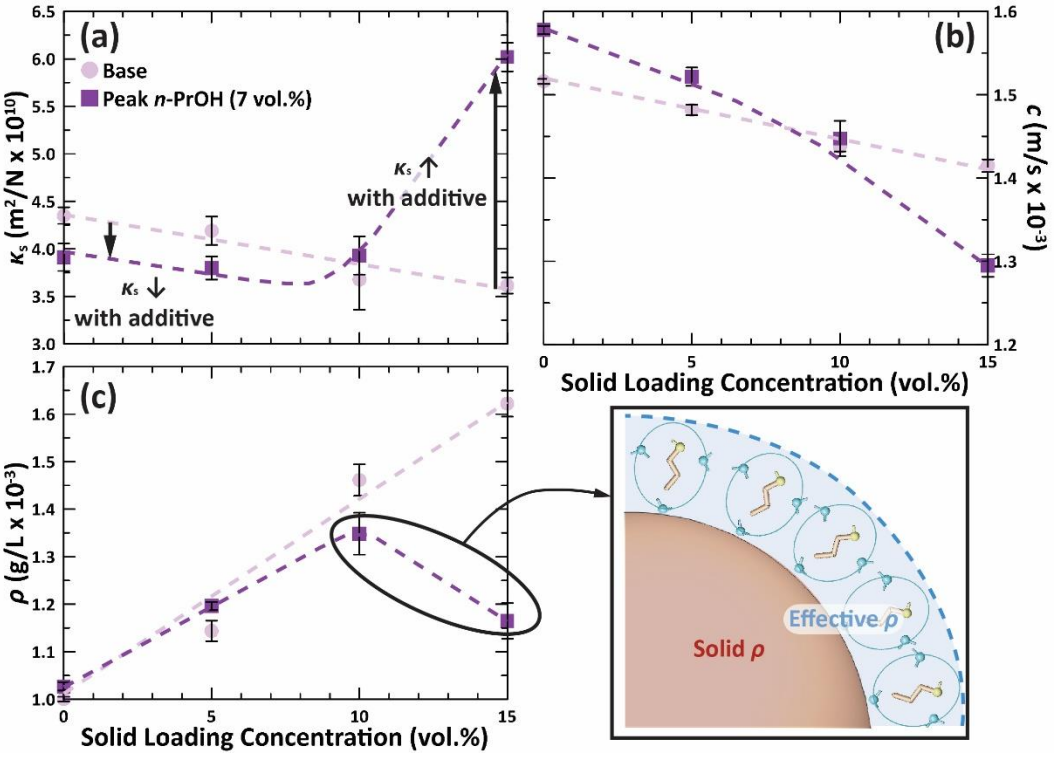

Figure 37. The effect of solid loading concentration on adiabatic compressibility **(a)** At concentrations < 5 vol.% ZrO_2 particles, the addition of 7 vol.% *n*-PrOH causes a decrease in κ_s, which is similar to results on binary mixtures of monofunctional alcohols and H_2O due to the effects of hydrophobic hydration. At concentrations > 10 vol.% ZrO_2 particles, the addition of 7 vol.% *n*-PrOH causes a large increase in κ_s, inverting the response of κ_s to hydrophobic hydration; **(b)** The sound velocity, *c*, of both the base and *n*-PrOH 7 vol.% samples decrease with increasing solid loading; **(c)** The density, ρ, increases with solid loading in the base sample, but shows a decrease with the *n*-PrOH additive at 15 vol.% solid loading. This is proposed to be the effect of hydrates forming around the solid loading (inset). Data is presented as the mean ± one standard deviation of five measurements. Adapted with permission from [189].

This inversion of the relationship between slurries with alcohol and those without can be considered to be the result of a decrease in bulk ρ of the solid loading caused by the presence of hydrates. It has been shown that organic proteins (also known to form hydrates [199]) will increase the stability of slurries and colloids through hydration forces as the proteins coat the solid particles and create a hydrophilic shell [206]. In the current study it is proposed that the hydrates formed by the addition of alcohols can similarly stabilize and disperse the solid loading within the slurries. As previously discussed, when considering the compressibility of a slurry it has been shown that a suspended particle becomes associated with the layer of fluid that surrounds it causing a reduction it its effective density [204, 207]. Such a phenomenon would cause the slurry density to decrease as the total particle surface area increases and therefore (due to the inverse relationship between density and κ_s described in Equation 38) causing an increase in κ_s. This is supported by density measurements (Figure 37c) that show that the addition of *n*-PrOH to slurries at higher solid loading concentrations results in a deviation from an increasing linear trend. This deviation is proposed to be the direct effect to hydrophobic hydration creating large fluid layers surrounding the solid loading particles (as diagramed in Figure 37) and dispersing them.

Measurements of κ_s as a function of additive concentration for all slurries are shown in Figure 38. In each case, the slurries reach maxima in κ_s at the same concentrations as their peak A_p (Figure 32a). Given the results of the previous experiment, these maxima are considered to be linked to the saturation of hydrates due to hydrophobic hydration, with the solid loading causing the largest concentration of hydrates to occur at a maximum as opposed to a minimum as seen for binary mixtures. Importantly, the parabolic response of

κ_s with respect to additive concentration is able to provide an understanding of the maxima in pore size within the final freeze cast microstructures. This connection could not be fully explained by the simple presence of clathrate hydrates as there are no phases present at the concentrations associated with peak A_p values in any of the cases presented here or in previous reports. However, the largest increase in microstructural properties was observed with the addition of *n*-PrOH, which was the only additive in this study to that may display the presence of clathrate hydrates.

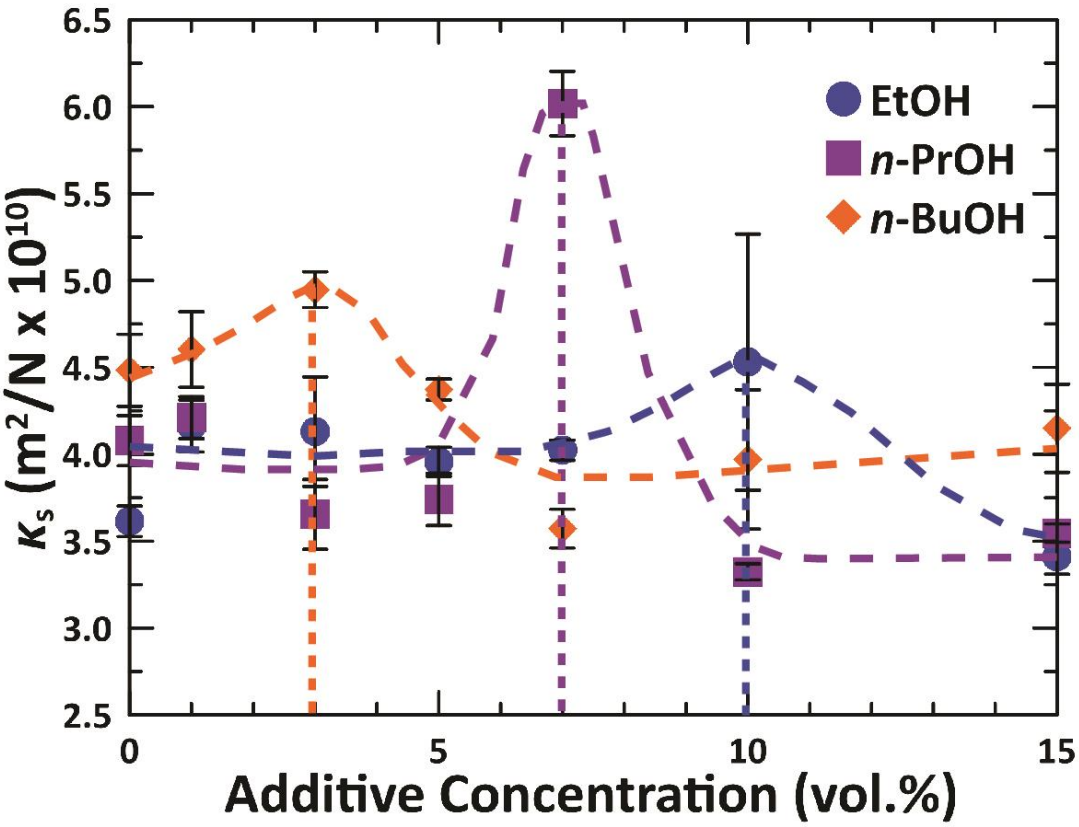

Figure 38. Adiabatic compressibility, κ_s, as a function of additive concentration for complete slurries. Maxima occur at the concentrations of 10, 7 and 5 vol.% for EtOH, *n*-PrOH and *n*-BuOH respectively. These maxima occur at the same concentrations as the observed peak A_p values and are associated with the effects of hydrophobic hydration. Data is presented as the mean ± one standard deviation of five measurements. Adapted with permission from [189].

The current results highlight the effect of hydrophobic hydration on the freeze casting process and provide a new avenue for intrinsic control. As diagramed in Figure 39, it is suggested that the presence of the enlarged hydrate structures in the liquid slurry ahead of the ice growth results in enlarged ice crystals, which in turn provide for the enlarged freeze cast microstructures described here. There are a multitude of potential additives known to form hydrates that could be employed including alcohols, polymers, amines, amides and amino acids [199]. Perhaps of greatest importance, this new work suggests that when considering the freeze casting process, attention should be given to the state of the slurry at room temperature, not just to the frozen or freezing states.

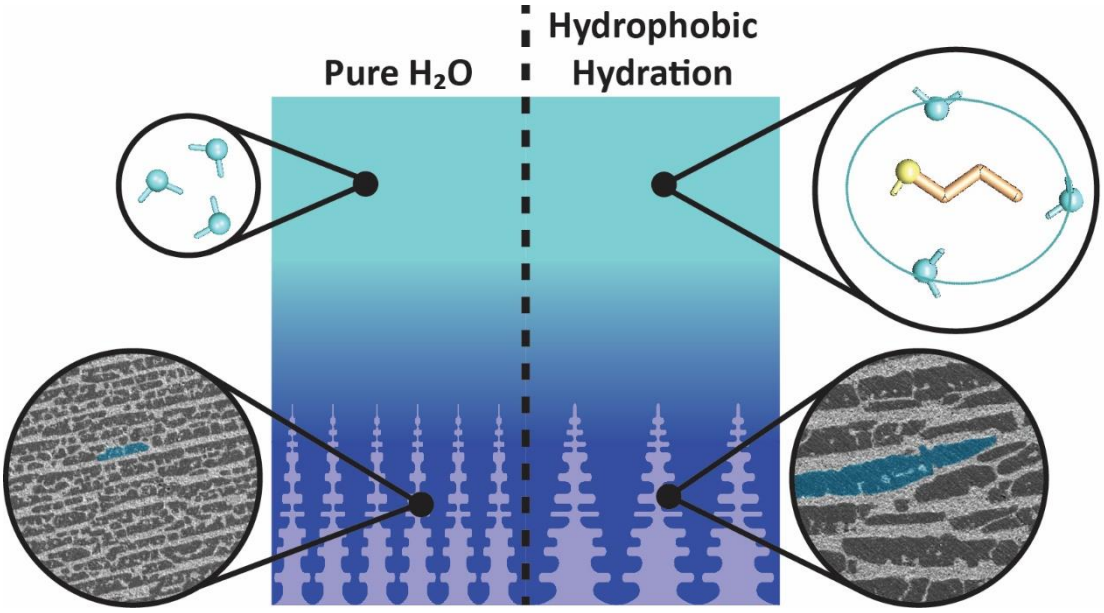

Figure 39. Diagram of the proposed mechanism connecting hydrophobic hydration to the enlarged porosity in the final freeze cast scaffolds. The presence of the enlarged hydrates in the liquid phase ahead of the freezing front results in enlarged ice crystals, which in turn result in larger porosity. Adapted with permission from [189].

4.2.3 Mechanical Analysis

Mechanical properties as a function of additive concentration are shown in Figure 40. Ultimate compressive strength (*UCS*, Figure 40a) and effective compressive modulus

(*E*, Figure 40b) are both displayed in a normalized form as described in Equation 37, allowing for clear comparison of how the trends are affected by the additives. The mechanical properties at the peak A_p for each additive are defined as, EtOH (*E* = 4.5 GPa, *UCS* = 147 MPa), *n*-PrOH (*E* = 3.3 GPa, *UCS* = 131 MPa) and *n*-BuOH (*E* = 4.0 GPa, *UCS* = 162 MPa). EtOH shows little change in mechanical properties regardless of concentration. Both *n*-PrOH and *n*-BuOH display peak values in mechanical properties at the same concentrations associated with their peak A_p's, with the greatest increase in both *UCS* and *E* occurring with the addition of *n*-PrOH. This shows that any increase in mechanical properties is most closely tied to the magnitude of A_p. Of note, the relative magnitude of the increase in mechanical properties from 0 vol.% to the maximum at 5 vol.% for both *UCS* (~1.5 times increase) and *E* (~2.5 times increase) are similar to those previously reported for similar ZrO_2 scaffold composites that used IPA as an additive [188].

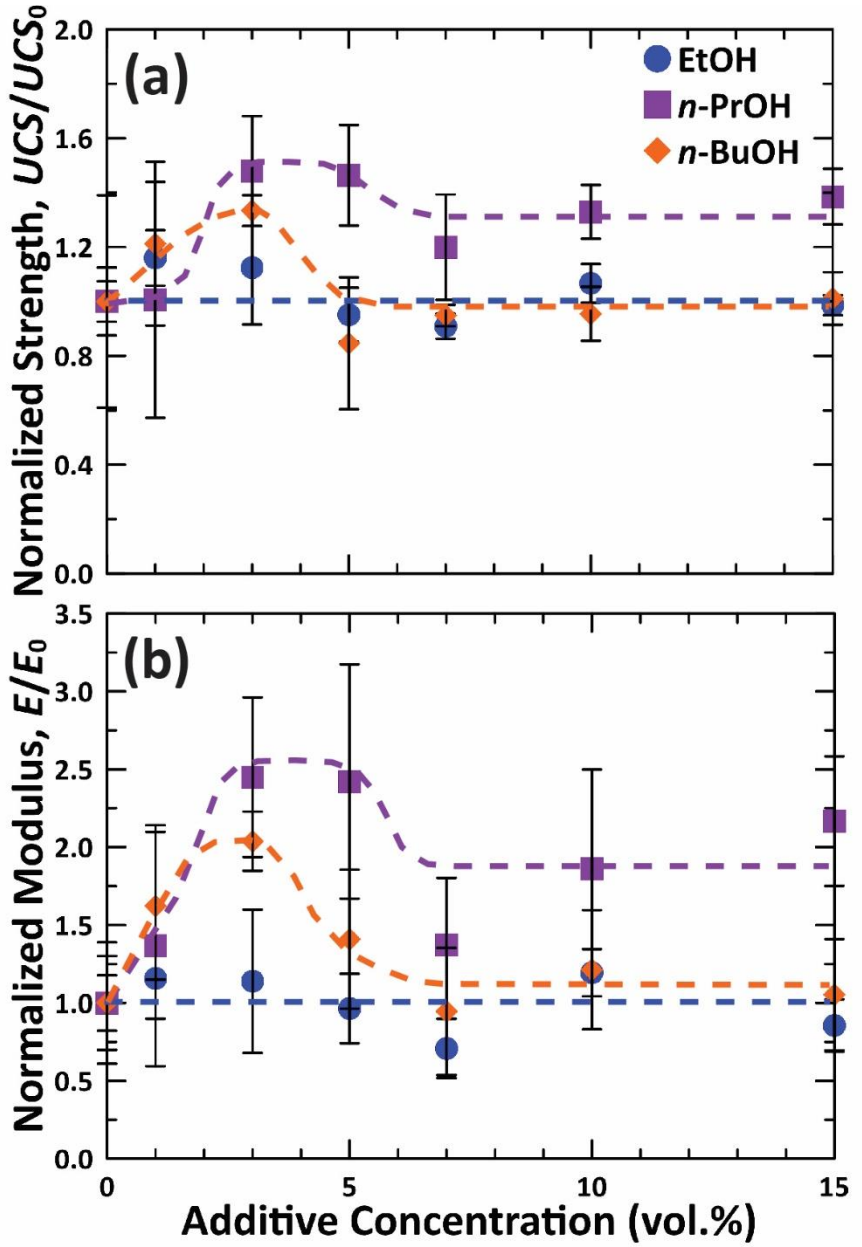

Figure 40. (a) Normalized ultimate compressive strength (divided by UCS_0, the ultimate compressive strength of a scaffold with 0 vol.% additive) and **(b)** normalized compressive modulus (divided by E_0, the modulus of a scaffold with 0 vol.% additive) data as a function of additive concentration for EtOH, *n*-PrOH and *n*-BuOH. To focus on the trends in mechanical properties, the values are all normalized. In both cases, EtOH shows little change regardless of additive concentration, *n*-PrOH reaches a maximum at 3 - 5 vol.% and *n*-BuOH reaches a maximum at 3 vol.%. Note that the magnitude of both *UCS* and *E* is greatest in the case of *n*-PrOH. Data is presented as the mean ± one standard deviation of five measurements. Adapted with permission from [189].

While the addition of EtOH, *n*-PrOH and *n*-BuOH are capable of realizing an increase in the mechanical properties the exact physical phenomena that drives this is yet unknown. Given that the scaffolds are ZrO_2 ceramic-epoxy two phase composites, the mechanical properties were analyzed by a simple rule of mixtures, given the relative volume fraction of the ceramic, V_c (Table 2, Table 3 and Table 4).

$$Q_{\mathrm{comp}} = Q_{\mathrm{ZrO2}} V_{\mathrm{c}} + Q_{\mathrm{epoxy}}(1 - V_{\mathrm{c}}) \qquad 40)$$

where Q_{comp}, Q_{ZrO2} and Q_{epoxy} are the mechanical properties (E and UCS) of the composite scaffold, ZrO_2 (for solid tetragonal ZrO_2, E_{ZrO2} = 210 GPa, UCS_{ZrO2} = 1200 MPa [208]) and epoxy (measured to be E_{epoxy} = 1.8 GPa, UCS_{epoxy} = 79.9 MPa) respectively. These results were found to be significantly in excess of the experimentally measured maximum values with E = 55 - 70 GPa and UCS = 360 - 450 MPa. This shows that the true fracture behavior cannot be explained with such a simplistic model.

When considering these lower than expected mechanical properties, the fracture mechanisms of each of the two phases must be considered. The rule of mixtures would suggest that both fail in pure compression. While this would be reasonable for a ductile and isotropic material such as the epoxy, it is much less so for the brittle ZrO_2, which takes on the form of tall, slender and lamellar walls upon freeze casting. Porter et al. [36] developed a simplified but effective model for uninfiltrated scaffolds of a similar structure that showed the low mechanical properties of were the result of Euler bucking of the lamellar walls. This model accurately predicts the diminishing mechanical properties of uninfiltrated scaffolds as the pore aspect ratio increases by analyzing a unit cell of constant material volume. Observing the current results, failure of the brittle ZrO_2 lamellar walls is assumed to again occur by Euler buckling. However, the infiltrating epoxy provides an

unknown level of resistance to buckling. A simplified estimation of this resistance to buckling can be determined by calculating the buckling mode, *n*, which corresponds to the number of fixed restraints (or buckling lobes) providing resistance to a column under axial compressive loading [209]. As it is clear that these ZrO_2 walls are unable to buckle freely, $n > 1$. However, given that *E* of ZrO_2 is almost two orders of magnitude larger than that of the epoxy, it would also be inappropriate to consider the interface between the two phases to be rigidly fixed, which would allow the composite to provide properties closer to the rule of mixtures analysis presented above. Therefore, an analysis of the effective *n* for the composites in this study will be presented. This analysis focuses upon the strength (*UCS*) of the composite materials at the peak A_p for each alcohol additive. This was done so examine the failure modes of those materials that, experimentally, provided the highest mechanical properties and would be the most likely candidates for structural applications.

To understand this interaction between the two constituents, a simplified model of the current freeze cast composites is assumed as a layered composite (Figure 41). With this assumption, the total ultimate compressive strength, UCS_T, of a 5 x 5 x 5 mm^3 sample (to match the physical testing) can be calculated by a rule of mixtures that incorporates the failure modes of each constituent: compression for the epoxy and buckling for the ZrO_2 ceramic, which is dependent upon the number of ceramic lamellar walls, N_w, within the sample:

$$UCS_T = UCS_{epoxy}(1 - V_c) + UCS_{ZrO2}(N_w) \quad (41)$$

where UCS_{epoxy} is assumed to be constant in all cases as the experimentally calculated value of 79.9 MPa. UCS_{ZrO2} is defined as the critical stress for Euler buckling [209]:

$$UCS_{\mathrm{ZrO2}} = UCS_{\mathrm{wall}} = n^2 \frac{\pi^2 q^2 E_{\mathrm{ZrO2}} I}{A_{\mathrm{w}}(kl)^2} \quad (42)$$

where q is a previously suggested empirical correction factor to incorporate experimental variability such as internal wall porosity and surface roughness (for this case and has been previously used [36], q = 0.02), I is the moment of inertia of the lamellar wall (Equation 43), A_w is the cross-sectional area of the wall, which is equal to the wall width, w (= 5 mm), times the wall thickness T_w (experimentally measured ranging from ~6 - 20 μm), k is a constant that depends on the geometry of the ends (for this case, k = 0.5 for fixed ends) and l is the wall length (= 5 mm, all geometries are imaged in Figure 41a).

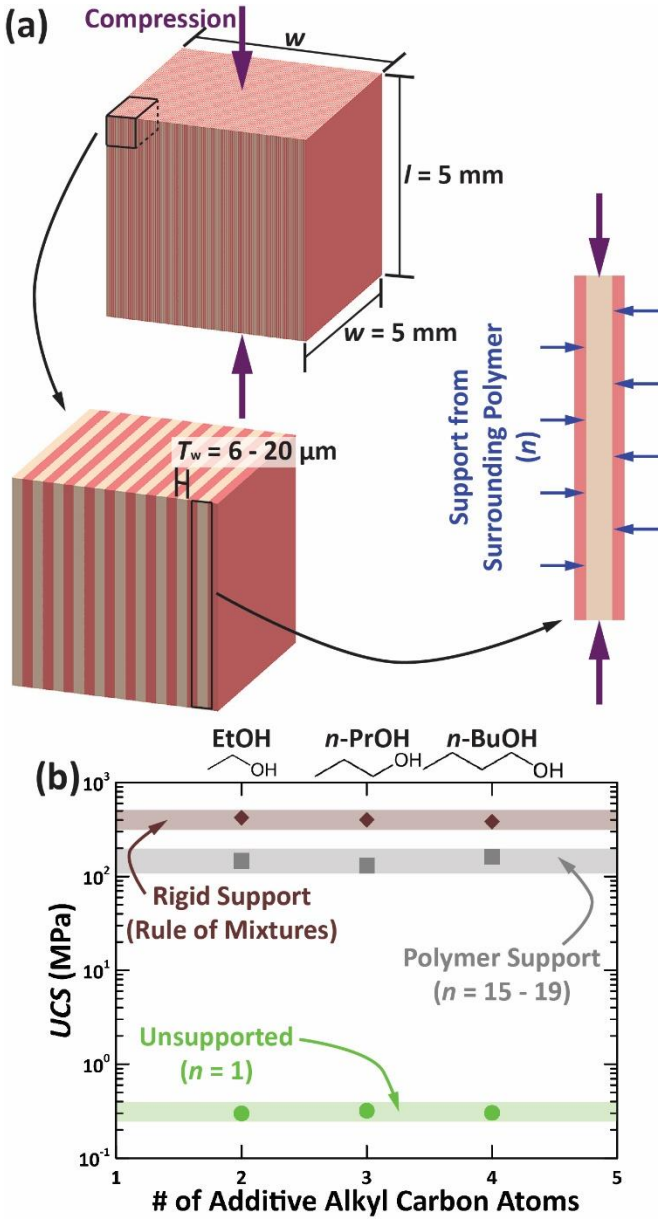

Figure 41. Mechanical property analysis of the current bioinspired composites. **(a)** A simplified two-phase (polymer in pink and ZrO_2 ceramic in yellow) layered composite model is considered using the experimentally measured geometric dimensions of *w*, *l* and T_w. The strength is considered to be a function of axial compression of the polymer phase and supported Euler buckling of the ZrO_2 ceramic; **(b)** While the current bioinspired composites are unable to provide rigid support (as would be predicted by the rule of mixtures), they do provide significant buckling resistance, which is estimated to result in a buckling mode of n = 15 - 19. This is orders of magnitude higher than the calculated strength of uninfiltrated, or unsupported, scaffolds (n = 1). Adapted with permission from [189].

The moment of inertia, *I*, is:

$$I = \frac{wT_w^3}{12} \quad 43)$$

The critical stress of buckling is calculated for a single wall. Therefore, the total stress of the numerous walls within the samples cannot be calculated as a simple volume fraction and must be considered to be additive. For this reason, N_w in each scaffold was estimated based upon the known volume fraction of ZrO_2 and the experimentally measured wall thickness:

$$N_w = \frac{V_c w}{T_w} \quad 44)$$

Substituting Equation 42, Equation 43 and Equation 44 into Equation 41, a final simplified model for the strength of the composite scaffolds that takes into account the varying failure modes is developed:

$$UCS_T = UCS_{epoxy}(1 - V_c) + n^2 \frac{\pi^2 q^2 E_{ZrO2} w V_c T_w}{12(kl)^2} \quad 45)$$

Finally, Equation 45 is rearranged to solve for the effective resistance to buckling, *n*:

$$n = \frac{kl}{\pi q} \sqrt{\frac{12(UCS_T - UCS_{epoxy}(1 - V_c))}{E_{ZrO2} w V_c T_w}} \quad 46)$$

By setting UCS_T equal to the peak A_p strength values measured for each additive, it was found that *n* = 18, 15 and 19 for EtOH, *n*-PrOH and *n*-BuOH respectively. This represents a high level of interaction and suggests that the infiltration of this second phase, while not able to provide rigid support and ensure compressive failure of the lamellar walls (as would have been predicted by a rule of mixtures), does provide a substantial impact on

the mechanical and buckling stability of these structures. To further explore this effect, the *UCS* of uninfiltrated scaffolds can be calculated from Equation 45 by setting $UCS_{epoxy} = 0$ and $n = 1$ (denoting a failure of unsupported, mode 1 buckling). This unsupported case predicts very low peak A_p strengths of 0.30, 0.32 and 0.30 MPa for EtOH, *n*-PrOH and *n*-BuOH respectively. Of note, these values are similar to those previously reported in experiments on TiO_2 freeze cast scaffolds with similar microstructures that utilized IPA as an additive (0.7 MPa) [36]. The results of this analysis are summarized in Figure 41b.

This analysis demonstrates that, while improved over uninfiltrated scaffolds, the lamellar walls of the current bioinspired composite materials still fail in a buckling mode, thus reducing their strength. In addition, the level of interaction between the two phases can explain the observed increasing trend in mechanical properties with the increase in X_p and A_p, which stands in opposition to previous reports of uninfiltrated freeze cast scaffolds [36, 44]. The dependence of this buckling mode of failure on T_w, which generally follows a similar parabolic trend as A_p, tends to produce higher strengths with increasing X_p and A_p. When attempting to create a stronger material for structural applications, the use of a an infiltrate that more closely matches the elastic properties of the ZrO_2 ceramic would provide greater support to the lamellar walls, allowing the mechanical properties to approach the elevated properties described by the rule of mixtures analysis.

This level of complex interaction is also present in biological materials with many organisms forming layered structural design elements that consist of numerous interfaces with large changes in mechanical properties, usually resulting from alternating layers of rigid and compliant phases (e.g. ceramic and polymeric respectively) [12]. These are found throughout nature in structural biological materials such as the nacre of abalone [14, 118,

119], the spicules of some sea sponges [66, 117] and the lamella of cortical bone [210]. The controlled, intrinsic templating of freeze casting through the use of hydrophobic hydration and clathrate hydrates allows for the creation of similar bioinspired designs. Mechanically, these layered structures are known to provide additional toughness through the deflection and blunting of cracks along with other toughening mechanisms ahead of the crack and in its wake [12]. The mechanical analysis presented here on bioinspired freeze cast composites suggests an additional mechanical advantage of these structures as the compliant phases are capable of providing buckling resistance of brittle plates and lamellae.

4.3 Conclusions

The current experimental study of epoxy-infiltrated, freeze cast ZrO_2 bioinspired composites with ethanol (EtOH), *n*-propanol (*n*-PrOH) and *n*-butanol (*n*-BuOH) as additives for intrinsic control enables the following conclusions:

- The addition of EtOH, *n*-PrOH and *n*-BuOH all result in an increase in microstructural pore size up to a peak pore area (peak A_p), which occurs at 10, 5 - 7 and 3 vol.% respectively, then a subsequent decrease with increasing concentration. The peak A_p magnitude was largest when *n*-PrOH was employed as the additive and, in this case, occurred at the same concentration as previous reports on the use of isopropanol in the freeze casting process.
- Differential scanning calorimetry experiments designed to mimic the freeze casting process suggested that clathrate hydrates were present in *n*-PrOH-H_2O binary mixtures, but not in those involving EtOH or *n*-BuOH.
- Sound velocity experiments to determine the compressibility of the slurries examined in this study showed that hydrophobic hydration occurred in all cases. The effects of

hydrophobic hydration were also shown to be greatest at the same additive concentrations where the peak A_p occurred for each additive. Additionally, experiments on the effect of the solid loading showed that slurry's solid loading particles cause the effect of hydrophobic hydration to be inverted.

- The current study highlights that, when considering the freeze casting process, the effect of hydrophobic hydration at room temperature prior to freezing must be considered, in addition to the low temperature and freezing states.
- Mechanical properties (ultimate compressive strength and modulus) of two-phase, bioinspired ZrO_2-epoxy composites showed an increase in the cases of *n*-PrOH and *n*-BuOH additives, but little change in the case of EtOH. Analysis of the mechanics demonstrated that the composites are incapable of failing in pure compression as would be described by the rule of mixtures due to the preferential Euler buckling mode of the ZrO_2 phase. However, the presence of the epoxy provided a large resistance, which was estimated to force the structures to fail in bending modes of n = 18, 15 and 19 for EtOH, *n*-PrOH and *n*-BuOH respectively.
- The current analysis suggests that layered structural design elements, found throughout nature, may be harnessing this resistance to Euler buckling in order to provide additional strength.

Chapter 4, in part, is a reprint of the material as it appears in "Bioinspired intrinsic control of freeze cast composites: Harnessing hydrophobic hydration and clathrate hydrates" Acta Materialia, vol. 114, pp 67-79, 2016. The dissertation author was the primary investigator and author on this paper. This paper was co-authored by Christopher

F. Yu, Rachel L. Hsiong, Arijit Sengupta, Peter M. Hildebrand, Marc A. Meyers and Joanna McKittrick.

5. Physical Phenomena of Hydrate Freeze Casting by 2D Freezing Front Observation

The research presented in chapters 3 and 4 have gone to propose and validate the effect of both clathrate hydrates and hydrophobic hydration on the freeze casting process. These structures, induced by the addition of the monofunctional alcohols ethanol (EtOH), isopropanol (IPA), *n*-propanol (*n*-PrOH) and *n*-butanol (*n*-BuOH), have been shown to create enlarged porosity in the final freeze cast microstructure [36, 188, 189]. This can be directly observed through measurements of the pore area, A_p, as a function of the alcohol additive concentration. Figure 42 displays such data, normalized to the pore area with no additive (A_{p0}) and it can be seen that, in all cases, the pore area increases up to a peak value (10, 5 to 7, 5 to 7 and 3 vol.% for EtOH, IPA, *n*-PrOH and *n*-BuOH respectively) then decreases with increasing additive concentration [189].

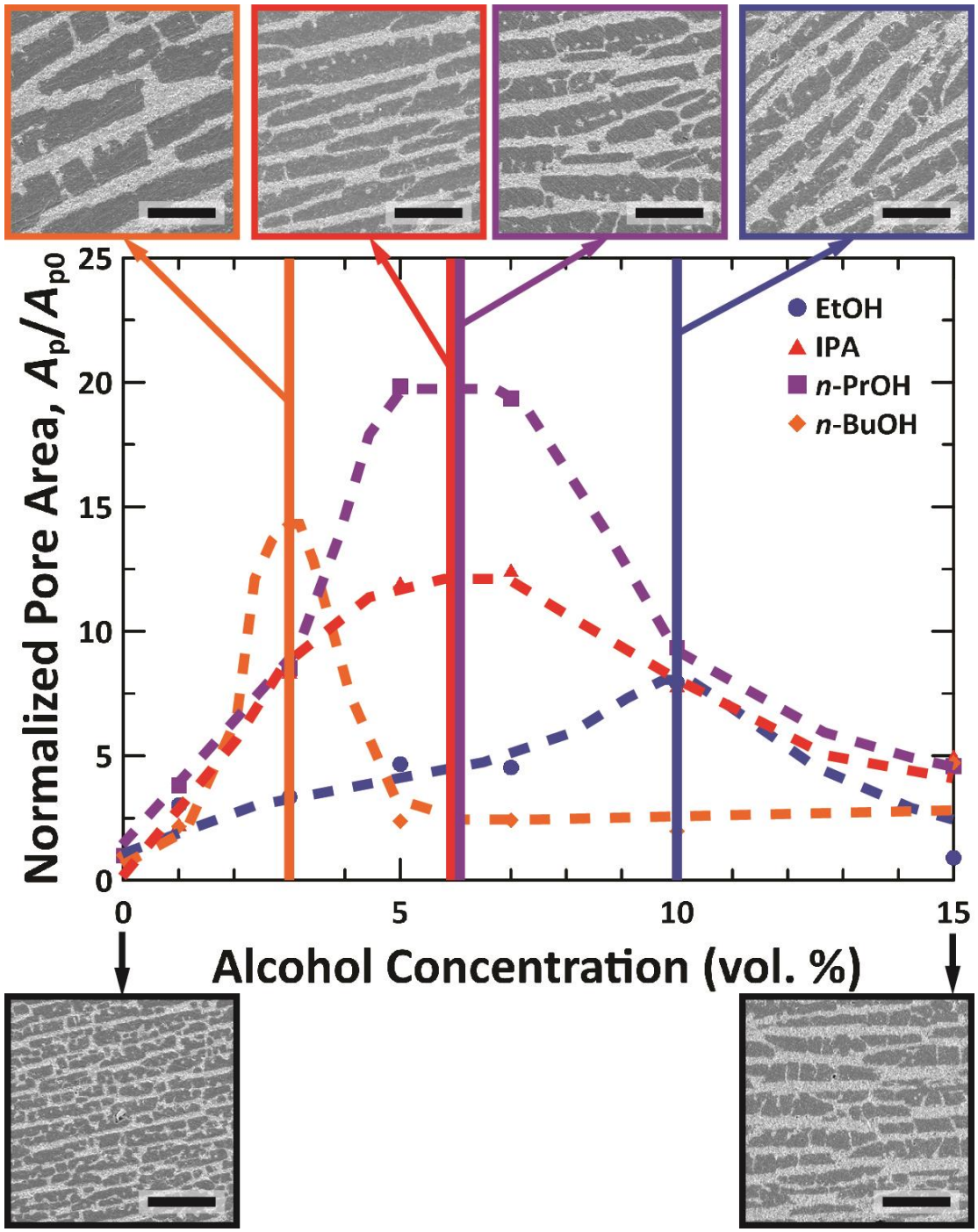

Figure 42. Historical normalized pore area (A_p) data and micrographs for freeze cast scaffold fabricated with the monofunctional alcohol additives EtOH, IPA, *n*-PrOH and *n*-BuOH. In all cases, A_p increases up to a peak value (10, 5 to 7, 5 to 7 and 3 vol.% for EtOH, IPA, *n*-PrOH and *n*-BuOH respectively) then declines with increasing additive concentration. Data adapted from [189]. Micrograph scale bars: 100 μm.

While the presence and final effect of these structures is well established, the exact nature of how these microstructures come about during the freezing process is still unknown. However, two potential mechanisms appear to be most likely:

(1) The enlarged crystal structure of the clathrate hydrates is directly related to an enlarged ice crystal during the freeze casting process. As an example, the crystal structure of the clathrate hydrates induced by isopropanol in the freeze casting process are known to have a cubic crystal structure with a lattice parameter of a = 1.26 nm [54], considerably larger than the hexagonal crystal structure of ice with lattice parameters of a = 0.45 nm, c = 0.73 nm [211]. This could also explain the observed trends that monofunctional alcohols that clearly create clathrate hydrates during the freeze casting process (i.e. IPA and *n*-PrOH) induce relatively larger final porosities than those that are more likely only governed by hydrophobic hydration during the freeze casting process (i.e. EtOH, *n*-BuOH).

(2) The clathrate hydrate and hydrophobic hydration or indeed simply the presence of monofunctional alcohols (antifreezes) could cause the slurry to freeze at a slower rate during the freeze casting process. This slower rate could be measured as a function of the freezing front velocity, v, which can be related through a power law (as shown in the equation below) to the resultant ice lamellae wavelength, λ (i.e. the resultant size of the ice crystal) [27, 212]:

$$\lambda = Av^{-\mathrm{n}} \qquad 47)$$

where A and n are constants that depend upon the materials employed in the freeze casting technique. Due to the negative exponent, a decrease in v will result in an increase in λ (i.e. an increase in the size of the ice crystals during the freeze casting

process). This increase in ice crystal size would directly relate to an increase in the final scaffold porosity.

As the increase in pore size (which is directly related to the ice crystal size and λ) is already established for freeze cast scaffolds fabricated with monofunctional alcohols as additives, these two potential mechanisms can be differentiated through observations of the freezing front velocity, v. Mechanism (1) would allow for increased pore size through larger crystal unit cells without necessitating any change in the freezing front velocity with additive concentration. Alternatively, mechanism (2) would, by definition, result in a considerable decrease in the freezing front velocity as the driving force behind the observed increase in pore area.

In this chapter, the author designs, fabricates and employs a 2D freeze casting setup, inspired by Hunger et al. [213], to take measurements of the freezing front velocity of freeze cast slurries with monofunctional alcohols as additives. This study elucidates the specific physical phenomena involved with the previously reported increase in pore area observed in such freeze cast scaffolds [36, 188, 189].

5.1 Materials and Methods

5.1.1 2D Freeze Caster

To facilitate these experiments a new 2D freeze casting setup was designed and fabricated (Figure 43a). This setup consists of a copper and aluminum cold finger that supports a freeze casting mold and sits within a liquid nitrogen bath so as to induce directional freezing. A thermocouple is attached to the mold to collect temperature measurements. The mold was designed to allow for observation of the freezing front. The side and back walls were fabricated out of polycarbonate and the front out of glass (Figure

43b). The back wall can be adjusted to alter the total depth of the mold. After preliminary experimentation, the mold was fixed to provide an internal chamber that was 20 x 50 x 1.5 mm.

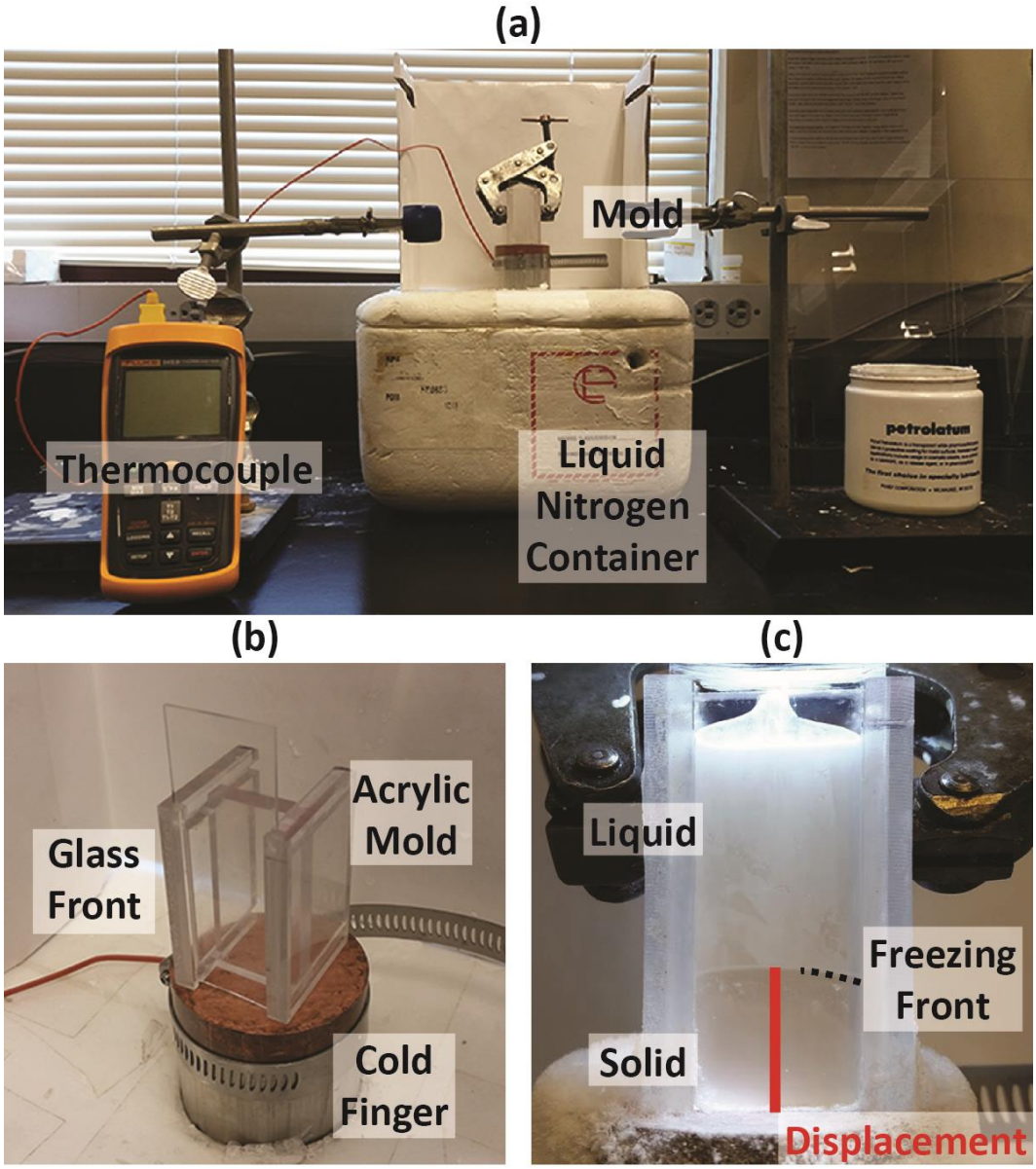

Figure 43. Custom 2D freeze casting setup. **(a)** The important components of the liquid nitrogen chamber, the cold finger, the mold and the attached thermocouple; **(b)** the mold itself is created out of acrylic with a glass front so as to observe the freezing front; **(c)** an example freezing front measurement. Measurements were taken from the top of the cold finger to the crest of the freezing front.

5.1.2 Slurry Preparation

Utilizing the methods described in chapter 1.6, freeze cast slurries were prepared. Aqueous slurries were prepared to investigate the effects of a series of linear monofunctional alcohols on the freezing front velocity; EtOH, IPA, *n*-PrOH and *n*-BuOH (on the freeze casting process. Slurries were prepared with 15 vol.% ZrO_2 powders, 1 wt.% PEG and 1 wt.% PVA as a polymeric binders and 1 wt.% Darvan 811 as an anionic dispersant. In addition, a small amount of food coloring (~1 - 2 mL) was included to ease observation of the freezing front during the freezing process. Slurries were prepared by varying two parameters: the volume fraction (0, 1, 3, 5, 7, 10 and 15 vol.%) and the additive (EtOH, IPA, *n*-PrOH and *n*-BuOH) for a total of 21 slurries.

5.1.3 Freezing Front and Ice Crystal Observations

Samples of approximately 5 mL of the degassed slurry were poured into the custom 2D freeze caster and directionally frozen. During the freezing process images were captured at 2 min intervals over a 30 min period (for a total of $N = 15$ measurements per trial). Images were analyzed utilizing ImageJ software (Nation Institutes of Health, Bethesda, MD, USA) to take measurements of the freezing surface to the crest of the freezing front (as shown in Figure 43c) to calculate a thickness of solid slurry, *s*, in each case. The velocity, *v*, was calculated as the change in *s* at each time interval, divided by the elapsed time.

Measurements were taken of the ice crystal diameters directly after freezing of the slurry in the 2D freeze caster. This ice crystal diameter is proportional to the final pore diameter in freeze cast scaffolds made with similar slurries. Images were collected and

were analyzed by Image J software. A total of five measurements were taken to calculate an average and standard deviation of the ice crystal diameter.

5.2 Results and Discussion

Observation of the freezing front velocity is displayed in Figure 44. Logarithmic trend lines are shown for each alcohol concentration. In all cases, *v* is shown to begin at a high value, then decrease to a constant value with time. Of note, observations of the freezing front velocity of freeze cast slurries with alumina [214] and silica [215] as the solid loading both provided similar freezing front velocity profiles with a high initial velocity, which degrades to a lower and constant value with time. Of greater note, as can be seen from the trend lines, there is no definitive change in the trend with increasing additive concentration regardless of the alcohol or concentration. This provides opposition to mechanism (2) that would require a decrease in the *v* to nucleate larger ice crystals and create the enlarged pores found within the final freeze cast scaffolds.

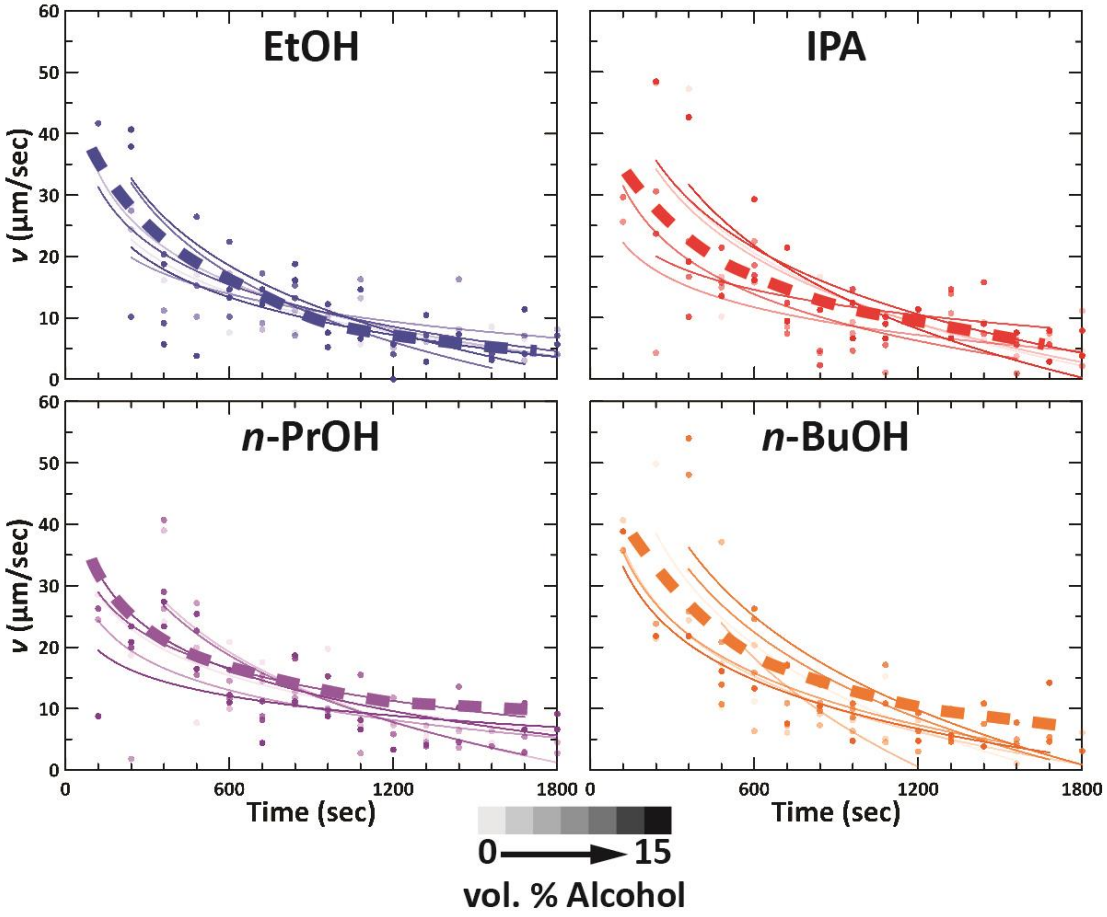

Figure 44. Freezing front velocity, *v*, data for EtOH, IPA, *n*-PrOH and *n*-BuOH. Solid trend lines represent a logarithmic best fit of the data at each alcohol concentration, while the dashed line represents general trend for all alcohol concentrations. In all cases it can be seen that, regardless of alcohol concentration, a similar trend in v is observed.

To better observe the properties that occur during the range of freezing that directly relates to the section of freeze cast scaffolds that are general observed and tested, that which occurs during steady state freezing, the average velocity of the freezing front after 600 seconds as a function of additive concentration is shown in Figure 45. This data is overlaid with experimentally measured, normalized ice crystal diameter data, which displays the same trend as previously reported pore areas of freeze cast scaffolds prepared with identical slurries [189] In accordance with Equation 47, if the enlarged porosity was due to a

decrease in *v*, the peak values in pore area should correspond to minima in *v*. However, it can be seen that steady state growth *v* values are effectively constant at ~ 10 μm/sec regardless of concentration or additive type.

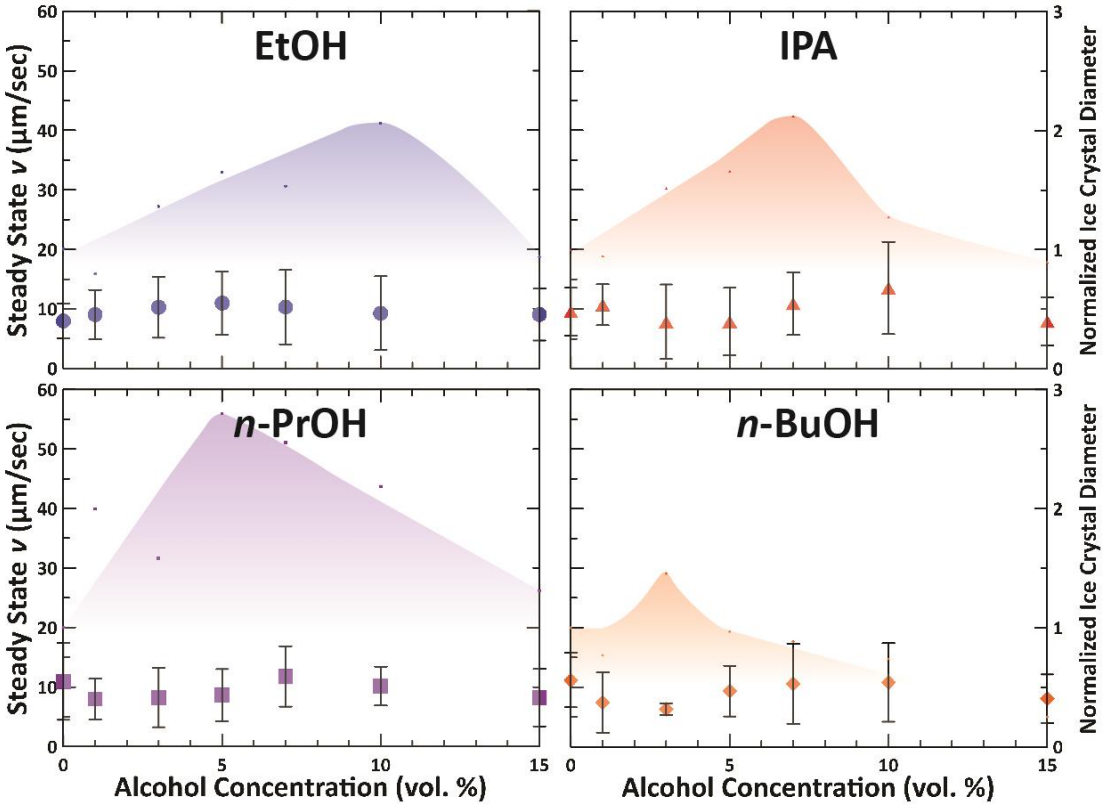

Figure 45. Steady state velocity (taken as the average *v* after 600 seconds) as a function of additive concentration. Data is overlaid with measurements taken from the 2D freeze caster of the observed ice crystal diameter. It can be see that the steady state *v* is roughly constant with additive and independent from the overserved change in ice crystal diameter.

As a function of either the freezing front profile or the steady state freezing front, there is no observed correlation between the additive concentration and *v*. This serves as evidence that the presence of monofunctional alcohols within the freeze casting process does not retard the freezing front and, therefore, this effect is not responsible for the observed increase in pore area within the materials. Given this, and as previously suggested [188, 189], it is proposed that the enlarged nanostructures created by the effects of clathrate

hydrates and hydrophobic hydration are the direct cause of the enlarged final microstructures observed in the freeze casting process when monofunctional alcohols are employed as additives.

5.3 Conclusions

The current experimental study of the active freezing of ZrO_2 based freeze cast slurries with various monofunctional alcohol additives, observed through a custom 2D freeze casting setup enables the following conclusions:

- As shown by measurements of the freezing front during the freezing process, it can be determined that regardless of the additive type (ethanol, isopropanol, *n*-propanol or *n*-butanol) or concentration (0 - 15 vol.%), there is no noticeable trend in the freezing front velocity profile as a function of additive.
- The velocity of steady state ice growth, as a function of alcohol concentration, showed no correlation to the observed ice dendrite size.
- Given that there was no observed correlation between the additive concentration and freezing front velocity (both the general profile and the steady state velocity), it is shown that the enlarged porosity found in freeze cast scaffolds with monofunctional alcohols is not related to a reduction in freezing caused by these additives. It is therefore suggested that the enlarged structures are due to the enlarged nanostructures of clathrate hydrates and hydrophobic hydration, as suggested by previous reports.

6. 3D Printed Templating of Freeze Casting for Macro-Micro Porous Bioinspired Scaffolds

Freeze casting has been has been explored in a number of reports for the fabrication of bioinspired bone [40, 44, 216-218]. This is largely due to the processes ability to mimic the materials and, to some extent, porous structure of natural bone. However, the porosity in bone occurs at multiple length scales, with larger osteons and vascular channels (occurring on the length scale of ~100 μm) and smaller lacuna spaces (occurring on the length scale of ~10 μm) [75]. While the freeze casting technique has been able to produce a variety of complex microstructures, to the knowledge of the author, these structures have never been demonstrated at multiple length scales within a single material.

In this chapter the author proposes a novel extrinsically controlled freeze casting method for the creation of bioinspired materials that exhibit porosity at multiple length scales through the use of a 3D printed template to supplement the templating of growing ice crystals that are integral to freeze casting. These structures are able to mimic the material and hierarchical porosity that occurs in biological materials such as bone and are therefore proposed as potential, biocompatible bone replacement materials.

6.1 Materials and Methods

Utilizing the methods described in chapter 1.6, freeze cast scaffolds were prepared. Aqueous slurries were prepared to investigate the effects of a variety of 3D printed templates on the freeze casting process. Slurries were prepared with 15 vol.% HA powders, 1 wt.% PEG and 1 wt.% PVA as a polymeric binders and 1 wt.% Darvan 811 as an anionic dispersant. All prepared slurries were identical in composition.

6.1.1 Sample Preparation

To induce macro-porosity in freeze cast scaffolds, templates were 3D printed using a ProJet 3510 HD printer (3D Systems, Rock Hill, SC, USA). Templates were fabricated out of a ProJet VisiJet M3-X polymer (similar in properties to extruded ABS plastic [219]). These templates were designed with an array of high aspect ratio pins as well as a support structure (solid models shown in Figure 46). This support structure consists of longitudinal beams as well as transverse brackets and were necessary to ensure stability of the pins during the printing and freezing processes. Templates were created with pins of with a round cross-section and diameters of 600 μm, 700 μm and 800 μm. Templates were printed together, connected with sacrificial material, so as to limit manufacturing time.

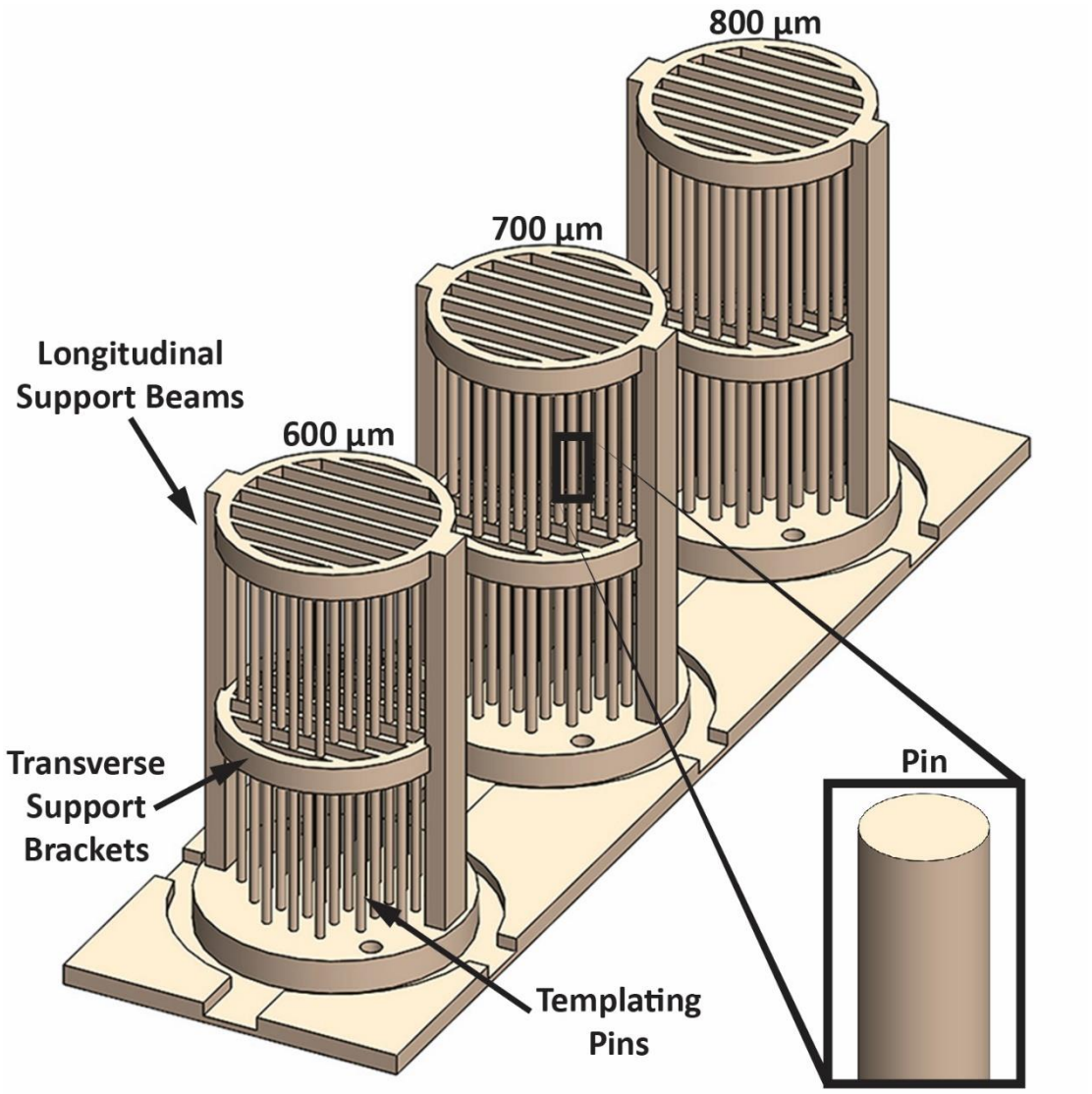

Figure 46. Solid models of the 3D printed templates, highlighting the templating pins, longitudinal support beams and transverse support brackets. Templates with 600 µm, 700 µm and 800 µm diameter pins were connected with sacrificial material so as to be printed together. The inset shows the circular cross-section of each of the pins.

During the freeze casting process a 3D printed template was suspended upside down in the slurry, as shown in Figure 47. In each case, a set of four samples were prepared with a control sample (no template) and templates with pins of diameter 600 µm, 700 µm and 800 µm. During this sintering process of the freeze casting procedure, the polymeric 3D printed template was completely burned out, leaving macro-porosity in its wake.

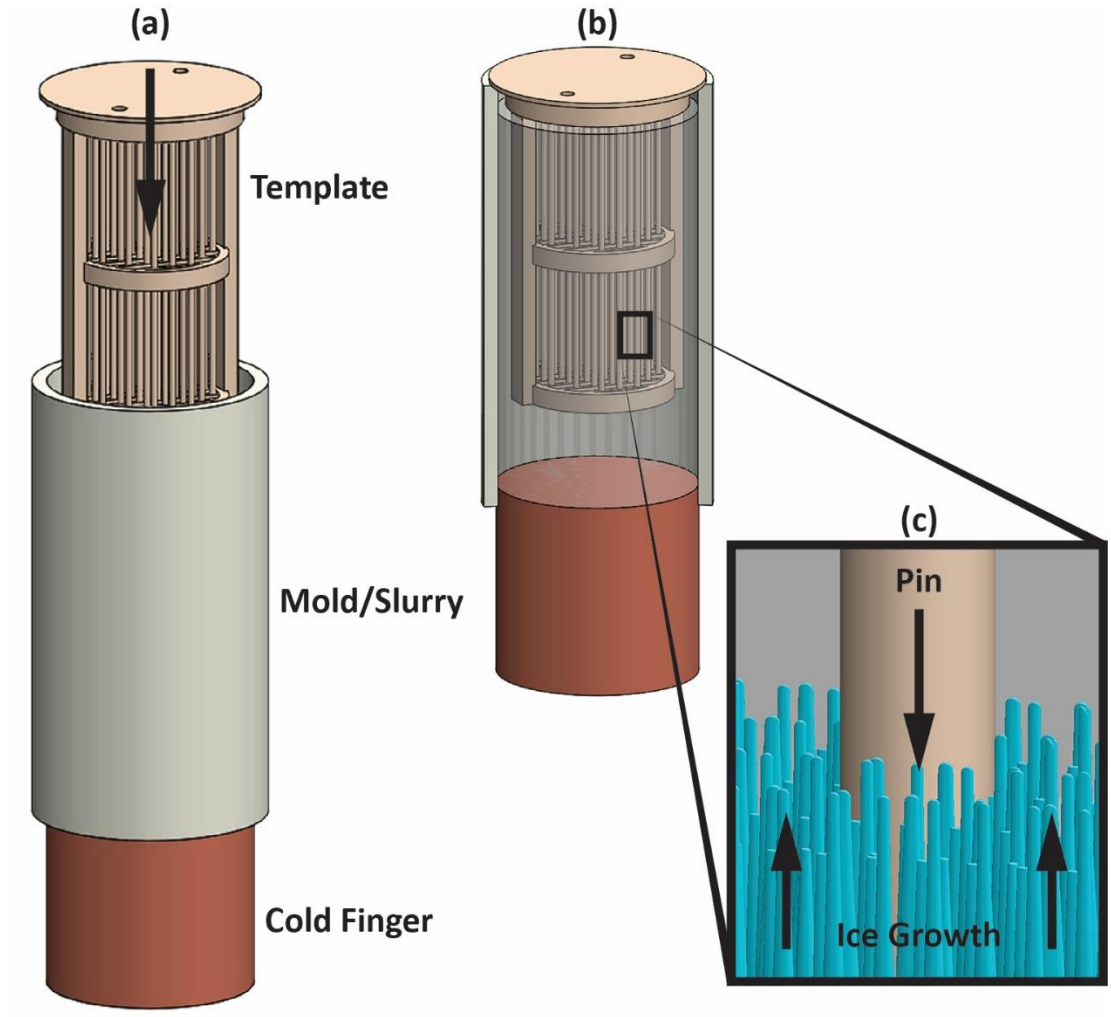

Figure 47. Methodology for templated freeze casting. **(a)** A 3D printed template was placed within a mold and immersed in slurry, which is affixed on top of a cold finger to provide directional freezing; **(b)** The template was suspended above the cold finger but fully immersed within the slurry; **(c)** During freezing, the template deflects ice growth, allowing for two length scales of porosity after sintering.

6.1.2 Cell Culture

To test the cell viability, preliminary cell culture tests were performed. Scaffolds were sterilized by steam sterilization with gravity cycles. Each scaffold was seeded with 1 x 10^5 osteoblast-like MG63 cells. A culturing solution of dulbecco's modified eagle medium (DMEM, Sigma Aldrich, St. Louis, MO, USA) with 10% fetal bovie serum and 1% penicillinestreptomycin was used. Cells were cultured in a humidified incubator with

5% CO_2 at 37 °C for 24 h. After culturing, cells were fixed using 4% paragormaldehyde for 30 min and washed with PBS three times. Cells were stained using DAPI (to stain the nuclei blue) and F-actin (to stain the actin filaments red) and imaged using confocal microscopy.

6.2 Results and Discussion

Micrographs of the templated freeze cast microstructures are shown in Figure 48. These show a clear differentiation between the larger macro-porosity, created by the 3D printed template and the small micro-porosity, created by the growth of ice crystals (as shown in Figure 47c). Measurements of both micro- and macro-pores are shown in Table 5. The micro-porosity produces similar values regardless of the presence or size of the template, in all cases producing pores of $A_p \approx 2200$ μm^2 and $X_p \approx 6$. The dimensions of these pores are comparable to previous reports on freeze casting with a similar concentration of hydroxyapatite solid loading and a H_2O freezing agent [44, 220].

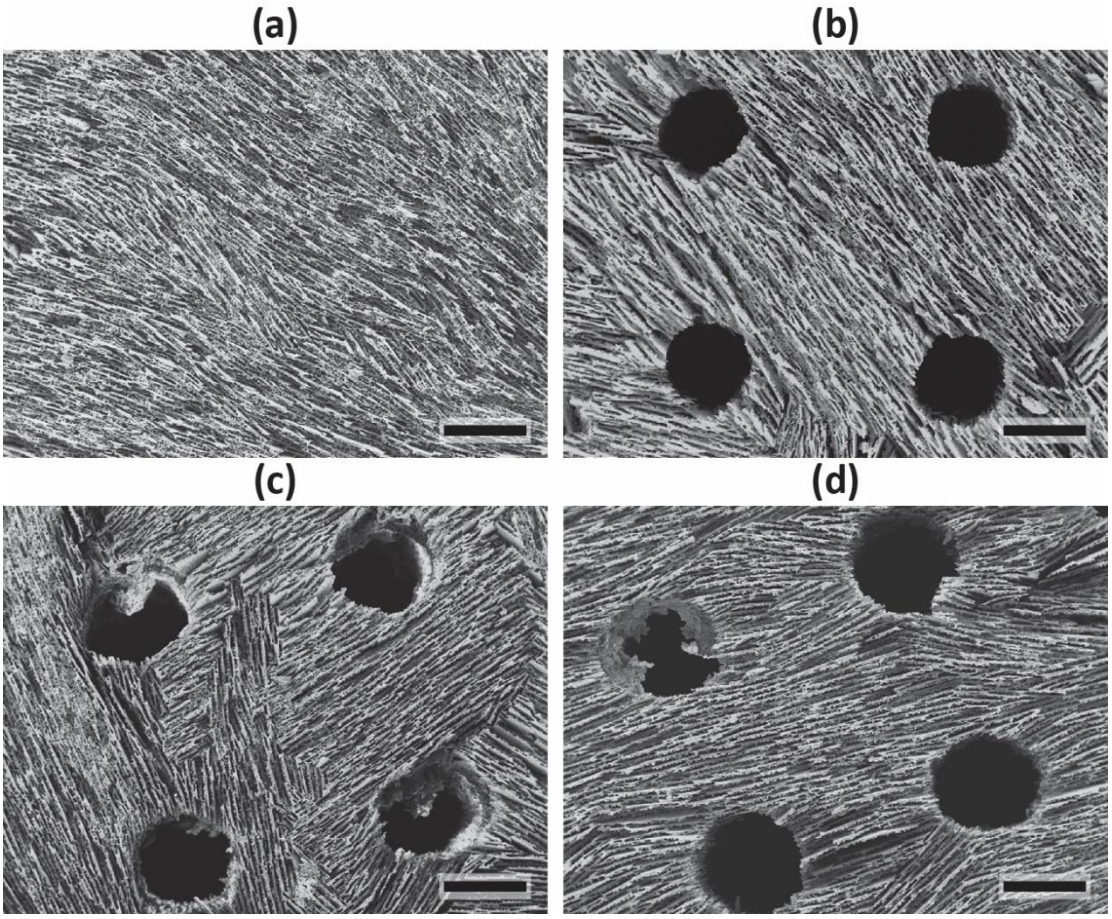

Figure 48. Micrographs of scaffolds extrinsically templated with round pins. **(a)** Control sample with no template; **(b)** 600 μm pins; **(c)** 700 μm pins; **(d)** 800 μm pins. Scale bars: 500 μm.

Table 5. Pore measurements for both micro- and macro-porosity. Results are shown as the average ± standard deviation for 40 measured pores in the case of micro-porosity and 20 measured pores in the case of macro-porosity.

		Control	600 µm	700 µm	800 µm
Micro-Porosity	***a* (µm)**	124.9 ± 38.7	135.2 ± 42.1	144.0 ± 44.9	118.5 ± 37.9
	***b* (µm)**	20.5 ± 4.4	21.8 ± 5.0	19.3 ± 4.2	23.6 ± 8.0
	A_p (µm^2)	2058 ± 903	2354 ± 960	2211 ± 973	2266 ± 1208
	X_p	6.24 ± 1.90	6.39 ± 2.14	7.72 ± 2.46	5.38 ± 2.00
Macro-Porosity	***a* (µm)**		585.6 ± 36.5	688.8 ± 29.8	748.5 ± 30.6
	***b* (µm)**		512.1 ± 30.8	573.4 ± 32.5	659.7 ± 34.9
	A_p (µm^2)		235551 ± 20161	310476 ± 26200	387695 ± 23947
	X_p		1.15 ± 0.10	1.20 ± 0.07	1.14 ± 0.08
	D_{eff} (µm)		548.9 ± 23.8	631.1 ± 26.1	704.1 ± 21.4

Dimensions of the macro-porosity are plotted in Figure 49. In most cases the circular cross-section has been slightly distorted in to an ellipse resulting in values of X_p = 1.14 - 1.20. This is most likely the result of the sintering process where the templating pin was incinerated. Given this distortion, to make comparisons between the initial template and the final macro-porosity, an effective diameter, D_{eff}, was calculated as $D_{eff} = (a + b)/2$. This is listed in Table 5 and plotted along with the measured values of a and b in Figure 49a. When comparing this to the ideal pore (i.e. with the exact diameter of the initial template) the final macro-porosity D_{eff} is only reduced by 10% in all cases. Similarly, A_p only experiences a reduction of 20% compared to the ideal pore (Figure 49b). As a result, this method is capable of consistently providing pores similar in size to the initial template.

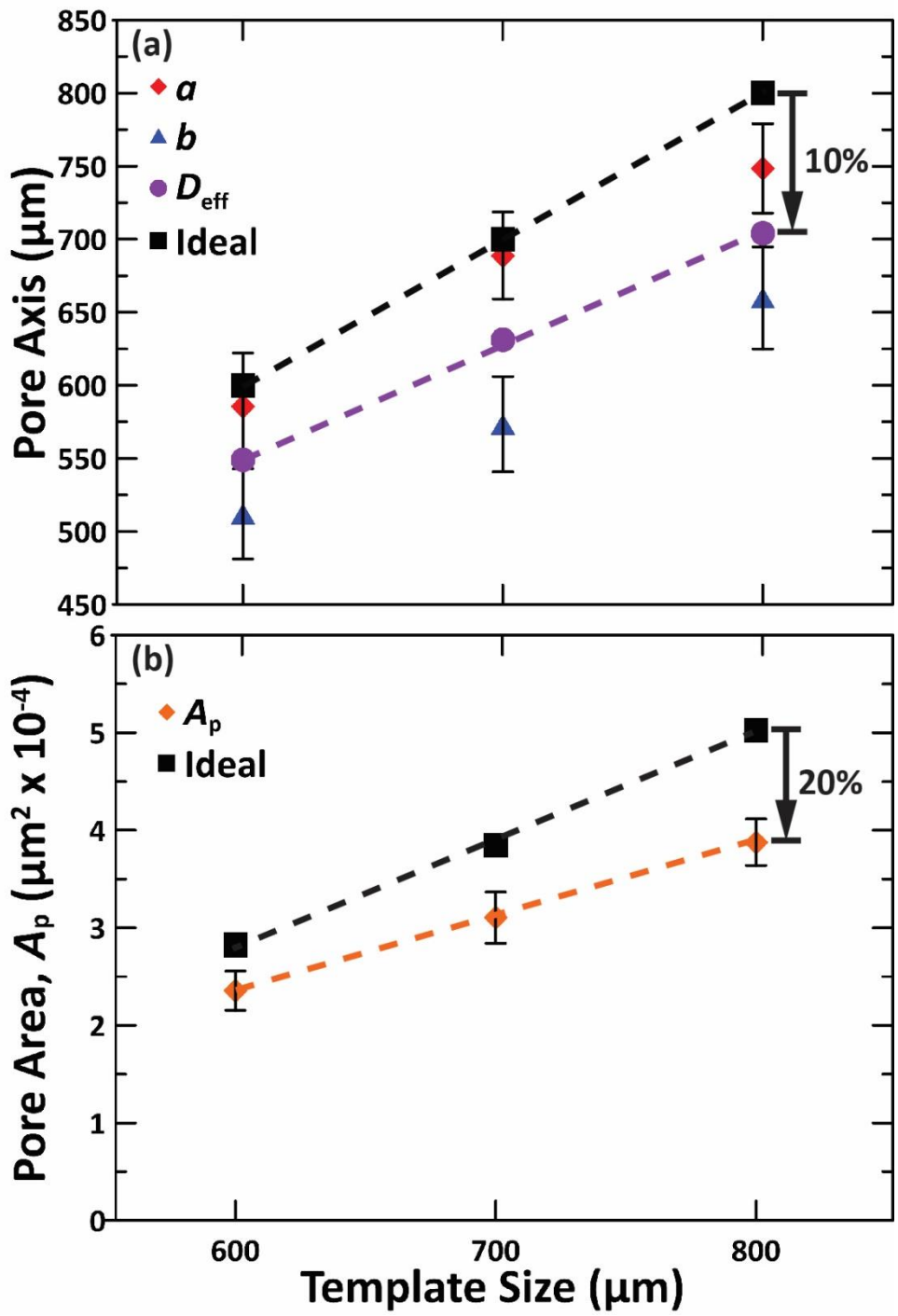

Figure 49. Dimensions for macro-porosity as a function of the initial template size. It can be seen for **(a)** the pore axes and **(b)** the pore cross-sectional area, 90% and 80% of the ideal measurements (taken from the initial 3D printed pins), respectively, were maintained in the final freeze cast scaffold.

In addition to control of the macro-porosity size of the within the final scaffold, the use of a 3D printed template allows for interpenetration between micro- and macro-porosity within the final scaffolds (Figure 50). The low thermal conductivity of the template (~0.15 W/m K) combined with the lack of contact between the template and the cold finger (as seen in Figure 47b) result in a negligible temperature gradient between the solidifying slurry and the template during the freeze casting process. As a result, ice crystals do not nucleate from the template itself and all ice growth within the slurry is maintained in a single direction, progressing from the cold finger to the top of the slurry. It has previously been shown for freeze cast scaffolds that the nucleation point of ice within the slurry results in denser material that transitions to a more porous and lamellar structure [28, 43]. No such gradient in porosity is observed in any of the current scaffolds (as is shown in Figure 48). When observing the interface between micro- and macro-porosity it can be seen that the micro-porosity runs directly into the macro-porosity, resulting a continuous system of porosity at multiple length scales (Figure 50b). This could be beneficial for infiltration of fluids within these scaffolds for the fabrication of composites or for their use as filters.

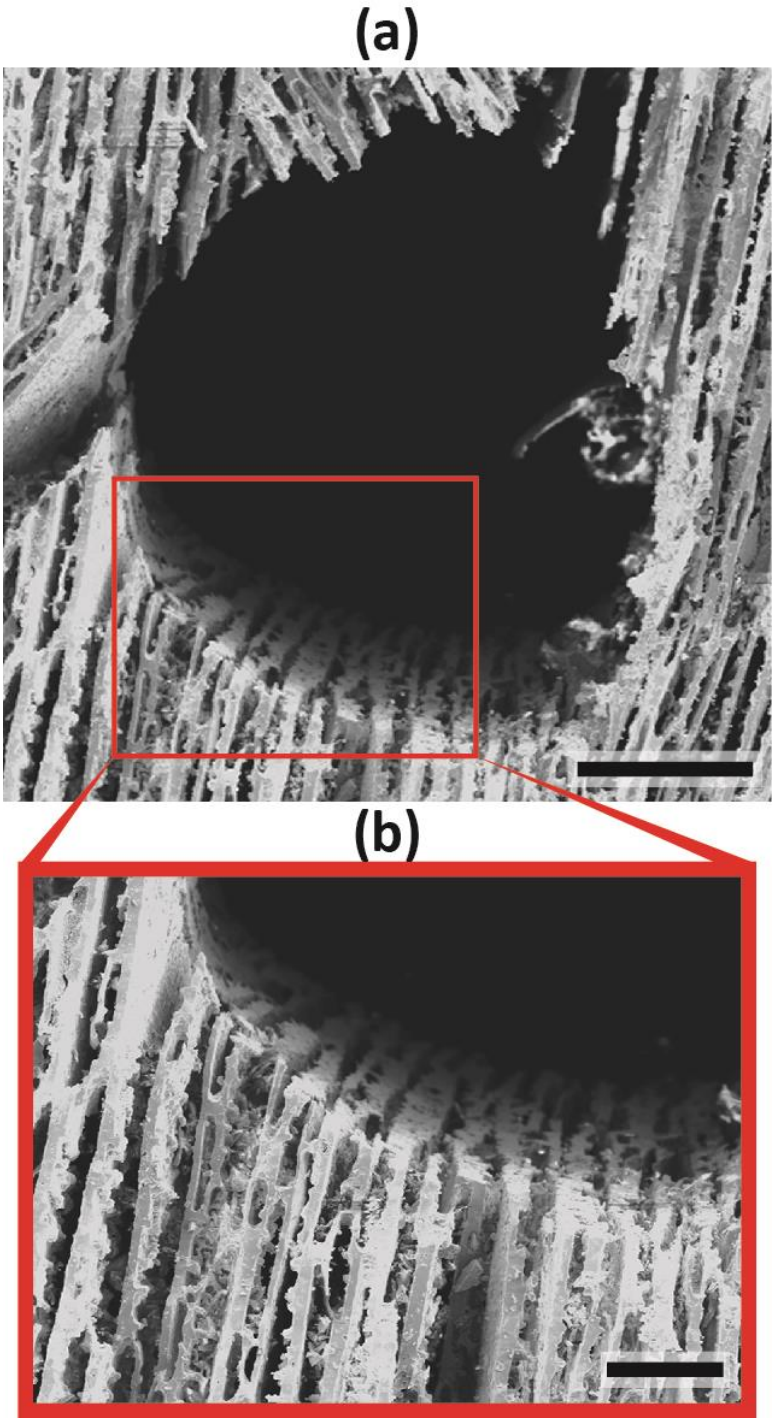

Figure 50. (a) Interface between macro- and micro-porosity; **(b)** When observing the interior wall at increased magnification it can be seen that the micro-porosity runs directly into the macro-porosity, creating a system of interpenetrating porosity. Scale bars: **(a)** 200 μm, **(b)** 100 μm.

Preliminary cell culture testing, after 24 hours of growth, demonstrated that cells had adhered and aligned within the freeze cast porosity of the scaffolds (Figure 51). In addition, these tests demonstrated that the freeze cast structures were viable and non-toxic for osteoblast-like cells. Future testing will look to demonstrate cell proliferation and differentiation.

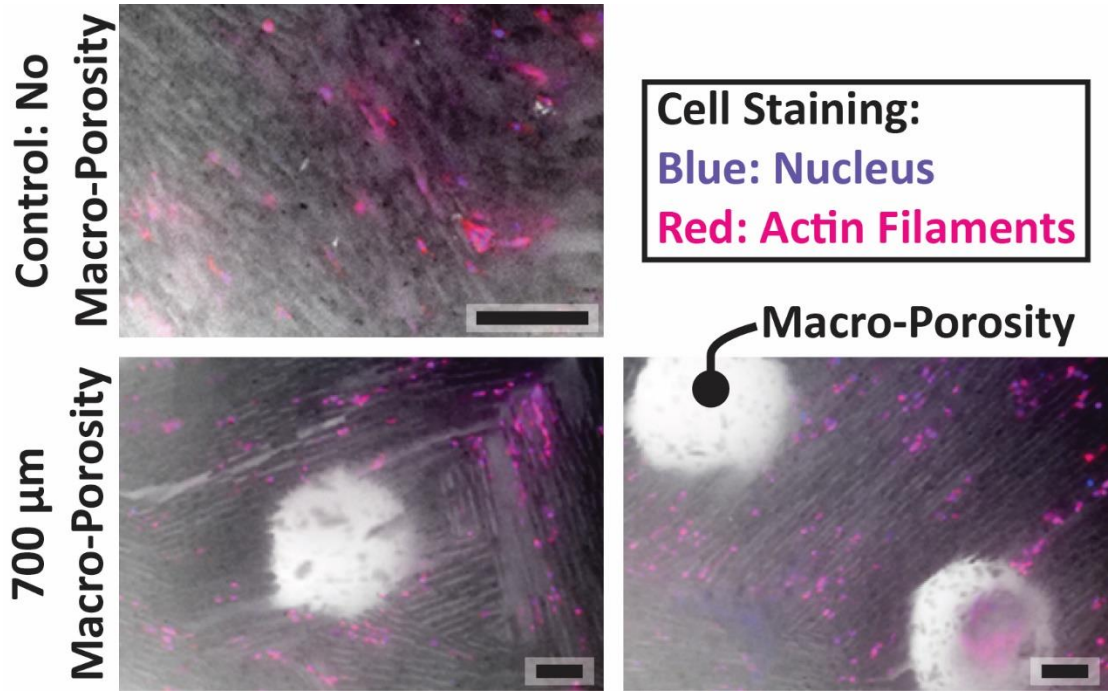

Figure 51. Preliminary cell culture results on a control scaffold and extrinsically templated scaffolds (using a 700 µm template). Results show that, after 24 hours, cells have survived and aligned within the freeze cast porosity. Scale bars: 200 µm.

Given that the fabrication of the macro-porosity in this technique is driven by the use of 3D printed templates, the shape is not limited to a circular cross-section. As proof of this concept, alternative square and star-shaped macro-porosity templates were prepared and freeze cast (Figure 52). The only change to the process was to the design of the templating array (as shown in Figure 46) so as to feature pins with square and star cross-sectional shapes. As with the circular macro-pores, there is some warping to the original

shape in each case. However, this level of control could provide an attractive method of creating microstructures with porosity tailored to specific experimental requirements.

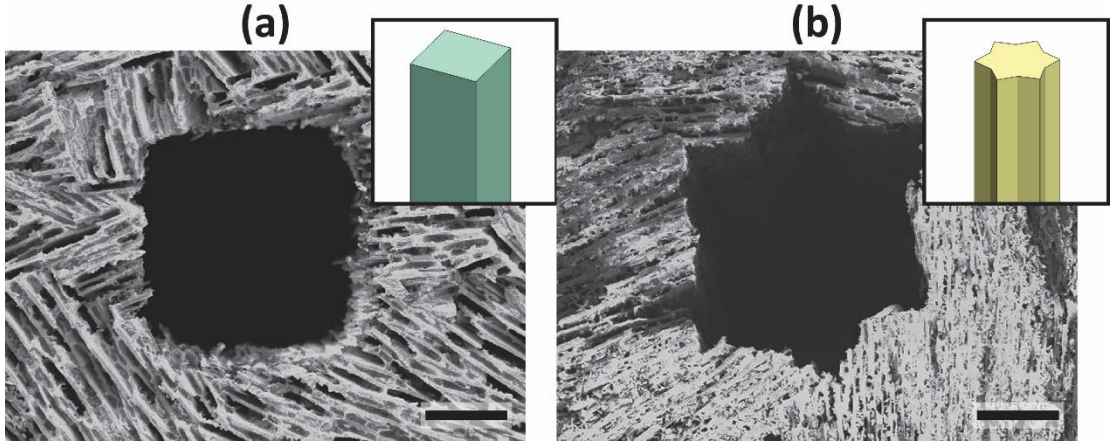

Figure 52. Alternative macro-pore shapes. **(a)** square; **(b)** star. The inset shows the cross-sections of the solid models of the pins that were used. Scale bars: 200 μm.

6.3 Conclusions

The current experimental study of HA freeze cast scaffolds, extrinsically controlled through the use of 3D printed templates for biomaterials enables the following conclusions:

- The use of 3D printed templates as a method of extrinsic control to the freeze casting process allows for the creation of porous structures at two length scales, similar to the hierarchical porosity in natural bone.
- The larger, macro-pores, are able to maintain 90% of the diameter and 80% of the cross-sectional area of the original template. In addition, the smaller, micro-porosity and macro-porosity are interpenetrating.
- Preliminary cell culture testing with osteoblast-like cells demonstrated that cells were able to survive and align within the freeze cast porosity after 24 hours.
- Due to the 3D printed nature of the extrinsic templates, many other macro-pore shapes and sizes are possible.

7. Reproducibility of ZrO_2-Based Freeze Casting for Biomaterials

The freeze casting process, as discussed here and in literature, has been greatly researched as an attractive method to fabricate bioinspired materials and composites [25-29, 50, 176, 188, 189, 221, 222]. Given that the constituents and mechanical properties can be tailored, a common prospective application for these scaffolds and composites is mimetic bone [39, 42-44, 221]. While this application shows great promise, any biomedical implant material will need to undergo rigorous certification and testing. Additionally, any commercial applications will require that numerous samples be made that are effectively, if not entirely, the same. In both cases, samples will need to be reproducibly created with similar mechanical and geometric properties. However, to the knowledge of the authors there has yet to be any statistical study on the reproducibility of this freeze casting method.

In this chapter the author investigates the reproducibility of freeze cast composite materials for bioinspired and biomimetic applications. This is done by focusing upon three sets of ZrO_2–epoxy freeze cast composite scaffolds, which were frozen with H_2O as a freezing agent and varied in solid loading concentration. While other base constituents or variations on the freeze casting process may produce differing results, the author proposes this work as a reference point for not only academic research, but also potential commercial applications.

7.1 Materials and Methods

Utilizing the methods described in chapter 1.6 freeze cast scaffold composites were prepared, tested and analyzed. Aqueous slurries were prepared to investigate the reproducibility of the freeze casting process. Three individual sample sets with varying solid loading were created by mixing 10, 15 and 20 vol.% ZrO_2 powders with 1 wt.% PEG

and 1 wt.% PVA as polymeric binders and 1 wt.% Darvan 811 as an anionic dispersant. For each solid loading concentration (10, 15 and 20 vol.% ZrO_2) eight identical solutions (H_2O, PVA, PEG and dispersant) were created. Slurries were freeze casting, freeze dried, sintered and infiltrated with a two-part epoxy (Epoxicure 2) to create two-phase scaffold composites. A total of eight scaffold composites were created for each solid loading concentration (10, 15 and 20 vol.% ZrO_2) for a total of 24 scaffolds. The final composite scaffolds were each cylindrical in shape with an approximate diameter and height of 17 mm and 40 mm respectively. However, to avoid the more dense and distorted structures that are known to occur at the bottom of the scaffolds [28, 214], ~10 mm was cut off and removed. For clarity, the samples created and tests (as described in the subsequent sections) are schematically visualized in Figure 53.

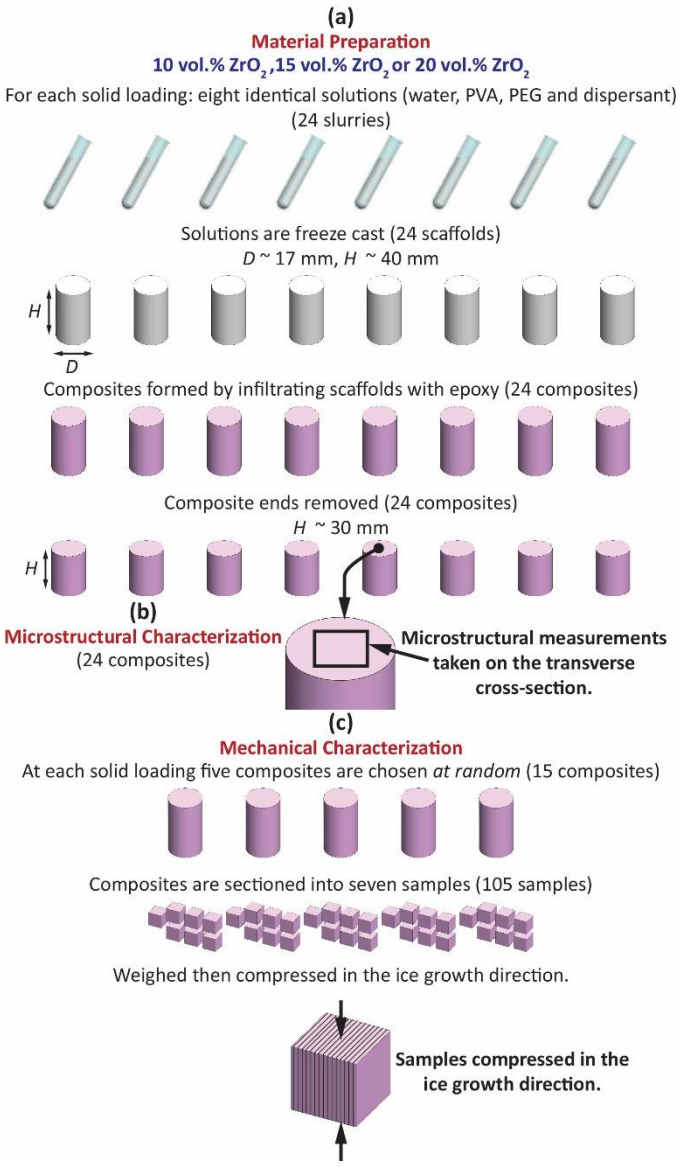

Figure 53. Schematic of the fabricated samples and performed tests for each solid loading (10, 15 and 20 vol.% ZrO_2). **(a)** For each solid loading, eight identical solutions (H_2O, PVA, PEG and dispersant) were created and freeze cast to form scaffolds with diameters and heights of ~17 and 40 mm respectively. Each scaffold was infiltrated with epoxy to form a composite and had the ends removed to result in a final height of ~30 mm; **(b)** microstructural characterization was performed by taking measurements from SEM analysis on the transverse cross-sections of each composite; **(c)** to perform mechanical characterization, at each solid loading five composites were selected at random and sectioned into seven samples, each 5 × 5 × 5 mm^3. These samples were weighed and compressed in the ice growth direction. Adapted with permission from [53].

The microstructure was investigated with SEM to determine the values of a, b, A_p, X_p and T_w of the porosity. These microstructural measurements were taken as they are amongst those most commonly utilized to describe the structure of freeze cast scaffolds in literature [36, 44, 212]. Volumetric and mechanical analysis of $N = 5$ samples from each scaffold composite were conducted to determine values of V_c, UCS and E.

7.1.1 Statistical Analysis

Measurements of a, b, A_p and X_p and the mechanical properties UCS and E were first analyzed using One-way ANOVA ($\boldsymbol{\alpha} = 0.05$). One-way ANOVA tests (Figure 54a) determine if the means of all individual composite scaffold measurements with the same solid loading concentration are equal through a comparison of the calculated mean square between composite scaffolds (MS_b) and the calculated mean square within an individual composite scaffold (MS_w) (e.g. are all of the composite scaffolds producing the same value of A_p?). This ratio of the between-groups mean square over within-groups mean square is called the F statistic [223]:

$$F = \frac{MS_b}{MS_w} \tag{48}$$

From the value of F and the chosen significance level ($\boldsymbol{\alpha} = 0.05$ for the tests in this study) a p-value, which indicates the probability of MS_b being greater than or equal to $F \times MS_w$, was determined. A value of $F = 1$ would denote that there is no significant difference between composite scaffold measurements. For $F > 1$, the greater the value of F, the more variability exists between composite scaffold measurements compared to within composite scaffold measurements. For example, for measurements of A_p in all eight composite

scaffolds with 15 vol.% ZrO_2 in this study, $F = 5.939$ and $p < 0.05$. This indicates that one or more of the composite scaffolds have values of A_p that vary significantly from the others.

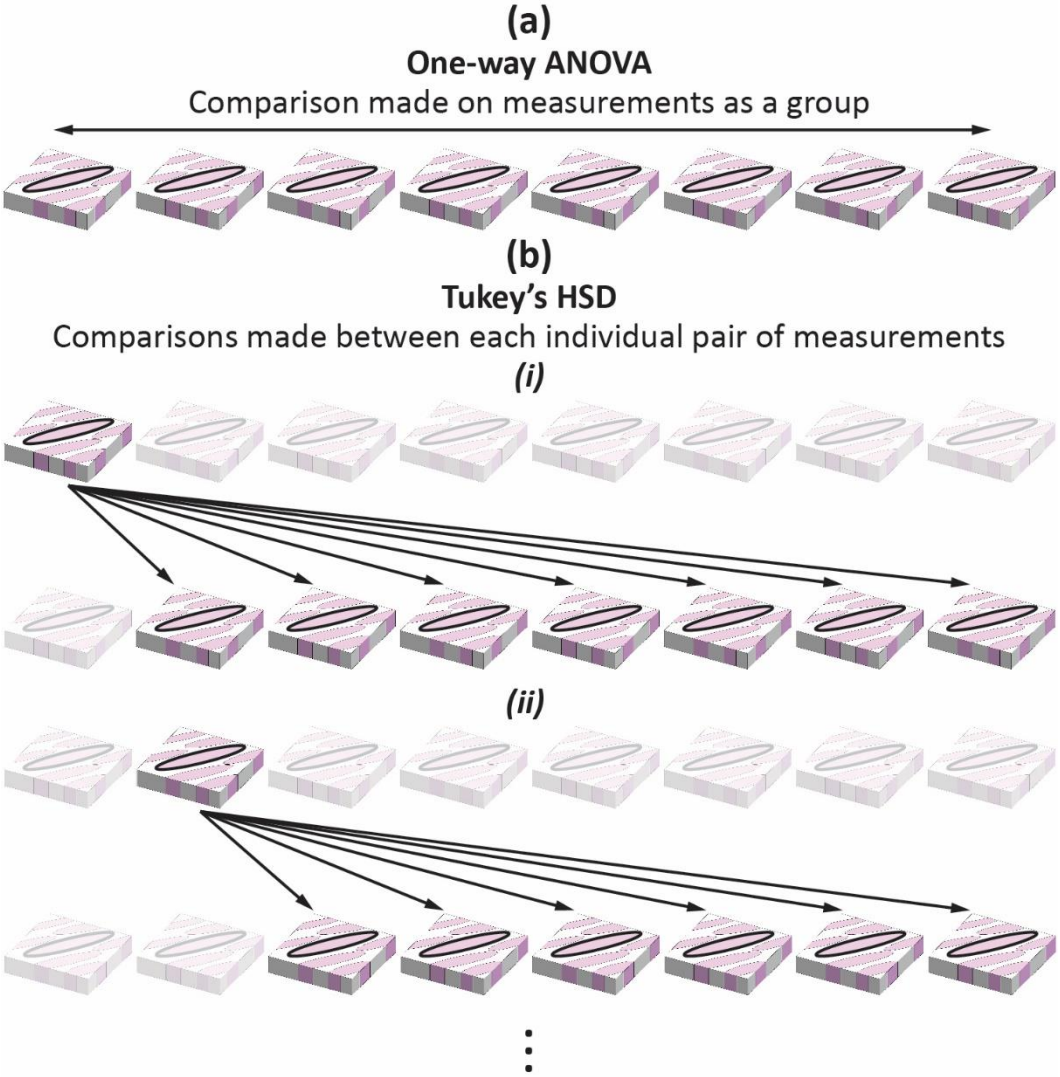

Figure 54. Schematic diagrams of the statistical analyses utilized to determine the statistical significance of the measurements in this study. In all cases, comparisons are made to determine if measurements show no statistically significant differences to $p < 0.05$ (represented here by arrows). The microstructural measurements of a, b, A_p, and X_p along with the volumetric and mechanical properties of V_c, E and UCS were all analyzed with this method. **(a)** One-way ANOVA looks to determine if all measurements are the same amongst a large group of samples but does not distinguish significance between samples; **(b)** Tukey's HSD determines if two individual, pairwise measurements within the group are the same. Tukey's HSD tests are repeated for every possible pair (e.g. (*i*), (*ii*)) of samples. Adapted with permission from [53].

In addition, post hoc Tukey honest significant difference (HSD) multiple comparison tests (Figure 54b) were used to investigate significant differences between composite scaffolds with the same solid loading concentration (e.g. is there a statistically significant difference between the measurements of A_p between two individual samples?). First, a critical value of the Tukey HSD Q statistic (Q_{crit}) is determined from the Studentized Range distribution ($\boldsymbol{\alpha} = 0.05$). Then, the Tukey HSD test statistic, $Q_{i,j}$, is calculated [223]:

$$Q_{i,j} = \frac{\left|\bar{x}_i - \bar{x}_j\right|}{\left(MS_w/n\right)^{1/2}} \quad 49)$$

where $\bar{x}_i$ and $\bar{x}_j$ are the mean measurement values for the two composite scaffolds being compared and n is the sample size of each measurement group (e.g. n = 40 for microstructural measurements and n = 7 for mechanical property measurements in this study). If $Q_{i,j} > Q_{crit}$, there is a statistically significant difference between the composite scaffolds for the given measurement. For example, when comparing measurements of A_p between these first two composite scaffolds with 15 vol.% ZrO_2 listed in Table 6, $Q_{i,j}$ = 3.594. This is less than the value of Q_{crit} = 4.316, therefore there is no significant variance in A_p between the two samples. These statistical tools have been previously employed to determine the significance of mechanical data in biomedical materials [224, 225]; additional information about these methods can be found in Tabachnick and Fidell [223].

Table 6. Values of pore major axis, *a*, pore minor axis, *b*, pore area, A_p, pore aspect ratio, X_p, and lamellar wall thickness, T_w, for all ZrO_2 scaffolds infiltrated with epoxy. Data reported as mean ± standard deviation of 40 measurements. Adapted with permission from [53].

Sample set	*a* (μm)	*b* (μm)	A_p (μm^2)	X_p	T_w (μm)
10 vol.%	71.4 ± 22.1	18.7 ± 4.6	1070 ± 496	3.98 ± 1.39	4.7 ± 1.7
ZrO_2	95.8 ± 31.8	11.9 ± 2.7	908 ± 416	8.32 ± 2.79	3.3 ± 1.1
	97.1 ± 34.3	15.5 ± 4.0	1178 ± 482	6.74 ± 3.07	3.3 ± 1.2
	84.9 ± 20.7	16.8 ± 4.4	1132 ± 386	5.32 ± 1.91	3.2 ± 1.4
	84.3 ± 20.9	16.0 ± 3.8	1071 ± 395	5.49 ± 1.69	3.0 ± 1.0
	78.1 ± 21.0	12.4 ± 2.9	760 ± 276	6.67 ± 2.25	2.2 ± 0.9
	88.0 ± 28.4	18.9 ± 4.9	1337 ± 594	4.91 ± 1.75	3.3 ± 1.5
	79.7 ± 26.1	15.8 ± 3.7	999 ± 428	5.31 ± 2.25	3.0 ± 0.9
Mean	*84.9 ± 8.7*	*15.8 ± 2.6*	*1057 ± 175*	*5.84 ± 1.34*	*3.2 ± 0.7*
15 vol.%	59.6 ± 26.4	15.4 ± 3.7	752 ± 474	3.94 ± 1.59	6.3 ± 2.0
ZrO_2	58.0 ± 25.3	11.9 ± 3.3	579 ± 398	4.92 ± 1.78	4.6 ± 1.4
	56.0 ± 27.1	10.8 ± 2.4	509 ± 333	5.08 ± 1.87	5.0 ± 2.0
	50.1 ± 16.5	11.4 ± 2.5	461 ± 203	4.49 ± 1.50	4.7 ± 1.6
	41.4 ± 20.2	10.1 ± 2.3	340 ± 208	4.17 ± 2.01	5.1 ± 1.6
	56.5 ± 19.5	12.5 ± 2.7	564 ± 259	4.66 ± 1.67	5.1 ± 1.6
	55.6 ± 19.2	10.9 ± 2.0	484 ± 223	5.20 ± 1.86	4.8 ± 2.0
	64.5 ± 24.4	10.8 ± 1.7	550 ± 223	6.10 ± 2.54	4.9 ± 1.9
Mean	*55.2 ± 6.9*	*11.7 ± 1.7*	*530 ± 118*	*4.82 ± 0.67*	*5.1 ± 0.5*
20 vol.%	55.7 ± 24.1	12.8 ± 3.3	591 ± 377	4.41 ± 1.58	7.5 ± 3.2
ZrO_2	68.8 ± 36.0	14.3 ± 2.7	785 ± 460	4.87 ± 2.34	8.1 ± 2.8
	55.9 ± 22.6	10.9 ± 2.6	489 ± 256	5.26 ± 2.06	7.5 ± 1.7
	49.6 ± 18.7	14.2 ± 3.1	571 ± 299	3.54 ± 1.17	8.3 ± 2.6
	50.8 ± 23.7	13.2 ± 3.1	546 ± 324	3.90 ± 1.65	7.1 ± 2.2
	55.1 ± 30.3	16.7 ± 3.2	754 ± 524	3.28 ± 1.55	9.2 ± 3.1
	55.2 ± 27.1	16.7 ± 3.2	747 ± 451	3.34 ± 1.59	8.8 ± 3.2
	60.5 ± 21.0	13.0 ± 3.3	650 ± 342	4.69 ± 1.33	8.1 ± 3.6
Mean	*56.4 ± 6.0*	*14.0 ± 2.0*	*641 ± 110*	*4.16 ± 0.75*	*8.1 ± 0.7*

7.2 Results and Discussion

Microstructural dimensions of the sets of composite scaffolds with 10, 15 and 20 vol.% ZrO_2 are listed in Table 6 and displayed in Figure 55 (all data points are plotted as mean ± one standard deviation). In addition, the global mean values for all composite

scaffolds at each solid loading concentration (e.g. values of A_p, commonly used to describe freeze cast scaffold porosity = 1057, 530 and 641 μm^2 for 10, 15 and 20 vol.% ZrO_2 respectively) were determined (Table 6). It is of note that the standard deviations are very large, in some cases up to half of the measured mean. All microstructural dimensions for each composite scaffold are roughly within one standard deviation of each other. In addition, the microstructures from each of the sets, as seen in the example micrographs shown in Figure 56, appear relatively similar. The ANOVA results showed that the microstructural dimensions (a, b, A_p, X_p) of each set had significant differences ($2.1 < F < 17.3$, $p < 0.05$), demonstrating that at each solid loading concentration, the composite scaffolds are not similar. This is of note given that, at each solid loading concentration, all eight composite scaffolds were prepared with the exact same processing techniques and conditions and therefore, theoretically, should produce the same microstructure. This suggests that the processing technique itself is the most likely source of this deviation within the composite scaffolds. This is mostly likely due to the process being dependent upon the growth of ice crystals that template the solid loading and create the pores. As this ice crystal growth is only controlled in a single direction, there is likely a large amount of variability in the exact pattern of the ice growth from sample to sample, thus resulting in the variation in resultant microstructure. Despite the significant potential of the process of freeze casting for biomedical applications, the current results suggest a complication in the mass production of these composite scaffolds for commercialization.

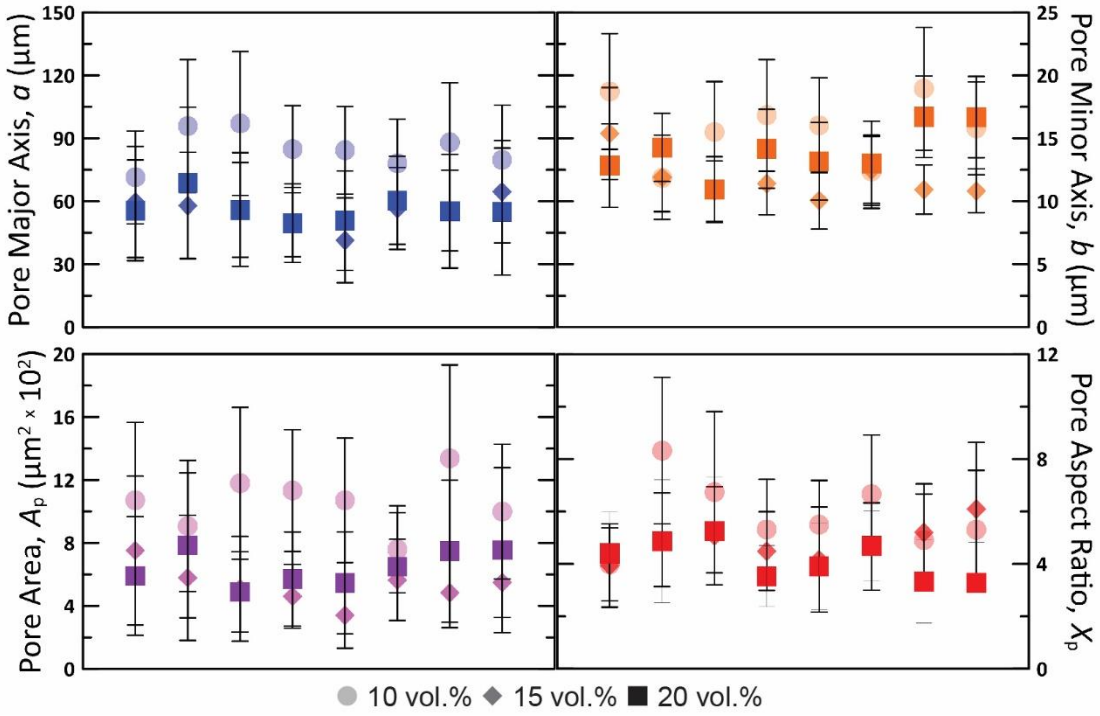

Figure 55. Microstructural measurements. In each case measurements for each of the eight composite scaffolds are plotted as mean ± one standard deviation of 40 measurements. Adapted with permission from [53].

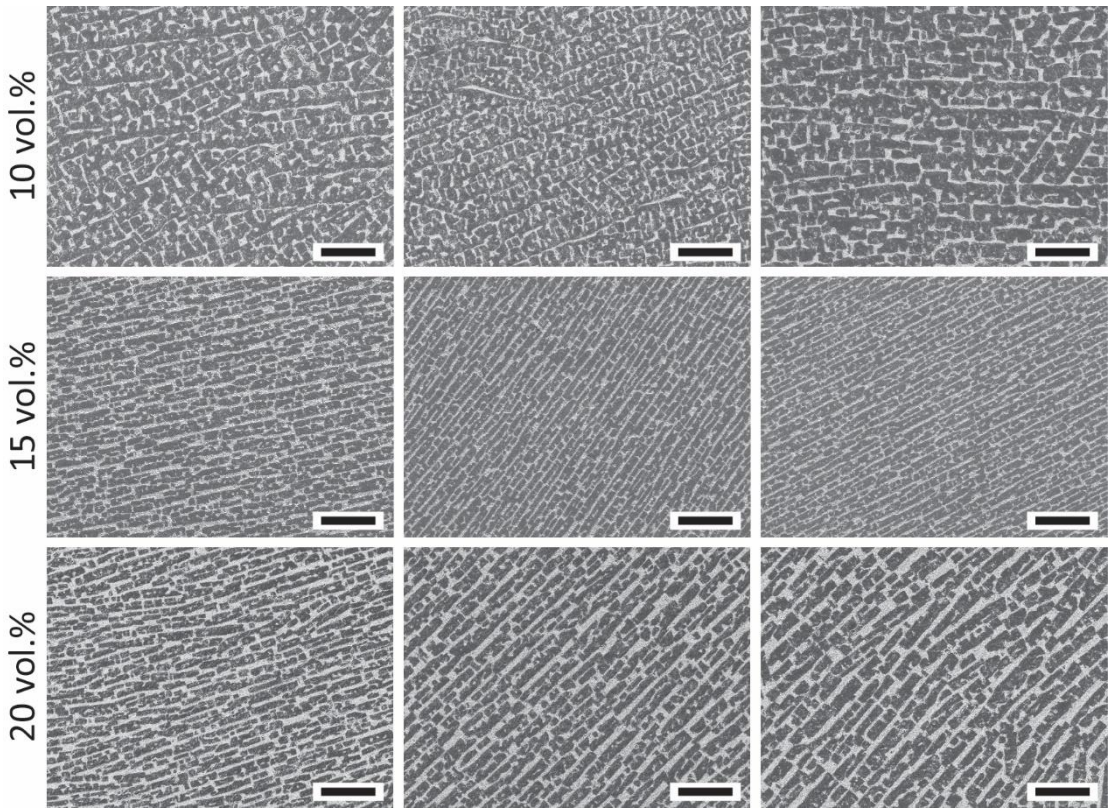

Figure 56. Three example micrographs for each set of composite scaffolds (10, 15 and 20 vol.% ZrO_2). Microstructures appear relatively similar at each solid loading concentration. Sintered ZrO_2 ceramic is light gray and epoxy polymer is dark gray. Scale bars: 100 μm. Adapted with permission from [53].

Although the ANOVA analysis showed that the composite scaffolds for each set had statistically significant differences, observing each pair of composite scaffolds in a set through Tukey's HSD test revealed more similarities in many cases (summarized in Table 7) This test observes the 28 possible pairwise comparisons within each composite scaffold set. Measurements of b and X_p, in general, displayed relatively high levels or variability with > 50% of pairs showing statistically significant variability in some cases. However, measurements of a and A_p at all solid loading concentrations resulted in ≤ 25% of pairs showing statistically significant variation. The more in-depth Tukey's HSD test highlights that the majority of microstructures were similar within the measurements of a and A_p. This

enforces the importance of performing this post-hoc test in order to better understand the statistical significance of results as, for some applications, specific measurements (such as A_p in cases where infiltration is important) may be of greater priority.

Table 7. Summary of results from the Tukey HSD tests. Results are presented as the % of significantly different pairwise comparisons for microstructural measurements (28 pairs) and mechanical properties (10 pairs). Adapted with permission from [53].

	Microstructural (%)				Mechanical Properties (%)	
Sample set	*a*	*b*	A_p	X_p	*UCS*	*E*
10 vol.% ZrO_2	11	61	25	67	20	20
15 vol.% ZrO_2	11	32	25	14	20	30
20 vol.% ZrO_2	7	54	4	32	40	*N/A*[a]

[a] ANOVA found no statistically significant differences in values of *E* between scaffolds with 20 vol.% ZrO_2. Therefore no Tukey HSD test was necessary.

Previous research has shown that changes in the microstructural measurements analyzed here can greatly alter the mechanical properties [36, 50, 188, 189]. *E*, *UCS* and V_c are listed in Table 8 and *E* and *UCS* are displayed in Figure 57 for all five composite scaffolds at each solid loading concentration. When compared to the experimentally determined properties of the infiltrating epoxy, the mean composite scaffold was able to provide at least modest gains. Each composite scaffold only consists of ~15 – 27 vol.% ZrO_2; however, the mechanical properties are considerably lower than what would be expected by a simple rule of mixtures, which predicts $UCS \approx 400 – 650$ MPa (using values of infiltrating epoxy and ZrO_2 monoliths from Table 8), which is considerably larger than the measured values of $UCS \approx 105 – 125$ MPa. This is likely due to internal porosity within the lamellar walls and the failure mode of Euler buckling of the lamellar walls, both of which have been previously reported to have a significant effect upon the mechanical properties of freeze cast scaffolds [36]. This would also explain the low values for *E*, as the porous walls would be unable to provide their ideal (dense) elastic strength. This could

be improved by altering the sintering conditions, such as increasing the temperature or adding a sintering aid, both of which would increase the density of the lamellar walls.

Table 8. Values of ultimate compressive strength, *UCS*, Young's modulus, *E*, and ceramic volume percent, V_c, for all samples. In addition, experimentally determined mechanical properties for the infiltrating epoxy are included. Data reported as mean ± standard deviation of seven measurements. Adapted with permission from [53].

Sample set	*UCS* (MPa)	*E* (GPa)	V_c (vol.% ZrO_2)
10 vol.% ZrO_2	103.5 ± 16.7	2.59 ± 0.58	13.8 ± 1.1
	112.5 ± 15.0	3.17 ± 0.67	13.6 ± 1.2
	107.9 ± 7.5	2.66 ± 0.39	12.7 ± 0.5
	92.9 ± 12.6	1.93 ± 0.39	14.5 ± 1.3
	113.7 ± 8.9	2.68 ± 0.16	15.8 ± 0.4
Mean	*106.1 ± 14.1*	*2.61 ± 0.60*	*14.1 ± 1.4*
15 vol.% ZrO_2	150.6 ± 25.8	4.25 ± 1.02	27.1 ± 0.4
	107.5 ± 42.4	1.80 ± 1.03	26.2 ± 1.7
	130.6 ± 17.1	2.40 ± 0.97	28.2 ± 0.5
	136.0 ± 20.0	3.16 ± 0.80	24.1 ± 1.1
	99.7 ± 26.1	2.60 ± 0.88	28.4 ± 1.6
Mean	*124.9 ± 32.2*	*2.84 ± 1.22*	*26.8 ± 1.9*
20 vol.% ZrO_2	140.7 ± 17.9	2.98 ± 0.70	27.4 ± 0.7
	134.8 ± 21.6	3.26 ± 0.74	27.2 ± 0.6
	124.3 ± 10.8	2.12 ± 0.43	28.8 ± 0.7
	92.3 ± 14.5	2.70 ± 0.81	23.0 ± 1.0
	133.5 ± 21.3	3.12 ± 1.05	28.0 ± 1.8
Mean	*125.1 ± 24.1*	*2.84 ± 0.83*	*26.9 ± 2.3*
Infiltrating epoxy	79.9 ± 4.0	1.80 ± 0.35	
ZrO_2 monoliths [208, 226]	2200 ± 522	205 ± 5	

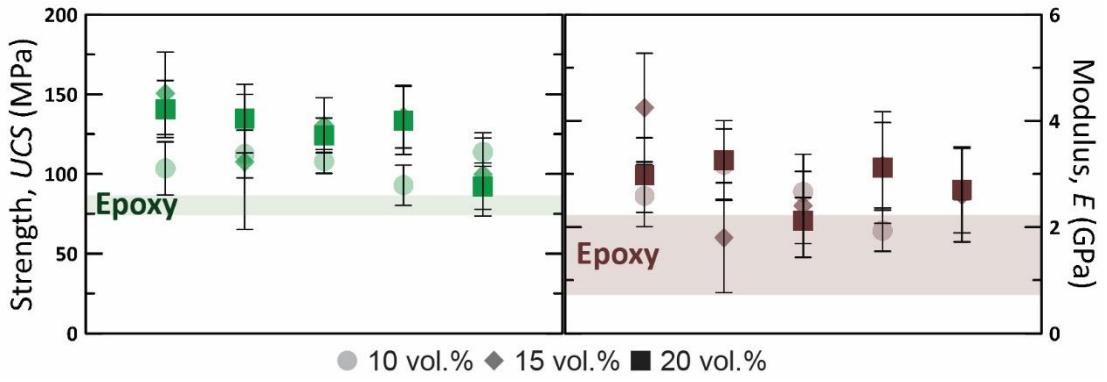

Figure 57. Mechanical properties. In each case measurements for each of the five composite scaffolds are plotted as mean ± one standard deviation of seven measurements. Bands are shown that represent the mean ± one standard deviation of experimentally determined mechanical properties for the infiltrating epoxy. Adapted with permission from [53].

When observed visually in Figure 57, mechanical properties within each solid loading are generally always within one standard deviation of each other. However, ANOVA analysis showed that the measurements of *E* and *UCS* for composite scaffold sets, regardless of solid loading concentration, had significant differences ($3.1 < F < 8.3$, $p < 0.05$), with the exception of values of *E* for 20 vol.% ZrO_2. However, as observed for the microstructures, Tukey's HSD tests revealed that relatively few of the 10 possible pairwise comparisons, only 20% and 30% of pairs for *E* in scaffold composites with 10 and 15 vol.% ZrO_2, respectively and 20%, 20% and 40% of pairs for *UCS* in scaffold composites with 10, 15 and 20 vol.% ZrO_2, respectively, showed statistically significant differences (Table 7). While these results support previous reports that changes in the microstructure can be connected to variability in the mechanical properties, the majority of composite scaffolds were able to produce comparable mechanical properties or, as was the case for the moduli of scaffolds with 20 vol.% ZrO_2, mechanical properties that showed no statistical differences.

It is the explicit intent of this work to observe the reproducibility of ZrO_2-based freeze casting with a consistent set of processing parameters. However, as the three composite scaffold sets within this work vary through only one parameter (the solid loading concentration) it can also be noted that this processing method may not be able to consistently produce variation of the mechanical properties. Previous results on freeze cast scaffolds show an increasing trend in pore size with decreasing initial solid loading concentration [44, 227]. However, there is known to be significant scatter in data linking initial solid loading concentration to final pore size due to numerous effects during freeze casting such as the size distribution and morphology of the particles [44, 227]. Regardless, it would be logical to suggest that composite scaffolds with more solid loading would produce higher mechanical properties. This is seen when observing the difference between 10 and 15 vol.%, however, as can be seen in Figure 57 as well as Table 8, the mean mechanical properties and V_c between scaffold composites with 15 and 20 vol.% ZrO_2 are effectively the same. The only parameter to vary consistently is T_w, which increases with increased solid loading concentration (Table 6). It has been previously reported in freeze cast scaffolds with hydroxyapatite that increasing the solid loading concentration makes it more difficult for a freezing front moving through the slurry to repel the solid particles [44], which would lower the freezing front velocity, v. The freezing front dendritic ice wavelength, $\lambda = b + T_w$ is proportional to $1/v$. The current data shows that the mean λ increases from 16.8 to 22.1 μm between 15 and 20 vol.% (Table 6). A decrease in v due to higher solid loading increases λ, which results in the enlarged pores observed for 20 vol.% ZrO_2. This is proposed to be the cause of the relatively similar mechanical results between 15 and 20 vol.% ZrO_2.When considering V_c, it is well known that there is a structural

gradient within freeze cast scaffolds with more dense material (which would hold a higher concentration of solid loading particles) at the initial ice nucleation front giving way to lamellar ice growth (associated with the lamellar wall microstructures observed here) further through the scaffold [49]. To avoid this dense structure, all samples for microstructural and mechanical testing have been taken far from the surface where the ice originally nucleated. However, it has been reported that a slower v (as is proposed to be present in 20 vol.% ZrO_2) results in a smaller structural gradient throughout the scaffold [49], which would result in a relatively larger volume of dense material near the initial ice nucleation front. This would result in a lower proportion of solid loading within the observed lamellar region of the scaffolds and is proposed to be the cause of the lower than expected V_c results at 20 vol.% ZrO_2. However, to the knowledge of the author, there are no kinetic models for the growth of ice interacting with solid particles that take into account the concentration of particles. This highlights an area of research into freeze casting that must be further investigated in order to improve the reproducibility of the process.

The current results prove the variability of the freeze casting process. Of note individual pairings (i.e. individual values of *UCS* for samples of 15 and 20 vol.% ZrO_2) of the samples show the expected trends (e.g. decreased A_p, increased *UCS* with increasing solid loading concentration). However, the variability between composite scaffolds results in pairings that show the opposite trends as well.

The process of freeze casting holds significant potential for biomedical and structural applications, but the current results highlight that reproducibility of scaffolds and composite scaffolds will likely stand as an impediment to mass-production or commercialization. However, while predominantly not statistically reproducible, the

microstructures and properties created through the freeze casting process in this study did show a great deal of similarity (as determined through Tukey's HSD tests). This provides hope that additional research and refinement of the freeze casting method may be able to provide reproducible materials. There are a number of simple alterations to the process that could improve the reproducibility. To ensure homogeneity between slurries they could be produced in a single batch as opposed to individually. During freezing, heterogeneous ice nucleation can be reduced by controlling the temperature to provide a more uniform freezing front, using a larger mold to avoid edge effects and smoothing the mold walls. In addition, one of the largest contributors is likely to be that the process is generally only controlled in a single direction. As the slurry is directionally frozen in the principal step of freeze casting, the direction of ice growth is the only true control of the process. The recent example of magnetic freeze casting [2, 103, 217] provides control of the microstructure in multiple orthogonal directions through both the ice crystal growth and an applied magnetic field (oriented perpendicular to the ice growth during the freezing process). Additionally, scaffolds with a centrosymmetric structure have been reported that employ two cold sources oriented at perpendicular directions, thus inducing two ice growth directions [52]. Additional research into methods such as these that provide control in multiple directions may provide more reproducible microstructures and properties.

7.3 Conclusions

The current experimental study of the reproducibility of epoxy infiltrated, freeze cast ZrO_2 composite scaffolds enables the following conclusions:

- Based upon a One-way ANOVA test, statistically significant variability between scaffolds was determined in all microstructural dimensions regardless of the solid

loading concentration (a, b, A_p and X_p). As a result, the scaffolds within this study cannot be said to be the same. Post-processing through Tukey's HSD tests revealed that, regardless of solid loading concentration, the majority of scaffolds produced similar measurements of a and A_p, as $\leq 25\%$ of pairs showed statistically significant variability.

- Mechanical properties (Young's modulus, E, and ultimate compressive strength, UCS) showed statistically significant variability between samples in almost all cases in a One-way ANOVA test. The sole exception came when observing scaffold composites with 20 vol.% ZrO_2 where no significant differences were found within values for E between scaffold samples. Post-processing through Tukey's HSD tests revealed that in all cases, the majority of pairs for E and UCS showed no statistically significant variability.
- While not similar overall, results from Tukey's HSD tests revealed that many of the composite scaffolds fabricated in this study were similar in specific microstructural and mechanical properties.
- Freeze casting holds significant potential for biomedical applications, but more research is required to ensure reliable production of similar scaffold microstructures and mechanical properties.

Chapter 7, in part, is a reprint of the material as it appears in "Reproducibility of ZrO2-based freeze casting for biomaterials" Materials Science and Engineering C, vol. 61, pp 105-112, 2016. The dissertation author was the primary investigator and author on this paper. This paper was co-authored by Kate C. Fickas, Yajur N. Maker, Marc A. Meyers and Joanna McKittrick.

8. Recommendations for Future Work

This dissertation encapsulates a significant amount of work and research. However, as is always the case in science, there is much future work to do. This chapter provides the author's ideas and concepts of fruitful future directions this work can take, touching first on intrinsic control with hydrophobic hydration and clathrate hydrates, then on extrinsic control with 3D printed templates. Finally, in a more general sense, the author will provide his thoughts on the state of bioinspired freeze casting as a whole and what he considers to be the most beneficial future area of research within the field.

The work into intrinsic freeze casting with monofunctional alcohols as additives to the slurry is generally complete. However, the work as a whole provides a critical insight into control of the freeze casting process that can promote future studies. The bulk of research in the freeze casting community focuses upon the dynamics occurring within either the frozen slurry or at the liquid-solid interface (the freezing front). This work, specifically with respect to the effect of hydrophobic hydration, highlights that the properties and dynamics of the liquid slurry prior to freezing should be considered when attempting to control the final microstructures of freeze casting. While the current work focused upon one group of additives in monofunctional alcohols, there are many other materials (most non-electrolytes in fact [199]) that also form hydrates. Perhaps the most interesting of these to study in the future would be the polymeric binders (PEG and PVA) that are added to all of the freeze cast slurries described here and many reported elsewhere in literature. Alterations to the polymer's molecular weight and therefore the slurry viscosity have been shown to have some control over the final microstructure [36]. However, the potential effect of hydrophobic hydration caused by the presence of

polymeric binders on the freeze casting process has never been considered. This could be an especially intriguing area of research given that the polymeric binder is expected to become incorporated into the lamellar walls during the freeze casting process and therefore may bring the water molecules that associate to it (through its hydrate) into the wall as well, resulting in internal wall porosity.

The work included in this dissertation on extrinsic control of freeze casting has many avenues that could be further explored, with the current work acting more as a proof of concept. Given this, the resultant microstructures that were formed featured only circular (by cross-section) and parallel macro-porosity at three sequential diameters (600, 700 and 800 μm) so as to provide a well-controlled experiment. However, to the knowledge of the author, this is the first instance of mechanical templates used in the freeze casting process to exert extrinsic control and therefore there is a multitude of work that could be inspired by it. As shown in Chapter 6, the use of 3D printing in the fabrication of the extrinsic templates allows for other macro-porosity cross-sections to be created, with square and star-shaped pores given as examples. Not only could the cross-section be controlled in different ways, but the through-thickness orientation could be altered as well from the current system of parallel and straight pins. This could be utilized to maximize the internal surface area for filtration or catalysis. In addition, the current templating pins are made of a polymer with low thermal conductivity so as to negate ice growth nucleation from the pins and create a final system of interpenetrating micro- and macro-porosity, a beneficial effect for the currently proposed application of cell culture. However, templating pin materials with higher thermal conductivity could be used that would result in dense regions

around the macro-porosity, potentially similar to the reinforced tubule structures found in materials such as tooth dentin [12].

In a more general sense, the greatest source of future work into the use of bioinspired freeze casting should be improvement on the technique's inherent variability. As detailed in Chapter 7, the most basic form of freeze casting cannot be considered to be reproducible, as samples made with the exact same processing conditions resulted in statistically significant variability in the final microstructural and mechanical properties. For the technique of freeze casting to ever be translated to commercial applications and realize its full potential as a structural and biomedical material, this must be overcome. The majority of research into the control of freeze casting to this point has been into either the basic process itself or into intrinsic control, which is generally only capable of altering the structure at the smaller scale of the pores. The author proposes that more research should be conducted into the extrinsic control of freeze casting, where control can be asserted across the entire microstructure. This could be realized through the use of external forces such as magnetic fields, the study of which is already ongoing. It is the belief of the author that these extrinsic control methods will be the avenue to truly reproducible freeze cast materials and final commercialization of this powerful technique.

9. Conclusions

For hundreds of millions of years the process of evolution has designed and shaped the organisms and structures of the natural world. Through this, amazing creatures have managed to inhabit and thrive in every corner of our world, from the inky darkness of the deepest ocean to the frozen peak of the highest mountain. This provides not only incredible biodiversity, but a treasure trove of scientific knowledge to be tapped. As materials scientists and engineers, this can be done through bioinspiration, where the fundamental science behind the success of nature's creatures is employed to advanced fabrication techniques to create novel designs and structures to benefit society.

The system of eight structural design elements presented here allows for classification and characterization of the many ways that nature provides structural support for itself. This system also allows for an easy framework for bioinspiration as these nature-approved structures can and have been employed for similar functions in synthetic materials and devices. One such bioinspired example, the fabrication process of freeze casting, was the primary focus of this dissertation. Freeze casting is a process that mimics the natural templating that occurs in structures such as mammalian bone and abalone nacre, where a template of biopolymer formats and directs the deposition and formation of a biomineral. Similarly, freeze casting employs a template of a growing ice crystal to direct and align a mineral component and create porous, ceramic scaffolds.

One of the greatest advantages of the freeze casting process is the ability to significantly alter the structure and properties of the final produced materials through relatively simple alterations to the process. It was proposed in this dissertation that these changes can be considered to be of two general categories:

- *Intrinsic control*, which acts within the freeze casting process by altering the chemistry or dynamics of the freezing process itself.
- *Extrinsic control*, which acts on the freeze casting process from the exterior.

This dissertation described one bioinspired freeze casting example of each case. Intrinsic control was demonstrated through the use of chemical additives to the freeze casting process in the form of monofunctional alcohols: ethanol, isopropanol, *n*-propanol and *n*-butanol. In all cases there was shown to be an increase in the microstructural pore area at an additive concentration that was inversely proportional to the size of the additive molecule with maximum pore areas occurring at 10 vol.% for ethanol, 5 - 7 vol.% for both iso- and *n*-propanol and 3 vol.% for *n*-butanol. In the cases of both propanol additives, differential scanning calorimetry demonstrated that clathrate hydrates, non-stoichiometric solid structures with an enlarged crystal structure induced by the presence of hydrophobic molecules in a frozen aqueous environment, were present. This was determined to be, in part, the cause of the increase in the microstructural pore area. However, these were not found in the cases of ethanol or *n*-butanol. The adiabatic compressibility of all systems was tested and it was shown that hydrophobic hydration, a room temperature phenomena where hydrophobic molecules will template the liquid H_2O molecules around them, was occurring in all cases. Given the enlarged nature of the structures created by hydrophobic hydration, it was determined that these were the cause of the enlarged microstructures.

To determine the physical cause of the enlarged structures during the freezing process itself, measurements of the freezing front velocity were taken in each system. This demonstrated that the freezing front velocity does not significantly change with variations in the additive or additive concentration, however the resultant ice crystals did increase in

size. This provides evidence that the observed increase in pore area when the freeze casting process is intrinsically controlled through the use of monofunctional alcohols is not due to the anti-freeze properties of the additives, which would cause a decrease in the freezing front velocity. Instead it is suggested to be due to the increase in the size of frozen microstructures created by the presence of hydrophobic hydration and clathrate hydrates.

The mechanics of structures intrinsically controlled by the use of additive monofunctional alcohols was also investigated. The porous scaffolds were infiltrated with a second, polymeric phase and mechanically compressed. It was found that the introduction of this second phase provides buckling resistance to the ceramic structures within the freeze cast scaffolds, creating an effective buckling mode of 15 - 19 in the ceramic lamellar walls.

Extrinsic freeze casting was demonstrated through the use of sacrificial 3D printed templates. To mimic the hierarchical porosity of natural bone, which includes pores on multiple length scales, structures were created using the freeze casting process to induce smaller porosity and sacrificial 3D printed templates to induce larger porosity. The final structures, created out of biocompatible hydroxyapatite, were tested for their biocompatibility and cell viability through cell culture experiments. Preliminary results show that, after 24 hours, osteoblast-like cells had survived and aligned within the freeze cast porosity, thus providing evidence that these structures may be viable for biomedical materials.

While both intrinsic and extrinsic control have been demonstrated, the basic freeze casting process itself is subject to a significant amount of variability. Results of statistical analysis upon basic freeze cast scaffold composites at a number of different solid loadings demonstrated there is statistically significant variability in the results between individual

samples even when all of the processing conditions are held constant. This highlights the need for additional research into both intrinsic and extrinsic control of the freeze casting process to reduce this variability and ensure that samples can be created in a reproducible manner for use in biomedical and commercial applications.

Given the immense potential for bioinspired designs and techniques, freeze casting being one of them, there is a continued need for research and development within this impressive field. While the challenges that face the world can seem arduous, tapping nature's approved designs can help to ease the burden and accelerate science's path to useful solutions.

References

[1] Frank MB, Naleway SE, Wirth TS, Jung J-Y, Cheung CL, Loera FB, Medina S, Sato KN, Taylor JRA, McKittrick J. A protocol for bioinspired design: A ground sampler based on sea urchin jaws. Journal of Visualized Experiments 2016:e53554.

[2] Porter MM. Bioinspired Design: Magnetic Freeze Casting: University of California, San Diego; 2014.

[3] Reich M, Smith AB. Origins and biomechanical evolution of teeth in echnoids and their relatives. Paleontology 2009;52:1149-68.

[4] Meyers MA, Chen P-Y, Lin AYM, Seki Y. Biological materials: Structure and mechanical properties. Progress in Materials Science 2008;53:1-206.

[5] Meyers MA, McKittrick J, Chen P-Y. Structural biological materials: Critical mechanics-materials connections. Science 2013;339:773-9.

[6] Chen P-Y, Lin AYM, Lin YS, Seki Y, Stokes AG, Peyras J, Olevsky EA, Meyers MA, McKittrick J. Structure and mechanical properties of selected biological materials. Journal of the Mechanical Behavior of Biomedical Materials 2008;1:208-26.

[7] Chen P-Y, McKittrick J, Meyers MA. Biological materials: Functional adaptations and bioinspired designs. Progress in Materials Science 2012;57:1492-704.

[8] Arzt E. Biological and artificial attachment devices: Lessons for materials scientists from flies and geckos Materials Science and Engineering C 2006;26:1245-50.

[9] Meyers MA, Chen P-Y, Lopez MI, Seki Y, Lin AYM. Biological materials: A materials science approach. Journal of the Mechanical Behavior of Biomedical Materials 2011;4:626-57.

[10] Naleway SE, Taylor JRA, Porter MM, Meyers MA, McKittrick J. Structure and mechanical properties of selected protective systems in marine organisms. Materials Science and Engineering C 2016;59:1143-67.

[11] Wegst UGK, Ashby MF. The mechanical efficiency of natural materials. Philosophical Magazine 2004;84:2167-81.

[12] Naleway SE, Porter MM, McKittrick J, Meyers MA. Structural design elements in biological materials: Application to bioinspiration. Advanced Materials 2015;27:5455-76.

[13] Blank S, Arnoldi M, Khoshnavaz S, Treccani L, Kuntz M, Mann K, Grathwohl G, Fritz M. The nacre protein perlucin nucleates growth of calcium carbonate crystals. Journal of Microscopy-Oxford 2003;212:280-91.

[14] Barthelat F, Tang H, Zavattieri PD, Li CM, Espinosa HD. On the mechanics of mother-of-pearl: A key feature in the material hierarchical structure. Journal of the Mechanics and Physics of Solids 2007;55:306-37.

[15] Espinosa HD, Juster AL, Latourte FJ, Loh OY, Gregoire D, Zavattieri PD. Tablet-level origin of toughening in abalone shells and translation to synthetic composite materials. Nature Communications 2011;2.

[16] Addadi L, Joester D, Nudelman F, Weiner S. Mollusk shell formation: A source of new concepts for understanding biomineralization processes. Chemistry 2006;12:980-7.

[17] Lin AYM, Meyers MA, Vecchio KS. Mechanical properties and structure of Strombus gigas, Tridacna gigas, and Haliotis rufescens sea shells: A comparative study. Materials Science and Engineering C 2006;26:1380-9.

[18] Lin AYM, Chen P-Y, Meyers MA. The growth of nacre in the abalone shell. Acta Biomaterialia 2008;4:131-8.

[19] Lin A, Meyers MA. Growth and structure in abalone shell. Materials Science and Engineering A 2005;390:27-41.

[20] Meyers MA, Lim CT, Li A, Nizam BRH, Tan EPS, Seki Y, McKittrick J. The role of organic intertile layer in abalone nacre. Materials Science and Engineering C 2009;29:2398-410.

[21] Lopez MI, Martinez PEM, Meyers MA. Organic interlamellar layers, mesolayers and mineral nanobridges: Contribution to strength in abalone (*Haliotis rufescence*) nacre. Acta Biomaterialia 2014;10:2056-64.

[22] Chen P-Y, Toroian D, Price PA, McKittrick J. Minerals form a continuum phase in mature cancellous bone. Calcified Tissue International 2011;88:351-61.

[23] Olszta MJ, Cheng XG, Jee SS, Kumar R, Kim YY, Kaufman MJ, Douglas EP, Gower LB. Bone structure and formation: A new perspective. Materials Science and Engineering R 2007;58:77-116.

[24] Ducheyne P, Qiu Q. Bioactive ceramics: The effect of surface reactivity on bone formation and bone cell function. Biomaterials 1999;20:2287-303.

[25] Munch E, Launey ME, Alsem DH, Saiz E, Tomsia AP, Ritchie RO. Tough, bio-inspired hybrid materials. Science 2008;322:1516-20.

[26] Munch E, Saiz E, Tomsia AP, Deville S. Architectural control of freeze-cast ceramics through additives and templating. Journal of the American Ceramic Society 2009;92:1534-9.

[27] Deville S, Saiz E, Nalla RK, Tomsia AP. Freezing as a path to build complex composites. Science 2006;311:515-8.

[28] Deville S, Saiz E, Tomsia AP. Ice-templated porous alumina structures. Acta Materialia 2007;55:1965-74.

[29] Porter MM, McKittrick J, Meyers MA. Biomimetic materials by freeze casting. JOM 2013;65:720-7.

[30] Binner J, Chang H, Higginson R. Processing of ceramic-metal interpenetrating composites. Journal of the European Ceramic Society 2009;29:837-42.

[31] Chen HM, Yin YF, Dong HB, Tong Y, Luo M, Li X. Porous alumina infiltrated with melt and its dynamic analysis during pressureless infiltration. Ceramics International 2014;40:6293-9.

[32] Rao BS, Jayaram V. New technique for pressureless infiltration of Al alloys into Al_2O_3 preforms. Journal of Materials Research 2001;16:2906-13.

[33] Porter MM, Lee S, Tanadchangsaeng N, Jaremko MJ, Yu J, Meyers MA, McKittrick J. Porous hydroxyapatite-polyhydroxybutyrate composites fabricated by a novel method via centrifugation. Mechanics of Biological Systems and Materials 2013;5:63-71.

[34] Launey ME, Munch E, Alsem DH, Barth HB, Saiz E, Tomsia AP, Ritchie RO. Designing highly toughened hybrid composites through nature-inspired hierarchical complexity. Acta Materialia 2009;57:2919-32.

[35] Russias J, Saiz E, Nalla RK, Gryn K, Ritchie RO, Tomsia AP. Fabrication and mechanical properties of PLA/HA composites: A study of in vitro degradation. Materials Science and Engineering C 2006;26:1289-95.

[36] Porter MM, Imperio R, Wen M, Meyers MA, McKittrick J. Bioinspired scaffolds with varying pore architectures and mechanical properties. Advanced Functional Materials 2013;24:1978-87.

[37] Glicksman ME. Principles of solidification: An introduction to modern casting and crystal growth concepts. New York: Springer; 2011.

[38] Jackson KA. Constitutional supercooling surface roughening. Journal of Crystal Growth 2004;264:519-29.

[39] Wegst UGK, Schecter M, Donius AE, Hunger PM. Biomaterials by freeze casting. Philosophical Transactions of the Royal Society A 2010;368:2099-121.

[40] Lee S, Porter MM, Wasko S, Lau G, Chen P-Y, Novitskaya EE, Tomsia AP, Almutairi A, Meyers MA, McKittrick J. Potential bone replacement materials perpared by two methods. Materials Research Society Symposium Proceedings 2012;1418.

[41] Zhang H, Hussain I, Brust M, Butler MF, Rannard SP, Cooper AI. Aligned two- and three-dimensional structures by directional freezing of polymers and nanoparticles. Nature Materials 2005;4.

[42] Wegst UGK, Bai H, Saiz E, Tomsia AP, Ritchie RO. Bioinspired structural materials Nature Materials 2015;14:23-36.

[43] Xia ZM, Yu XH, Jiang X, Brody HD, Rowe DW, Wei M. Fabrication and characterization of biomimetic collagen-apatite scaffolds with tunable structures for bone tissue engineering. Acta Biomaterialia 2013;9:7308-19.

[44] Deville S, Saiz E, Tomsia AP. Freeze casting of hydroxyapatite scaffolds for bone tissue engineering. Biomaterials 2006;27:5480-9.

[45] Bai H, Walsh F, Gludovatz B, Delattre B, Huang C, Chen Y, Tomsia AP, Ritchie RO. Bioinspired hydroxyapatite/poly(methyl methacrylate) composite with a nacre-mimetic architecture by a bidirectional freezing method. Advanced Materials 2015:in press.

[46] Ritchie RO. Mechanisms of fatigue-crack propagation in ductile and brittle solids. International Journal of Fracture 1999;100:55-83.

[47] Han J, Hong C, Zhang X, Du J, Zhang W. Highly porous ZrO2 ceramics fabricated by a camphene-based freeze-casting route: Microstructure and properties. Journal of the European Ceramic Society 2010;30:53-60.

[48] Deville S, Viazzo C, Guizard C. Ice-structuring mechanism for zirconium acetate. Langmuir 2012;28:14892-8.

[49] Deville S, Maire E, Lasalle A, Bogner A, Gauthier C, Leloup J, Guizard C. Influence of particle size on ice nucleation and growth during the ice-templating process. Journal of the American Ceramic Society 2010;93:2507-10.

[50] Porter MM, Yeh M, Strawson J, Goehring T, Lujan S, Siripasopsotorn P, Meyers MA, McKittrick J. Magnetic freeze casting inspred by nature. Materials Science and Engineering A 2012;556:741-50.

[51] Zhang Y, Hu L, Han J. Preparation of a dense/porous bilayered ceramic by applying an electric field during freeze casting. Journal of the American Ceramic Society 2009;92:1874-6.

[52] Tang YF, Miao Q, Qiu S, Zhao K, Hu L. Novel freeze-casting fabrication of aligned lamellar porous alumina with a centrosymmetric structure. Journal of the European Ceramic Society 2014;34:4077-82.

[53] Naleway SE, Fickas KC, Maker YN, Meyers MA, McKittrick J. Reproducibility of ZrO_2-based freeze casting for biomaterials. Materials Science and Engineering C 2016;61:105-12.

[54] Aladko LS, Mankov AY, Ogienko AG, Ancharov AI. New data on phase diagram and clathrate formation in the system water-isopropyl alcohol. Journal of Inclusion Phenomena and Macrocyclic Chemistry 2009;63:151-7.

[55] Ott JB, Goates JR, Waite BA. (Solid + liquid) phase-equilibria and solid-hydrate formation in water + methyl, + ethyl, + isopropyl, and + tertiary butyl alcohols. Journal of Chemical Thermodynamics 1979;11:739-46.

[56] Murthy SSN. Detailed study of ice clathrate relaxation: Evidence for the existence of clathrate structures in some water-alcohol mixtures. Journal of Physical Chemistry A 1999;103:7927-37.

[57] Manakov AY, Aladko LS, Ogienko AG, Ancharov AI. Hydrate formation in the system n-propanol-water. Journal of Thermal Analysis and Calorimetry 2013;111:885-90.

[58] Takaizumi K. Liquid-solid phase diagrams of PrOH-water and BuOH-water systems from differential scanning calorimetry. Journal of Solution Chemistry 2000;29:377-88.

[59] Mora C, Tittensor DP, Adl S, Simpson AGB, Worm B. How many species are there on earth and in the ocean? PLOS one 2011;9:e1001127.

[60] McKittrick J, Chen P-Y, Tombolato L, Novitskaya EE, Trim MW, Hirata GA, Olevsky EA, Horstemeyer MF, Meyers MA. Energy absorbent natural materials and bioinspired design strategies: A review. Materials Science and Engineering C 2010;30:331-42.

[61] Fudge DS, Gardner KH, Forsyth VT, Riekel C, Gosline JM. The mechanical properties of hydrated intermediate filaments: Insights from hagfish slime threads. Biophysical Journal 2003;85:2015-27.

[62] Ottani V, Martini D, Franchi M, Ruggeri A, Raspanti M. Hierarchical structures in fibrillar collagens. Micron 2002;33:587-96.

[63] Kluge JA, Rabotyagova O, Leisk GG, Kaplan DL. Spider silks and their applications. Trends in Biotechnology 2008;26:244-51.

[64] Lenau T, Barfoed M. Colours and metallic sheen in beetle shells - A biomimetic search for material structuring principles causing light interference. Advanced Engineering Materials 2008;10:299-314.

[65] Weaver JC, Milliron GW, Miserez A, Evans-Lutterodt K, Herrera S, Gallana I, Mershon WJ, Swanson B, Zavattieri P, DiMasi E, Kisailus D. The stomatopod dactyl club: A formidable damage-tolerant biological hammer. Science 2012;336:1275-80.

[66] Aizenberg J, Weaver JC, Thanawala MS, Sundar VC, Morse DE, Fratzl P. Skeleton of Euplectella sp.: Structural hierarchy from the nanoscale to the macroscale. Science 2005;309:275-8.

[67] Bechtle S, Fett T, Rizzi G, Habelitz S, Klocke A, Schneider GA. Crack arrest within teeth at the dentinoenamel junction caused by elastic modulus mismatch. Biomaterials 2010;31:4238-47.

[68] Cribb BW, Rathmell A, Charters R, Rasch R, Huang H, Tibbetts IR. Structure, composition and properties of naturally occurring non-calcified crustacean cuticle. Arthopod Structure & Development 2009;38:173-8.

[69] Miserez A, Schneberk T, Sun CJ, Zok FW, Waite JH. The transition from stiff to compliant materials in squid beaks. Science 2008;319:1816-9.

[70] Chen P-Y, Schirer J, Simpson A, Nay R, Lin Y-S, Yang W, Lopez MI, Li J, Olevsky EA, Meyers MA. Predation versus protection: Fish teeth and scales evaluated by nanoindentation. Journal of Materials Research 2012;27:100-12.

[71] Kinney JH, Marshall SJ, Marshall GW. The mechanical properties of human dentin: A critical review and re-evaluation of the dental literature. Critical Reviews in Oral Biology and Medicine 2003;14:13-29.

[72] Yang W, Gludovatz B, Zimmermann EA, Bale HA, Ritchie RO, Meyers MA. Structure and fracture resistance of alligator gar (Atractosteus spatula) armored fish scales. Acta Biomaterialia 2013;9:5876-89.

[73] Tombolato L, Novitskaya EE, Chen P-Y, Sheppard FA, McKittrick J. Microstructure, elastic properties and deformation mechanisms of horn keratin. Acta Biomaterialia 2010;6:319-30.

[74] Yang W, Chao C, McKittrick J. Axial compression of a hollow cylinder filled with foam: A study of porcupine quills. Acta Biomaterialia 2013;9:5297-304.

[75] Chen P-Y, Stokes AG, McKittrick J. Comparison of the structure and mechanical properties of bovine femur bone and antler of the North American elk (Cervus elaphus canadensis). Acta Biomaterialia 2009;5:693-706.

[76] Hamza S, Slimane N, Azari Z, Pluvinage G. Structural and mechanical properties of the coral and nacre and the potentiality of their use as bone substitutes. Applied Surface Science 2013;264:485-91.

[77] Yang W, Naleway SE, Porter MM, Meyers MA, McKittrick J. The armored carapace of the boxfish. Acta Biomaterialia 2015;23:1-10.

[78] Krauss S, Monsonego-Ornan E, Zelzer E, Fratzl P, Shahar R. Mechanical function of a complex three-dimensional suture joining the bony elements in the shell of the red-eared slider turtle. Advanced Materials 2009;21:407-12.

[79] Li Y, Ortiz C, Boyce MC. A generalized mechanical model for suture interfaces of arbitrary geometry. Journal of the Mechanics and Physics of Solids 2013;61:1144-67.

[80] Porter MM, Novitskaya EE, Castro-Cesena AB, Meyers MA, McKittrick J. Highly deformable bones: Unusual deformation mechanisms of seahorse armor. Acta Biomaterialia 2013;9:6763-70.

[81] Dastjerdi AK, Barthelat F. Teleost fish scales amongst the toughest collagenous materials. Journal of the Mechanical Behavior of Biomedical Materials 2015:in press.

[82] Connors MJ, Ehrlich H, Hog M, Godeffroy C, Araya S, Kallai I, Gazit D, Boyce M, Ortiz C. Three-dimensional structure of the shell plate assembly of the chiton *Tonicella marmorea* and its biomechanical consequences. Journal of Structural Biology 2012;177:314.

[83] Vollrath F. Strength and structure of spiders' silk. Molecular Biotechnology 2000;74:67-83.

[84] Fudge DS, Gosline JM. Molecular design of the alpha-keratin composite: Insights from a matrix-free model, hagfish slime threads. Proceedings of the Royal Society B 2004;271:291-9.

[85] Fudge DS, Levy N, Chiu S, Gosline JM. Composition, morphology and mechanics of hagfish slime. Journal of Experimental Biology 2005;208:4613-25.

[86] Sherman VR, Yang W, Meyers MA. The materials science of collagen. Journal of the Mechanical Behavior of Biomedical Materials 2015.

[87] Gautieri A, Vesentini S, Redaelli A, Buehler MJ. Hierarchical structure and nanomechanics of collagen microfibrils from the atomistic scale up. Nano Letters 2011;11:757-66.

[88] Lanir Y. Structure-strength relations in mammalian tendon. Biophysical Journal 1978;24:541-54.

[89] Freed AD, Doehring TC. Elastic model for crimped collagen fibrils. Journal of Biomechanical Engineering 2005;127:587-93.

[90] Ogden RW. Large deformation isotropic elasticity - Correlation of theory and experiment for incompressible rubberlike solids. Proceedings of the Royal Society of London Series A 1972;326:565-84.

[91] Arruda EM, Boyce MC. A 3-dimensional constitutive model for the large stretch behavior of rubber elastic-materials. Journal of the Mechanics and Physics of Solids 1993;41:389-412.

[92] Fung YC. Biomechanics: Mechanical Porperties of Living Tissues. 2 ed. New York, NY: Springer; 1993.

[93] Yamamoto T, Hasegawa T, Sasaki M, Hongo H, Tabata C, Liu ZS, Li MQ, Amizuka N. Structure and formation of the twisted plywood pattern of collagen fibrils in rat lamellar bone. Journal of Electron Microscopy 2012;61:113-21.

[94] Weaver JC, Aizenberg J, Fantner GE, Kisailus D, Woesz A, Allen P, Fields K, Porter MJ, Zok FW, Hansma PK, Fratzl P, Morse DE. Hierarchical assembly of the siliceous skeletal lattice of the hexactinellid sponge Euplectella aspergillum. Journal of Structural Biology 2007;158:93-106.

[95] Bouligand Y. Twisted fiberous arrangements in biological materials and cholesteric mesophases. Tissue & Cell 1972;4:189-217.

[96] Zimmermann EA, Gludovatz B, Schaible E, Dave NKN, Yang W, Meyers MA, Ritchie RO. Mechanical adaptability of the Bouligand-type structure in natural dermal armour. Nature Communications 2013;4:2634.

[97] Yang W, Sherman VR, Gludovatz B, Mackey M, Zimmermann EA, Chang EH, Schaible E, Qin Z, Buehler MJ, Ritchie RO, Meyers MA. Protective role of

Arapaima gigas fish scales: Structure and mechanical behavior. Acta Biomaterialia 2014;10:3599–614.

[98] Neville AC. Biological fibrous composites: Devlopment beyond the cell membrane. New York, NY: Cambridge University Press; 1993.

[99] Zhu D, Ortega CF, Motamedi R, Szewciw L, Vernerey F, Barthelat F. Structure and mechanical performance of a "modern" fish scale. Advanced Engineering Materials 2012;14:B185-B94.

[100] Guarín-Zapata N, Gomez J, Yaraghi N, Kisailus D, Zavattieri PD. Shear wave filtering in naturally-occurring Bouligand structures. Acta Biomaterialia 2015;23:11-20.

[101] Kingsley MCS, Ramsay MA. The spiral in the tusk of the narwhal. Arctic 1988;41:236-8.

[102] Skatter S, Kucera B. Spiral grain—An adaptation of trees to withstand stem breakage caused by wind-induced torsion Holz als Roh- und Werkstoff 1997;55:207-13.

[103] Porter MM, Meraz L, Calderon A, Choi H, Chouhan A, Wang L, Meyers MA, McKittrick J. Torsional properties of helix-reinforced composites fabricated by magnetic freeze casting. Composite Structures 2015;119:174-84.

[104] Thompson DAW. On growth and form. Cambridge: Cambridge University Press; 1917.

[105] Harary G, Tal A. The natural 3D spiral. Computer Graphics Forum 2011;30:237-46.

[106] Bruet BJF, Song JH, Boyce MC, Ortiz C. Materials design principles of ancient fish armour. Nature Materials 2008;7:748-56.

[107] Roy S, Basu B. Mechanical and tribological characterization of human tooth. Materials Characterization 2008;59:747-56.

[108] Suresh S. Graded materials for resistance to contact deformation and damage. Science 2001;292:2447-51.

[109] Suresh S, Giannakopoulos AE, Alcala J. Spherical indentation of compositionally graded materials: Theory and experiments. Acta Materialia 1997;45:1307-21.

[110] Choi IS, Dao M, Suresh S. Mechanics of indentation of plastically graded materials - I: Analysis. Journal of the Mechanics and Physics of Solids 2008;56:157-71.

[111] Giannakopoulos AE, Suresh S. Indentation of solids with gradients in elastic properties .1. Point force. International Journal of Solids and Structures 1997;34:2357-92.

[112] Giannakopoulos AE, Suresh S, Finot M, Olsson M. Elastoplastic analysis of thermal cycling - Layered materials with compositional gradients. Acta Metallurgica 1995;43:1335-54.

[113] Kim AS, Suresh S, Shih CF. Plasticity effects on fracture normal to interfaces with homogeneous and graded compositions. International Journal of Solids and Structures 1997;34:3415-32.

[114] Kim AS, Besson J, Pineau A. Global and local approaches to fracture normal to interfaces. International Journal of Solids and Structures 1999;36:1845-64.

[115] Imbeni V, Kruzic JJ, Marshall GW, Marshall SJ, Ritchie RO. The dentin-enamel junction and the fracture of human teeth. Nature Materials 2005;4:229-32.

[116] Miserez A, Rubin D, Waite JH. Cross-linking chemistry of squid beak. Journal of Biological Chemistry 2010;285:38115–24.

[117] Woesz A, Weaver JC, Kazanci M, Dauphin Y, Aizenberg J, Morse DE, Fratzl P. Micromechanical properties of biological silica in skeletons of deep-sea sponges. Journal of Materials Research 2006;21:2068-78.

[118] Menig R, Meyers MH, Meyers MA, Vecchio KS. Quasi-static and dynamic mechanical response of Haliotis rufescens (abalone) shells Acta Materialia 2000;48:2383-93.

[119] Barthelat F, Espinosa HD. An experimental investigation of deformation and fracture of nacre-mother of pearl. Experimental Mechanics 2007;47:311-24.

[120] Hughes PM. Insect cuticular growth layers seen under the scanning electron microscope: a new display method. Tissue & Cell 1987;19:705-12.

[121] Anderson TL. Fracture Mechanics Fundamentals and Applications. 3rd ed. Boca Raton: Taylor & Francis Group; 2005.

[122] Nalla RK, Kruzic JJ, Ritchie RO. On the origin of the toughness of mineralized tissue: Microcracking or crack bridging? Bone 2004;34:790-8.

[123] Launey ME, Buehler MJ, Ritchie RO. On the mechanistic origins of toughness in bone. Annual Review of Materials Science 2010;40:25-53.

[124] Launey ME, Chen P-Y, McKittrick J, Ritchie RO. Mechanistic aspects of the fracture toughness of elk antler bone. Acta Biomaterialia 2010;6:1505-14.

[125] Ritchie RO, Buehler MJ, Hansma P. Plasticity and toughness in bone. Physics Today 2009;62:41-7.

[126] Ritchie RO. The conflicts between strength and toughness. Nature Materials 2011;10:817-22.

[127] Menig R, Meyers MH, Meyers MA, Vecchio KS. Quasi-static and dynamic mechanical response of Strombus gigas (conch) shells Materials Science and Engineering A 2001;297:203-11.

[128] Kasapi MA, Gosline JM. Design complexity and fracture control in the equine hoof wall. Journal of Experimental Biology 1997;200:1639-59.

[129] Trim MW, Horstemeyer MF, Rhee H, Le Kadiri H, Williams LN, Liao J, Walters KB, McKittrick J, Park SJ. The effects of water and microstructure on the mechanical properties of bighorn sheep (Ovis canadensis) horn keratin Acta Biomaterialia 2011;7:1228-40.

[130] Chen P-Y, Lin AYM, McKittrick J, Meyers MA. Structure and mechanical properties of crab exoskeletons. Acta Biomaterialia 2008;4:587-96.

[131] Kasapi MA, Gosline JM. Exploring the possible functions of equine hoof wall tubules. Equine Veterinary Journal 1998;26:10-4.

[132] Nalla RK, Kinney JH, Ritchie RO. Effect of orientation on the in vitro fracture toughness of dentin: The role of toughening mechanisms. Biomaterials 2003;24:3955-68.

[133] Ritchie RO, Kinney JH, Kruzic JJ, Nalla RK. A fracture mechanics and mechanistic approach to the failure of cortical bone. Fatigue & Fracture of Engineering Materials & Structures 2005;28:345-71.

[134] Petrtyl M, Hert J, Fiala P. Spatial organization of the haversian bone in man. Journal of Biomechanics 1996;29:161-9.

[135] Seki Y, Schneider MS, Meyers MA. Structure and mechanical behavior of a toucan beak. Acta Materialia 2005;53:5281-96.

[136] Rhee H, Horstemeyer MF, Hwang Y, Lim H, El Kadiri H, Trim W. A study on the structure and mechanical behavior of the Terrapene carolina carapace: A pathway to design bio-inspired synthetic composites. Materials Science and Engineering C 2009;29:2333-9.

[137] Gibson LJ, Ashby MF. Cellular Solids: Structure and Properties. 2 ed. Cambridge: Cambridge University Press; 1997.

[138] Ashby MF. The mechanical-properties of cellular solids. Metallurgical and Materials Transactions A 1983;14:1755-69.

[139] Gibson LJ. Biomechanics of cellular solids. Journal of Biomechanics 2005;38:377-99.

[140] Yang W, McKittrick J. Separating the influence of the cortex and foam on the mechanical properties of porcupine quills. Acta Biomaterialia 2013;9:9065-74.

[141] Seki Y, Bodde SG, Meyers MA. Toucan and hornbill beaks: A comparative study. Acta Biomaterialia 2010;6:331-43.

[142] Liu ZQ, Jiao D, Meyers MA, Zhang ZF. Structure and mechanical properties of naturally occurring lightweight foam-filled cylinder - The peacock's tail coverts shaft and its components. Acta Biomaterialia 2015;17:137-51.

[143] Karam GN, Gibson LJ. Elastic buckling of cylindrical-shells with elastic cores .1. Analysis. International Journal of Solids and Structures 1995;32:1259-83.

[144] Karam GN, Gibson LJ. Elastic buckling of cylindrical-shells with elastic cores .2. Experiments. International Journal of Solids and Structures 1995;32:1285-306.

[145] Gill FB. Ornithology. 3rd ed. New York, NY: W.H. Freeman & Company; 2007.

[146] Proctor NS, Lynch PJ. Manual of Ornithology: Avian Structure and Function. New Haven, CT: Yale University Press; 1993.

[147] O'Connor PM, Claessens LPAM. Basic avian pulmonary design and flow-through ventilation in non-avian theropod dinosaurs Nature 2005;436:253-6.

[148] Currey JD, Alexander RM. The thickness of the walls of tubular bones. Journal of Zoology 1985;206:453-68.

[149] Young WC, Budynas RG, Sadegh AM. Roark’s Formulas for Stress and Strain. 8 ed. New York, NY: McGraw Hill; 2012.

[150] Pennycuick CJ. Modelling the Flying Bird. San Diego, CA: Elseview Academic Press; 2008.

[151] Chen IH, Yang W, Meyers MA. Leatherback sea turtle shell: A tough and flexible biological design. Acta Biomaterialia 2015;28:2-12.

[152] Nicolay CW, Vaders MJ. Cranial suture complexity in white-tailed deer (Odocoileus virginianus). Journal of Morphology 2006;267:841-9.

[153] Jaslow CR. Mechanical-properties of cranial sutures. Journal of Biomechanics 1990;23:313-21.

[154] Song JH, Reichert S, Kallai I, Gazit D, Wund M, Boyce MC, Ortiz C. Quantitative microstructural studies of the armor of the marine threespine stickleback (Gasterosteus aculeatus). Journal of Structural Biology 2010;171:318-31.

[155] Gebeshuber IC, Kindt JH, Thompson JB, Del Amo Y, Stachelberger H, Brzezinski MA, Stucky GD, Morse DE, Hansma PK. Atomic force microscopy study of living diatoms in ambient conditions. Journal of Microscopy-Oxford 2003;212:292-9.

[156] Chen IH, Kiang JH, Correa V, Lopez MI, Chen P-Y, McKittrick J, Meyers MA. Armadillo armor: Mechanical testing and micro-structural evaluation. Journal of the Mechanical Behavior of Biomedical Materials 2011;4:713-22.

[157] Li Y, Ortiz C, Boyce MC. Bioinspired, mechanical, deterministic fractal model for hierarchical suture joints. Physical Review E 2012;85:031901.

[158] Li Y, Ortiz C, Boyce MC. Stiffness and strength of suture joints in nature. Physical Review E 2011;84:062904.

[159] Lin E, Li YN, Weaver JC, Ortiz C, Boyce MC. Tunability and enhancement of mechanical behavior with additively manufactured bio-inspired hierarchical suture interfaces. Journal of Materials Research 2014;29:1867-75.

[160] Yang W, Chen IH, Gludovatz B, Zimmermann EA, Ritchie RO, Meyers MA. Natural flexible dermal armor. Advanced Materials 2013;25:31-48.

[161] Sosinka A, Rost-Roszkowska MM, Vilimova J, Tajovsky K, Kszuk-Jendrysik M, Chajec L, Sonakowska L, Kaminska K, Hyra M, Poprawa I. The ultrastructure of the midgut epithelium in millipedes (*Myriapoda*, *Diplopoda*). Arthopod Structure & Development 2014;43:477-92.

[162] Browning A, Ortiz C, Boyce MC. Mechanics of composite elasmoid fish scale assemblies and their bioinspired analogues. Journal of the Mechanical Behavior of Biomedical Materials 2013;19:75-86.

[163] Lin YS, Wei CT, Olevsky EA, Meyers MA. Mechanical properties and the laminate structure of Arapaima gigas scales. Journal of the Mechanical Behavior of Biomedical Materials 2011;4:1145-56.

[164] Vernerey FJ, Barthelat F. Skin and scales of teleost fish: Simple structure but high performance and multiple functions Journal of the Mechanics and Physics of Solids 2014;68:66-76.

[165] Vernerey FJ, Barthelat F. On the mechanics of fishscale structures International Journal of Solids and Structures 2010;47:2268-75.

[166] Vernerey FJ, Musiket K, Barthelat F. Mechanics of fish skin: A computational approach for bio-inspired flexible composites. International Journal of Solids and Structures 2014;51:274-83.

[167] Zhu DJ, Szewciw L, Vernerey F, Barthelat F. Puncture resistance of the scaled skin from striped bass: Collective mechanisms and inspiration for new flexible armor designs Journal of the Mechanical Behavior of Biomedical Materials 2013;24:30-40.

[168] Porter MM, Adriaens D, Hatton RL, Meyers MA, McKittrick J. Why the seahorse tail is square. Science 2015;349:aaa6683.

[169] Lazaris A, Arcidiacono S, Huang Y, Zhou J-F, Duguay F, Chretien N, Welsh EA, Soares JW, Karatzas CN. Spider silk fibers spun from soluble recombinant silk produced in mammalian cells. Science 2002;295:472-6.

[170] Xia X-X, Qian Z-G, Ki CS, Park YH, Kaplan DL, Lee SY. Native-sized recombinant spider silk protein produced in metabolically engineering Escherichia coli results in a strong fiber. PNAS 2010;107:14059-63.

[171] Vollrath F, Knight DP. Liquid crystalline spinning of spider silk. Nature 2001;410:541-8.

[172] Zhang SG. Fabrication of novel biomaterials through molecular self-assembly. Nature Biotechnology 2003;21:1171-8.

[173] Grunenfelder LK, Suksangpanya N, Salinas C, Milliron G, Yaraghi N, Herrera S, Evans-Lutterodt K, Nutt SR, Zavattieri P, Kisailus D. Bio-inspired impact-resistant composites. Acta Biomaterialia 2014;10:3997-4008.

[174] Milliron G. Lightweight impact-resistant composite materials: Lessons from mantis shrimp: UC Riverside; 2012.

[175] Erb RM, Libanori R, Rothfuchs N, Studart AR. Composites reinforced in three dimensions by using low magnetic fields Science 2012;335:199-204.

[176] Bouville F, Maire E, Meille S, Van de Moortele B, Stevenson AJ, Deville S. Strong, tough and stiff bioinspired ceramics from brittle constituents Nature Materials 2014;13:508-14.

[177] Corni I, Harvey TJ, Wharton JA, Stokes KR, Walsh FC, Wood RJK. A review of experimental techniques to produce a nacre-like structure. Bioinspiration & Biomimetics 2012;7:031001.

[178] Kou L, Gao C. Bioinspired design and macroscopic assembly of poly(vinyl alcohol)-coated graphene into kilometers-long fibers. Nanoscale 2013;5:4370-8.

[179] Tampieri A, Sprio S, Ruffini A, Celotti G, Lesci IG, Roveri N. From wood to bone: Multi-step process to convert wood hierarchical structures into biomimetic hydroxyapatite scaffolds for bone tissue engineering Journal of Materials Chemistry 2009;19:4973-80.

[180] Compton BG, Lewis JA. 3D-printing of lightweight cellular composites Advanced Materials 2014;26:5930-5.

[181] Mirkhalaf M, Dastjerdi AK, Barthelat F. Overcoming the brittleness of glass through bio-inspiration and micro-architecture Nature Communications 2014;5:3166.

[182] Hench LL. Bioceramics - from concept to clinic. Journal of the American Ceramic Society 1991;74:1487-510.

[183] van der Waals JH, Platteeuw JC. Clathrate Solutions. Advances in Chemical Physics 1959;2:1-57.

[184] Englezos P. Clathrate hydrates. Industrial and Engineering Chemistry Research 1993;32:1251-74.

[185] Klapp SA, Bohrmann G, Kuhs WF, Murshed MM, Pape T, Klein H, Techmer KS, Heeschen KU, Abegg F. Microstructures of structure I and II gas hydrates from the Gulf of Mexico. Marine and Petroleum Geology 2010;27:116-25.

[186] Potts AD, Davidson DW. Ethanol hydrate. Journal of Physical Chemistry 1965;69:996-1000.

[187] Rottger K, Endriss A, Ihringer J, Doyle S, Kuhs WF. Lattice-constants and thermal-expansion of H2O and D2O ice Ih between 10 and 265 K. Acta Crystallographica B 1994;50:644-8.

[188] Naleway SE, Yu CF, Porter MM, Sengupta A, Iovine PM, Meyers MA, McKittrick J. Bioinspired composites from freeze casting with clathrate hydrates. Materials & Design 2015;71:62-7.

[189] Naleway SE, Yu CF, Hsiong RL, Sengupta A, Iovine PM, Hildebrand JA, Meyers MA, McKittrick J. Bioinspired intrinsic control of freeze cast composites: Harnessing hydrophobic hydration and clathrate hydrates. Acta Materialia 2016:accepted.

[190] Burakowski A, Glinski J. Additivity of adiabatic compressibility with the size and geometry of the solute molecule. Journal of Molecular Liquids 2008;137:25-30.

[191] Jerie K, Baranowski A, Rozenfeld B, Glinski J, Ernst S. Positron-annihilation in and compressibility of water alcohol mixtures. Physica Scripta 1987;35:729-34.

[192] Glinski J, Burakowski A. Compressibility of aqueous solutions of nonelectrolytes: An equilibrium model. Journal of Chemical Physics 2010;132:124507.

[193] Chapoy A, Anderson R, Haghighi H, Edwards T, Tohidi B. Can n-propanol form hydrate? Industrial & Engineering Chemistry Research 2008;47:1689-94.

[194] Zelenin YM. Effect of pressure on clathrate formation in a water-ethanol system. Journal of Structural Chemistry 2003;44:130-6.

[195] Franks F, Desnoyers JE. Alcohol-water mixtures revisited. Water Science Reviews 1985;1:171-232.

[196] Galamba N. Water's structure around hydrophobic solutes and the iceberg model. Journal of Physical Chemistry B 2013;117:2153-9.

[197] Burakowski A, Glinski J. Hydration numbers of non-electrolytes - Application of the acoustic method of Pasynski. Chemical Physics 2007;332:336-40.

[198] Bowron DT, Filipponi A, Roberts MA, Finney JL. Hydrophobic hydration and the formation of a clathrate hydrate. Physical Review Letters 1998;81:4164-7.

[199] Burakowski A, Glinski J. Hydration numbers of nonelectrolytes from acoustic methods. Chemical Reviews 2012;112:2059-81.

[200] Glinski J, Burakowski A. Modification of the Pasynski method for determining the hydration numbers of nonelectrolytes. Chemical Physics Letters 2013;566:21-4.

[201] Glinski J, Burakowski A. Hydration constants of simple non-electrolytes in aqueous solutions determined by the acoustic method. Chemical Physics Letters 2014;614:49-52.

[202] Glinski J, Burakowski A. New interpretation of the concentration dependence of the compressibility of aqueous solutions of nonelectrolytes. International Journal of Thermophysics 2011;32:786-94.

[203] Urick RJ. A sound velocity method for determining the compressibility of finely divided substances. Journal of Applied Physics 1947;18:983-7.

[204] Horváth-Szabóa G, Høiland H. Compressibility determination of silica particles by ultrasound velocity and density measurements on their suspensions. Journal of Colloid and Interface Science 1996;177:568-78.

[205] Caravaca MA, Mino JC, Perez VJ, Casali RA, Ponce CA. *Ab initio* study of the elastic properties of single and polycrystal TiO_2, ZrO_2 and HfO_2 in the cotunnite structure. Journal of Physics: Condensed Matter 2009;21:015501.

[206] Molina-Bolivar JA, Ortega-Vinuesa JL. How proteins stabilize colloidal particles by means of hydration forces. Langmuir 1999;15:2644-53.

[207] Sherman NE. Ultrasonic velocity and attenuation in aqueous kaolin dispersions. Journal of Colloid and Interface Science 1991;146:405-14.

[208] Piconi C, Maccauro G. Zirconia as a ceramic biomaterial Biomaterials 1999;20:1-25.

[209] Boresi AP, Schmidt RJ. Advanced Mechanics of Materials. 6 ed. Hoboken, NJ: Wiley; 2003.

[210] Weiner S, Traub W, Wagner HD. Lamellar bone: Structure-function relations. Journal of Structural Biology 1999;126:241-55.

[211] Rottger K, Endriss A, Ihringer J, Doyle S, Kuhs WF. Lattice-constants and thermal-expansion of H_2O and D_2O ice Ih between 10 and 265 K. Acta Crystallographica B 1994;50:644-8.

[212] Deville S. Freeze-casting of porous ceramics: A review of current achievements and issues. Advanced Engineering Materials 2008;10:155-69.

[213] Hunger PM, Donius AE, Wegst UGK. Platelets self-assemble into porous nacre during freeze casting. Journal of the Mechanical Behavior of Biomedical Materials 2013;19:87-93.

[214] Deville S, Maire E, Lasalle A, Bogner A, Gauthier C, Leloup J, Guizard C. In situ X-ray radiography and tomography obsercations of the solidification of aqueous alumina particle suspensions-Part I: Initial instants. Journal of the American Ceramic Society 2009;92:2489-96.

[215] Deville S, Adrien J, Maire E, Scheel M, Di Michiel M. Time-lapse, three-dimensional in situ imaging of ice crystal growth in a colloidal silica suspension. Acta Materialia 2013;61:2077-86.

[216] Bai H, Wang D, Delattre B, Gao WW, De Coninck J, Li S, Tomsia AP. Biomimetic gradient scaffold from ice-templating for self-seeding of cells with capillary effect. Acta Biomaterialia 2015;20:113-9.

[217] Porter MM, McKittrick J. It's tough to be strong: Advances in bioinspired structural ceramic-based materials. American Ceramic Society Bulletin 2014;93:18-24.

[218] Yoon B-H, Koh Y-H, Park C-S, Kim H-E. Generation of large pore channels for bone tissue engineering using camphene-based freeze casting. Journal of the American Ceramic Society 2007;90:1744-52.

[219] http://www.3dsystems.com/materials/visijetr-m3-x.

[220] Fu Q, Rahaman MN, Dogan F, Bal BS. Freeze-cast hydroxyapatite scaffolds for bone tissue engineering applications. Biomedical Materials 2008;3:025005.

[221] Naleway SE, Jung J-Y, Hur SS, Maker YN, Ix M, Chien S, Meyers MA, McKittrick J. 3D printed templating of freeze casting for macro-micro porous bioinspired scaffolds. 2016:in preparation.

[222] Deville S. Ice-templating, freeze casting: Beyond materials processing. Journal of Materials Research 2013;28:2202-19.

[223] Tabachnick BG, Fidell LS. Using Multivariate Statistics. 6 ed. Boston, MA: Pearson; 2013.

[224] Manhart J, Kunzelmann KH, Chen HY, Hickel R. Mechanical properties of new composite restorative materials. Journal of Biomedical Materials Research 2000;53:353-61.

[225] Albakry M, Guazzato M, Swain MV. Fracture toughness and hardness evaluation of three pressable all-ceramic dental materials. Journal of Dentistry 2003;31:181-8.

[226] Chun KJ, Lee JY. Comparative study of mechanical properties of dental restorative materials and dental hard tissues in compressive loads. Journal of Dental Biomechanics 2014;5:1-6.

[227] Deville S. Freeze-casting of porous biomaterials: structure, properties and opportunities. Materials 2010;3:1913-27.